Munazza Mohsin

Accelerated Voltage Cycling Tests of Polymer Electrolyte Membrane Fuel Cells

DOCTORAL THESIS

For obtaining the academic degree of

Doctoral Programme of Technical Sciences

Technical Chemistry

Graz University of Technology

Supervisor: Assoc.Prof. Dipl.-Ing. Dr.techn. Viktor Hacker

Institute of Chemical Engineering and Environmental Technology

Laboratory for Fuel Cell Systems, Graz, Austria

2011

Dedicated

To

My Parents who nurtured and groomed me,

My mother in law who inspired me,
&
My family

(Fatima, Qasim & Mohsin) who supported me

Acknowledgement

First of all I would like to express immense gratitude to Almighty God who created me as human being, blessed me with all the senses to understand the meaning of creation as it has been stated in His Holy Book, Quran, “Behold! In the creation of the heavens and the earth and the alternation of night and day, there are indeed signs for men of understanding (chapter 3, Al-imran, verse, 90)’’. To explore the knowledge and, further, moving towards research is the basic understanding of the above Verse.

My thrust of acquiring knowledge also came from the great saying of the last prophet Muhammad (peace be upon him), “Acquisition of knowledge is a duty incumbent on every muslim, male and female’’.

It is a time to pen down few lines about honorable supervisor, Assoc.Prof. Dipl.-Ing. Dr.techn. Viktor Hacker. I would offer my heartiest gratitude and special respect to him for his dedicated mentorship and tremendous amount of support. His kind and sophisticated attitude prevailed throughout the PhD programme. During my entire stay in the fuel cell laboratory, I never felt hesitation to communicate with him. No matter how hectic his schedule and how insignificant my question, he always spared some time to listen my problems.

I am highly indebted to the Ao.Univ.-Prof. Dipl.-Ing. Dr.techn. Karl Gatterer who took the onus of responsibility of being the external advisor for the dissertation. Prof Gatterer is a fabulous advisor: sharp, cheery, perceptive and mindful of things that truly matter.

I am very much grateful to the Head of the Institute and chair of the dissertation committee, Univ.-Prof. Dipl.-Ing. Dr.techn. Matthäus Siebenhofer for his prestigious and caring style of dealings with the colleagues and the students.

I wish to acknowledge the support of Oberrat Dipl.-Ing. Dr.techn. Univ.-Doz. Peter Pölt and Mrs. Sanja simic regarding SEM and EDS measurements at the Institute for Electron Microscopy and Fine Structure Research, TUGraz, Austria.

Special thanks for my colleagues Gerd, Markus T., Immanuel, Reinhard, Daniel, Astrid and Eva for their co-operation and assistance in experimental work and thought provoking discussions. The company of my ex-colleagues; Marta, Adina, Reingard, Betina, Markus P. and Peter shall be remembered for their co-operation and kindness. I am also thankful to the secretary, Carmen for being so helpful with bureaucratic matters and more.

It is worth to mention the role being played by Higher Education Commission (HEC) of Pakistan. The present pursuit for PhD studies was only possible with financial assistance from HEC.

The fulfillment of my dream, to acquire the PhD degree, could not be possible without the wholehearted support of my mother in law. Whose real efforts bore the fruit but alas now she is no more with us in this world, but her efforts shall never be faded up.

It is also high time to mention the practical role of my parents being played in my whole life, especially for education and knowledge. From my childhood up to higher education in all steps, I found them standing with me like a pillar. My father though no longer with us, remains the compass of my life. I also thank my sister and two brothers for their generous support and love. They all shared the idea that I had the capacity in my mind worth cultivating.

Solute to my husband Muhammad Mohsin-Ul-Mulk for his unending support and encouragement along with his extra ordinary co-operation in taking care of children (especially my daughter ,Fatima who was born during the Ph.D. duration).Extensive long hours of research work without any tension was impossible without the moral support encouragement, understanding and love. Above all I am also thankful to my children (Qasim and Fatima) who brought me the unprecedented joy during arduous working hours.

Abstract

Polymer Electrolyte Membrane (PEM) fuel cell is considered as an alternative energy converter to be used for automotive, portable and stationary applications. The degradation of carbon supported Pt catalysts play an important role in decreasing the life time of PEM fuel cells. Test series were performed to investigate the durability of Pt based catalyst of PEM fuel cell for automotive industry. In this test series the Pt surface area loss at the cathode side of the fuel cells due to peak-power to idle load cycling was measured.

Eleven Fuel cells were fabricated with two different types of commercial Membrane Electrode Assemblies (MEAs) and examined through the accelerated voltage cycling test at different values of relative humidity (RH). During the experiment the in-situ diagnostic techniques were utilized to record Polarization Curves, Electrochemical Impedance Spectra (EIS), Hydrogen Diffusion Current Measurements and Cyclic Voltammograms (CV) after completion of specific number of voltage cycles for each fuel cell. With these Cyclic Voltammograms the active Pt surface area for all the cells were calculated. The results show that with the increase of the number of voltage cycles there is a continuous decrease in the active platinum surface area and the life time of the fuel cell operated at 90% relative humidity was proved to be the maximum as compare to the other cells operated at the values of relative humidity lower than 90%. Ex-situ analyses of the MEAs are presented and discussed.

Kurzfassung

Polymer-Elektrolyt-Membran-Brennstoffzellen (PEMBZ) gelten als alternative Energiewandler für den Einsatz in Automobilen sowie für portable und stationäre Anwendungen. Die Degradation des Platin-Katalysators spielt eine wichtige Rolle in der Verkürzung der Lebensdauer von PEM-Brennstoffzellen. Es wurden Versuchsreihen zur Untersuchung der Lebensdauer von Platin-basierenden Katalysatoren von PEM-Brennstoffzellen für die Automobilindustrie durchgeführt. In diesen Versuchsreihen wurde der Verlust von Platin-Oberfläche auf der Kathodenseite der Brennstoffzelle infolge der zyklischen Wechselbeanspruchung von Spitzen- zu Leerlaufleistung gemessen.

Es wurden 11 Brennstoffzellen mit zwei unterschiedlichen kommerziellen Membran-Elektroden-Einheiten (MEE) hergestellt und mittels Accelerated-Voltage-Cycling-Test bei verschiedenen Werten für die relative Feuchtigkeit (RH) untersucht. Während des Experiments wurden In-situ-Diagnosetechniken verwendet, um für jede Brennstoffzelle nach Beendigung einer bestimmten Anzahl von Spannungszyklen Polarisationskurven, Elektrochemische Impedanzspektren (EIS), Wasserstoffdiffusionsstrommessungen und Zyklische Voltammogramme (CV) aufzunehmen. Mithilfe der Zyklischen Voltammogramme wurde die aktive Platin-Oberfläche aller Zellen bestimmt. Die Ergebnisse zeigen eine kontinuierliche Abnahme der aktiven Platin-Oberfläche mit steigender Zahl von Spannungszyklen. Weiters konnte festgestellt werden, dass die Lebensdauer der mit 90% relativer Feuchtigkeit betriebenen Brennstoffzelle im Vergleich zu den anderen Zellen mit niedrigerer Befeuchtung maximal war. Ex-Situ-Analysen der Membran-Elektroden-Einheit werden dargestellt und diskutiert.

STATUTORY DECLARATION

I declare that I have authored this thesis independently, that I have not used other than the declared sources / resources, and that I have explicitly marked all material which has been quoted either literally or by content from the used sources.

…… ……..

date (signature)

Table of Contents

1 Introduction

Ever increasing population of the world, diminishing size of fossil fuel resources and rapid change in global climate due to the utilization effects of the fossil fuels have moved the world in burgeoning the demand for clean and sustainable energy. Fuel cell technology is fulfilling this demand by using renewable produced hydrogen as a fuel in stead of the fossil fuels. Figure 1.1 illustrates the annual increase in the fuel consumption and total energy demand, at a rate of 0.9% and 1.4% respectively from 2007 to 2035.

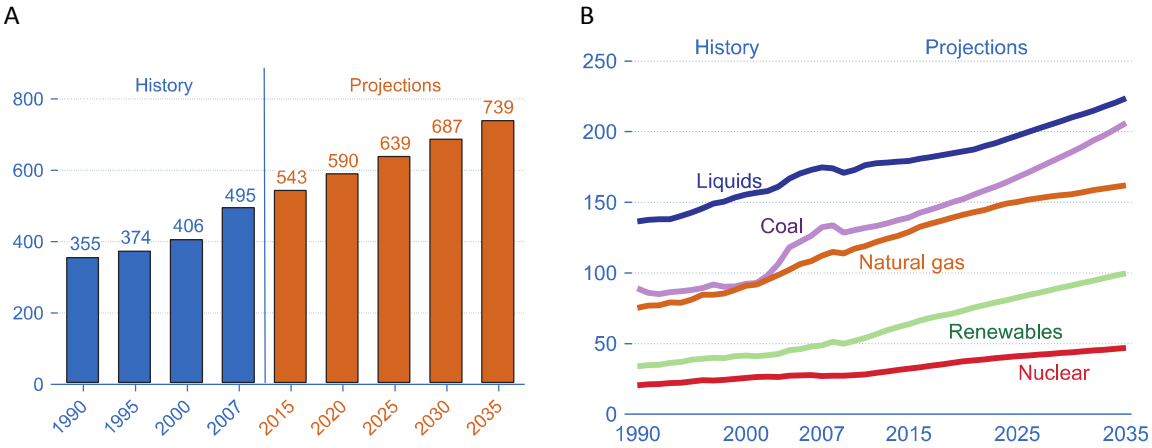

Figure 1.1: (A) World marketed energy consumption from 1990 to 2035 (quadrillion Btu), (B) World marketed energy used by fuel type, 1990-2035 (quadrillion Btu) [1]

With the employment of the fuel cells in the energy sector, the elevation in the world wide energy utilization, greenhouse gas emissions and dependence on fossil fuels can be reduced. A lot of research has been performed in the last couple of decades for the improvement and development of the fuel cell technology.

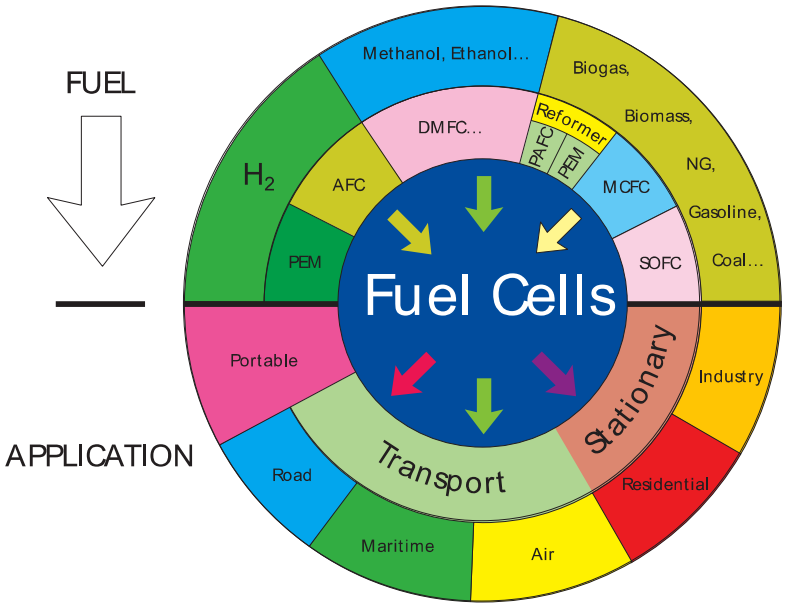

Figure 1.2: fuel cells and their applications [2]

Among different types of fuel cells, the Polymer Electrolyte Membrane (PEM) fuel cells have the capability to convert the chemical energy of the fuel (hydrogen), effectively into electrical energy with the formation of pure water as the only byproduct. Their significant features of high power density, low operating temperature, easy and fast start-up/shut-down processes make PEM fuel cells a promising candidate to the next generation power source for transportation, portable and stationary applications [3]. Factors like durability and cost are still the main hurdles to overcome before commercialization.

Great efforts have been performed to cut the price for manufacturing fuel cells. The price was reduced from $275/KW in 2002 to $108/KW in 2006 and $93/KW in 2007. Figure 1.3 shows the decrease in the fuel cell costs but still it is more than 50% higher ($61 /KW in 2009) than the goal set by US department of energy (DOE), i.e., $30 /KW for 2015 in order to compete with the combustion engine technology [4]. The main cost represents the membrane electrode assembly (MEA), with platinum based catalysts coated on Nafion membranes. Both Nafion membranes and Pt are expensive. In the course of the research and development throughout the last decade, the reduction in Pt loading has been attained to 0.3mg/cm^2, but US Department of Energy set the target of achieving the Pt loading of 0.2mg/cm^2 by 2015. Figure 1.4 exhibits that the maximum amount of funds was given for catalyst research in 2010 by US Department of Energy.

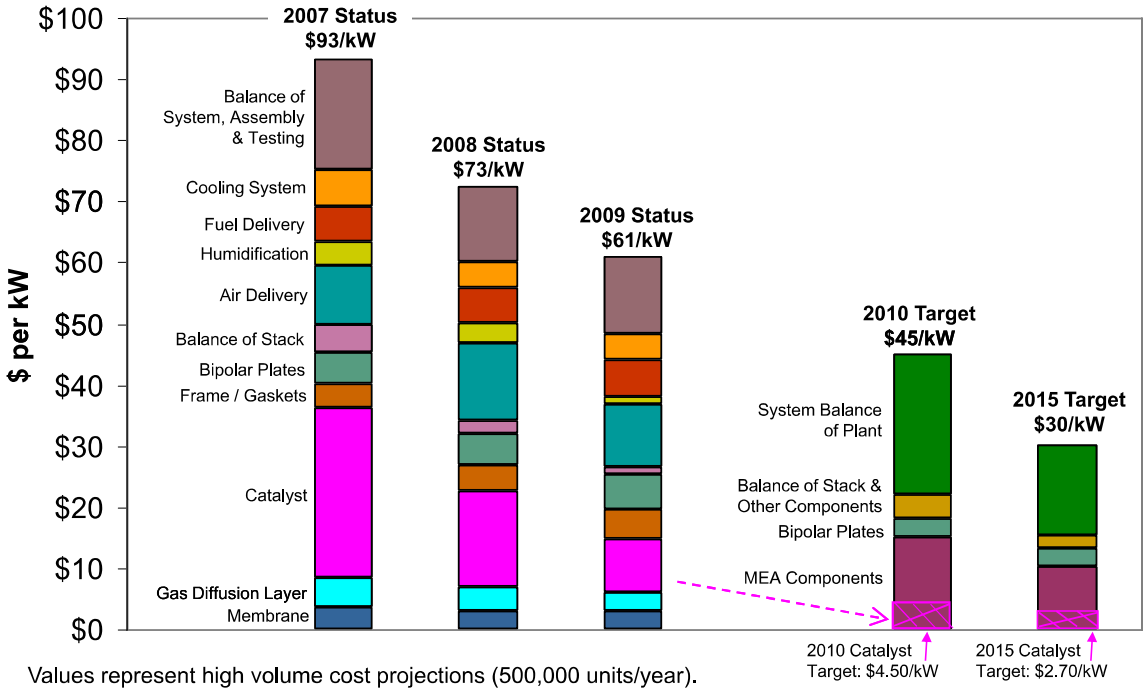

Figure 1.3: Fuel cell cost breakdown [4]

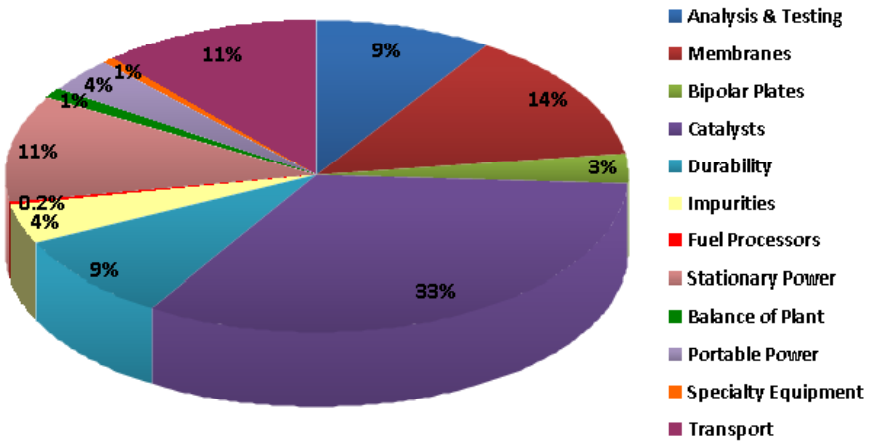

Figure 1.4: Fuel cells 2010 Funding breakdown, FY10 Appropriation: $ 77.480 Million [4]

In transportation sector PEM fuel cells have the potential to replace the internal combustion engines due to their high efficiency and environment friendly nature. Most of the world renowned car producing companies like Toyota, Honda, Hyundai, Daimler and General Motors are using PEM fuel cells for the fuel cell vehicles (FCV) and they plan to commercialize fuel cell vehicles by 2015.[5]

Durability and lifetime of the fuel cell is another important issue to handle before commercialization. The US Department of Energy set the target of lifetime of PEM fuel cell for stationary applications as 40,000 h by 2011 and for transportation sector as 5,000 h by 2015 with an efficiency of 40% and 60% respectively. Currently 3M Company, through single-cell voltage cycling experiment attained a durability of the MEA of over 7,300 hours [4].

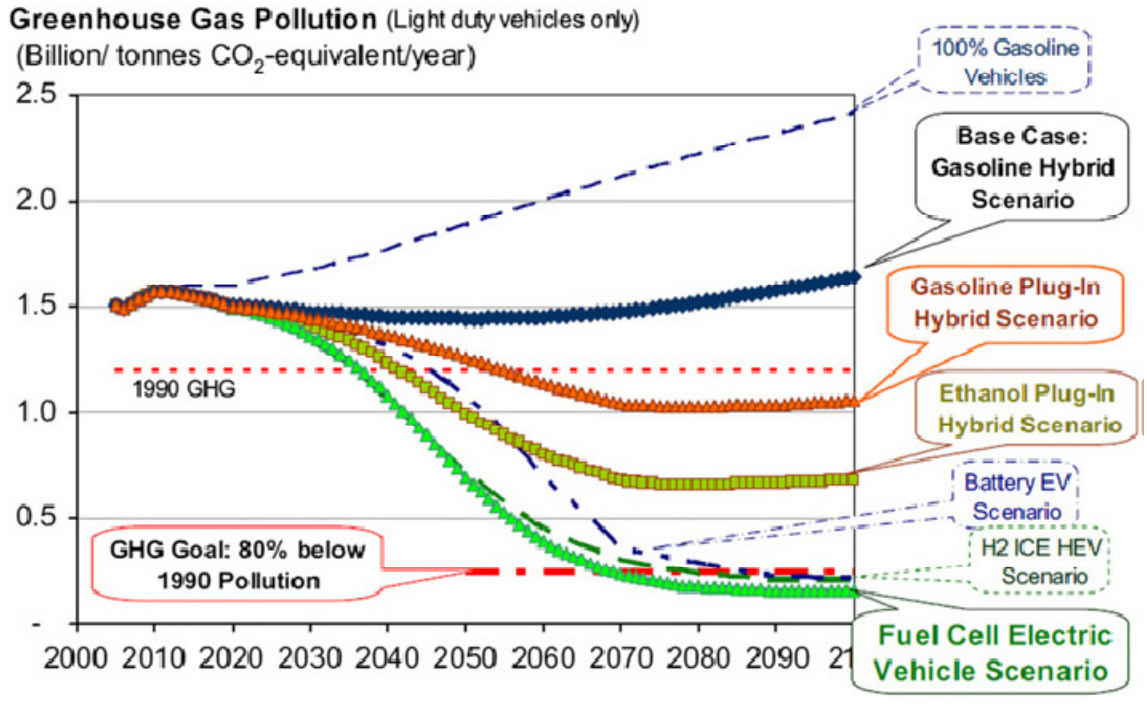

Figure 1.5: Primary model output showing the greenhouse gas pollution over the century for a reference case with no alternative vehicles, the four main vehicle scenarios and two secondary scenarios; the upper dotted horizontal line corresponds to the 1990 light duty vehicle GHG pollution, and the lower line represents an 80% reduction below the 1990 level [6]

The Accelerated voltage cycling test (AVCT) or accelerated stress test (AST) or accelerated durability test (ADT) is considered as a short cut to find out a reciprocal relation ship between morphology of the MEA and the performance of PEM fuel cell with the objective of commercialization.

In this research work accelerated voltage cycling tests were conducted by changing humidification values of the inlet gases of single unit cell assemblies, in order to find out the effects of humidification on the lifetime and durability of the PEM fuel cells.

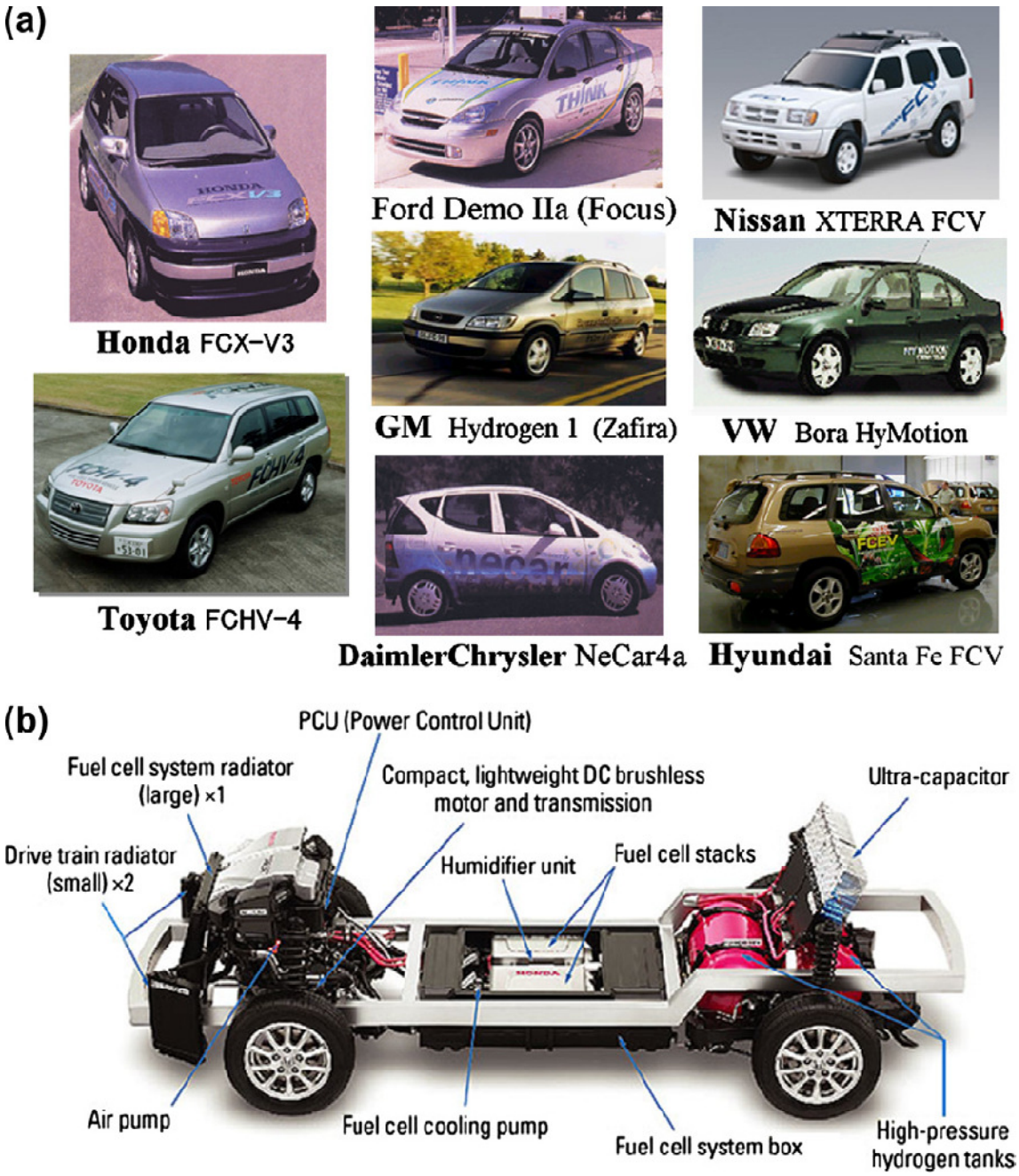

Figure 1.6: (a) Fuel cell vehicles of different automobile companies, (b) Detail of Honda FCX Power train [3]

1.1 Thesis Structure

The aim of this thesis was to investigate the degradation effects, which occur on the cathode of the PEM fuel cell during life long testing. For this purpose the fuel cells were examined by accelerated voltage cycling test at different values of relative humidity.

Chapter 2 deals with an overview of the state of the art concerning historical background of the fuel cell, description of different types of fuel cells, life time investigation methods and the degradation effects on different components of polymer electrolyte membrane fuel cells. Different types of catalyst materials and support materials used by the researchers were also discussed in this chapter.

Chapter 3 explains the detail of the fuel cell assemblies, test equipments and the diagnostic techniques employed for this research work. Test equipment consists of the instruments used for the preparation of gasket and two testrigs, one for accelerated voltage cycling test and the other for recording of the in-situ characterization curves of the fuel cells.

The results of all the fuel cells of type-F, obtained after investigating the fuel cells by accelerated voltage cycling test at different values of relative humidity and implementation of in-situ and ex-situ characterization techniques on theses cells before, during and after the test are summarized in chapter 4.

Chapter 5 explores the results of all the fuel cells of type-G, undergoing life time investigations through accelerated voltage cycling tests at different humidification levels of the inlet gases and analyses through in-situ and ex-situ diagnostic techniques. The results of cyclic voltammetry of the fuel cells F_1, F_2, G_1 and G_2 have been published in the proceedings of ´´Fundamentals and Developments of Fuel Cells Conference 2011``[7].

The comparative performance of two different types of membrane electrode assemblies, used during test series is described in chapter 6.

The whole research work of this thesis is summarized in chapter 7.

2 State of the Art

2.1 Fuel Cell

Fuel cells are electrochemical devices that directly convert chemical energy stored in the fuel like hydrogen into electrical energy. The efficiency can be as high as 60% for electrical energy conversion and over all 80% in co-generation of electrical and thermal energies with >90% reduction in major pollutants [4].

First Fuel cells were invented in 1839 by Sir William Robert Grove (an English lawyer turned scientist). General Electric Company (GE) started to develop fuel cells in 1950 and was able to get a contract of Gemini space mission in 1962. The platinum loading for 1KW Gemini fuel cell system was $35mg_{Pt}/cm^2$. This fuel cell system was capable to produce a current density of $37mA/cm^2$ at 0.78 volt. In 1960s GE improved the fuel cell by using Teflon in the catalyst layer next to the electrolyte. From early 1970s the fuel cell technology progressed by incorporating the fully fluorinated Nafion® membrane for the first time. For another couple of decades no special research was done in this field due to the lack of funding. Later on the scientists of Los Almos National Laboratory (LANL) with the collaboration of other researchers improved the methods of reduction of catalysts (platinum) on the electrodes of PEMFC. Especially D Raistrick (LANL) introduced a catalyst-ink technique for the manufacturing of the electrodes. This technique helped to minimize the precious platinum metal catalyst loading. No doubt many breakthroughs have been achieved in this field but still some challenges like cost reduction, durability and stability of the fuel cells are ahead before commercialization.

2.2 Types of Fuel Cell

Fuel cells can be classified due to the electrolyte employed in them and their different operating temperatures.

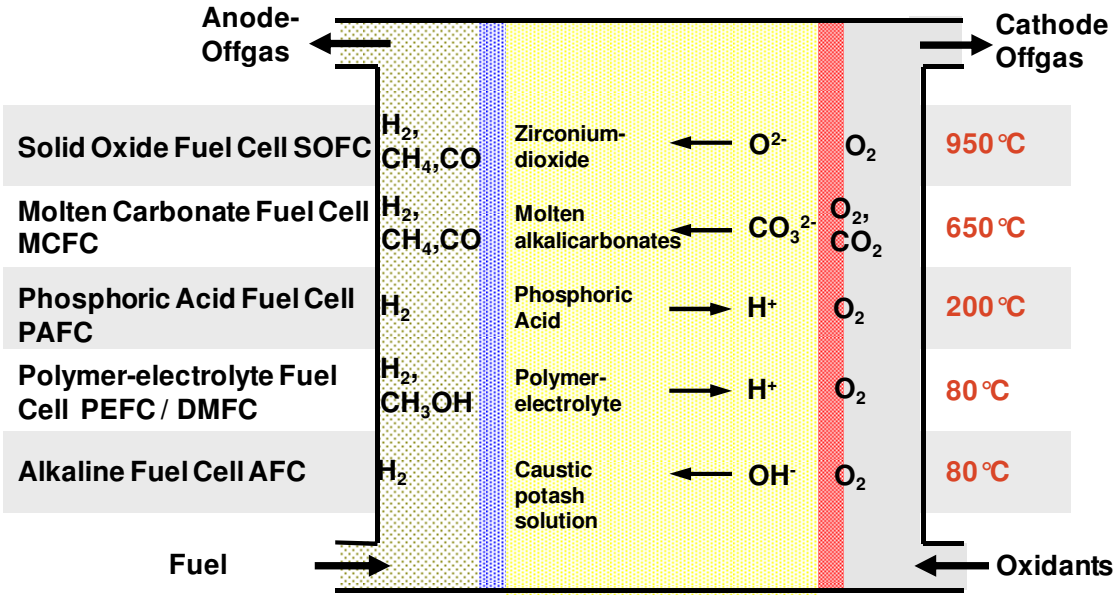

Figure 2.1:. Types of Fuel Cell [8]

Following are the five major types of the fuel cell.

- Polymer electrolyte membrane (PEM) fuel cell or PEMFC (also called PEFC)
- Solid oxide fuel cell (SOFC)
- Alkaline fuel cell (AFC)
- Phosphoric acid fuel cell (PAFC)
- Molten carbonate fuel cell (MCFC)

2.3 Polymer Electrolyte Membrane Fuel Cell

Polymer electrolyte membrane (PEM) fuel cell is also known as proton exchange membrane fuel cell. It is evident from its name that PEM fuel cells are fabricated by utilizing the polymer electrolyte membrane as proton conductor. Precious metals like platinum (Pt) are used as catalysts for PEM fuel cells.

The noteworthy features of PEM fuel cell are the highest power density of all the other fuel cell types (300-1000mW/cm^2), low operating temperature and the fastest start-up/shut down characteristics. Due to its extra ordinary characteristics, PEM fuel cell is considered as a promising candidate for the next generation portable, power and transport applications [60].

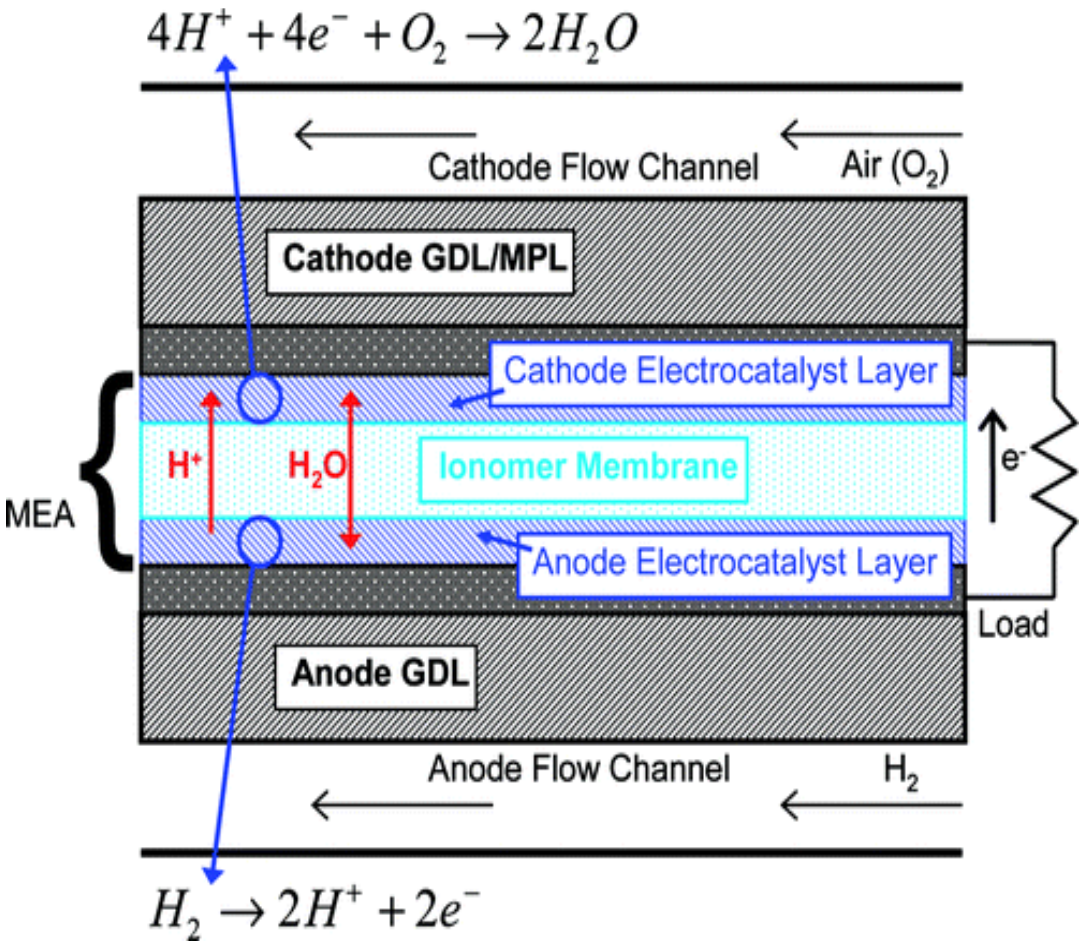

Figure 2.2 schematic of PEM fuel cell cross-section [13]

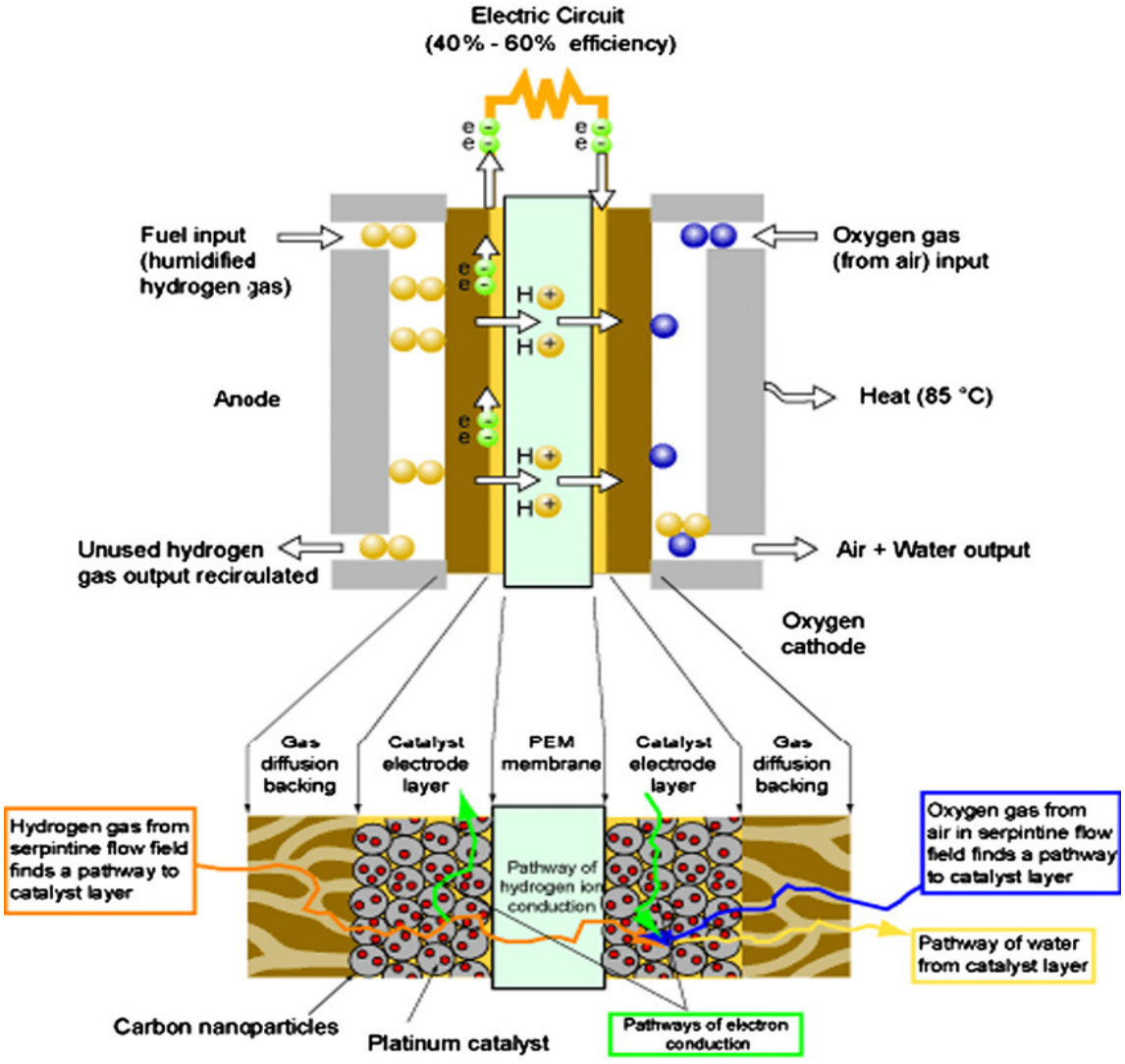

Figure 2.3. Two dimentional sectional view of phenomenon in PEM fuel cell [9]

Primarily PEM fuel cells are quite suitable for transportation applications due to their fast start-up time, low sensitivity to orientation and favorable power-to-weight ratio. The hydrogen storage in the fuel cell vehicles is a critical issue. The fuel cell vehicles (FCVs) powered by pure hydrogen usually store the hydrogen on-board as a compressed gas in pressurized tanks. Due to the low-energy density of hydrogen, it is difficult to store enough hydrogen on-board to allow vehicles to travel the same distance as gasoline-powered vehicles before refueling, typically 300–400 miles. Higher-density liquid fuels, such as methanol, ethanol, natural gas, liquefied petroleum gas, and gasoline, can be used for fuel, but the vehicles must have an on-board fuel processor to reform the hydrocarbon to hydrogen. This requirement increases costs and maintenance. The reformer also releases carbon dioxide (a greenhouse gas), though less than that emitted from current gasoline-powered engines [10].

2.4 Durability of PEM Fuel Cell

The enhancement of the durability and life time of the Polymer Electrolyte Membrane Fuel Cell (PEMFC) is the current requirement. The target set by Department of Energy (DOE) USA for PEM fuel cell is 5,000 operating hours for car applications, 20,000 operating hours for bus applications and

40,000 operating hours for stationary applications [11]. It is necessary to know how to cope up with the failure modes and mitigation strategies in order to improve the durability and life time of PEMFCs.

The over all performance of the PEM fuel cell in terms of main sources of losses (overvoltages) can be exhibited from Figure 2.4. It is visible from the figure that cathode electrode overvoltage is maximum in comparison to other losses and the anode electrode overvoltage is minimum. The membrane resistive overvoltage is higher for elevated current densities.

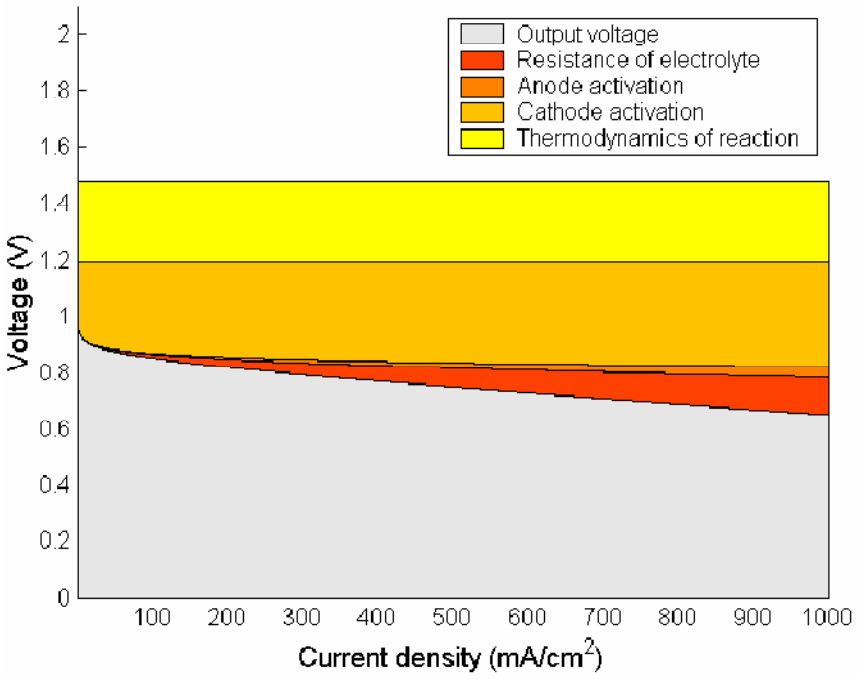

Figure 2.4: Performance characteristics of a PEM fuel cell [12]

Different aspects of fuel cell durability issues have been published in many reviews. Borup et al [13] explicitly described about the different important aspects of PEMFC durability and degradation.

2.5 Life Time Investigation Methods

The durability of a fuel cell can be estimated by a steady-state life time test, but this method is lengthy and costly, as 5,000 hours mean approximately 7 months and 40,000 hours mean approximately 4.6 years. Therefore, accelerated stress tests (ASTs) or accelerated durability tests (ADTs) methodologies have been developed for lifetime studies of PEM fuel cells. With the help of ASTs the duration of the experiments for lifetime evaluation has been decreased. Following are the types of ASTs :

- Electrochemical Potential Cycling
- On/Off, Start-up/shut-down Cycling
- Freeze/Thaw Cycling

2.5.1 Electrochemical Potential Cycling

The life time of fuel cell is severely affected if it is operated at voltage cycles. Electrochemical Potential Cycling has been used by many researchers in order to determine the durability and

lifetime of fuel cells with different experimental conditions [14,15,16,17,18,19]. Triangle potential cycling was proved to be more severe than step potential cycling [20].

Wu Bi et al [21] examined PEM fuel cells by potential cycling tests at 60°C and determined the effect of relative humidity and oxygen partial pressure on platinum catalyst degradation. According to their studies the decrease of relative humidity from 100% to 50 % resulted in three times reduction of the loss rate of platinum mass and two times reduction in the catalyst active surface area whereas the effects of oxygen partial pressure on cathode degradation were not prominent. Platinum electrochemical oxidation by water and platinum dissolution were slightly affected by changing the relative humidity.

2.5.2 On/Off, start-up/Shut-down Cycling

On/off cycling is a useful methodology to investigate the durability of a fuel cell for automotive and mobile applications. Dongho Seo et al. [22] investigated about the life time of PEM fuel cells by on/off cycling test at different values of relative humidity and concluded that low humidification levels are severe condition for MEA durability in the PEMFC operation.

2.5.3 Freeze/Thaw Cycling

Polymer Electrolyte Membrane fuel cells are working usually at higher temperature than the freezing point of water but it is quite possible that during the lifetime the fuel cell can encounter the freezing temperature e.g., during transportation and storage. Many researchers investigated the effect of freezing on the physical properties and performance of different components of the PEM fuel cell by Freeze/Thaw cycling test. [23,24,25,26]

2.6 Material Degradation

The life span of the fuel cell depends upon the performance of individual components. Degradation processes are interrelated. Degradation of one component can initiate or influence the degradation of other components. Catalyst degradation and degradation of other components of the fuel cell decreases the performance of the cell, but it has a less important role in the sudden failure of the cell [27].

- Degradation of Membrane
- Degradation of Catalyst
- Degradation of Electrode, Carbon Corrosion
- Degradation of GDL

2.7 Membrane Accelerated Stress Test

2.7.1 Membrane Degradation Mechanism

The proton exchange membrane (PEM) is the major component of the membrane electrode assembly. The role assigned to the proton exchange membrane in the fuel cell is to permit the passage of protons through it (from anode to cathode) and to stop the movement of fuel and oxidant (hydrogen and oxygen) between the electrodes (anode and cathode). Usually PEMs are perflourosulfonic acid (PFSA) membranes like Nafion® having really high protonic conductivity as well as good thermal, mechanical and chemical stability. Chemical structure of Nafion® is given below.

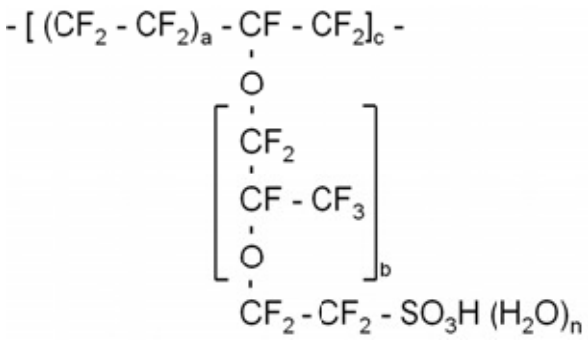

Figure 2.5: Chemical Structure of Nafion®, a = 5-11, b = 1-3, c ≈ 1000, n = 1-14

Nafion® is a polyelectrolyte having hydrophobic polytetrafluoroethylene backbone with perfluorinated-vinyl-polyether side chains, containing hydrophilic sulfonic acid end groups, which can bind water molecules.

Commonly the membrane degradation in the fuel cell is taking place due to thermal, chemical and mechanical mechanisms under severe operating conditions.

Mechanical loss results in the form of membrane cracks, punctures, tears and pinholes. Due to these losses membrane failure occur in the early stage of its life. This is the case especially for thin membranes.

The increase of temperature results also in the faster deterioration of the polymer membrane. For chemical damage it has been suggested, that due to incomplete reduction in the oxygen reduction reaction (ORR), hydrogen per oxide is generated and forms OH and HO_2 species. The chemical degradation mechanisms are considered to be due to the breakage of the per-flourocarbon backbone and side-chain groups in the Nafion® membrane which ultimately decrease the mechanical strength and proton conductivity. Consequently the total cell resistance increases [28].

The recommended chemical reaction is as follows [29]

$$\boldsymbol{Rf - CF_2COOH + OH \rightarrow Rf - CF_2 + CO_2 + H_2O} \qquad \textbf{2.1}$$

$$\boldsymbol{Rf - CF_2 + OH \rightarrow Rf - CF_2OH \rightarrow R_f - COF + HF} \qquad \textbf{2.2}$$

$$\boldsymbol{Rf - COF + H_2O \rightarrow Rf - COOH + HF} \qquad \textbf{2.3}$$

For the life time investigations, the changes in the gas crossover rate, fluoride-ion emission rate (FER), and ion exchange capacity (IEC) are used to describe the level of degradation. Table 2.1 elaborates methods for membrane degradation and their effects in detail.

Table 2.1 Comparison of several metrics for membrane degradation analysis [28]

Testing Items	Technologies	Positive Characteristic	Negative Characteristic
Gas crossover rate	Electrochemical method (Linear sweep voltammogram)	Non-destructive analysis	Need to stop the operation of the fuel cell for measurement
Flouride ion emission rate	Ion (fluoride) selective electrode	Can be conducted either in-situ or ex-situ	Cannot provide detailed information for the degradation site of the membrane
Morphology change Ion exchange capacity change	Scanning electron microscopy (SEM) Standard chemical method	Visual representation Gives information on the degradation ratio of backbone of side-chain groups	Postmortem analysis Postmortem analysis

2.7.2 Accelerated Stressor for Membrane Degradation

- Undesirable temperature and relative humidity
- Open circuit voltage
- Load cycling
- Fenton`s test
- Freeze/thaw cycling and subzero start up

2.8 Pt Catalyst Accelerated Stress Test

Usually PEM fuel cell electrocatalysts are made of nanoscaled Pt (or Pt-alloy) particles (specifically 2-6 nm in diameter) supported on high surface area carbon.

2.8.1 Catalyst Degradation Mechanism

Catalyst degradation results in cracking, delamination of the layer, catalyst ripening, catalyst particle migration, catalyst washout, electrolyte dissolution (Nafion® ionomer) and carbon coarsening. Due to all these effects the apparent activity loss occurs in the catalyst layer. The decrease in electrochemical active surface area (ECSA) of the catalyst plays an important role in the apparent activity loss of the catalyst layer. ECSA can be measured by cyclic voltammetry (CV), CO stripping voltammetry and CO gas-phase chemisorptions. Scanning electron microscopy (SEM) and transmission electron microscopy (TEM) are used to observe the microstructural changes occur in the catalyst layer.

2.8.1.1 Pt agglomeration

The nano sized Pt particles have high specific surface energy. So they can quickly agglomerate into larger particles. As soon as their size increases their specific energy decreases and the process of agglomeration becomes slow. Under extreme operating conditions the agglomeration process speeds up. As a result of it the number of Pt active sites decreases and ultimately there is a decline in the electrochemical active surface area (ECSA).

Ferreira et al. [15] investigated the degradation of PEMFC through potential cycling tests and after that observed the crossectional view of the cycled MEA with transmission electron microscope (TEM)

and proposed that two phenomena were responsible for changes in the structure of Pt particles. Figure 1 explains this in detail.

2.8.1.1.1 Ostwald ripening

Small Pt particles dissolve in the ionomer phase and redeposit on bigger Pt particles. The distance between two such particles is a few nanometers. This is called Ostwald ripening on the name of the scientist Wilhelm Ostwald described this phenomenon for the first time in 1896.

2.8.1.1.2 Micrometer-scale diffusion process:

The dissolved Pt species diffuse towards the membrane, are reduced by hydrogen due to crossover from anode and then precipitate as Pt particles in the ionomer phase of the electrode or in the membrane.

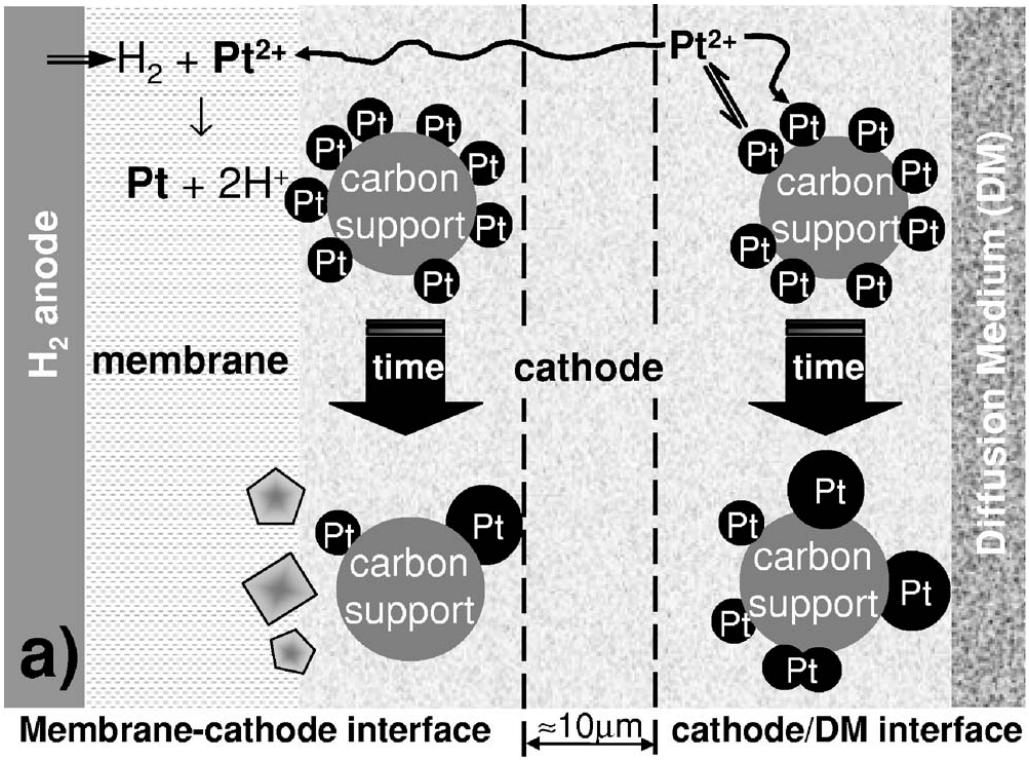

Figure 2.6: Platinum surface area loss on nanometer scale and micrometer scale in the PEMFC [15]

2.8.1.2 Pt migration/ Pt dissolution into the electrolyte

In spite of Pt particle agglomeration, detachment of Pt particles also occurs. Then Pt particles migrate either into the membrane or to the electrode-membrane interface. This results, into the reduction of ECSA, which further leads to performance deterioration of PEMFC.

2.8.2 Accelerated Stressor for Pt Catalyst Degradation (Factors which affect the Pt Catalyst Degradation)

2.8.2.1 Temperature and Relative Humidity

Borup et al. [16] described in detail about the effect of temperature on catalyst durability. According to their studies, rising the temperature enhance the Pt particle growth rate. Thermal and

electrochemical deterioration of fuel cell catalysts was part of the detailed experimental study by Cai et al. [30]. By comparing the effects of these two parameters they concluded that Platinum surface area loss during 10h of thermal degradation under their experimental condition was equal to the electrochemical deterioration after 500 potential cycles. Potential was set between 0 and 1.2 V. Dam and de Bruijn [31] investigated the effect of potential and temperature on platinum thin film dissolution in 1M $HCLO_4$ solution by using the quartz crystal microbalance. They reported that dissolution was minimal at low temperatures like 40°C, but by increasing the temperature from 60 to 80°C the Pt dissolution rate was increased from 0.87ng/hcm^2 to 1.58µg/hcm^2 at the potential of 1.15 V. Xie et al. [32] performed PEFC durability tests at high value of relative humidity and observed morphological changes and migration of Pt particles with the help of TEM. For 1000 h durability test, prominent agglomeration happened during the first 500 h of the test. Borup et al [33, 16] concluded through load-cycling test that the size of Pt particle was directly proportional to the relative humidity. Xu et al. [34] investigated about Pt surface oxidation in the PEMFC cathode at different values of RH and reported that by increasing the RH from 20% to 72%, the level of Pt oxidation also increased continuously but above 72% RH, there was no more increase in Pt oxidation level.

2.8.2.2 Potential Control

Most researchers used the methodology of potential control for life time investigation of PEMFCs. Usually square-wave potential cycles or sometimes triangular-wave potential cycles were employed for catalyst durability tests [35]. If the potential is set less than 0.9 V, only the catalyst can degrade but above this potential there is the possibility of corrosion of carbon support, too. A literature survey shows that due to the potential cycling test the Pt particles agglomerate as well as migrate and the Pt dissolution rate depends upon the value of potential set for the durability test. By enhancing the potential from 0.85 to 1.15 V at 80°C in 1M solution of $HClO_4$ Dam and de Bruijn [31] reported that the Pt dissolution rate increased almost 54 times to the original value. Above 1.15 V no further increase in the dissolution rate was observed. They justified it with the formation of protected surface Pt oxide at elevated potentials. Wang et al. [36] founded that the concentration of dissolved Pt was increased monotonically for the potential from 0.65 V to 1.1 V but above 1.1V a decrease in the dissolved Pt concentration was observed. The reason of this decrease was also a protective oxide film.

After accelerated durability test through potential cycling to OCV or higher potentials, migration of the Pt particles was also observed through ex-situ diagnostic techniques. Pt migration at the cathode side is more severe than at the anode side. Ferreira et al. [15] performed potential cycling tests at OCV by using H_2/air supply and after 2000 h of cell operation a Pt band was observed near the cathode/membrane interface. Bi et al. [37,38] used a square wave potential between 0.87 V and 1.2 V vs. RHE at different values of temperature and found a Pt band in the membrane near the cathode side through ex-situ experimental results. Figure 2.7 shows the SEM images of degraded MEA. The white band represents the high concentration of Pt particles in the membrane and in other wards the loss of Pt particles from the cathode.

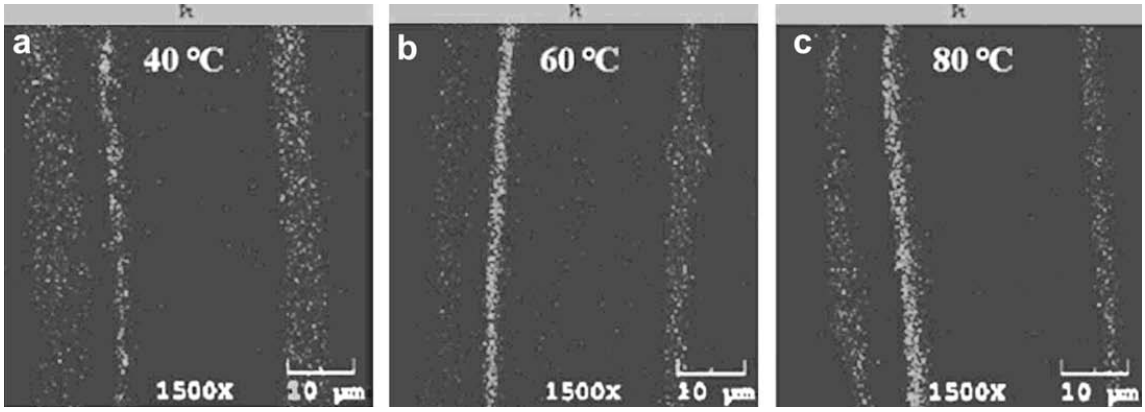

Figure 2.7. Crossectional view of degraded MEA at different temperatures. (Left cathode).

It is also visible from the figure that bigger, wider and brighter Pt band formed when temperature rised up. Xie et al. [32] also observed the Pt migration at the anode membrane interface for high value of RH and Guilminot et al. [39] found the same effect at voltages greater than 0.6 V vs. RHE. Platinum dissolution and deposition out of the catalyst layer was greatly reduced when a platinum black electrode was employed instead of carbon black [40].

2.8.2.3 Contamination

Contamination of the electrocatalyst is one of the most important factors of deterioration of PEM fuel cell. Contaminants can be divided into two groups, depending upon the source:

- Fuel contaminants
- Air contaminants.

Fuel contaminants may contain hydrocarbon (CH_4), carbon oxides (CO, CO_2), sulfur compounds (H_2S, sulfur organics) and ammonia (NH_3). Air contaminants may contain nitrogen oxides (NO, NO_2), sulfur oxides (SO_2, SO_3), carbon oxides (CO, CO2), ozone and other organic chemical species [28]. It has been demonstrated that even trace amounts of impurities (Fe^{3-}, Ni^{2+}, Cu^{2+}, Cr^{3+}, Na^{+}, Ca^{2+}) or silicon present in the fuel or air streams or fuel cell system components (bipolar metal plates, membrane, sealing gaskets, storage systems,etc.) can severely poison the anode, membrane, and cathode, particularly at low-temperature operation [41]. In the literature, the most extensively investigated impurity is CO. By using Pt-Ru/C electrocatalysts the effect of CO can be diminished.

Garzon et al. [42] demonstrated the impact of hydrogen fuel contaminants on long-term PEMFC performance. According to their observation, fuel cells exposed to 1ppm of H_2S operated at constant potential of 0.5 V, the performance losses were evident after just 4h of exposure and the cell faced complete failure after 21 hours of operation. By continuing the experiment with ultra pure hydrogen for many hours, no improvement was observed showing the irreversibility due to the poisoning of H_2S. With H_2S as low as 10ppb, the PEM fuel cell performance degradation was also observed.

SO_2 is another sulfur containing species which also acts as a severe impurity by poisoning the cell to irreversible damage. Mohtadi et al. [43] reported that the performance degradation of the cell at the cathode side is directly proportional to bulk concentration of SO_2. The damage does not only depend upon the bulk concentration of SO_2 but also the presence of SO_2 in air even in low quantities can produce severe deterioration to the cell. Wang et al. [44] founded that the poisoning ability of SO_2 in

air does not only depend on the dosage, but also depends on its concentration. SO_2 was proven to be very poisonous for the cathode catalyst even when its concentration in air was as low as 0.1 ppm.

Some other impurities like NO_2 in the feeding gas can also damage the cell but this damage is reversible. By treating the cell with neat air, the performance of the cell can be recovered [43].

Contaminants like NH_3 in the fuel can also cause deterioration in the cell depending upon its concentration as well as the exposure time. Uribe et al. [45] demonstrated that high trace level (e.g., 30ppm) and long exposure (e.g. 15h) to NH_3- contaminated fuel caused severe and irreversible disability to the PEM fuel cell whereas for short time of exposure (1 to 3h) the original performance could be fully recovered.

Table 2.2- General reasons for catalytic activity loss in Pt-based catalysts [28]

Classification of catalytic activity losses	Failure Mechanism	Characterization Techniques
Catalyst agglomeration	Ostwald ripening; thermal sintering	SEM; TEM; CV; XRD
Catalyst migration	Metal dissolution and re-deposition	SEM-EDS; TEM
Catalyst sites poison	Contamination from the gas supply or system	CV; EIS
Others	Layer delaminations; Pt trapped in the ionomer, etc.	SEM; TEM; EIS

2.9 Carbon Corrosion Accelerated Stress Test

2.9.1 Carbon Corrosion Mechanism

Carbon is an ideal support material used for an electrocatalyst in the PEM fuel cell. It has unique electrical and structural properties. Under normal conditions, carbon allows a very smooth mass transport of reactants and fuel cell reaction products, but under extreme conditions of high potential, high temperature, high oxygen concentration, high water content and low pH [46], corrosion (oxidation) of carbon starts quickly. The standard potential for corrosion of carbon is 0.207 V. Due to the carbon corrosion the bond between the Pt particles and the carbon surface becomes weak and ultimately Pt particles detach from the carbon support. These Pt particles can agglomerate and cause performance deterioration of the fuel cell. The process of carbon corrosion can be explained by the following equations

$$C_s \rightarrow C_s^+ + e^- \quad \textbf{2.4}$$

$$C_s^+ + H_2O \rightarrow C_sO + 2H + e \quad \textbf{2.5}$$

$$2C_sO + H_2O \rightarrow C_sO + CO_{2(g)} + 2H^+ + 2e^- \quad \textbf{2.6}$$

The subscript “s’’ means the surface species.

First two equations show the incomplete oxidation which includes electron transfer and hydrolysis with the formation of surface group. Third equation shows complete oxidation by forming CO_2 [47]. For the potential range between 0.4 and 0.7, V there is no prominent carbon corrosion but at higher values of potential there is a great possibility of carbon corrosion. Also during cell operation, the reversal of potential can create irreversible damage to the fuel cell [48,49,50]

2.9.2 Accelerated Stressor for Carbon Support Degradation

2.9.2.1 Fuel Starvation

Gross fuel starvation is one of the major causes of carbon corrosion. Basically, when fuel is insufficient for providing the required current to the cell, the anode potential increases continuously, but the cell potential decreases. The reversal in the cell operation can also be quite possible with greater value of anode potential than that of cathode potential. At this stage the oxidation of water (equation 2.7)and carbon (equation 2.8)occurs at the Pt based anode electrocatalyst which results in the formation of electrons and protons for the oxidation reduction reaction at the cathode side of the cell [51].

$$H_2O = 1/2\,O_2 + 2H^+ + 2e^- \qquad E_{298k} = +1.23\,V\ vs.RHE \qquad (2.7)$$

$$C + 2H_2O = CO_2 + 4H + 4e^- \qquad E_{298k} = +0.207\,V\ vs.RHE \qquad (2.8)$$

Mayer and Darling [49] presented a mathematical model of carbon corrosion in PEM fuel cell and proposed that with the use of careful system control and design, carbon corrosion can be minimised.

2.9.2.2 Start-Up/Shut-Down Cycling

Carbon corrosion can also be accelerated by non uniform supply of fuel to the anode of the cell. Chizawa et al. [52] presented that rapid potential changes during start-up and shut down can accelerate carbon corrosion significantly. For automotive application a fuel cell can have 30,000 start-up/ shut-down cycles [53]. Tang et al. [54] demonstrated that the air fuel boundary at the anode side developed after a fuel cell shut down and its restart caused extremely rapid corrosion of carbon support of the cathode which leads to the catalytic active surface area loss and the deterioration of the cell performance. The experiment was performed by using single cell and a dual-cell configuration and concluded that first 30 cycles of corrosion process were more severe when air and hydrogen were supplied to the anode alternatively. After about 50 such cycles, the electrochemical active surface area of the cathode remained 30% of its original value and after 80 cycles the thickness of the cathode decreased to 1/3 of its initial value. This phenomenon explains the lesser thickness of the cathode layer than the anode layer after start-up/ shut down tests.

2.9.2.3 Cold start-up at subzero temperatures

Another mode for enhanced carbon corrosion is cold start-up of fuel cell at subzero temperature. During cold start-up in subzero environment, water produced in the electrodes may freeze instantaneously at the electrochemical active sites of the catalyst layer, covering these reaction sites and hence decreasing the reaction area, as well as plugging the open pores of reactant passage. Thus local reactant starvation is a severe condition for carbon corrosion [55,56]. At temperatures below freezing, water produced at the cathode freezes on the surface of the catalyst. Due to this ice formation, local starvation can happen which is the main cause of carbon corrosion in cold start-up. A lot of work has been done to find out the minimum temperature for fuel cell start-up and proper functioning. Hishinuma et al. [57] investigated the cold start-up performance of single cells at different temperatures (–3 to –25°C) and analyzed the results through simulations. They concluded

that heat generated in the fuel cell is effective to warm the cell up and makes self starting at –5°C possible, but an additional external heat source would be required in order to start fuel cell, below –5°C.

2.9.2.4 Potential control

High potential is another factor for enhanced carbon corrosion. Makharia et al. [53] performed 2000-h tests at 80°C and found weight losses of carbon of approximately 2% at 0.9 V vs. RHE and 5% at OCV (≈1.0 V). Borup and co-workers [16] observed the increase in carbon corrosion with increasing potential through potential cycling tests, when the voltage was changed from 0.1 V to 0.96 V, 1.0 V, 1.2 V and 1.5 V. Roen et al. [58] explained the influence of platinum on carbon corrosion with the help of characterisation by on-line mass spectroscopy during cyclic voltammetry. From the results they concluded that the rate of CO_2 emission was higher in case of Pt/C catalysts than when carbon alone was used as electrode at temperatures less than 50°C. Carbon corrosion could be possible at 1.1V vs. RHE or at higher value in case of pure carbon electrodes but when 10% Pt was used as catalyst, the CO_2 peak appeared at 0.55 to 0.6 V vs. reversible hydrogen electrode. Maass et al. [59] analysed the carbon support oxidation in PEM fuel cell cathodes and concluded that hydrogen peroxide formation on carbon support and on platinum catalyst led to increased corrosion at low potentials.

2.10 Gas Diffusion Layer (GDL) Accelerated Stress Test

2.10.1 GDL Degradation Mechanism

The gas diffusion layer (GDL) is a carbon based porous layer (carbon cloth or carbon paper), placed between the flow field and the catalyst layer in the PEM fuel cell. An ideal GDL must have high electrical conductivity, high gas permeability, high stability against corrosion, proper water transport and good mechanical support [60]. GDL has hydrophilic pores for water transport and hydrophobic pores for gas transport [61]. For proper mass transport especially for water removal, the number of these pores should remain constant. Ineffective water management will lead to liquid-phase water blockage (flooding) and mass-transport limited performance, or to decrease proton conductivity as a result of ionomer dehumidification [28]. Due to flooding of water in the GDL, the transport of the reactant gases will be blocked which is the main reason for fuel starvation and carbon corrosion of the microporous layer (MPL).

2.10.2 Accelerated Stressor for GDL

Less work has been done on durability studies of GDL. Detail investigations are missing.

2.10.2.1 In-situ stressors

To find out the effect of freeze/thaw cycles on the GDL, Kim et al. [62] performed experiments at temperatures -40°C to 70°C and observed interfacial delamination between CL and GDL after 100 freeze/thaw cycles. Mukundan and co-workers [63] also conducted freeze/thaw cycles at -80°C and found the same results.

Borup et al. [33] reported that the hydrophobicity of GDL decreased with the increase of operating temperature and nitrogen environment caused more severe performance degradation of a GDL than that of air environment.

2.10.2.2 Ex-situ stressor

Many researchers used ex-situ methods to study the individual aging effect of GDL without testing the whole cell or stack. By dipping the GDL samples in liquid water at different temperatures and

with different oxygen concentration, Wood and co-workers [64] observed the decrease in hydrophobicity with exposure time and an increase in hydrophobicity with high water temperatures specifically at greater oxygen concentrations. By immersing the GDL in hydrogen peroxide solutions Frisk et al. [65] found a weight loss and an increase in contact angle of the micro porous layer. Lee and Mérida [66] performed a test series under steady-state and freezing conditions to detect the compression strain of GDL. After AST of 1500 h a maximum strain of 0.98% was measured. They observed that the structure of MPL became weak under freezing conditions and air flow through GDL was a major cause of material loss. In-plane and through-plane flow caused 18% and 80% increase in air permeability, which was seen as the ultimate reason of material loss and GDL degradation.

2.11 Materials used as catalyst

Catalysts are used in the PEMFC for enhancing the reaction rates on anode as well as on cathode [67]. Catalysts can be catagorised into different types [68]:

- Single metal catalyst (Pt/C)
- Binary catalysts (Pt-Ru/C, Pt-Mo/C, Au-Pd/C)
- Tertiary catalysts (Pt-Ru-Mo/C, Pt-Ru-W, Pt-Ru-Al_4)

2.11.1 Platinum

Often platinum is used as catalyst in polymer electrolyte membrane fuel cell. Usually 10 to 40% Pt on carbon is used as catalyst in PEMFC. Platinum develops a large overpotential (around 400mv at moderate current densities) on cathode. The exchange current density for the hydrogen oxidation reaction (HOR) on a platinum surface is orders of magnitude faster than that for the ORR [69] and thus the total cell overpotential is less. This is the case when pure hydrogen is used. When H_2 is obtained from hydrocarbon fuels by a reforming process, CO and CO_2 accompany it because it is difficult and costly to remove CO. CO adsorbs on Pt. surfaces. As a result of this the overpotential at the anode increases. The overpotentials at cathode and anode decrease the cell performance. Therefore a lot of efforts are invested to search for improved catalysts for PEMFCs [67].

2.11.2 Platinum alloys (Ru, Mo, Co, Ta, Au, Sn)

Some researchers used Platinum alloys and studied their improved performance. The elements used to form Pt-alloys are [M=Ru, Mo, Co, Ta, Sn]. They have also been studied to find out their effect on CO tolerance. Actually CO forms strong bonds with platinum and can not easily be removed. Ralph and Hogarth [70] and Wee and Lee [71] discussed this in detail.

2.11.2.1 Pt-Ru alloys

Pt-Ru alloy is helpful to improve CO tolerance. The HOR performance of this alloy has been studied extensively [72,73], and it was found that HOR overpotential decreases by increasing the Ruthenium content. By adding Ru to Pt, CO tolerance can be improved either by a ligand effect [74] or by a bifunctional mechanism [75]. According to the ligand model, ruthenium changes the electronic properties of platinum, by weakening the bond between Platinum and CO. In this way a decrease in the CO electro-oxidation potential occurs. On the other side bifunctional mechanisms propose that a reaction takes place between Ru and water to form Ru-OH which reacts with adsorbed CO.

$$Pt - CO_{ads} + Ru - OH_{ads} \rightarrow Pt + Ru + CO_2 + H^+ + e^- \qquad 2.9$$

This, in turn, frees the platinum surface for the HOR. The overpotential for a given current density decreases [67].

2.11.2.2 Pt–Mo alloys

Pt-Mo alloys have better CO-tolerance than pure platinum [76,77]. It has been considered that oxygenated species on the molybdenum surface are helpful to remove CO from platinum at low potentials, similar to that of bifunctional mechanisms in case of Pt-Ru alloys [67].

2.11.2.3 Pt–Co alloys

Pt-Co alloys may be useful catalysts for H_2 oxidation in the presence of CO because Cobalt is used to increase CO oxidation in reformers [78,79]. Pt–Co alloys have been proposed as improved methanol oxidation catalysts [80], because cobalt may assist CO removal (CO is an intermediate in methanol electro-oxidation) through a mechanism like bifunctional mechanism in Pt−Ru alloys. Pt–Co alloys have also been found as improved ORR catalysts [81,82,83]. Additionally, they also showed good performance in direct methanol fuel cells (DMFCs) [84].

2.11.2.4 Pt–Au alloys

Pt–Au alloys are not considered good catalysts for PEM fuel cells. But they have been studied as potential DMFC catalysts and have shown methanol oxidation activity [85]. Gold catalysts are also effective for removing CO from H_2 gas streams in reformers [86]. However, gold is considered to be a poor choice as a fuel cell electrocatalyst.

2.11.2.5 Pt–Sn alloys

Pt−Sn alloys have been studied by many researchers. And Pt_3Sn alloy was considered to be a more CO tolerant electro oxidation catalyst than pure Pt. Its activity depends upon the surface orientation. Especially the (111) face is very active for CO electro-oxidation [87]. Due to high CO tolerance it is also useful to improve DMFC performance [88].

2.11.2.6 Pt-Tantalum alloys

Tantalum is highly resistant to corrosion because it forms a passivation layer under all practical operating conditions [67]. In one report, $Pt_{1-x}\,Ta_x$ alloys were exposed to 0.5M $H_2\,SO_4$ at 80°C for 1 week and all of the Tantalum was retained [89]. It concluded that Pt-Ta alloys can show good performance in fuel cell with the course of the experiment. Papageorgopoulos et al [90] concluded that Pt-Ta alloys (Pt_6Ta) were a good choice in PEMFC for hydrogen oxidation in the presence of CO.

2.11.3 PtNi & PtCo

N. Travitsky et al. [91] reported that the performance of catalysts can also be improved by using Pt-based alloys with transition metals like Ni, Co, Cr, Fe and Mn. There are two benefits of these alloys. On one side they reduce the activation potential of cathode, on the other side they reduce the cost of the catalyst and ultimately of the fuel cell. It has been reported that these alloys increase the activity of the catalyst for ORR considerably. [92,93,94,95,96,97,98].

Table 2.3 shows that the grain size of Pt with silica support is larger and ECSA is smaller than that of XC-72 carbon support. Also for alloys with Nickel and Cobalt, the grain size decreases and ECSA increases. The catalyst spherical grain size and its surface area can be related as follows [99].

$$S = \frac{6 * 10^3}{\rho d} \qquad \textbf{2.10}$$

where S is surface area (m^2 g^{-1}), d the particle diameter and ρ is a metal lattice density. With this equation it is possible to estimate the effect of alloying on the degree of agglomeration. For carbon-supported catalysts the reduction of the platinum-catalyst grain size is caused by alloying it with nickel and with cobalt. (Table 2.3). However, ECSA enhancement is more pronounced (57/18 for PtNi/XC-72 and 32/18 for PtCo/XC-72). It can be concluded that alloying platinum with nickel and cobalt does not only lower the grain size, but also reduces the degree of agglomeration of the catalyst grains. This indicates that nickel eliminates agglomeration of nano-particles more effectively. The decrease in agglomeration is attributed to the "anchoring effect" of nickel and cobalt on platinum [91].

Table 2.3 Effect of alloying on Pt catalyst grain size and ECSA

Catalyst code	Catalyst composition by EDSA (a)	Grain size	Maximal ECSA (m^2/gm)	Lattice parameters (°A) (b)
BN5	Pt.65%/XC72	4.3	18	3.9151
BN13	Pt51Ni49 65%/XC72	2.2	57	3.8486
BN15	Pt48Co52 65%/XC72	2.7	32	3.8732
BT9	Pt 93%/SiO_2	5.8	3	3.9182
BT14	Pt45Ni55 85%/SiO_2	3.2	6	3.8204
	Pt72Co28 85%/SiO_2	3.7	5	3.8767

a-Weight percent of the metals is calculated from reagent concentration

b-Pure metal lattice parameters: a_0(Pt) = 3.9231°A, a_0(Ni) = 3.5238°A, a_0(Co) = 3.5447

2.11.4 Palladium based (Pd-Co-Carbon-Nitride)

Vito Di Noto et al. [100] worked on platinum free electrocatalysts for the oxygen reduction reaction (ORR) and the hydrogen oxidation reaction (HOR) in PEMFC. Palladium was found a suitable element because it has the following characteristics.

- It has relatively low over potential for ORR [101].
- It has three to four times lower cost than Platinum [102].
- It has higher tolerance, towards the methanol poisoning [103].

2.12 Support materials for catalyst

There are different types of materials used as catalyst support. On one hand these materials reduce the cost of the catalyst system used in PEM fuel cells, by lowering the catalyst loading required for acceptable catalytic activity while attaining optimum platinum utilization; on the other hand they are useful to enhance the performance of the PEM fuel cells.

2.12.1 Carbon

Various allotropic forms of carbon have been used as catalyst support material [104].

- Amorphous Carbons
- Graphitic Carbon Varieties

- Nitrogen-doped Carbon support & Boron –doped carbon support

2.12.1.1 Amorphous Carbons

Following are the amorphous carbon types.

- Carbon black
- Activated carbon (AC)

These have been the traditional support materials used in heterogeneous catalysis. The activated carbons have porous surfaces. They have large internal surface areas per unit weight [105]. Due to this high surface area they offer more sites for catalyst deposition than other varieties of carbon.

2.12.1.2 Graphitic Carbon Varieties

Graphitic carbon varieties discovered in recent years are

- Carbon nanofibers (CNF)
- Carbon nanotubes (CNT)

Both are very good electrical conductors. They have an impurity free surface (i.e. no catalyst poisons such as sulfur) [106]. Actually, by graphitization this carbon support becomes highly resistant to oxidation and carbon corrosion [107]. Due to these advantages many researchers investigated platinum deposition on fibrous supports such as nanotubes and nanofibers [106,108,109,110,111].

Wang [112] and Shao [113] have reported that if Pt is supported on multiwall carbon nanotubes then such catalysts become highly durable and show a higher catalytic activity than if Pt is supported on other support materials like Vulcan XC-72 carbon black [113].

2.12.1.3 Nitrogen-doped carbon support & Boron –doped carbon support

Nitrogen-doped [114,115,116] carbon support and boron-doped [117] carbon support were investigated and it was observed that electrocatalyst made up of these supporting materials were highly active and durable in PEMFC. It was concluded that nitrogen acts as electron donator and enhances the ability of graphite to donate electrons to O_2 and therefore facilitates the reaction of oxygen to water.

This electron donator nature of nitrogen also increases the delocalized π bonding of graphite layers in carbon nanotubes and carbon nanofibers [116]. In this way the interaction between the carbon support CNT/CNF and the metal becomes stronger and the catalysts become more durable.

2.12.2 Silica

High surface area carbon (Vulcan XC-72) is commonly used as support material for catalysts in PEMFCs but at elevated temperatures carbon corrodes. It has been observed that the oxidation of carbon support occurs even at moderate temperatures (125-195°C) [118], which results ultimately in the decrease of cell performance.

For avoiding all these problems, N. Travitsky et al. [91] suggested another support, i.e., hydrophilic nano−sized ceramic powder such as silica. It is shown that at high temperature platinum−silica bonds are more stable than platinum−carbon bonds. Pt/SiO_2 catalysts are also used effectively in exhaust gas after−treatment techniques at temperatures over 150°C [119,120,121,122]. Silica should improve due to its hydrophilic characteristics, the wetting of catalyst layer.

2.13 Polyelectrolyte in catalyst layer

The polyelectrolyte, used in the catalyst layer, is closely related to the electrode performance, Platinum utilization and MEA durability [123]. Usually Nafion ionomers are used as binder and proton conducting electrolyte in the catalyst of PEMFC [124]. It is helpful to extend the electrochemical triple phase boundary (TPB) formation. In the catalyst layer, the transport of reactants, protons and electrons, i.e. the formation of TPB is illustrated in Figure: 2.8[125].

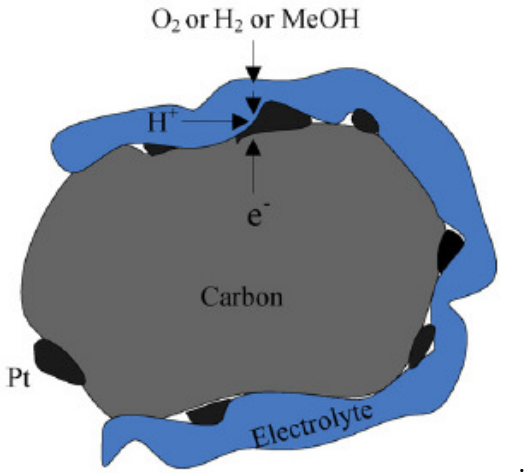

Figure: 2.8. Scheme of the reactant, proton and electron transport in catalyst layer of PEMFC electrode, i.e. the formation of the electrochemical triple-phase boundary.

Figure: 2.8 shows, the proton conducting electrolyte and the reaction site. It is necessary that the electrolyte must be permeable [126]. Electrolytes like aromatic hydrocarbons are more hydrophilic than Nafion [123]. Then there is the possibility that water can gather in the electrode which might block the transport of reactants (fuel and oxidant). In the cathode catalyst layer, oxygen is electrochemically reduced to H_2O and some amount of H_2O_2 is also produced in ORR. This amount increases with the decrease in agglomeration of Pt/C [127]. This HO is harmful to the polyelectrolyte [128]. But it is not known, what are the exact formation sites of H_2O_2 and how H_2O_2 harms the polyelectrolyte.

2.14 Types of Polyelectrolyte

Following materials are used as polyelectrolytes.

- Nafion
- Sulfonic acid group
- Aromatic hydrocarbons

It was observed that carbon supported noble metal catalysts were more active for ORR, when Nafion was used as electrolyte compared of Sulphonic acid. Sulphonic acid anions can not adsorb on platinum catalyst surfaces [129]. Permeability of hydrogen [130] and oxygen [131] for Nafion are greater than for other polyelectrolytes. For example, the oxygen permeability of Nafion is 1.5−3 times larger than that for sulfonated polyether sulfon membranes [132] and five times larger than that for SPEEK [133]. Nafion was also found to be more stable in a Fenton's reagent test.

2.15 Characterization Techniques

2.15.1 Cyclic Voltammetry (CV)

It is believed that the major cause of decrease in performance of PEMFC is the loss in Electro chemical Surface Area (ECSA) of catalysts. The ECSA loss of platinum at cathodes is greater than that at anodes [134]. The ECSA loss of Pt in cathodes for H3PO4/PBI high temperature PEMFC during the 520h life time test was measured by Cyclic Voltammetry (Figure 2.9).

The figure shows that the ECSA decreases first during about 300h fast, i.e. from 17.2 to 7.8 m^2/g_{Pt} with a rate of 0.03m^2/h g_{pt}. The loss in ESA is approx 55%. In the next 210h the decrease in ECSA is only about 5%.

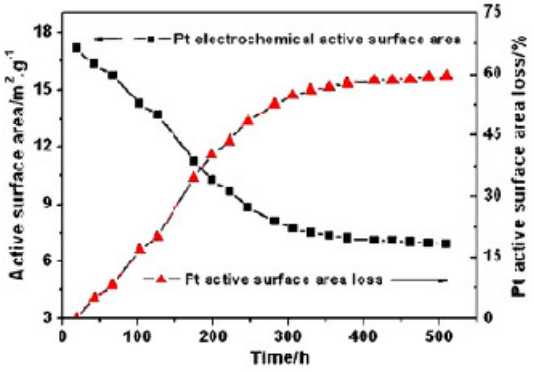

Figure 2.9: The Pt electrochemical surface area calculated during the 520 h intermittent test [135]

2.15.2 Transmission Electron Microscopy (TEM) Analysis

Figure 2.10 shows the TEM images of electrocatalysts, before test and after 100h, 300h, and 520h tests. The particle sizes were measured manually by bright field micrographs and were plotted in Figure 2.11.The mean diameter dn of the particle was calculated by the following formula [134].

$$d_n = \frac{\sum_{i=1}^{n} di}{n} \qquad 2.11$$

From Figure 2.9 it is visible that the size of Pt particle increases with the passage of time. After 100h, some coalescence of particles appears but majority particles are small. But after 300h, the majority of small crystallites disappear and after 520h, the size of almost all particles increases. Figure 2.11 shows that mean diameter of the particles increases from 4.0 nm to 9.0 nm after 520h life time test.

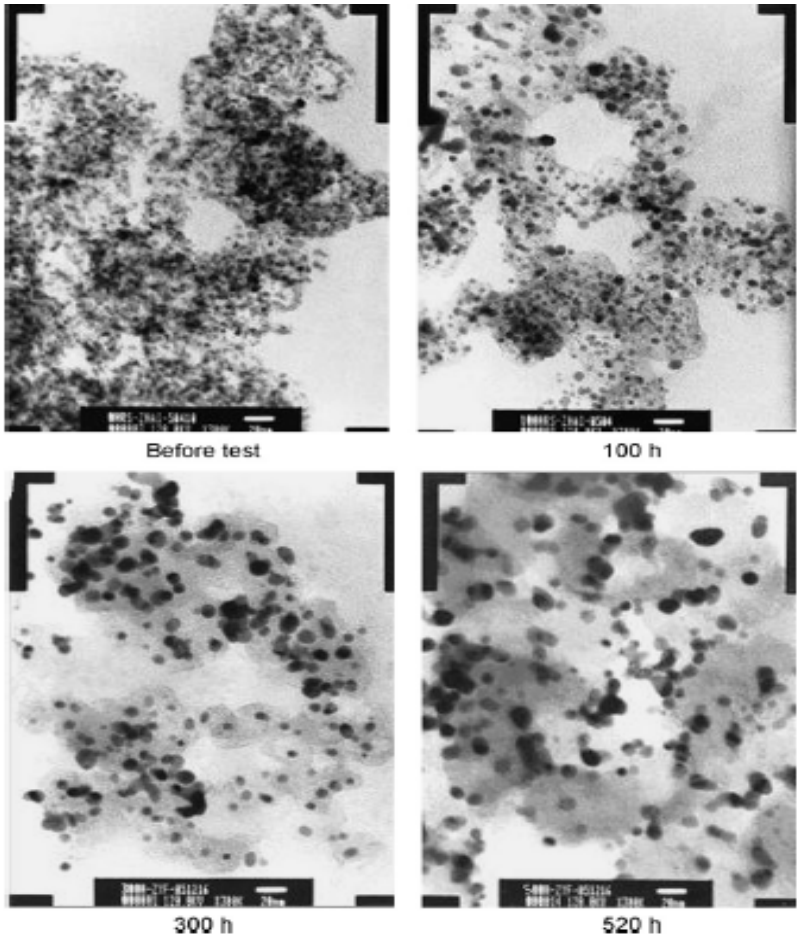

Figure 2.10: The TEM photographs of Pt/C in cathodes before and after 100, 300 and 520 h intermittent test [135]

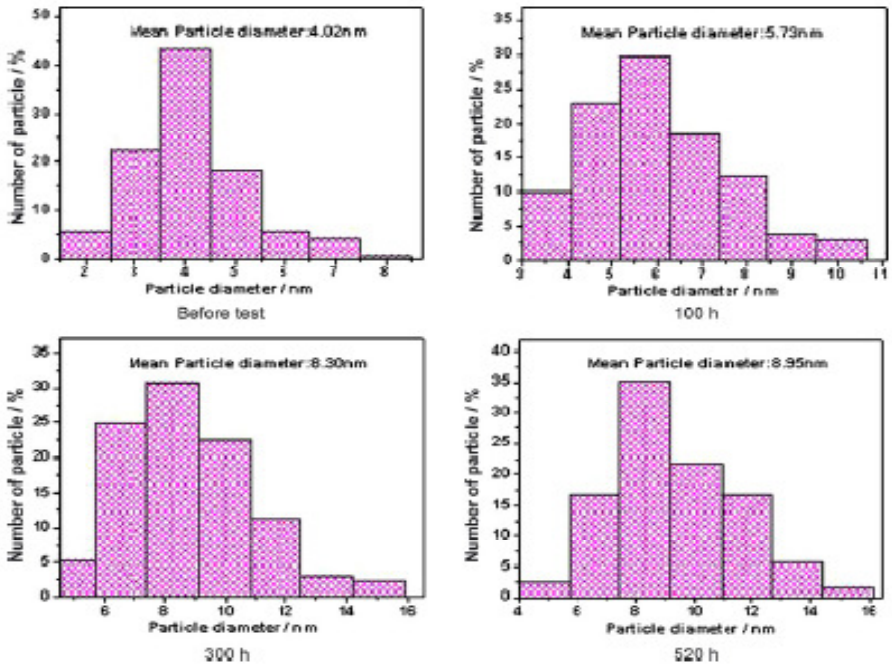

Figure 2.11: The histogram of Pt/C particles sizes distribution from the TEM photographs [135]

2.15.3 X-Ray Diffraction (XRD) Analysis

Yunfeng Zhai et al. [135] also investigated the electrocatalyst through XRD analysis. The results are shown in Figure 2.12. The characteristic diffraction peaks of the face centered cubic structure were detected in all the electrode samples. The figure shows that the diffraction peaks at 2θ values of 39.8°, 46.3°, 67.5° and 81.4° are linked with different Pt lattice planes. All the characteristic peaks of Pt in the cathode become sharper, because Pt particles grow during the life time test. The growth of Pt particles in the cathode is higher than in the anode.

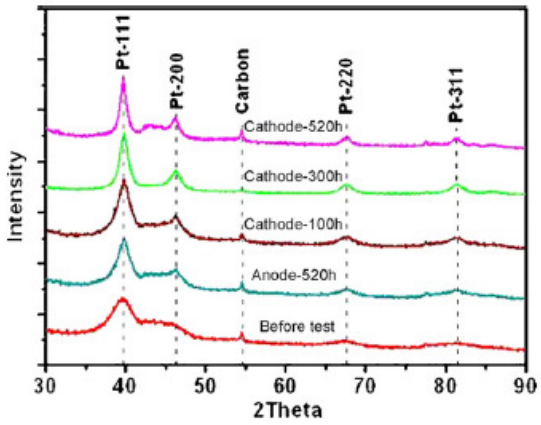

Figure 2.12: The XRD patterns of Pt/C in cathodes before and after 100, 300 and 520 h intermittent test [135]

2.15.4 Comparison between TEM and XRD Analysis

The mean size of the Pt particles in cathode was calculated by Scherer's formula on the basis of diffraction peaks. Figure 2.13 shows the results of the growth of Pt particle in cathode by TEM and XRD techniques. The average diameter of the particle calculated by X-Ray Diffraction is minutely different from that calculated by TEM. This is due to the fact that Pt particles, smaller than 1 nm can not be measured by TEM [136]. Therefore the average diameter calculated from TEM would be greater than that of X-ray diffraction. Otherwise the results are the same by the two techniques, i.e. there is a rapid increase in the size of Pt particle during the first 300h of operation. But during the next 220h the increase in the size of Pt particle is small.

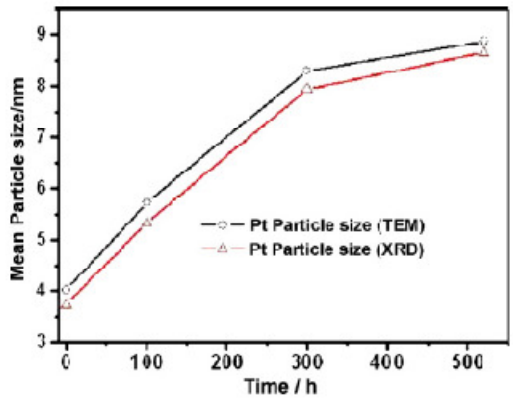

Figure 2.13: The change of Pt particles size in cathodes with test time [135]

2.16 PEM fuel Cell Diagnostics

Following in-situ and ex-situ diagnostic techniques are helpful to characterize the fuel cells.

2.16.1 In-situ Diagnostic Techniques (Electrochemical)

- Current-Voltage (j-V) measurements (Polarization Curve)
- Current Interruption
- Electrochemical Impedance Spectroscopy
- Cyclic Voltammetry
- CO Stripping Voltammetry
- Linear Sweep Voltammetry (LSV)

2.16.2 Ex-situ Diagnostic Techniques

- Scanning Electron Microscopy (SEM)
- Transmission Electron Microscopy (TEM)
- Energy Dispersive X-Ray spectrometry EDXS)
- X-Ray Diffraction (XRD)

3 Experimental Set-up and Diagnostic Techniques

3.1 Construction and Assembly of the Fuel Cell

The single unit polymer electrolyte membrane fuel cell (PEMFC) of active surface area 5cm^2 was used in this research work. This PEM fuel cell consists of

- a membrane electrode assembly (MEA)
- an electrically conducting gas diffusion layer
- a sealing (gasket) and
- electrically conductive flow fields to deliver the reactant gases via gas channels.

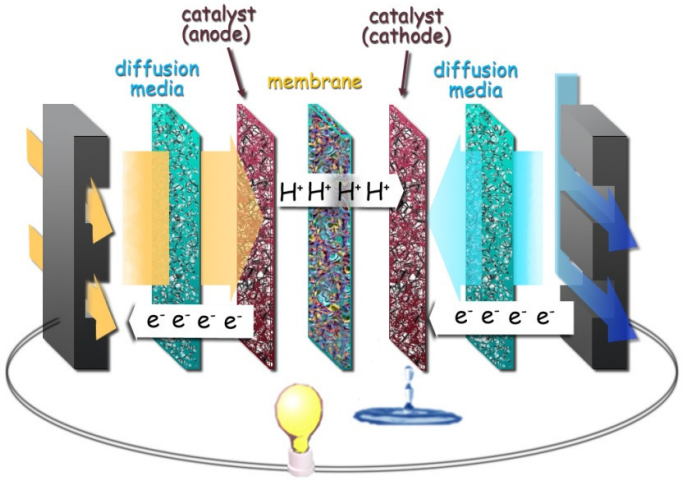

Figure 3.1 Separate components of PEM fuel cell [68]

3.1.1 Membrane Electrode Assembly (MEA)

The membrane electrode assembly consists of solid polymer electrolyte membrane (in the centre) coated with the electrodes on both sides. One side of the polymer electrolyte membrane (PEM) is anode and the other side is cathode as well. Some catalyst is added on the electrodes to enhance their chemical activity.

The PEM is ionic conductive and acts as separator for the reactant gases and prohibits the electronic transport. [137]. The anode catalyst layer (ACL) catalyses the hydrogen oxidation reaction and the cathode catalyst layer (CCL) catalyses the oxidation reduction reaction at the triple phase boundary.

$$H_2 \rightarrow 2H^+ + 2e^- \qquad (HOR) \qquad 3.1$$

$$O_2 + 4H^+ + 4e^- \rightarrow 2H_2O \qquad (ORR) \qquad 3.2$$

3.1.2 Gas Diffusion Layer (GDL)

In PEM fuel cell assembly the gas diffusion layer (GDL) is placed between the MEA and the flow field plates. GDLs are made of (Poly-Tetra-Fluoro-Ethene) PTFE-hydrophobized carbon paper or carbon cloth. The reactants (H_2 & O_2) transported to the catalyst layer and the products (H_2O) are transported to the gas channel. The function of the GDL is to [68]:

- provide reactant gas access from flow-field channels to catalyst layers including in-plane permeability to regions adjacent to flow field lands;
- provide passage for removal of product water formed at the cathode side of the catalyst layer to flow-field channels including in-plane permeability from regions adjacent to lands;
- provide electronic and thermal conductivity between bipolar plates and catalyst layer including in-plane conductivity to regions adjacent to channels;
- provide mechanical support to the MEA, especially when thin membranes are used, and a pressure difference between the anode and cathode gas channels is present.

3.1.2.1 Required Properties of GDL

An effective GDL must have the following properties.

- Very good mechanical strength against compression
- High porosity and good hydrophobic properties
- Very good electrical and thermal conductivity, especially through the plane
- Chemical and mechanical stability in operative conditions

3.1.2.2 Structure of GDL

GDLs consist of two layers.

- A macro-porous substrate or support layer (SL)
- A micro-porous layer coated on the support layer

The coating of the microporous layer on the SL ameliorates the water-gas management of the entire GDL as well as improves the better contact of the SL with the catalyst layer.

MPL typical pore size=100-500 nm

SL typical pore size=10-30 µm

Typical thickness of SL= 100-300 µm

Typical thickness of MPL= 5-50 µm

Widely used material for SL of GDL is carbon fiber paper (not woven) or woven carbon cloth. Scanning electron microscope images of the two diffusion media substrates show that the carbon-fiber paper is bound by webbing (carbonised thermo-set resin) whereas no binder is necessary in the carbon cloth due to its woven structure.

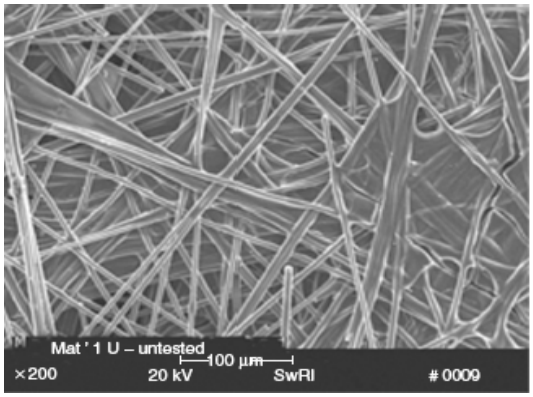

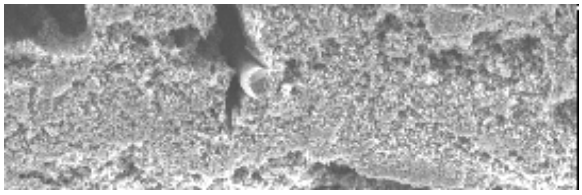

Figure 3.2. A carbon fiber paper normally used as SL (left), ***Carbon /PTFE Microporous layer (right) [68]***

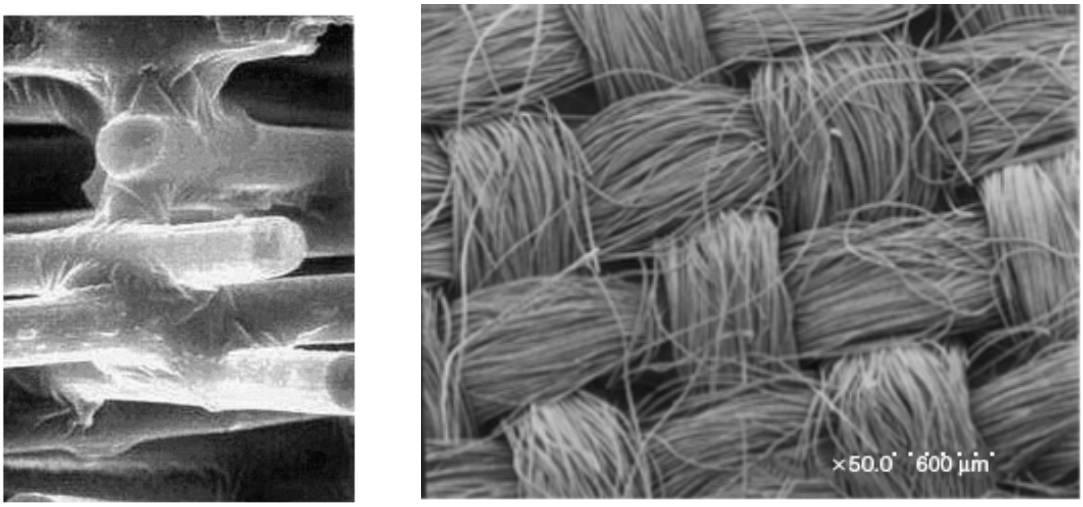

Figure 3.3: ***Inner structure of a Carbon fiber paper, not wet proofed (Left), Carbon cloth, Textron Avcarb 1071 HCB Not wet proofed (Right) [68]***

High PTFE content increases hydrophobicity but decreases porosity. Therefore microporous layers (PTFE content) should remain on the surface of the SL. Excess of its penetration can minimize the effectiveness of GDL.

The role of the GDL is different for anode and cathode. On the cathode side water is formed as a reaction product which has to be dropped out to prevent flooding. Otherwise it blocks the catalyst site and prohibits the entrance of oxygen into the catalyst layer. On the anode side some water must be kept in order to humidify the membrane.

3.1.3 Sealing (Gasket)

The fuel cell was sealed with two silicon seals, each of thickness 0.19 mm. The main function of the sealing is to avoid leaks, loss of fuel gas and overcompression, and to avoid mixing of the fuel gas hydrogen with oxygen. Furthermore they serve as electrical insulator. Commonly used sealing materials are silicon-based elastomers. They show a wide operating temperature range, excellent hardness, good electrical resistivity and dielelectrical strength as well as a good pressure sealing ability, low swelling in PEMFC fluids and low permeability to fuel gases.

The gaskets used in the fuel cell assemblies were prepared by the instrument as shown in Figure 3.4**.**

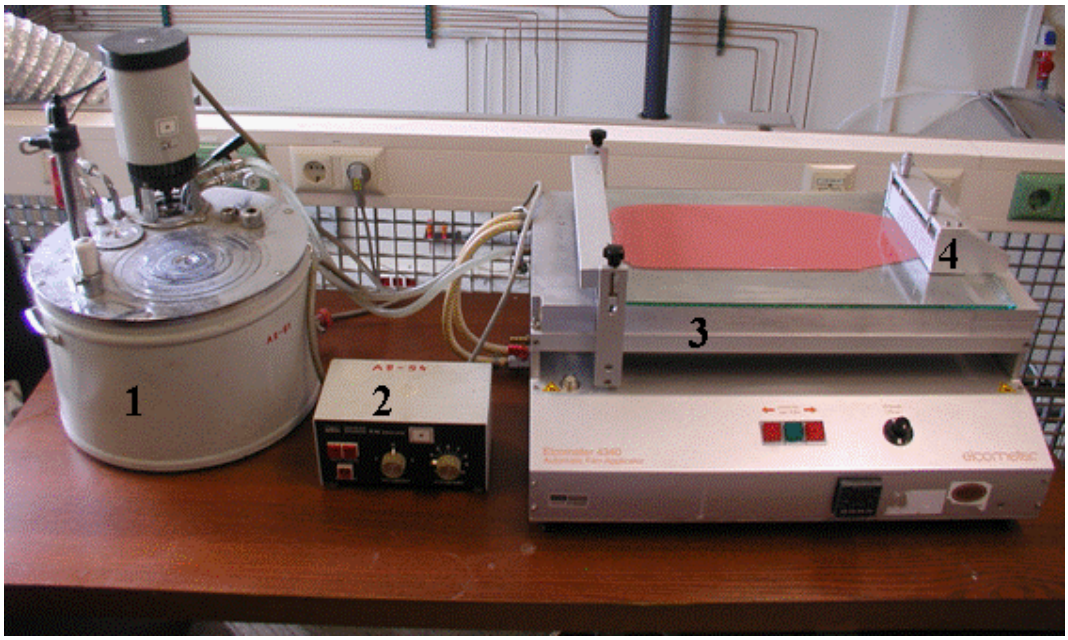

Figure 3.4: Gasket (sealing) preparation instrument, (1) Water heater, (2) Thermostat, (3) Film applicator, (4) Elcometer

3.1.4 Bipolar Plates

A pair of bipolar plates is used in PEM fuel cell, one for the anode side and the other for the cathode side of the fuel cell fixture. The bipolar plates have engraved channels for gas flow. These channels are known as flow fields. There are many types of flow fields. The bipolar plates with serpentine flow fields were used in this research study. The function of the bipolar plates is to

- Distribute the reactant gases to both electrodes.
- Transport electrons from anode to cathode.
- Drain liquid water at the cathode.
- Remove the produced heat

The bipolar plates are made of graphite. The bipolar plates used through out all the test series are shown from the Figure 3.5. On the cathode plate the width of the flow field channels is 1mm and on the anode plate the width of the flow field channels is 0.5mm. The geometry of the flow field channels maintained a constant pressure drop of about 100mbar, which is required to remove liquid water.

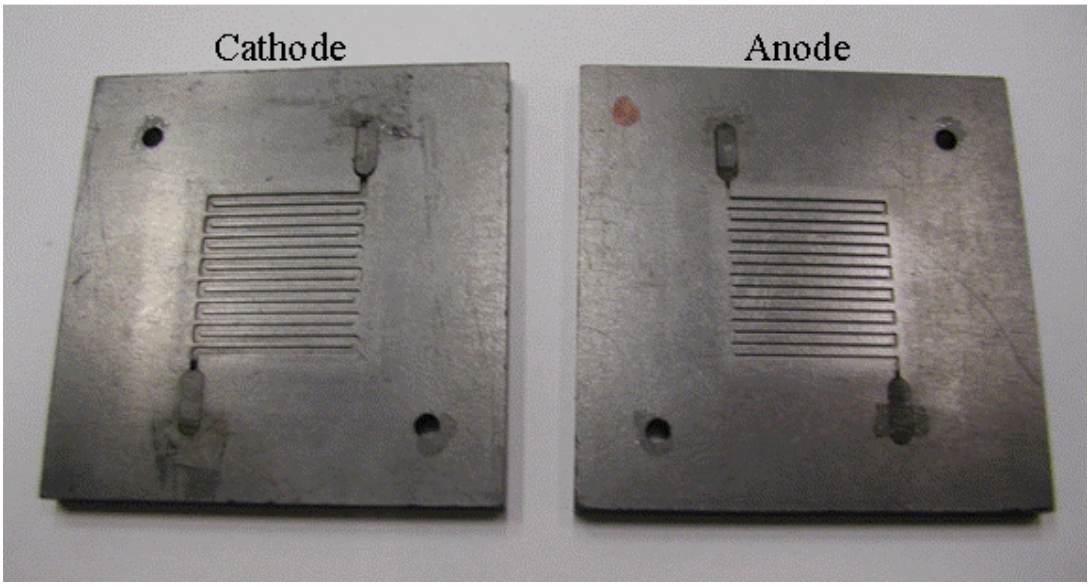

Figure 3.5: Bipolar plates used in the PEM fuel cell assembly

The gold plated copper current collector plates were put above the bipolar plates. Afterward two PTFE plates were used for electrical insulation to the end plates, made of aluminium. Water heating pipes run through the end plates to heat up the cell. The gases were supplied by the Teflon pipes, passed through the end plates.

The cell assembly was fixed with four screws and disc springs (20 disc springs covering 24.1mm length in each pillar) in such a way, that a mechanical pressure of 800N was applied at ambient temperature for the cell assembly to guarantee the reasonable electrode-membrane contact and to provide a uniform and reproducible compression force over the complete cell area. Each single unit cell has a water-based thermal management system to maintain a constant temperature of 70°C during operation [138].

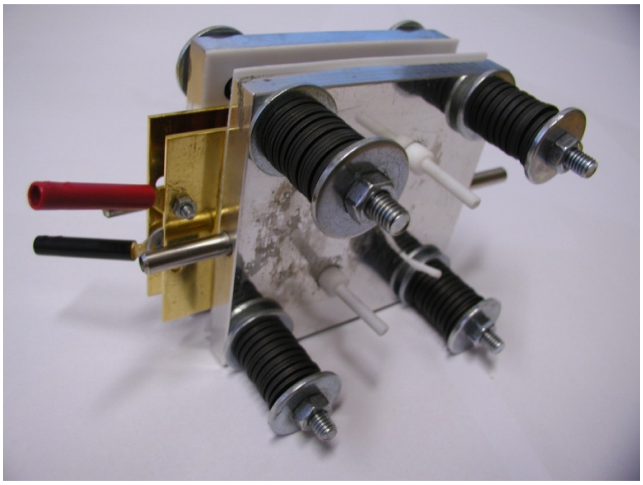

Figure 3.6: Fully assembled PEM fuel cell with 5 cm^2 active area

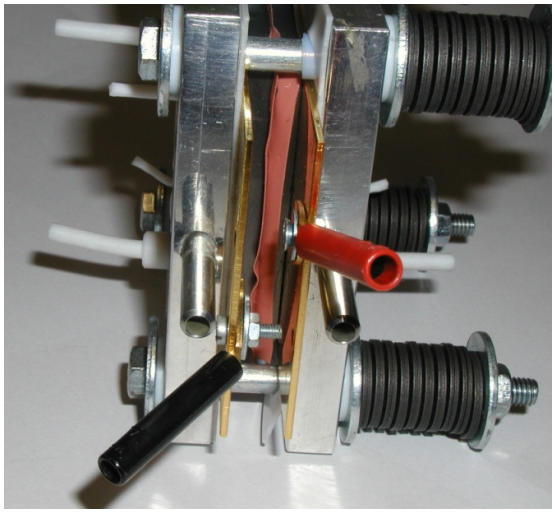

Figure 3.7: Crossectional view of the PEM fuel cell

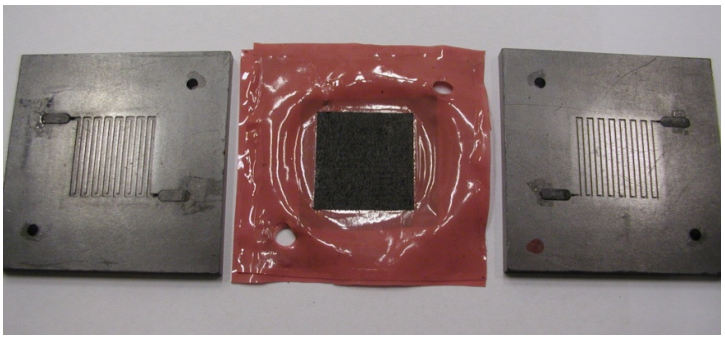

Figure 3.8: Two bipolar plates and MEA covered by GDL in the centre of two gaskets

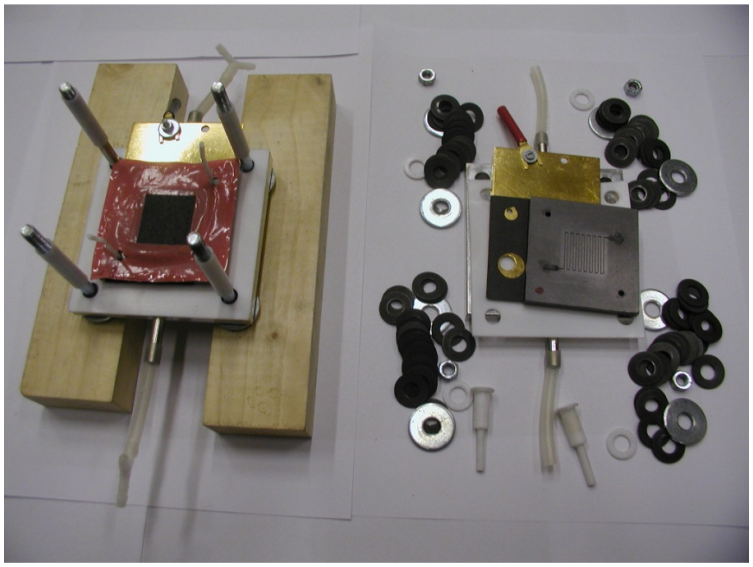

Figure 3.9: All components to assemble a PEM fuel cell of area 5cm^2

3.2 Test Rigs

The accelerated potential cycling test series and in-situ dynamic tests were conducted on two fuel cell test stations. Their detail is as follows.

3.2.1 Test Rig for Potential Cycling Test

This test rig is equipped with computerized control on gas flows, gas preheating and a control system for fuel cell potential and temperature (Figure 3.10).

The gases were moistened with the help of two water bubbled humidifiers per cell, which were heated serially by an oil circulation. The temperature of the oil was maintained by a temperature regulator (Julabo Top Tech MC-4). The humidifiers are connected with electrically heated pipes to the cell. (Figure 3.11)

The temperature of the cell is controlled by hot water circulation through the end plates of the fuel cell assembly, with another temperature regulator (Julabo Top Tech MC-4). In order to minimize the heat losses from gas pipes, they are heated with electric heat strings, which are controlled with the PCU.

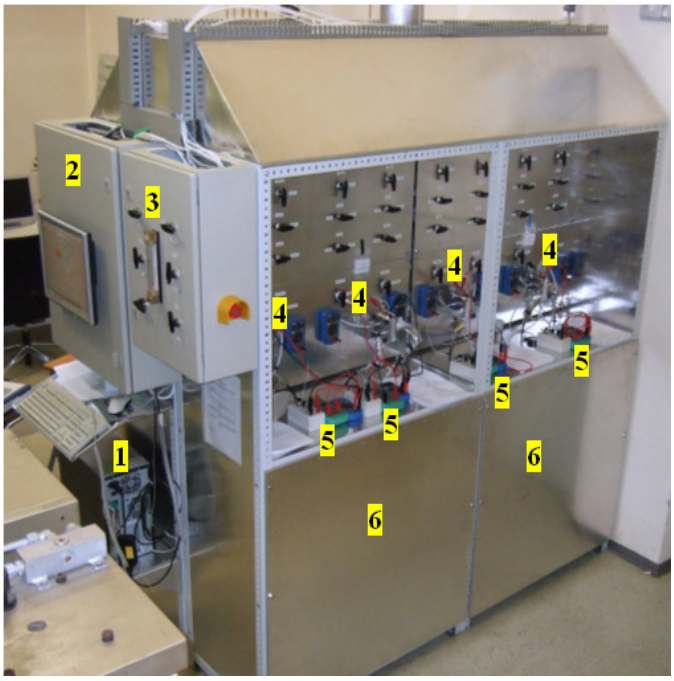

Figure 3.10: Test rig for potential cycling Test, (1) PCU, (2) Switchbox, (3) Gas mixing station, (4) Switches for water heating of the fuel cell, (5) Resistor and Multimeter, (6) position of the Humidifiers.

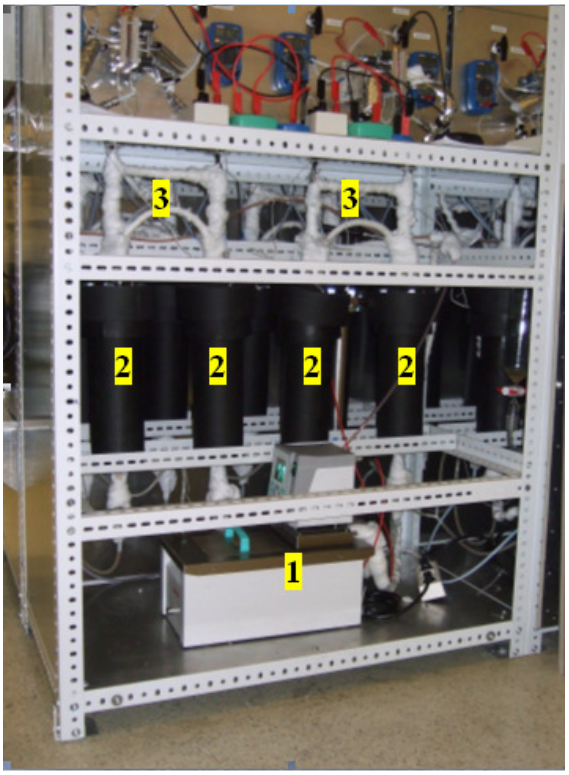

Figure 3.11: Humidifiers and temperature regulator for the humidifiers, (1) temperature regulator, (2) Water based humidifiers in insulating material, (3) isolated and heated Gas pipes

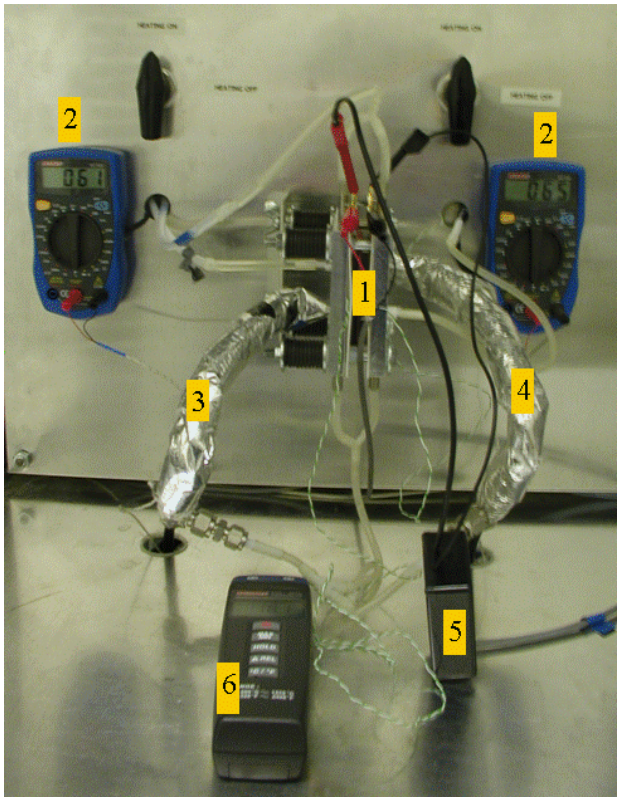

Figure 3.12: Fuel cell connecting to the potential cycling test rig, (1) Position of the fuel cell, (2) Humidifier temperature reader, (3) H_2 pipe, (4) Air pipe, (5) Transistors, (6) Fuel cell temperature reader

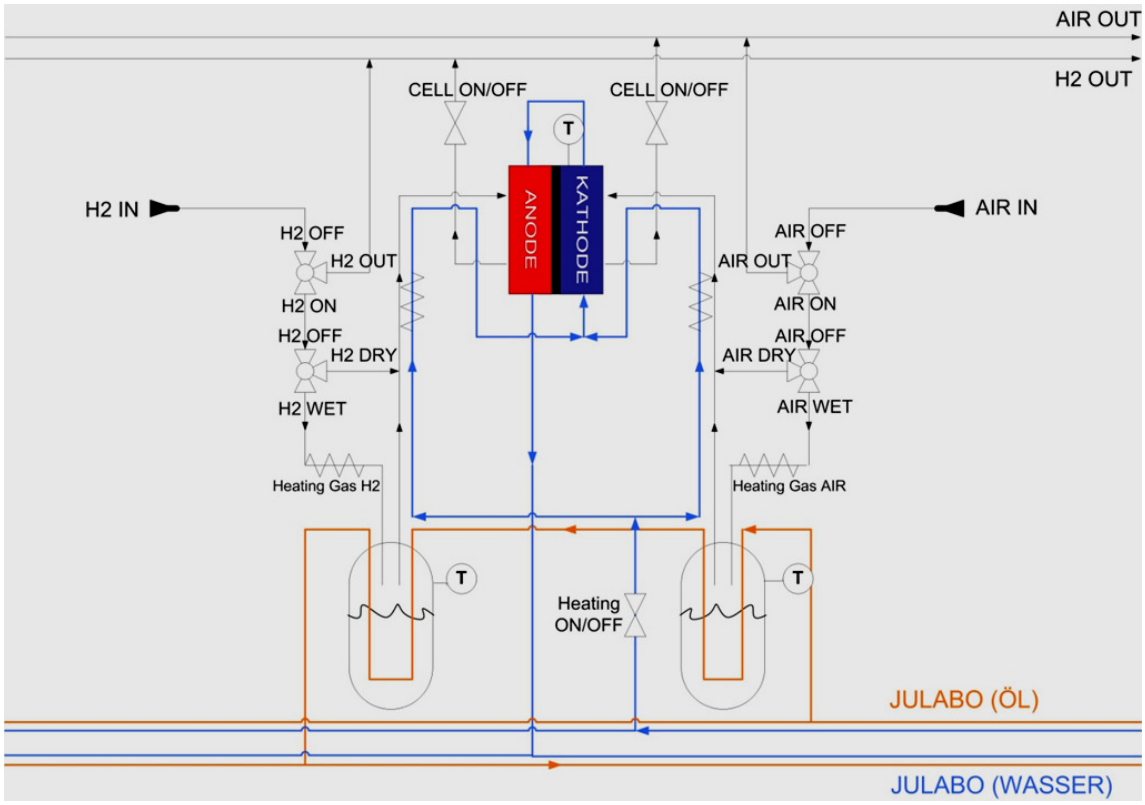

Figure 3.13: Schematic diagram of the teststand for a single cell

Figure 3.12 shows the PEM fuel cell connected to the teststand for potential cycling test. Figure 3.13 illustrates the schematic diagram of the teststand for single cell.

Figure 3.13 elaborates the schematic construction for the provision of the cell with moistened gases and the course of heat directions. The orange line indicates the course of the heating directions for the humidifiers. The blue line indicates the provision of the cell and the gas heating with hot water.

Figure 3.14 Graphic surface with (1) Massflow controller that changes the flow for H_2 / air (O_2) / N_2, (2) Display of the temperature for the inlet gases and (3) Display for the cell temperatures

Gas heating is controlled by Lab View programme (electrically heated system). Security valves (controlled by Lab View programme) are connected to the security system situated at the roof of the teststand (hydrogen sensor and temperature sensor). Security valves close the supply of H_2 and air and purge with N_2 automatically in case of emergency shut down.

3.2.2 Test Stand for Characterization of Fuel Cell

The in-situ dynamic tests were conducted with this test station. This teststand was also built up in the laboratory for fuel cell systems for characteristic measurements of the fuel cell. This teststand was also facilitated with the computerized control on gas flow, gas preheating, temperature of the humidifiers and security system for the potential of the fuel cell. The temperature of the fuel cell can also be visualized from the monitor. All these controls are applicable by using the Lab View software

The test rig has two heated bubble humidifiers for input gas humidification and is capable of supplying mixtures of hydrogen, nitrogen and oxygen gases utilizing computerized mass flow controllers at a given mass flow rate. The humidifiers and the gas pipes connecting the humidifiers with gas inlets of the fuel cell are insulated with the insulating materials for minimizing the heat losses.

The temperature of the fuel cell is controlled by the hot water circulation through the end plates of the fuel cell fixture. The distilled water is heated up by a revolutionize temperature regulator (Julabo. Top Tech MC-4).

For monitoring the fuel cell, a Zahner Electric Impedance Measurement System consisting of an IM6ex Electrochemical Workstation and a PP240 Power Potentiostat was used. IM6ex-ZAHNER is capable to measure the current of 2A whereas with the help of PP240 power potentiostat currents upto 40A can be measured [138].

3.2.2.1 Main Components of the Teststand

Figure 3.15 shows the main components of the teststandl.

1. Fuel Cell
2. Impedance measurement device
3. Gas supply station
4. Box of electric components for electronic control
5. Box for mass flow controller with movable screws
6. Humidifiers
7. Julabo water heater

Figure 3.16 shows another main part i.e., gas supply station of the teststand. With the help of screws either O_2 or air can be supplied to the cathode side of the MEA and H2 is fed to the anode side of the MEA. The supply of N2 to purge the fuel cell before and after the experiment is also possible from this gas supply station.

Figure 3.15: Single PEM fuel cell test stand

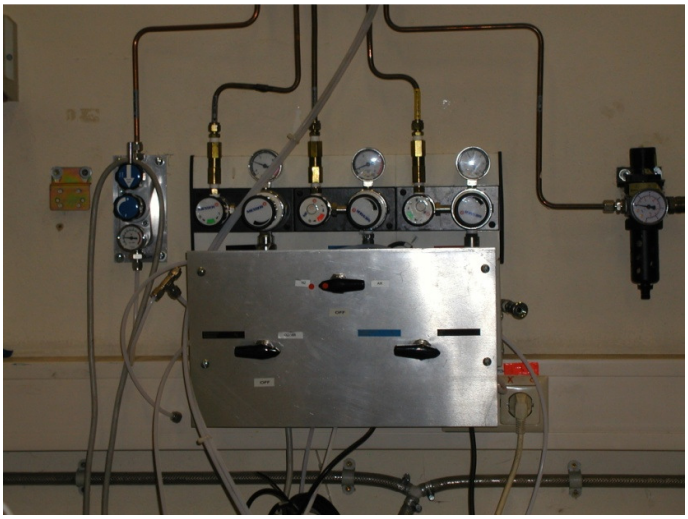

Figure 3.16. Gas supply station with movable screws

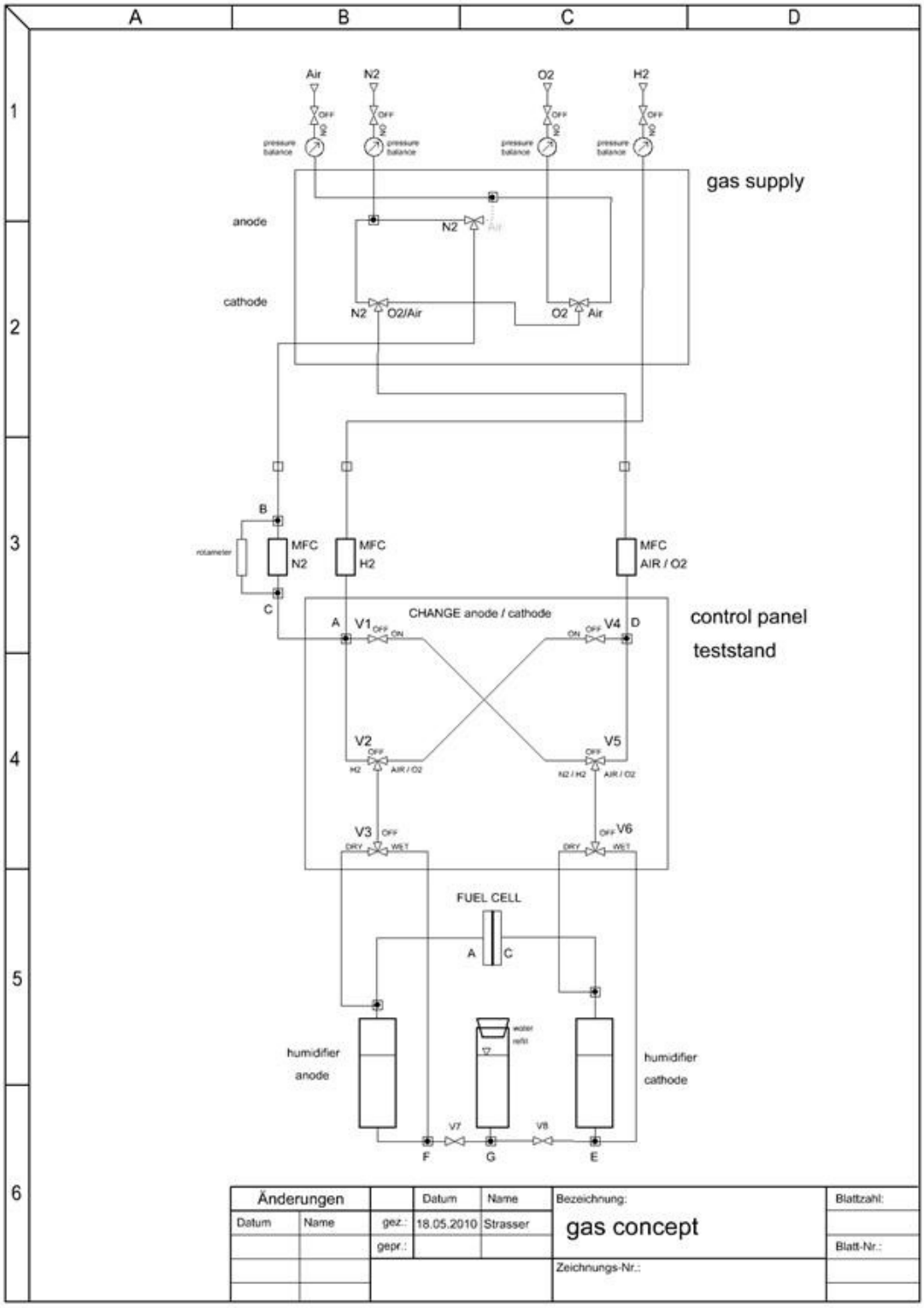

Figure 3.17: Schematic design of the test stand

3.3 Performance Test (Activation of MEA)

The measurements were started after activating the MEA. During the activation procedure the cells were operated for eight to ten consecutive cycles to get maximum performance. Each cycle consisted of a 15-min operation at 0.6V, 30 min operation at 0.4V and 1min operation at open circuit voltage (OCV) mode. After getting the maximum performance of the cell in terms of stable values of the cell current, the performance test was stopped.

Following the performance test, the diagnostic tests were conducted to understand the performance characteristics of each fuel cell.

3.4 Diagnostic Test

3.4.1 In-situ Electrochemical Diagnostic Techniques

Following diagnostic techniques were utilized to characterize the PEM fuel cells

- Polarisation Curve (PC)
- Electrochemical Impedance Spectroscopy (EIS)
- Cyclic Voltammetry (CV)
- Hydrogen Diffusion Current Measurements

3.4.1.1 Polarization Curve

The current-voltage curve, also called the polarization curve is a specific characteristic of the fuel cell which describes generally the overall performance of the fuel cell. Polarization curve is a special characterisation of the fuel cell which shows relationship between cell potential and current density under a set of constant operating conditions. This electrochemical technique is used to characterize the performance of a single fuel cell as well as a stack.

The efficiency of a fuel cell, which depends upon the operating conditions, can be calculated with the help of the polarization curve.

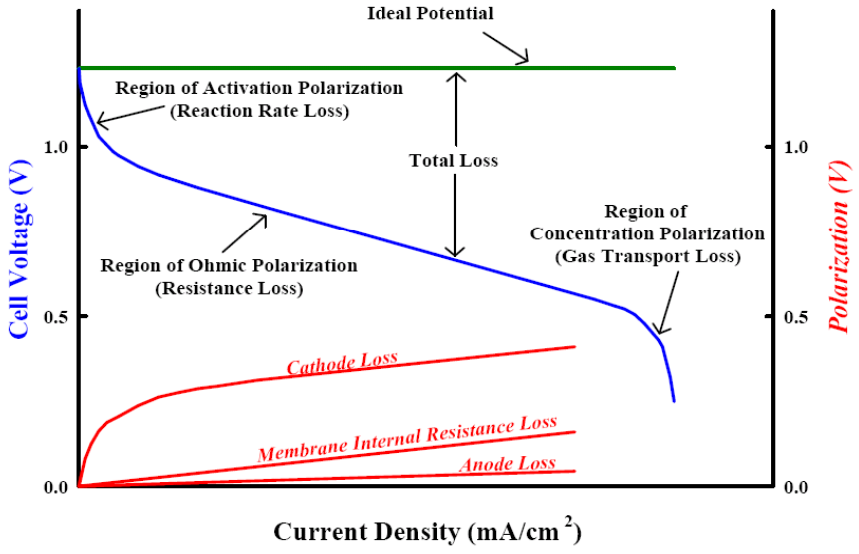

Figure 3.18: The Polarization Curve [139]

Following is the equation to model the polarization curve. [140]

$$E_{cell} = E_{Nernst} - R_{\Omega}\, j - \eta_{act} - \eta_{trans} \qquad 3.3$$

This equation shows that the fuel cell voltage depends upon the

- Nernst Voltage (dependence on feed gas composition)
- Ohmic resistance (the major contribution is protonic conductivity of the membrane)
- Activation losses (electrode processes, also called Polarization)
- Mass transport losses (mass transport limitation in MEA/GDL, also called diffusion overpotential).

Equation 3.3 can be expressed in more detail as the following equation. [141]

$$E_{cell}(T) = E^{\circ}(T) + \frac{RT}{2F}\, ln\, \frac{P_{H2O}}{P_{H2}P_{O2}} - R_{\Omega}(T)j - \frac{RT}{\alpha F}\, ln\, \frac{j}{j_{0\,(T)}} - \frac{RT}{\alpha F}\, ln\, \frac{j_{lim}}{j_{lim} - j} \qquad 3.4$$

R_{Ω} - Mean resistance of the MEA (ohmic resistance)

α – symmetry factor

J_0 – exchange current density

J_{lim} –limiting current density

Different voltage losses take place in the fuel cell operation. The detail of these losses is as follows [142].

3.4.1.1.1 Activation Losses

These losses are due to the slowness of the reactions taking place on the surface of the electrodes. A proportion of voltage generated is lost in driving the chemical reaction that transfers the electrons to or from the electrode. This voltage drop is highly non-linear.

3.4.1.1.2 Ohmic Losses

This voltage drop is the straightforward resistance to the flow of electrons through the material of the electrodes and the various interconnections, as well as the resistance to the flow of ions through the electrolyte. This voltage drop is essentially proportional to the current density, linear, and so is called ohmic losses, or sometimes as resistive losses.

3.4.1.1.3 Mass Transport or Concentration Losses

These losses are due to the change in concentration of the reactants at the surface of the electrodes as the fuel is used. Since the concentration affects the voltage, so this type of loss is nominated as concentration loss and the decrease in concentration is the result of a failure to transport sufficient reactants to the electrode surface, this type of loss is also often called as mass transport loss. The

third name of this loss is ´´Nernstian``. This is because of its connection with concentration, and the effects of concentration are modelled by the Nernst equation.

3.4.1.1.4 Fuel Crossover and Internal Currents

This energy loss results from the waste of fuel passing through the electrolyte, and, to a lesser extent, from electron conduction through the electrolyte. The electrolyte shoild only transport ions through the cell. However, a certain amount of fuel diffusion and electron flow will always be possible /except for direct methanol fuel cell), but it does have a marked effect on the OCV of the low temperature cells.

3.4.1.2 Electrochemical Impedance Spectroscopy (EIS)

Impedance spectroscopy is a specific branch of the tree of electrical measurements. The concept of electrical impedance was introduced by Oliver Heaviside in 1880. A. E. Kennelly and C. P. Steinmetz developed it as vector diagram and complex representation [143].

Electrochemical impedance spectroscopy is a more sophisticated technique to accurately differentiate between all the major sources of loss in a fuel cell. Impedance is a measure of the ability of a system to impede the flow of electrical current. It can deal with the time dependent or frequency dependent phenomena. Basically impedance is a ratio between time-dependent voltage and time-dependent current [144].

$$\boldsymbol{Z = \frac{V(t)}{I(t)}} \qquad \textbf{3.5}$$

Impedance measurements are performed by applying a small sinusoidal voltage perturbation, and monitoring the system's resultant current response.

$$\boldsymbol{V(t) = V_0\, cos\,(\,\omega t)} \qquad \textbf{3.6}$$

$$\boldsymbol{I(t) = I_0\, cos\,(\omega t - \phi)} \qquad \textbf{3.7}$$

V (t) Potential at time t

I (t) Current at time t

V_0 Amplitude of the voltage signal

I_0 Amplitude of the current signal

ω radial frequency (radians.s^{-1})

A graphical representation of the relationship between a sinusoidal voltage perturbation and a phase shifted current response for a linear system is exhibited in the Figure 3.19.

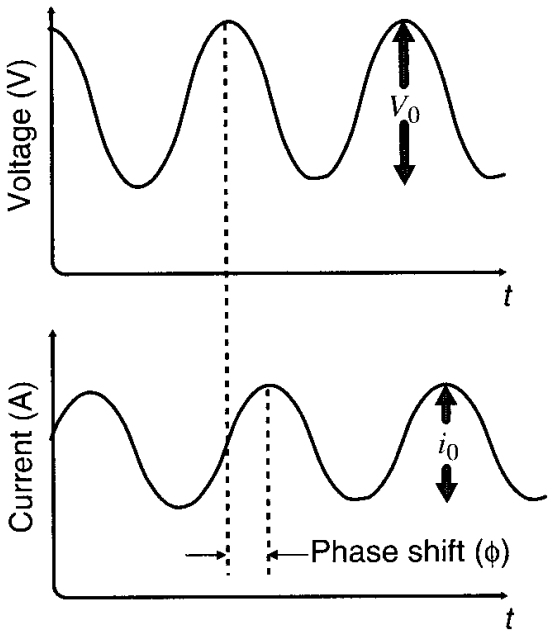

Figure 3.19: A sinusoidal voltage perturbation and resulting sinusoidal current response (both have same frequency, but the current response has a phase shift ($\boldsymbol{\phi}$) than voltage perturbation) [144].

The sinusoidal impedance response of a system can be written as follows:

$$\boldsymbol{Z} = \frac{\boldsymbol{V_0\, cos\,(\omega t)}}{\boldsymbol{I_0\, cos\,(\omega t - \phi)}} \qquad \textbf{3.8}$$

By using the complex notation the impedance response of a system in terms of real and imaginary component would be:

$$\boldsymbol{Z} = \frac{\boldsymbol{V_0\, e^{j\omega t}}}{\boldsymbol{I_0\, e^{(j\omega t - j\phi)}}} \quad = \boldsymbol{Z_0\, e^{j\phi}} \quad = \boldsymbol{Z_0}\ \boldsymbol{(cos\,\phi + j\, sin\ \phi)} \qquad \textbf{3.9}$$

The impedance of a system can therefore be expressed in terms of an impedance magnitude Z_0 and a phase shift $\boldsymbol{\phi}$, or in terms of a real component ($Z_{real} = Z_0\ cos\boldsymbol{\phi}$) and an imaginary component ($Z_{imag} = Z_0\ sin\boldsymbol{\phi}\ \boldsymbol{j}$). Here *j* is an imaginary number ($j = \sqrt{-1}$).

Impedance data is usually plotted in terms of real and imaginary components of impedance. Such graphical representations of impedance data are known as Niquist plots. These plots summarize the impedance behaviour of a system over many orders of magnitude in frequency [144].

For the electrochemical impedance spectroscopy measurements of the fuel cell, the processes that occur inside the fuel cell can be modelled using circuit elements. For example, a group of resistors and capacitors can assign to describe the behaviour of electrochemical reaction kinetics, ohmic conduction processes and mass transport phenomena. Such circuit based representations of fuel cell behaviour are known as equivalent circuit model. A fuel cell suffers from the following loss processes.

- Anode activation
- Cathode activation
- Cathode mass transfer
- Ohmic losses

Equivalent circuit diagram and corresponding Nyquist plot of a fuel cell can be exhibited from Figure 3.20.

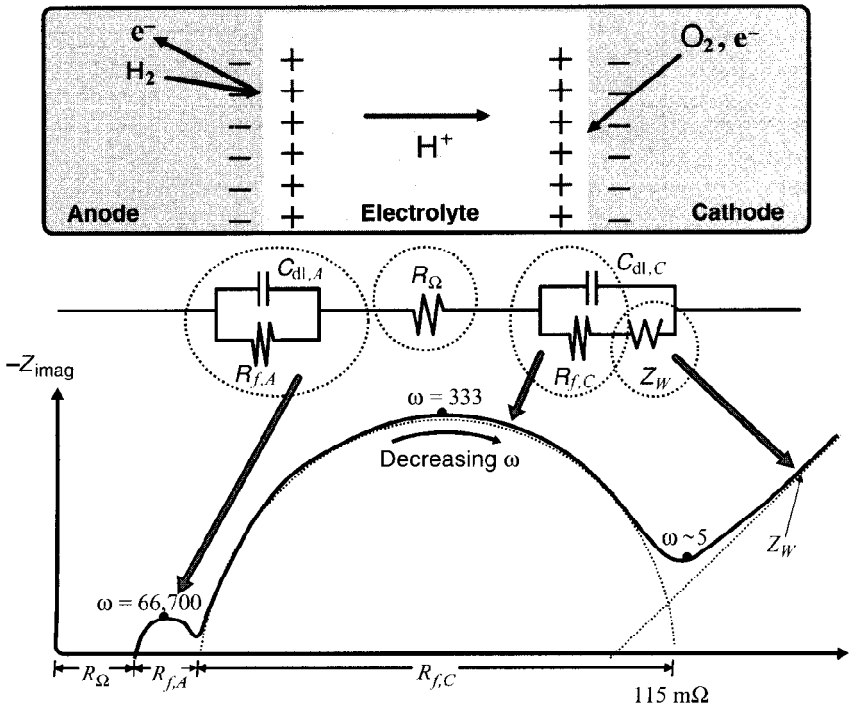

Figure 3.20: Physical picture, circuit diagram and Nyquist plot for a simple fuel cell impedance model [144]

The equivalent circuit for the fuel cell consists of two RC elements to model the anode and cathode activation kinetics, an infinite Warburg element to simulate cathode mass transfer effects, and an ohmic resistor to simulate the ohmic losses. The ohmic resistor is shown in the electrolyte region, but the ohmic losses arise from all parts of the fuel cell (electrolyte, electrode, etc.). Each circuit element contributes to the shape of the Nyquist plot as shown by the Figure 3.20.

The Nyquist plot shows the two semicircles followed by a diagonal line. The high-frequency (far left), real axis intercept corresponds to the ohmic resistance of the fuel cell. The first small semicircle corresponds to the RC model of the anode activation kinetics while the second large semicircle corresponds to the RC model of the cathode activation kinetics. The low frequency diagonal line comes from the infinite Warburg element.

The diameter of the first loop gives R_f for the anode while the diameter of the second loop gives R_f for the cathode. The diameter of the semicircle (R_f) gives the information about the electrochemical reaction kinetics at the interface. A small loop represents the smooth reaction kinetics whereas a large loop indicates the sluggish or slow reaction kinetics [144].

3.4.1.3 Cyclic Voltammetry (CV)

Cyclic voltammetry is a type of potentiodynamic electrochemical measurement technique. In a cyclic voltammetry experiment the potential of the working electrode is ramped or scanned linearly versus time, from an initial value to a predetermined limit V_2 (known as the switching potential) where the direction of the scan is reversed [145] and afterward it stopped on reaching some other preselected value V_1 Therefore the potential of the system is swept back and forth in CV measurement. The plot of resulting current versus voltage is called cyclic voltammogram.

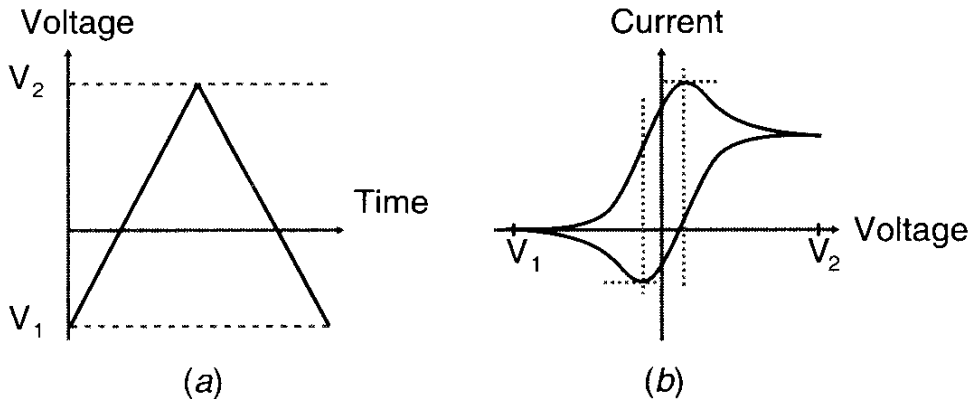

Figure 3.21: Schematic of a (CV) waveform and typical resulting current response. (a) Linear back and forth sweep of voltage between two voltage limits V_1 and V_2. (b) Plot of current as a function of voltage [144].

Cyclic voltammetry is specifically used to analyse fuel cell catalyst activity. CV measurement can determine the catalyst activity by using a special ´´hydrogen-pump-mode`` configuration. In this mode argon or nitrogen gas is fed to the cathode, whereas anode is supplied with hydrogen. The CV measurement is performed by sweeping the voltage of the system between about 0 and 1V with respect to the anode.

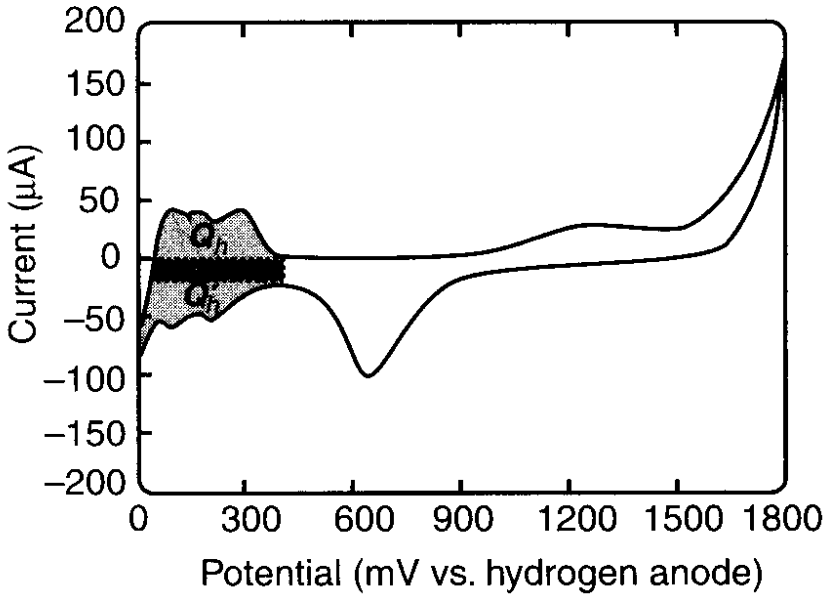

Figure 3.22: Cyclic voltammogram of a fuel cell. The peak marked Q_h and Q'_h represent the hydrogen adsorption and desorption peaks on the platinum fuel cell catalyst surface [145].

Figure 3.22 shows the hydrogen-pump-mode cyclic voltammogram fuel cell. The figure exhibits that a current begins to flow as the potential invreases from 0V. There are two contributions to this current. One contribution is constant, a capacitive charging current that flows in response to the linearly changing voltage. The second current response is nonlinear and corresponds to a hydrogen adsorption reaction occurring on the electrochemically active cathode catalyst surface. As the voltage increase further, this reaction current reaches a peak and then falls off as the entire catalyst surface becomes fully saturated with hydrogen. The active Pt surface area can be obtained by quantifying the total charge (Q_h) provided by hydrogen adsorption on the catalyst surface. The total charge corresponds to the area under the hydrogen adsorption reaction peak [144].

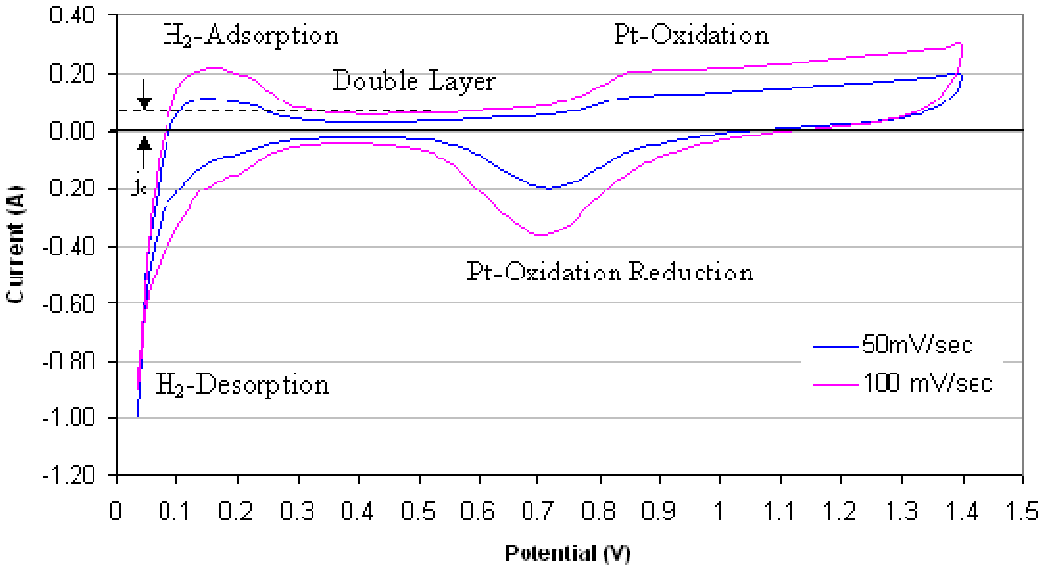

Figure 3.23: CV measurement of G-type MEA having 0.4 mg/cm2 Pt loading on cathode, with two scan rates, 50mV/sec and 100 mV/sec.

Cyclic voltammogram (Figure 3.23) can be devided into three different regions. The region between 0.1 and 0.3 V covers the hydrogen adsorption and desorption phenomena, then from 0.3V to 0.5V the region of double layer capacitance occur which followed the region of Pt oxidation and Pt oxidation reduction.

An active catalyst area coefficient may be calculated that represent the ratio of the measured active catalyst surface area compared to the active surface area of an atomically smooth catalyst electrode of the same size.

3.4.1.3.1 Calculation for Specific Active Pt surface Area

The specific active Pt surface area can be calculated as follows [146,147,148]

The current density for double layer charging is

$$j_c = C_d \frac{d\varphi}{dt} \qquad 3.10$$

$$\frac{d\varphi}{dt} = \nu \qquad 3.11$$

J_c Current density in double layer ($A.cm^{-2}$)

C_d Differential double layer capacitance ($C.V^{-1}.cm^{-2}$)

$d\boldsymbol{\varphi}$ Voltage interval (V)

dt Time interval (s)

$\boldsymbol{\nu}$ scan rate ($V.s^{-1}$)

$$\boldsymbol{Q_H = \int_{\Delta\varphi} i(\varphi) dt} \quad \textbf{3.12}$$

$$\boldsymbol{Q_H = \int_{\Delta\varphi} i(\varphi) dt \ \frac{d\varphi}{d\varphi}} \quad \textbf{3.13}$$

As $d\boldsymbol{\varphi}/dt = \boldsymbol{\nu}$

$$\boldsymbol{Q_H = \int_{\Delta\varphi} i(\varphi) \ \frac{d\varphi}{\nu}} \quad \textbf{3.14}$$

$$\boldsymbol{Q_H = \frac{1}{\nu} \int_{\Delta\varphi} i(\varphi) \ d\varphi} \quad \textbf{3.15}$$

$$\boldsymbol{A_{active} = \frac{Q_H}{210 * 10^{-6}}} \quad \textbf{3.16}$$

$$\boldsymbol{R_f = \frac{A_{active}}{A_{geometric}}} \quad \textbf{3.17}$$

210 $\mu C.cm^{-2}$ = 210 $*10^{-6}$($C.cm^{-2}$)-Adsorption charge for an atomically smooth platinum surface.

R_f Roughness factor

A_{active} Active Pt surface area (cm^2)

$A_{geometric}$ Geometric area of the electrode (cm^2)

$$\boldsymbol{A_c = \frac{A_{active}}{A_{geometric} * l_{pt}} * 0.1 = \frac{R_f}{l_{pt}} * 0.1} \quad \textbf{3.18}$$

A_c Specific active Pt surface area ($m^2.g^{-1}$)

l_{Pt} Pt loading on the electrode ($mg.cm^{-2}$)

3.4.2 Ex-situ Diagnostic Techniques

These techniques characterize the detailed structure or properties of the individual components composing the fuel cell, but generally only if components removed from the fuel cell environment in an unassembled, nonfunctional form [60].

- Scanning electron microscopy (SEM)
- Energy Dispersive X-Ray Spectrometry (EDXS)

3.4.2.1 Scanning Electron Microscopy (SEM)

Scanning electron microscope (SEM) uses electrons for the formation of an image. Before SEM light was used for this purpose. The idea of an electron microscope (EM) was proposed by Knoll and Ruska in 1932. Knoll developed the first concept of a scanning electron microscope in 1935. With the ongoing progress in this field, McMullan (Cambridge, UK) produced the first micrographs in 1953 showing the striking three-dimensional imaging characteristics of the modern-day SEM and first commercial SEM (Cambridge) was produced in 1965.

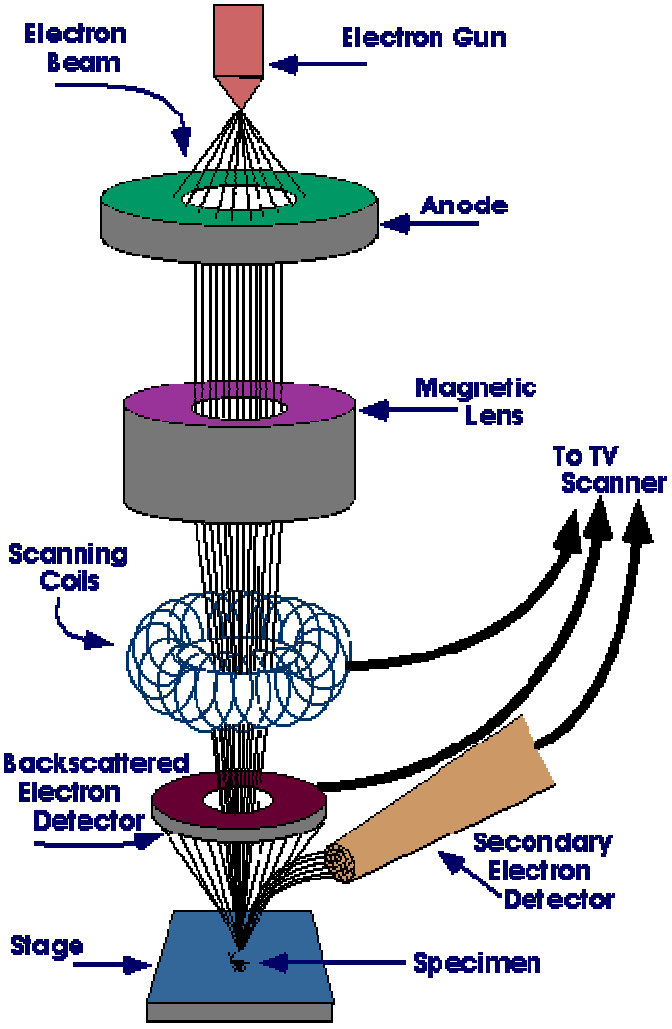

Figure 3.24: Scanning Electron Microscope [149]

A beam of electron is produced at the top of the microscope with the help of an electron gun. The electron beam travels through the electromagnetic fields and lenses by following a straight vertical path towards the sample, in side the microscope. As the beam strikes the sample, electrons and x-rays are ejected from the sample. Detectors collect these x-rays, backscattered electrons and secondary electrons and convert them into a signal. This signal produces the final image on a screen [149].

3.4.2.1.1 Principle of SEM

The electrons from a thermionic or field –emission cathode are accelerated by a voltage of 1-50 KV between cathode and anode. The gun cross-over with a diameter of 10-50 µm for thermionic and 10-100 nm for field emission guns, is demagnified by a two- or three-stage electron lens system, so that an electron probe of about 1-1000 nm carrying an electron probe current between 1 pA and 100 nA.

The final probe-forming lens has to operate with a relatively long working distance (between specimen and lower pole piece), so that the various particles and quanta emitted can be collected with the desired efficiency. This increases the spherical aberration of the probe forming lens and, therefore, the smallest attainable electron probe size.

A deflection coil system in front of the last lens scans the electron beam in a raster across the specimen in sync with an electron beam of a separate cathode ray tube (CRT). The intensity of the beam in the CRT is modulated by one of the recorded signals to form an image on the CRD [150].

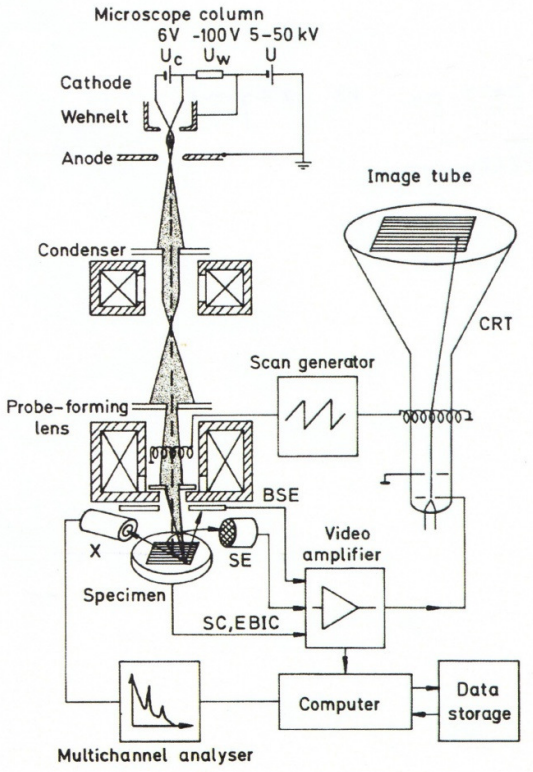

Figure 3.25: Principle of the scanning electron microscope (BSE = backscattered electrons, SE = secondary electrons, SC = specimen current, EBIC = electron beam induced current, X= x-rays, CRT = cathode-ray tube) [150].

3.4.2.2 Energy Dispersive X-ray Spectrometry (EDXS)

Energy dispersive spectrometer was developed in late 1960s and, by mid 1970s, it was rather widespread on electron beam instruments, such as SEMs. It has the three main parts, the detector, the processing electronics, and the multi channel analyzer (MCA) display.

The detector generates a charge pulse proportional to the X-ray energy. This pulse is first converted to a voltage. Then the signal is amplified through a field effect transistor (FET), isolated from other pulses, further amplified, and then identified electronically as resulting from an X-ray of specific energy. Finally, a digitized signal is stored in a channel assigned to that energy in the MCA [150].

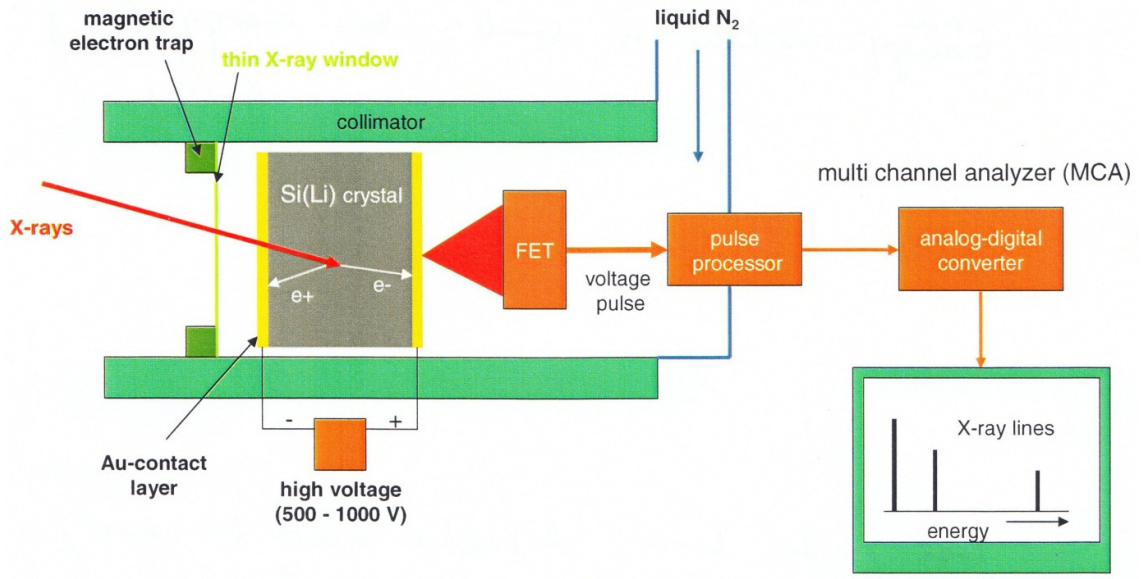

Figure 3.26: Principle of EDXS [150]

4 Characterization of the MEA F

4.1 Specification of MEA H25-F

Platinum loading on Cathode 0.6 mg/cm^2

Platinum loading on Anode 0.3 mg/cm^2

Membrane thickness------50 micrometer thick PFSA membrane

Cathode thickness-------8-10 microns (approximately)

Anode thickness---------4-5 micrometer (approximately)

4.2 Constant System Parameters

Hydrogen stoichiometry:	1.5
Oxygen stoichiometry:	2.0
Air stoichiometry:	2.2
Cell Temperature:	70°C
Cell Components:	
MEA:	H25-F
Active Area:	5 cm²
GDS:	SGL Carbon Group GDL 25BC
Sealing:	WACKER, 2-components Silicon
Carbon Plates:	SGL Carbon Group PPG 86
Measurement:	
Teststand:	Fuel Cell teststand for single cell
Potentiostat:	Zahner IM6ex und PP 240
SEM:	Zeiss Ultra 55
EDS:	EDAX phoenix

4.3 Experimental Procedure

Three fuel cells, (F, F1 & F2), each of area 5cm^2 were assembled. In all experiments, hydrogen (5.0), oxygen (5.5) and nitrogen (5.0) of ultra-high purity (>99.999%) and synthetic air (5.0) from compressed gas cylinders were used.

Firstly, MEA of the cell was activated through performance test. After activation of the MEA, each cell was characterised before starting the potential cycling experiment by recording a reference

characterisation curves. The activation of the MEA and the characterisation curves (Polarisation Curve, EIS, Cyclic Voltammogram and Hydrogen Diffusion Measurement) of the cell are recorded by connecting the fuel cell to the characterisation teststand (Figure 3.15). All the characterisation curves were recorded by using cathode as working electrode and anode as counter electrode. The pressure of the gases was maintained between 1 and 2 bar, almost (1.5 bar) with stoichiometric coefficients of 1.5 for H2, 2 for O2 and 2.2 for air respectively. The fuel cell was operated at 70°C. The temperature of the humidifier was set at 68°C. Thus the value of relative humidity (RH) applied for all characterization curves was 90%. The fuel cell was purged both on anode and cathode sides with dry and wet nitrogen before starting the experiment and after finishing the experiment.

Then the fuel cell was connected to the other teststand for potential cycling tests. At this teststand a parallel connection of transistors was used with each fuel cell in order to change its voltage from 0.7V to 0.9V and vice versa after every 30 seconds. Therefore one voltage cycle was set to complete in one minute.

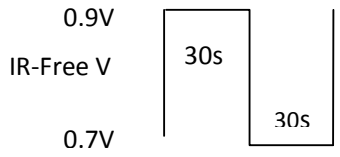

Figure 4.1: Change in potential between 0.7 V and 0.9 V (1voltage cycle= 1 minute)

The cells were tested at 70°C under H_2/air (H_2 at 50ml/min and air at 100 ml/min for each fuel cell.) and with different values of relative humidity. The pressure of the gases (H_2, N_2 and Air) was maintained between 1 and 2 bar (almost 1.5 bar). By setting the temperature of the humidifier at different values the potential cycling test series was conducted at different values of relative humidity.

During the test series each fuel cell was disconnected from the teststand and its characterisation curves were recorded after specific number of voltage cycles like 1000, 3000, 5000, 7500, 10000 and 15000 voltage cycles etc. After recording the characterisation curves, the cell was connected again to the other teststand for potential cycling test and this process was stopped when the cell potential became less than 0.9V.

When the fuel cell stopped working, it was disassembled and the MEA was analysed by the scanning electron microscope (SEM) and the cathode surface was also examined by energy dispersive spectroscope (EDS).

4.4 Test Sequence for Characterization Curves

For in-situ characterization measurements each fuel cell was connected to the teststand in such a way that the cathode of the cell was employed as working electrode and the anode as counter electrode. The cycle of the electrochemical experiment was started by recording polarisation curves at open circuit voltage (OCV), once with oxygen supply and then with air supply at the cathode of the fuel cell. This was followed by collecting the impedance spectrum with oxygen feed at the cathode side of the same cell. Then CV was carried out with the scan rate 50mV/sec and also with 100mV/sec. After recoding these characterization measurements the fuel cell was employed for accelerated voltage cycling test. At the completion of specific number of voltage cycles the fuel cell was subjected

again to record characterization curves. The same set of sequence was repeated every time for collecting these curves. At the end of lifetime of the cell hydrogen diffusion current measurement was also performed after recording cyclic voltammogramm.

4.4.1 Parameters for Characterization Curves

4.4.1.1 Polarization Curve

Polarization Curves were recorded in a dynamic scan mode with a resolution of 10mV and a scan rate of 10mV/sec. The current was set as 25A for cathode and 1A for anode

First	0V relative
Second	150mV
Third	150mV
Fourth	150mV

4.4.1.2 Electrochemical Impedance Spectroscopy(EIS)

Electrochemical Impedance Spectra were recorded between 50 mHZ and 10KHZ with an amplitude of 10mV. All EIS measurements were performed in "Galvanostatic mode'' with (-3A) current. Gas flow was set with the help of respective stoichiometric values for a current of 5A. The other parameters were as follows.

Lower Limit	50mHZ
Start	10KHZ
Upper	10KHZ
Amplitude	10mV

4.4.1.3 Cyclic Voltammetry

These measurements were recorded in the open circuit mode when the nitrogen was fed at the cathode side of the cell. Three cycles of voltammograms were recorded with the help of 300 samples /cycle in the voltage range between 30mV and 1.4V.

For every measurement two cyclic voltammograms were recorded at two different values of slew rates, i.e. 50mV/sec and 100mV/sec when the cell potential became 0.1 Vless than 0.4V.

E Start	100mV
E Upper	1.4V
E Lower	30mV
E End	100mV
No. of Cycles	3
Sample/Cycle	300
Gas Flow for current	5A

For all characterization measurements the pressure of the gases was maintained at 1.5 bar (abs) with stoichiometric coefficients of 1.5 for H2, 2 for O2 and 2.2 for air respectively. Flow of gases was set with the help of stoichiometric coefficients of the gases, for a current of 5A.

4.5 Electrochemical Analysis

Three fuel cells F, F_1 and F_2 were assembled by using MEA of type H25-F. The fuel cell F was tested at 92% RH, $F_1$was operated at 80% RH and F_2 was investigated at 90% RH. During the test series, after the completion of 1000, 3000, 5000, 7500, 10000 and 15000 voltage cycles the accelerated voltage cycling test was stopped and the fuel cells were characterised by polarisation curves, electrochemical impedance spectroscopy (EIS) and cyclic voltammetry (CV). The fuel cell F worked till 10,000 voltage cycles, F_1 and F_2 worked longer and stopped working after 12,570 voltage cycles and 17,536 voltage cycles respectively.

Table 4.1

Fuel Cell	% RH	Voltage Cycles Completed
F	92%	10,000
F1	80%	12,570
F2	90%	17,536

4.5.1 Polarization Curve

Polarization curves were recorded by feeding the cathode of the fuel cell with oxygen and then with air.

4.5.1.1 Polarization Curve with Oxygen Supply at cathode

4.5.1.1.1 Fuel Cell F-92% RH

Figure 4.2 illustrates the comparison of all polarization curves with oxygen at cathode for the fuel cell F. The graph indicates that the limiting current density with the fresh MEA is less than its value after 1000 voltage cycles but afterward the maximum current density decreases with the increase in the number of voltage cycles. The current density versus voltage curve at 10,000 voltage cycles shows the effect of mass transport limitation due to poor water balance.

It is also visible from Figure 4.2 that the current density versus potential curves, till 3,000 voltage cycles show large linear region of ohmic drop but the curves after 5000, 7500 and 10,000 voltage cycles exhibit a short region of ohmic losses with less values of limiting current densities.

Figure 4.2 also shows the power density curves for the fuel cell F with oxygen supply at its cathode. It is visible from the figure that the power density increased in the beginning from zero cycles to 1,000 voltage cycles. It might be due to proper humidification of the fuel cell at 1,000 VC. After that, the power density decreased until 7,500 VC.

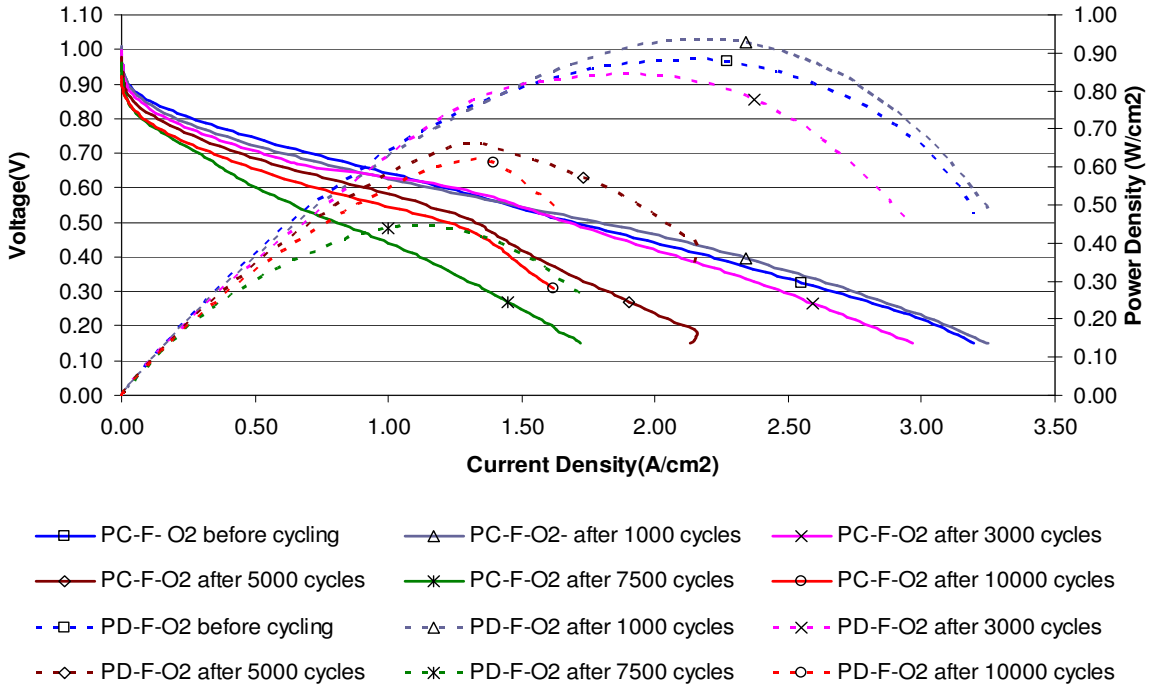

Figure 4.2: Comparison of all Polarization Curves and Power Density Curves with Oxygen supply at cathode of the fuel cell F (92% RH), Stoichiometry (H_2=1.5, O_2=2.0, Air=2.2), Cell Temperature <80°C, Area of fuel cell=5cm^2, Relative Humidity=92%, Pressure=Ambient (1.013 bar)

Table 4.2: Maximum current densities of fuel cell F with O_2 supply at the cathode.

Voltage Cycles	OCV (V)	Max. Current Density (A/Cm^2)
0	0.989	3.20
1000	1.01	3.25
3000	0.999	2.96
5000	0.972	2.13
7500	0.961	1.72
10000	0.923	1.62

4.5.1.1.2 Fuel Cell F_1-80% RH

Figure 4.3 shows the comparison of all the Polarization Curves with oxygen at cathode for the fuel cell F_1. The graph indicates that the current density increased until 3,000 voltage cycles. It means that at this stage the cell became completely activated. Then the value of the current density decreased (2.39A/cm^2 to 2.35A/cm^2 at 10,000 voltage cycles) but afterward there is a sudden and prominent decrease. Its value fell to 1.75 A/cm^2 at 12,570 voltage cycles.

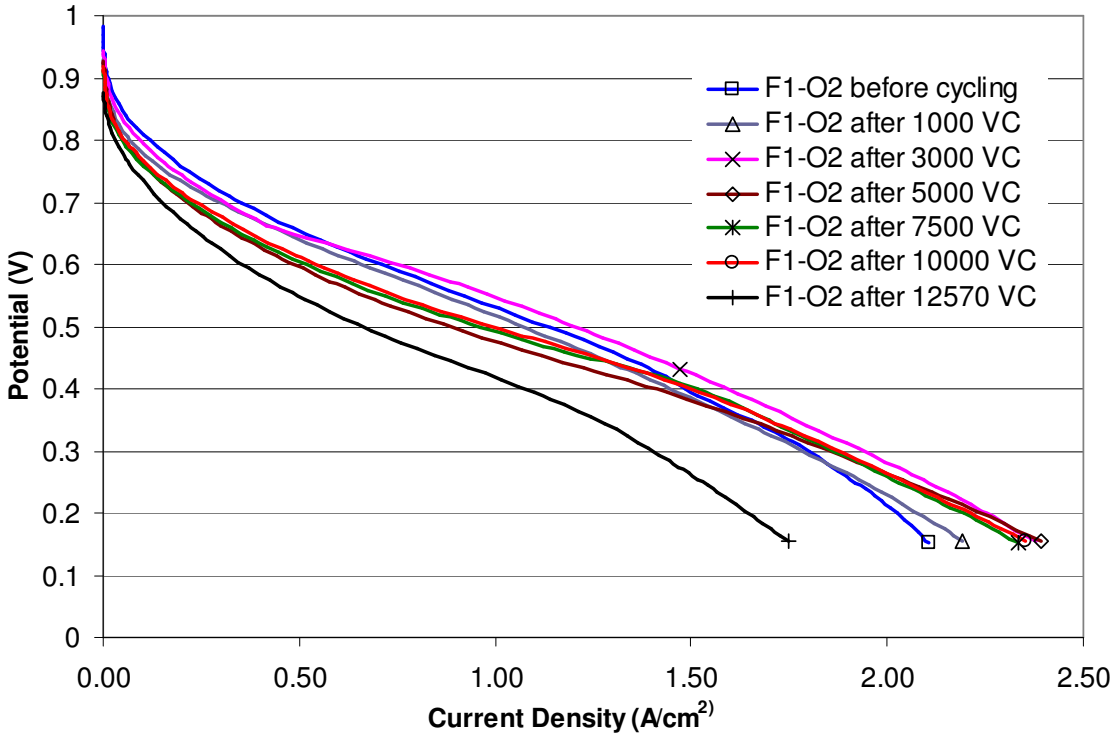

Figure 4.3: Comparison of all Polarization Curves with Oxygen supply at cathode of the fuel cell F_1 (80% RH), Stoichiometry (H_2=1.5, O_2=2.0, Air=2.2), Cell Temperature <80°C, Area of fuel cell=5cm^2, Relative Humidity=80%, Pressure=Ambient (1.013 bar)

The reason of this decrease was sudden accidently shut downed the humidifier heater and the heater for the cell. The fuel cell was operated the whole night with 25°C cell temperature and 22°C cathode humidifier temperature.

Table 4.3: Maximum current densities of fuel cell F_1 with O_2 supply at cathode.

Voltage Cycles	OCV (V)	Max. Current Density (A/cm^2)
0	0.979	2.11
1000	0.93	2.19
3000	0.944	2.38
5000	0.928	2.39
7500	0.914	2.33
10000	0.914	2.35
12570	0.875	1.75

4.5.1.1.3 Fuel Cell F_2-90% RH

Figure 4.4 shows all current densities / voltage curves for the fuel cell F_2 when oxygen was supplied to the cathode of the fuel cell. Here again the current density of the fresh MEA was less than its value after 1,000 voltage cycles. After 1,000 VC the current density reached the maximum but decreased until 5,000 voltage cycles. The current density /voltage curve after 7,500 voltage cycles operation showed zig zag changes in the ohmic loss portion due to membrane inefficiency. After that, the current density decreased until 17,536 voltage cycles. The current density versus voltage curve at 17,536 voltage cycles indicates a lot of activation losses as the curve intersects the voltage axis at

0.815 volts instead of at 0.943 volts (value for all other curves). This shows a prominent effect of catalyst loss after 17,536 voltage cycles.

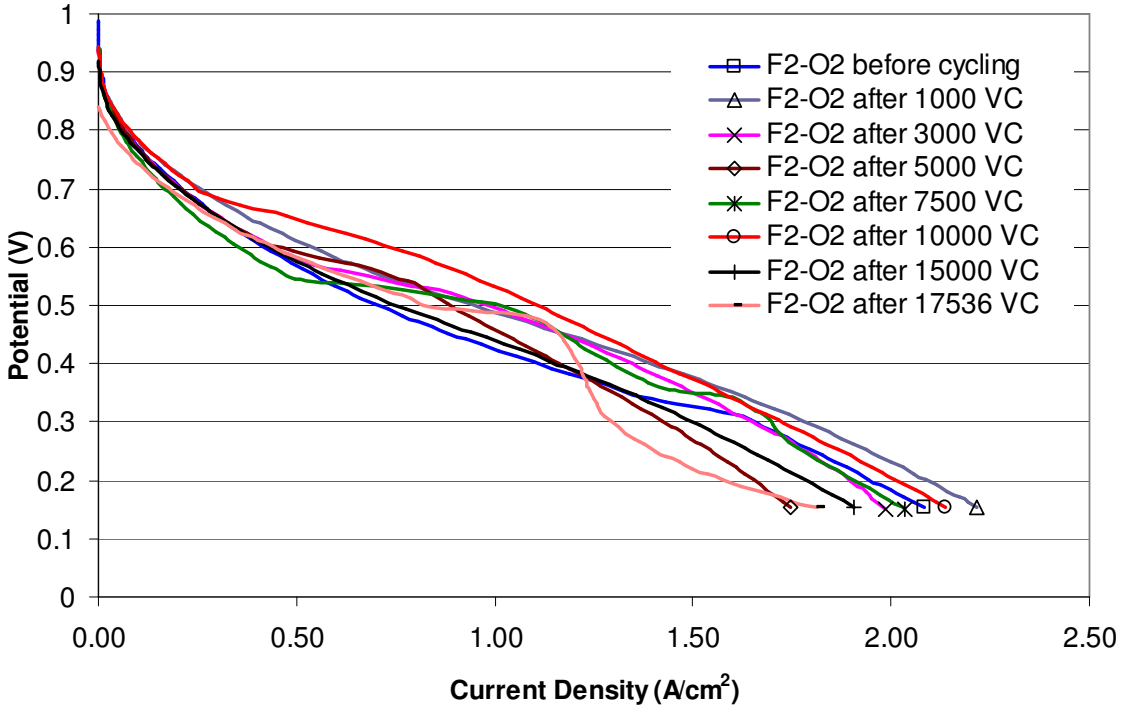

Figure 4.4: Comparison of all Polarization Curves with Oxygen supply at cathode of the fuel cell F_2 (90% RH), Stoichiometry (H_2=1.5, O_2=2.0, Air=2.2), Cell Temperature <80°C, Area of fuel cell=5cm^2, Relative Humidity=90%, Pressure=Ambient (1.013 bar)

The reasons of the catalyst loss, nonlinear ohmic losses and low current densities were that the cell was operated between 15,000 to 17,536 voltage cycles at 25°C cell temperature instead of 70°C and that the cathode humidifier temperature was 22°C instead of 68°C. This happened accidently.

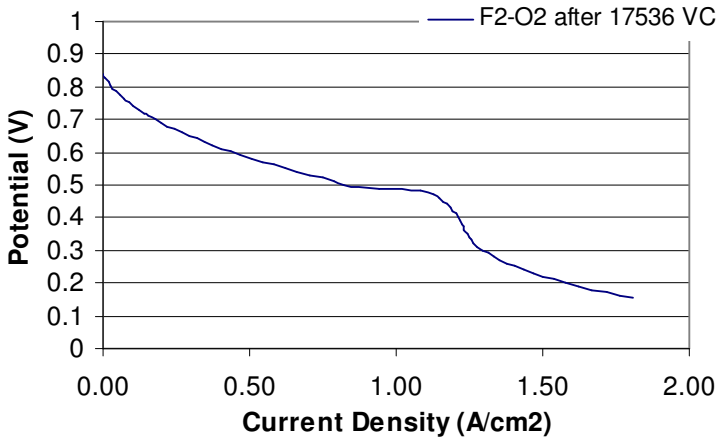

Figure 4.5: Polarization curve of the fuel cell after operation on dry conditions. Cell temperature: 25°C, Humidifier Temperature 22°C.

Table 4.4: Maximum current densities of fuel cell F_2 with O_2 supply at the cathode.

Voltage Cycles	OCV(V)	Max. Current Density (A/cm^2)
0	0.989	2.08
1000	0.938	2.22
3000	0.941	1.98
5000	0.933	1.75
7500	0.941	2.03
10000	0.942	2.14
15000	0.92	1.91
17536	0.835	1.81

4.5.1.2 Polarization Curve with Air supply at cathode

Polarisation curves were also recorded when air was fed to the cathode side of the fuel cells F, F_1 and F_2.

4.5.1.2.1 Fuel cell F-92% RH

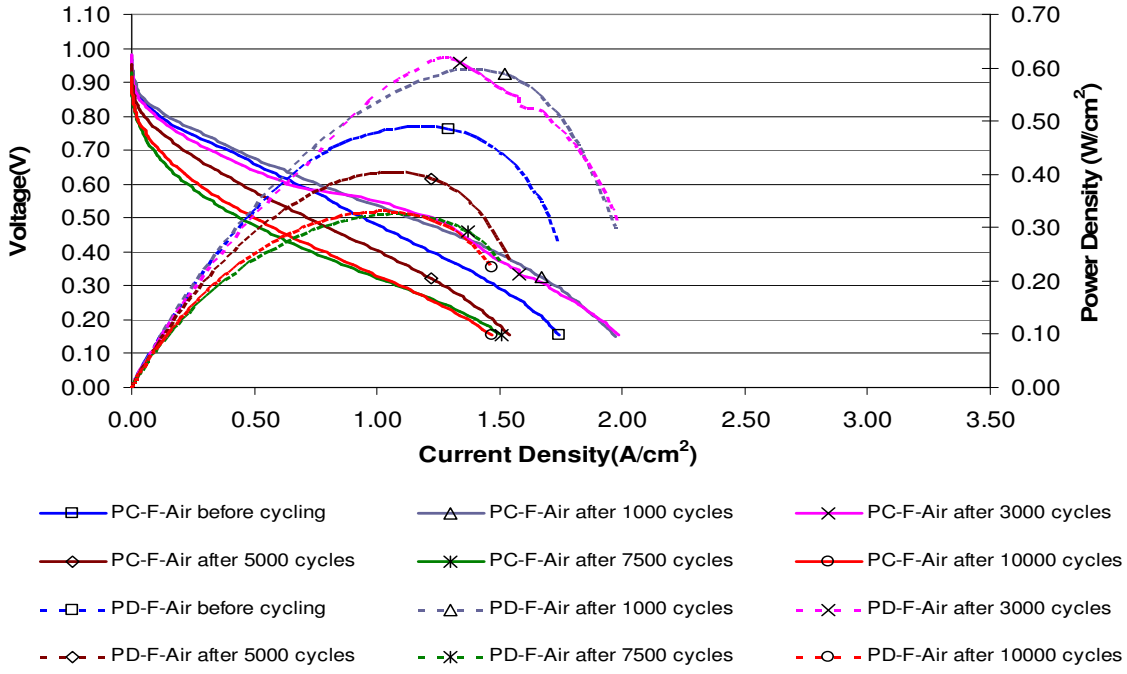

Figure 4.6: Comparison of all Polarization Curves and Power Density curves with Air supply at cathode side of the fuel cell F (92% RH), Stoichiometry (H_2=1.5, O_2=2.0, Air=2.2), Cell Temperature <80°C, Area of fuel cell=5cm^2, Relative Humidity=92%, Pressure=Ambient (1.013 bar)

Table 4.5: Maximum current densities of fuel cell F with air supply at the cathode.

Voltage Cycles	OCV (V)	Max. Current Density
0	0.969	1.74
1000	0.98	1.97
3000	0.983	1.99
5000	0.955	1.54
7500	0.928	1.51
10000	0.915	1.47

In Figure 4.6 the Shift of the maximum current density and the maximum power density can be seen. The current density and power density of the fuel cell with the fresh MEA is less than after 1000 and 3000 voltage cycles. These maximum values are the signs of proper and complete humidification and activation of the MEA. Afterward the current density and power density decreased and at 10,000 voltage cycles the minimum values were obtained. The current density decreased from 2 A/cm^2 to 1.47 A/cm^2 and the power density from 0.6 W/cm^2 to 0.3 W/cm^2. It can also be observed from the current versus voltage curve after 10,000 voltage cycles that the open circuit voltage (OCV) decreased from its maximum value of 0.98 V to 0.91V. This means that catalyst deteriorated.

4.5.1.2.2 Fuel Cell F_1-80% RH

Figure 4.7 shows all current densities / voltage curves for the fuel cell F_1 when air was supplied to the cathode of the fuel cell. The current density of the fresh MEA increased until 1,000 voltage cycles (1.25A/cm^2). Afterward, till 7,500 voltage cycles it stayed constant and it decreased slowly. A gross decrease was observed after 12,570 voltage cycles.

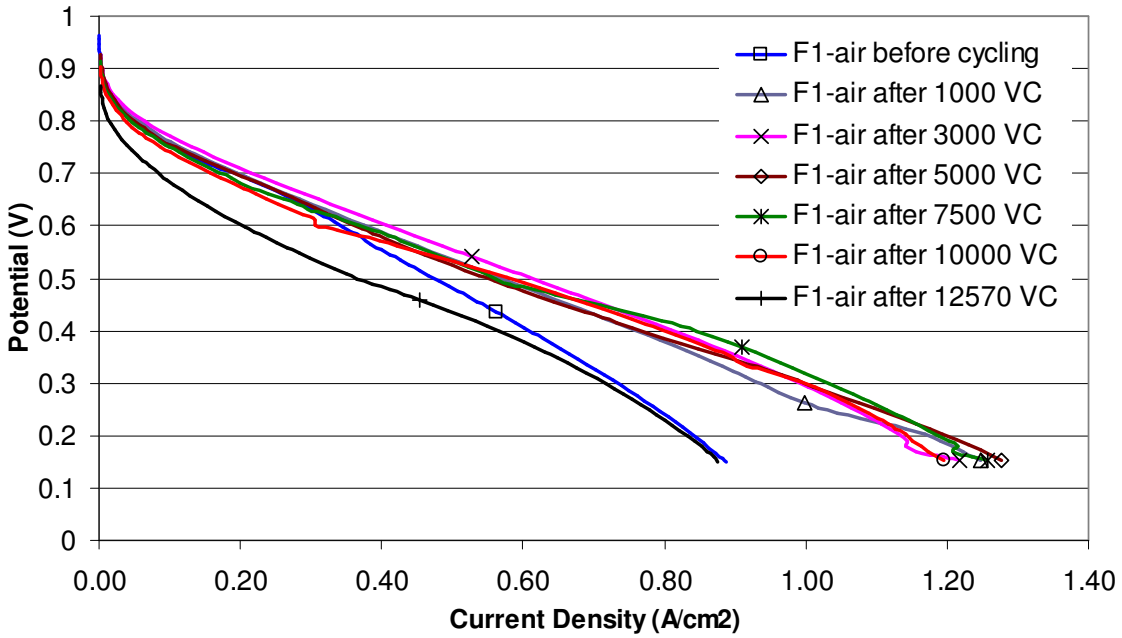

Figure 4.7: Comparison of all Polarization Curves with Air supply at cathode side of the fuel cell F_1 (80% RH), Stoichiometry (H_2=1.5, O_2=2.0, Air=2.2), Cell Temperature <80°C, Area of fuel cell=5cm^2, Relative Humidity=80%, Pressure=Ambient (1.013 bar)

Table 4.6: Maximum current densities of fuel cell F_1 with air supply at the cathode.

Voltage Cycles	OCV (V)	Max. Current Density (A/cm^2)
0	0.957	0.89
1000	0.921	1.25
3000	0.921	1.22
5000	0.921	1.28
7500	0.907	1.26
10000	0.899	1.19
12570	0.863	0.88

The reason of the sharp reduction after 12,570 VC was that the fuel cell F_1 was operated at cell temperature 25°C and cathode humidifier temperature 22°C due to the accidently shut down of the heaters. The decline of the OCV from 0.957V to 0.863V shows the catalyst degradation of the fuel cell F_1 operated at 80% relative humidity.

4.5.1.2.3 Fuel Cell F_2-90% RH

Figure 4.8 illustrates all current density / voltage curves for the fuel cell F_2 when air was supplied to the cathode of the fuel cell.

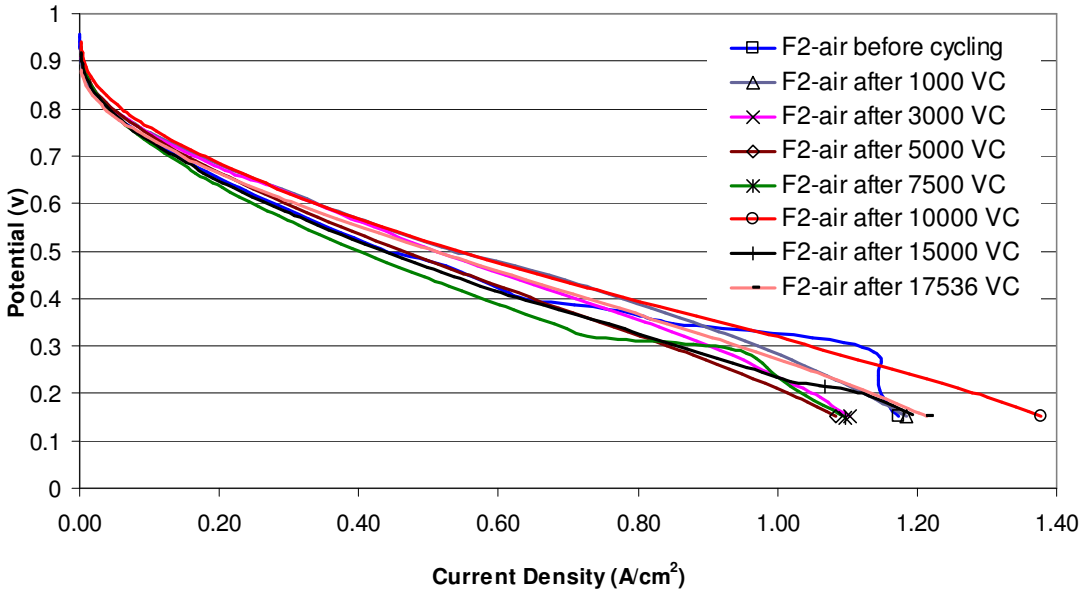

Figure 4.8: Comparison of all Polarization Curves with Air supply at cathode of the fuel cell F_2 (90% RH), Stoichiometry (H_2=1.5, O_2=2.0, Air=2.2), Cell Temperature <80°C, Area of fuel cell=5cm^2, Relative Humidity=90%, Pressure=Ambient (1.013 bar)

Table 4.7: Maximum current densities of fuel cell F_2 with air supply at the cathode.

Voltage Cycles	OCV (V)	Max. Current Density (A/cm^2)
0	0.957	1.17
1000	0.909	1.18
3000	0.924	1.10
5000	0.921	1.08
7500	0.925	1.10
10000	0.937	1.38
15000	0.919	1.19
17536	0.882	1.21

The value of the current density for the fresh MEA is large. Then it decreased with the increase of number of voltage cycles till 7500 voltage cycles. After 10,000 voltage cycles there is a sudden increase in the value of current density. This current density / voltage curve exhibits a large linear ohmic region.

The curves after 15,000 and 17,536 voltage cycles also show the same characteristic with less value of maximum current density. The reduction in the value of maximum current density through out the

experiment is due to membrane deterioration. The decrease in the OCV from the start to the end (0.952V to 0.857V) of the experiments is a measure of catalyst degradation.

4.5.2 Electrochemical Impedance spectroscopy (EIS)

The frequency dependent resistances of the cathodes of the fuel cell F, F_1 and F_2 were investigated by electrochemical impedance spectroscopy while they were operated at different values of relative humidity i.e., 92%, 80% and 90% respectively.

4.5.2.1 Nyquist Plot

With the help of Nyquist plots, the membrane resistance and the cathode resistance for the fuel cells F, F_1 and F_2 can be calculated.

4.5.2.1.1 Fuel Cell F (92% RH)

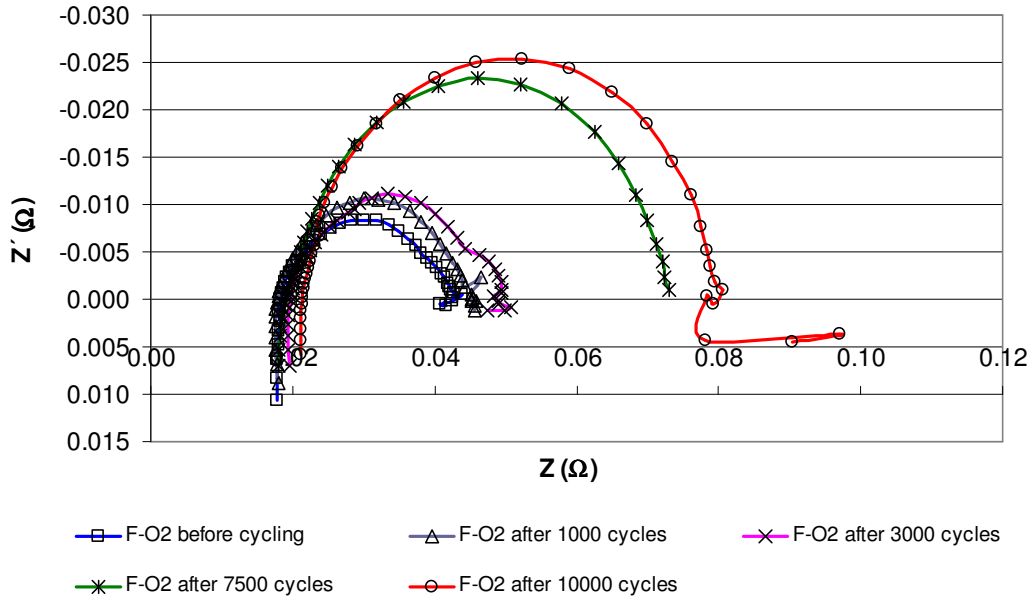

Figure 4.9: Nyquist Plots for the fuel cell F (92%RH), Galvanostatic operation at 5A, Cell Temperature <80°C, Area of Fuel Cell= 5cm^2, Relative Humidity=92%, Pressure= Ambient (1.013 bar)

Table 4.8: Resistances of the Fuel Cell F-(92% RH)

Voltage Cycles Completed	Membrane Resistance (a) (Ω)	Total Resistance (b) (Ω)	Cathode Resistance (b-a) (Ω)
0	0.018	0.043	0.025
1000	0.018	0.045	0.027
3000	0.020	0.049	0.030
7500	0.019	0.073	0.054
10000	0.021	0.080	0.058

Fuel Cell F was operated at 92% RH. Figure 4.9 shows the Nyquist plots when oxygen was supplied to the cathode side of the fuel cell. During the whole test no prominent increase in the membrane resistance can be exhibited from Table 4.8 but on the other hand the cathode resistance became double at the end of the experiment. Figure 4.10 shows the graphical representation of the increase in the cathode resistance over the voltage cycles.

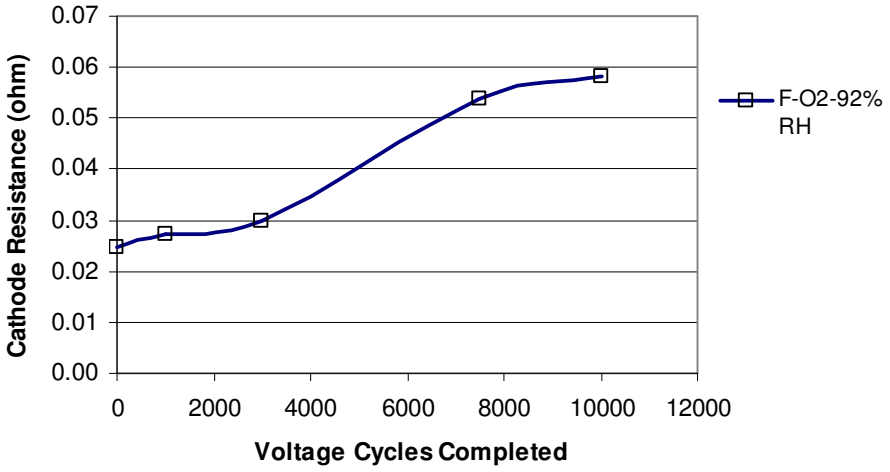

Figure 4.10: Increase in the cathode resistance for the fuel cell F

4.5.2.1.2 Fuel Cell F_1 (80% RH)

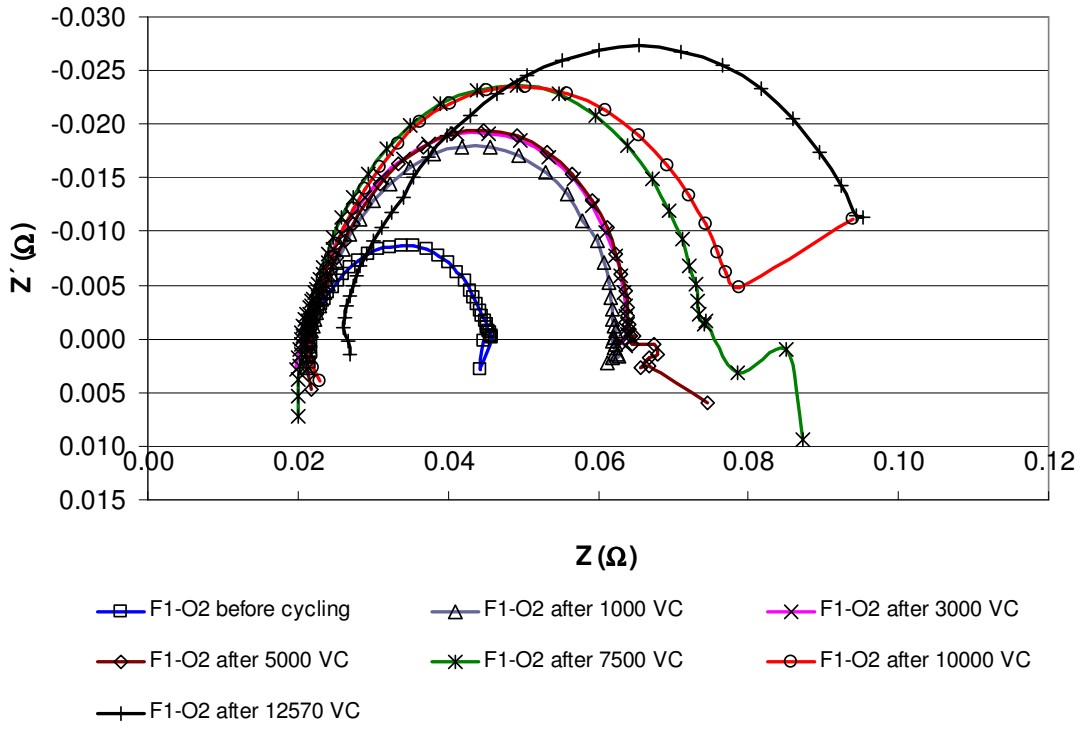

Figure 4.11: Nyquist Plots for the fuel cell F_1 (80%RH)

Fuel cell F_1 was tested at 80% relative humidity. Figure 4.11 represents all Nyquist plots when cathode of the cell was fed with oxygen. This cell operated till 12,570 voltage cycles. It is visible from the Table 4.9 that until 10,000 voltage cycles membrane resistance is almost the same but after 12570 voltage cycles an increase in it can be seen. This increase in the membrane resistance is due to

dry operating conditions at which the accelerated voltage cycling test was conducted from 10,000 to 12.570 voltage cycles.

Table 4.9: Resistances of the Fuel Cell F_1-(80% RH)

Voltage Cycles completed	Membrane Resistance (a) (Ω)	Total Resistance (b) (Ω)	Cathode Resistance (b-a) (Ω)
0	0.021	0.046	0.025
1000	0.022	0.062	0.040
3000	0.021	0.064	0.043
5000	0.022	0.065	0.043
7500	0.021	0.074	0.053
10000	0.022	0.079	0.057
12570	0.027	0.095	0.069

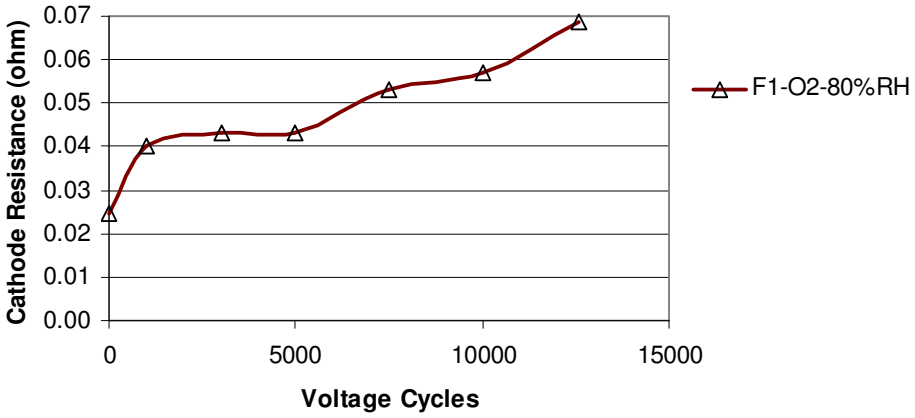

Figure 4.12: Increase in the cathode resistance for the fuel cell F_1

On the other side a gradual increase in the cathode resistance can be exhibited. Figure 4.12 illustrates the graphical representation of the enlargement in the cathode resistance with voltage cycles.

4.5.2.1.3 Fuel Cell F2 (90% RH)

Fuel Cell F_2 was operated at 90% RH. Figure 4.13 summarizes all Nyquist plots when oxygen was supplied to the cathode side of the fuel cell. After 15,000 and 17,536 voltage cycles some disturbances are present in the impedance spectra at low frequency region. These disturbances are, may be due to formation of water droplets in the gas flow channels.

Table 4.10 presents the increase and decrease of the membrane resistance of the fuel cell F_2 during the accelerated voltage cycling test. This shows the reduction of functional group by thinning the membrane. It is also visible from Table 4.10 that the cathode resistance increased with the increase of number of voltage cycles. Figure 4.14 shows the graphical presentation of cathode resistance enhancement.

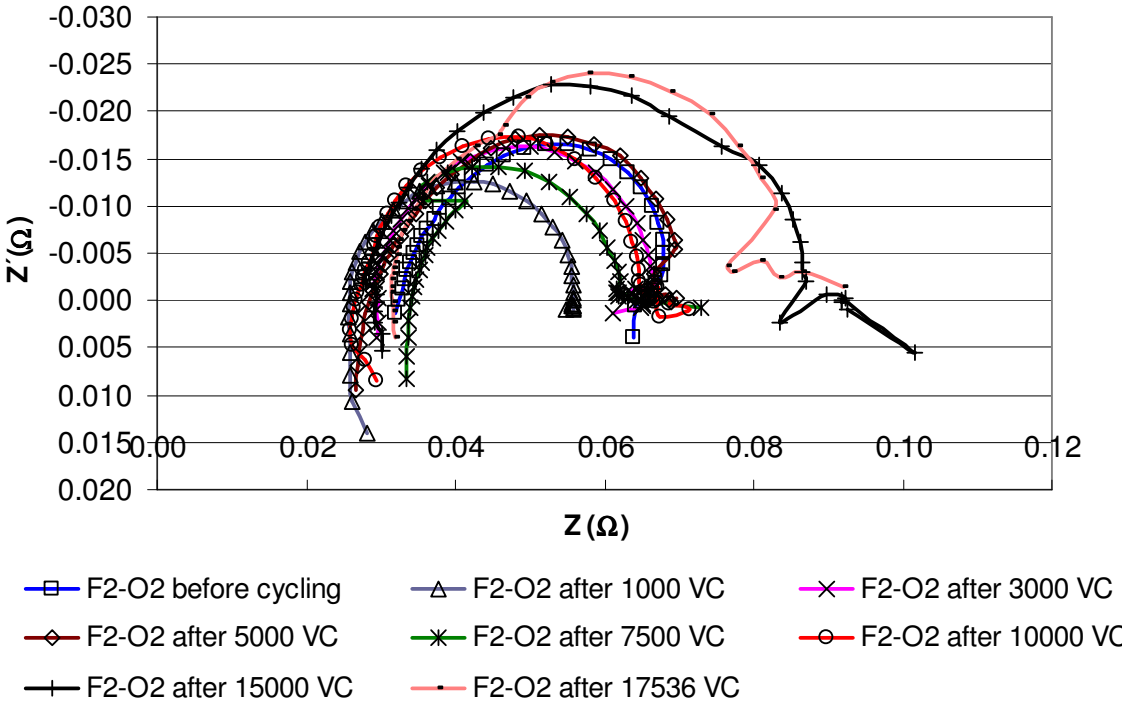

Figure 4.13: Nyquist Plots for the fuel cell F_2 (90%RH)

Table 4.10: Resistances of the Fuel Cell F_2-(90% RH)

Voltage Cycles completed	Membrane Resistance (a) (Ω)	Total Resistance (b) (Ω)	Cathode Resistance (b-a) (Ω)
0	0.033	0.064	0.032
1000	0.026	0.056	0.030
3000	0.030	0.065	0.036
5000	0.029	0.067	0.039
10000	0.027	0.067	0.041
15000	0.029	0.083	0.054
17536	0.032	0.094	0.063

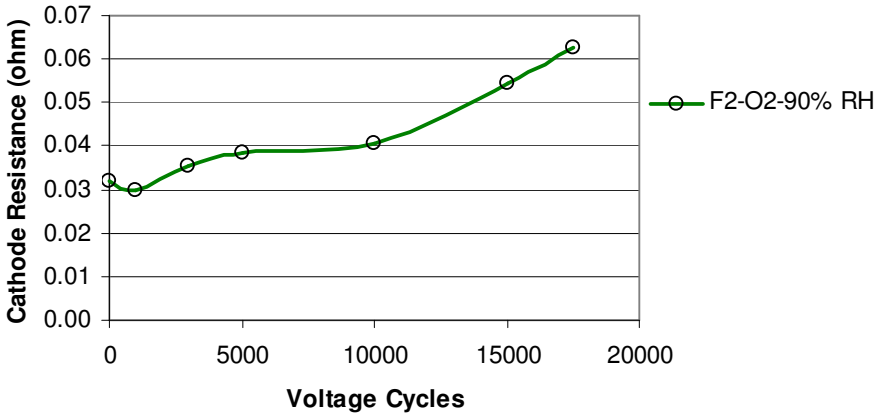

Figure 4.14: Increase in the cathode resistance for the fuel cell F_2

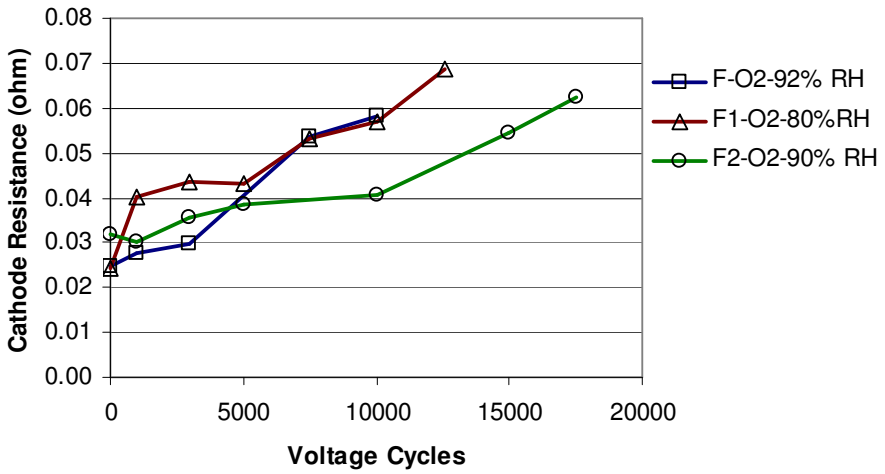

Figure 4.15: Increase in cathode resistance with potential cycles for different values of relative humidity

Figure 4.15 summarizes the comparison of enlargement in the cathode resistance for the fuel cells F, F1 and F2, operated at different values of relative humidity i.e., 92%, 80% and 90% respectively. It is visible from the figure that the fuel cell tested at 90% RH worked for larger number of voltage cycles (17,536 VC) and having lower cathode resistance than that of the fuel cell operated at 80% RH for 12,570 VC. These two cells would have worked longer if the humidifier heater and cell temperature heater would not have shut down accidently.

4.5.3 Cyclic Voltammetry (CV)

These measurements were carried out by supplying nitrogen at the cathode of the cell. Three Cycles of each CV were recorded with 300 samples per cycle between 0.03V and 1.4V for slew rate 50mV/sec and 100mV/sec in the open circuit mode. The anode was used as the counter electrode and the cathode was used as the working electrode. The active platinum surface area was calculated by using the equation (3.18) as explained in chapter 3 [146, 147, 148,151].

4.5.3.1 Mean Active Pt Surface Area

The mean active Pt surface areas for all three cycles of each measurement with scan rate of 50mV/sec were calculated.. Similarly the mean active Pt surface areas for all three cycles of each measurement with scan rate 100mV/sec were calculated. Afterward the mean value of these two was calculated.

4.5.3.2 Fuel Cell F (92% RH)

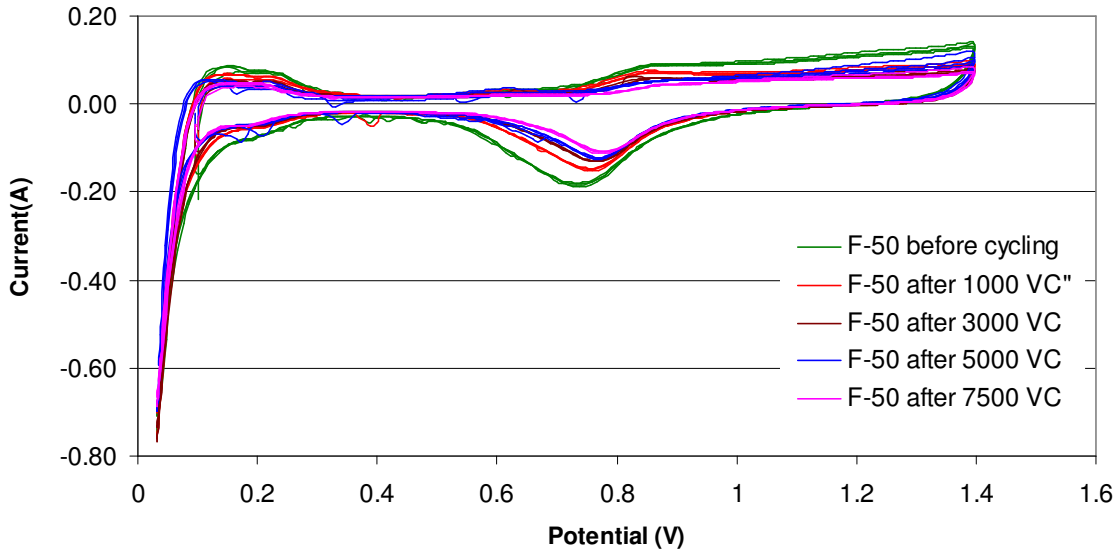

Figure 4.16: Cyclic voltammograms of fuel cell F at 50mV/sec

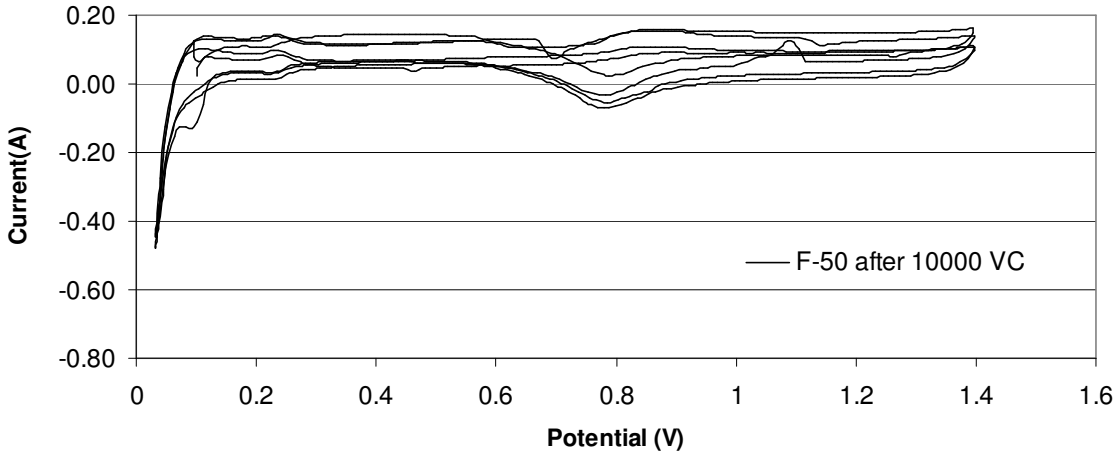

Figure 4.17: Cyclic voltammogram of fuel cell F at 50mV/sec after 10,000 VC

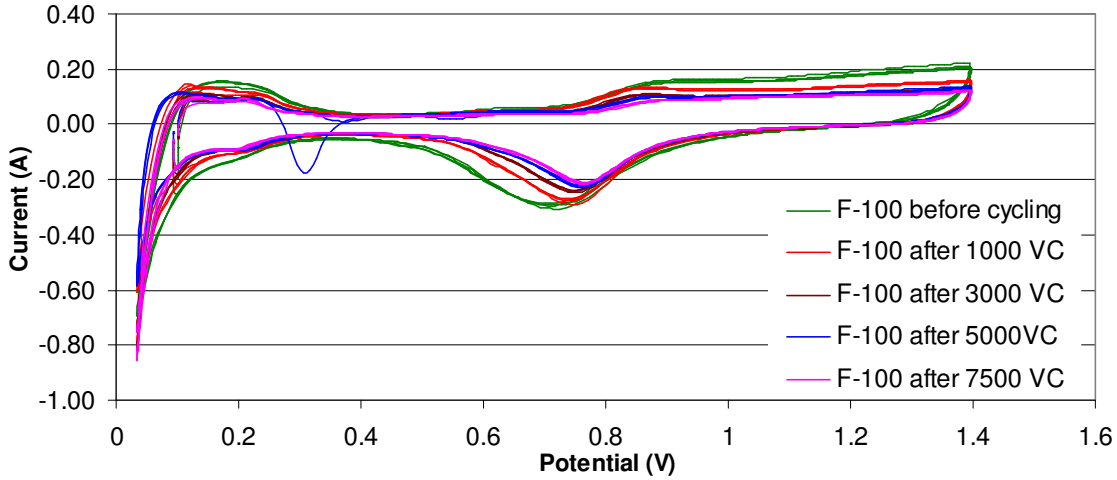

Figure 4.18: Cyclic voltammograms of fuel cell F at 100mV/sec

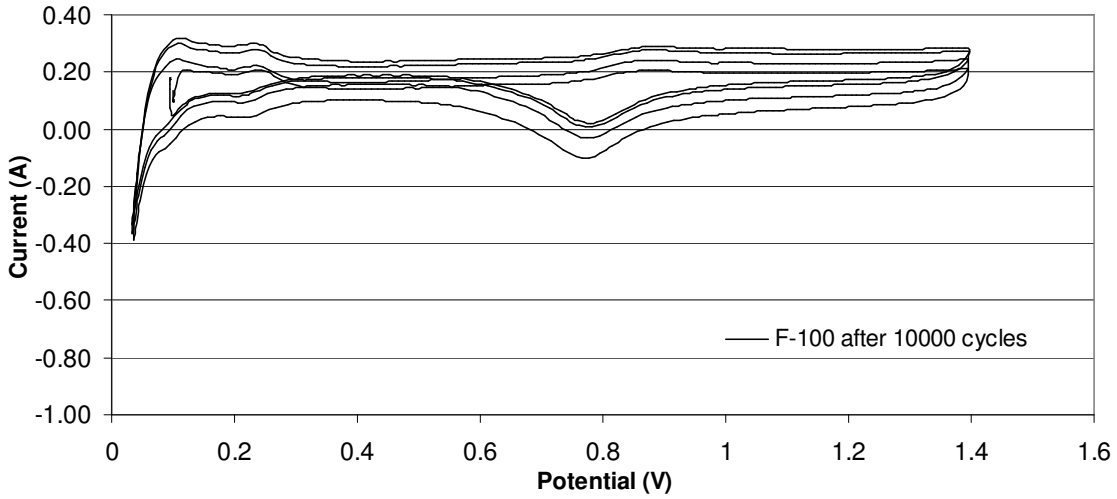

Figure 4.19: Cyclic voltammogram of fuel cell F at 100mV/sec after 10,000 VC

Table 4.11: Active Pt surface area for the fuel cell F

Voltage Cycles	Mean Active Pt Surface Area (m^2/g)
0	35.2
1000	27.2
3000	21.5
5000	21.0
7500	16.8
10000	16.7

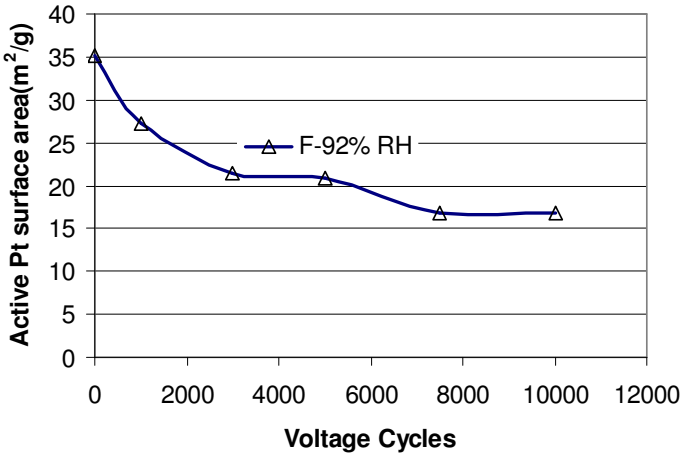

Figure 4.20: Decrease in Active Pt Surface Area as a function of Voltage Cycles for the Fuel Cell F (92% RH)

4.5.3.3 Fuel Cell F_1 (80% RH)

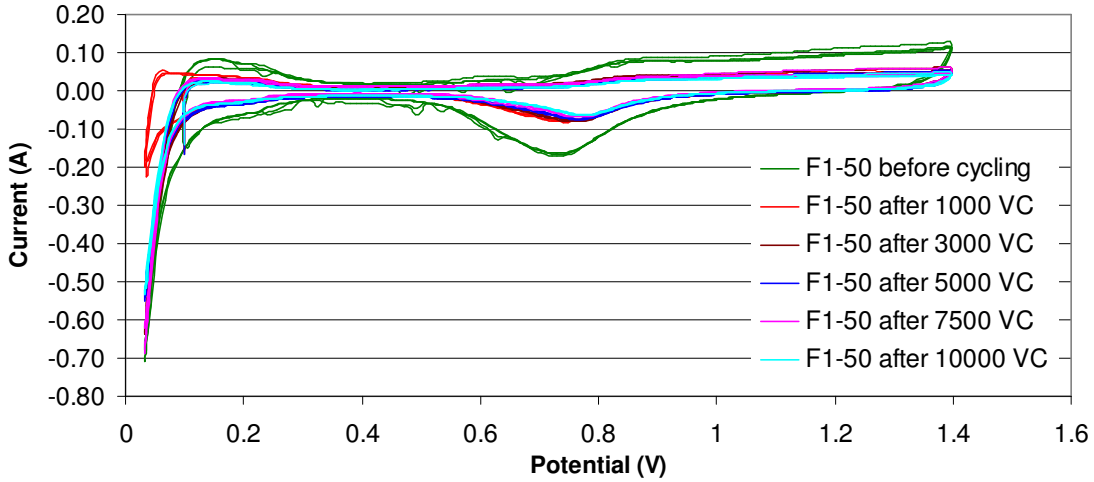

Figure 4.21: Cyclic voltammograms of fuel cell F_1 at 50mV/sec

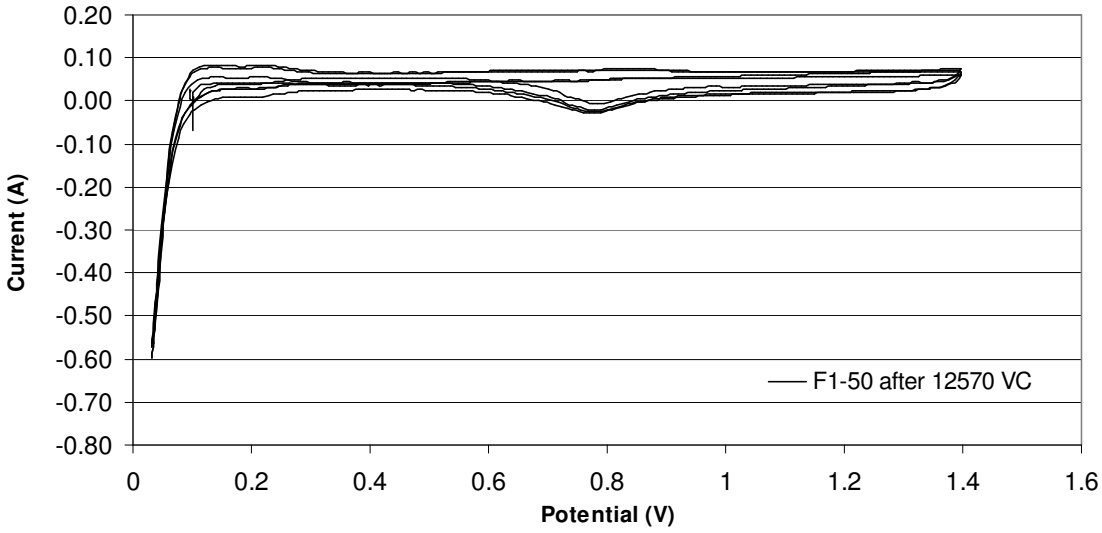

Figure 4.22: Cyclic voltammograms of fuel cell F_1 at 50mV/sec after 12,570 voltage cycles

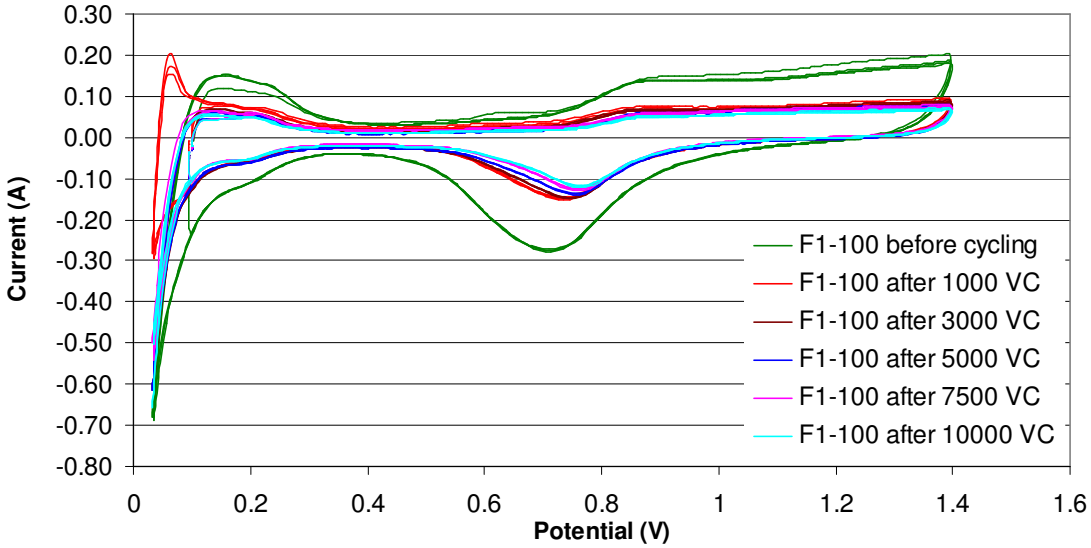

Figure 4.23: Cyclic voltammograms of fuel cell F_1 at 100mV/sec

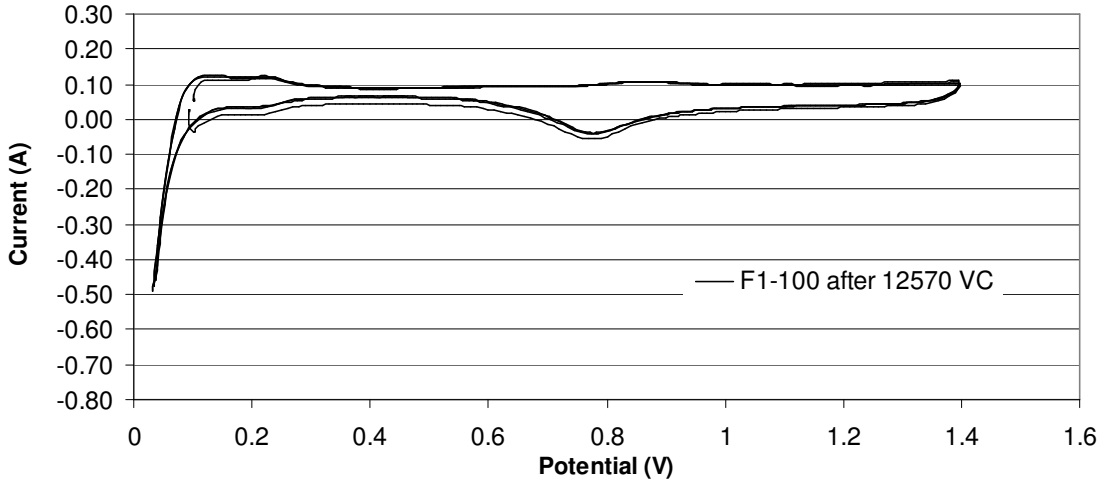

Figure 4.24: Cyclic voltammograms of fuel cell F_1 at 100mV/sec after 12570 voltage cycles

Table 4.12: Active Pt surface area for the fuel cell F_1

Voltage Cycles	Mean Active Pt Surface Area m^2/g
0	32.8
1000	25.5
3000	14.0
5000	12.8
7500	12.0
10000	10.8
12570	9.0

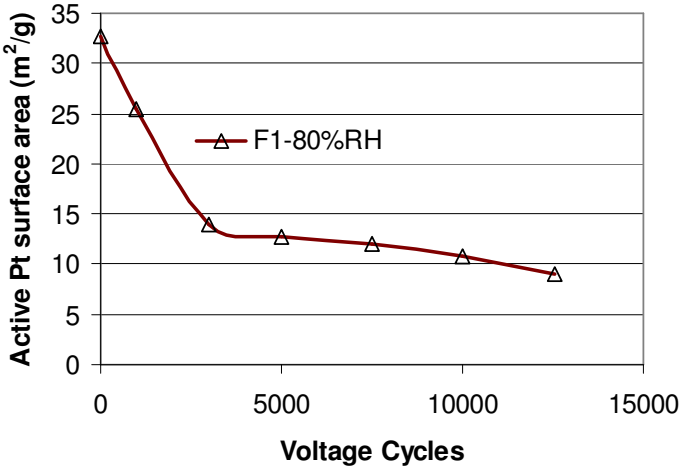

Figure 4.25: Decrease in Active Pt Surface Area as a function of Voltage Cycles for the Fuel Cell F_1 (80% RH)

4.5.3.4 Fuel Cell F_2 (90% RH)

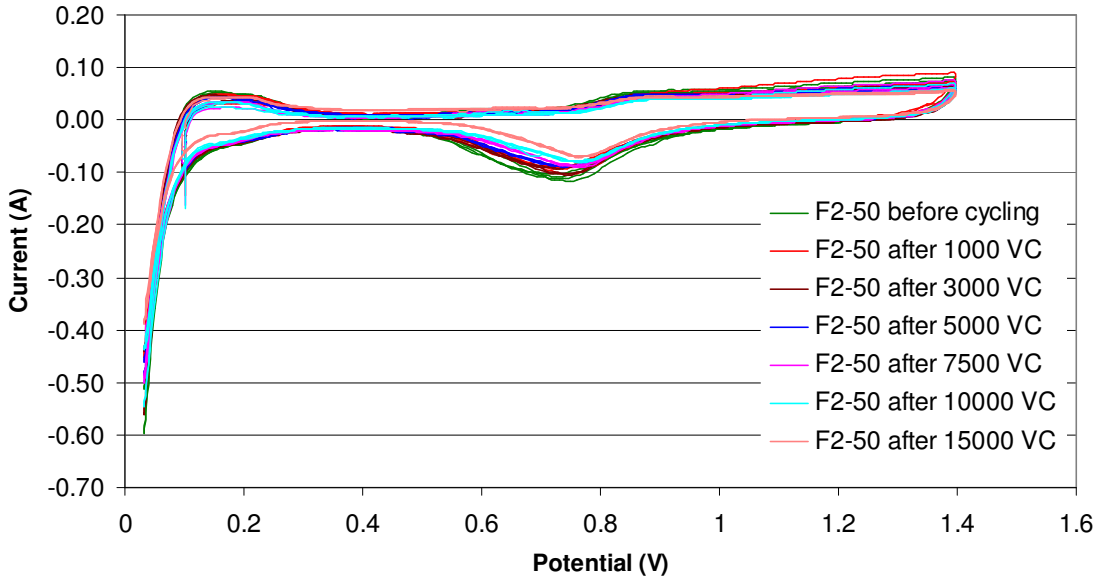

Figure 4.26: Cyclic voltammograms of fuel cell F_2 at 50mV/sec

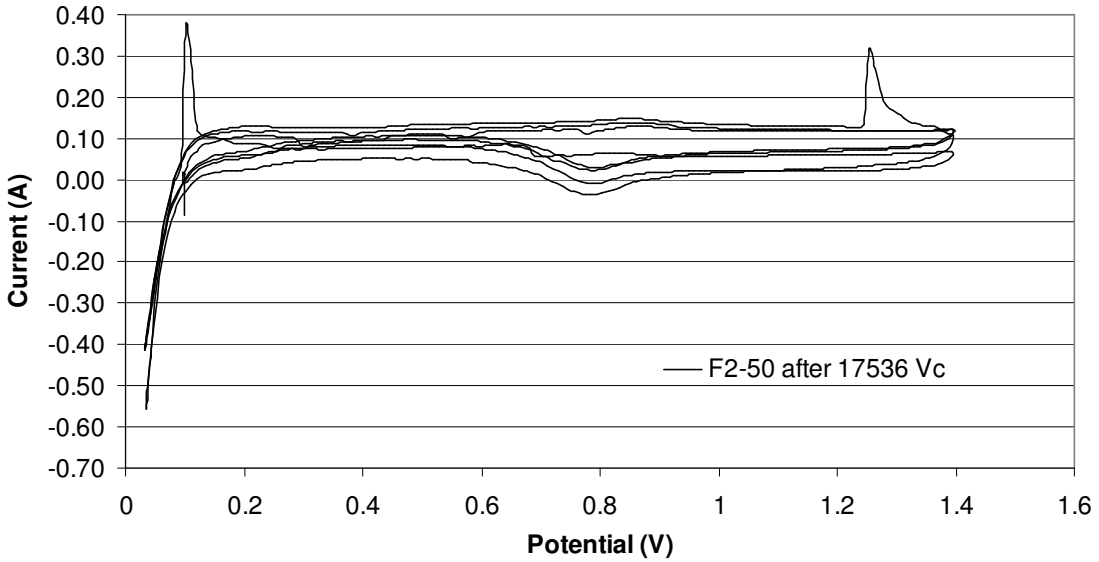

Figure 4.27: Cyclic voltammograms of fuel cell F_2 at 50mV/sec after 17536 voltage cycles

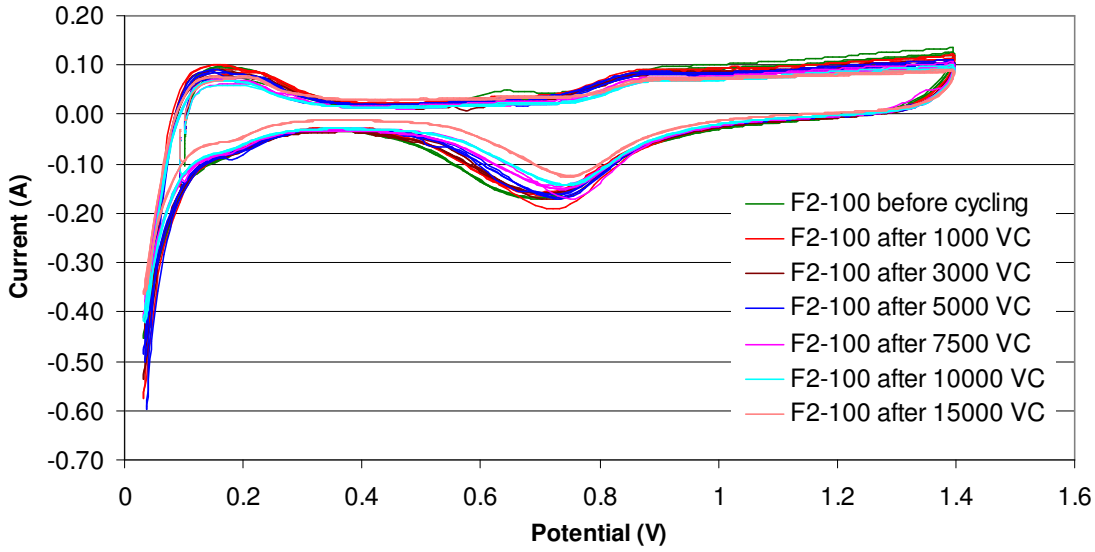

Figure 4.28: Cyclic voltammograms of fuel cell F_2 at 100mV/sec

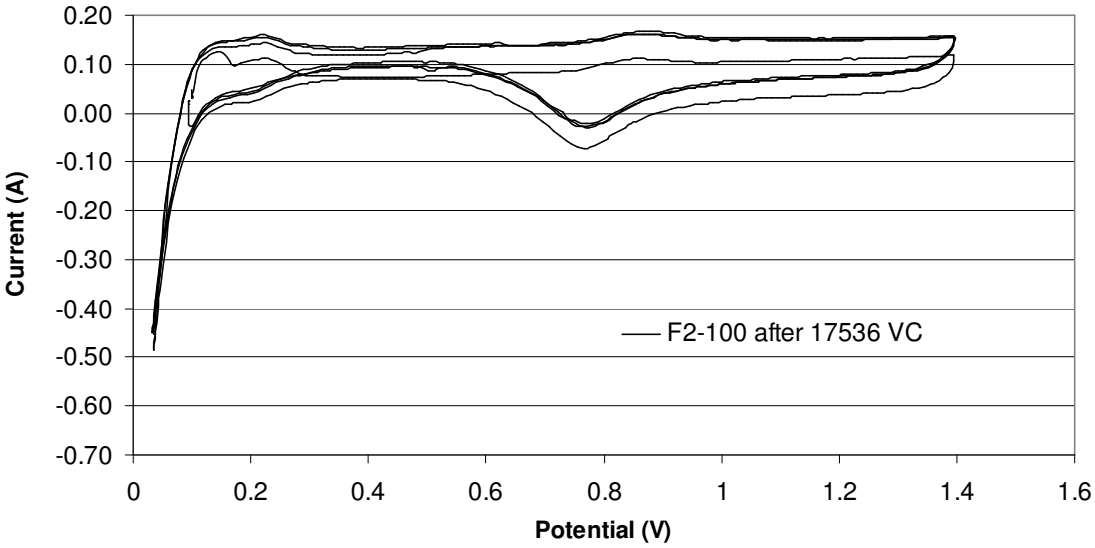

Figure 4.29: Cyclic voltammograms of fuel cell F_2 at 100mV/sec after 17536 voltage cycles.

Table 4.13: Active Pt surface area for the fuel cell F_2

Voltage Cycles	Mean Active Pt surface Area (m^2/g)
0	23.2
3000	20.5
5000	17.6
7500	14.1
10000	13.3
15000	12.2
17536	8.5

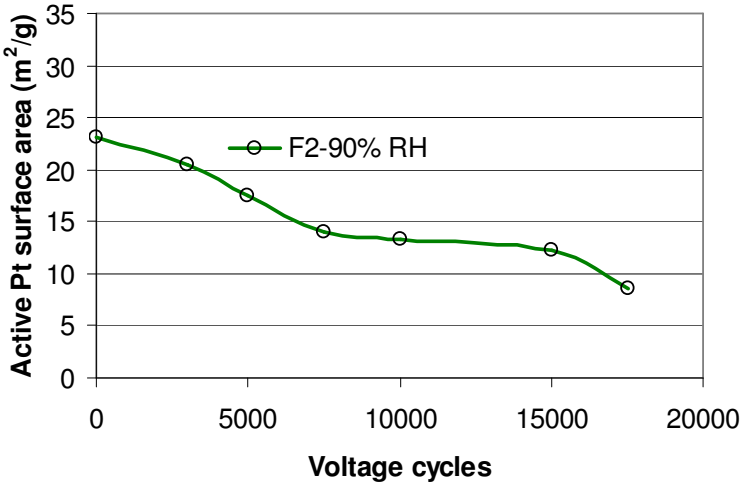

Figure 4.30: decrease in Active Pt Surface Area as a function of Voltage Cycles for the Fuel Cell F_2 (90% RH)

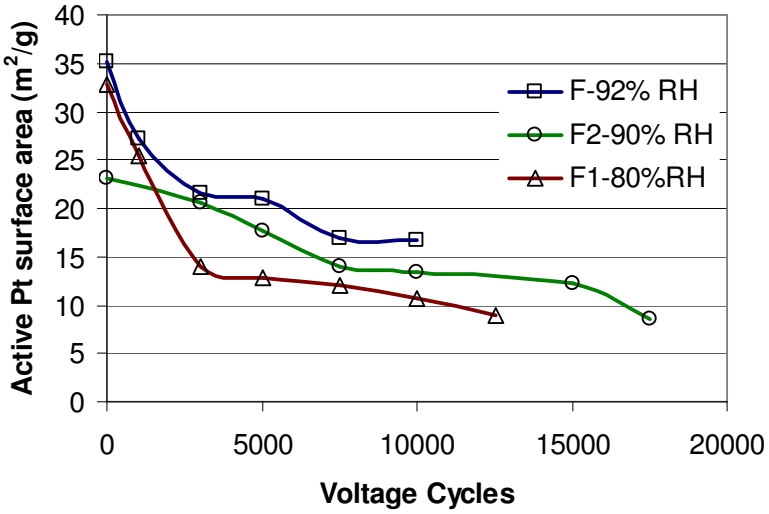

Figure 4.31: Comparison of the loss in active pt surface area for fuel cells F, F_1 and F_2

Figure 4.31 shows the Pt surface area loss as a function of voltage cycles for three PEM fuel cells F, F_1 and F_2 subjected to the accelerated voltage cycling protocol at different values of relative humidity. Figure 4.31 shows the graphical illustration of the active platinum surface area for the fuel cells F, F_1 and F_2. The effect of relative humidity (RH) on the performance and life time of fuel cells is obvious. Active platinum surface area of the fuel cell F_2 working at high value of relative humidity (90% RH) decreased gradually in comparison of the loss in active platinum surface area of fuel cell F_1 operated at low value of relative humidity (80%RH). It is also visible from the Figure 4.31 that there is a gross decline in the active Pt surface area of the fuel cell F_1 (80% RH) during the first 3,000 voltage cycles while in comparison for the fuel cell F_2 (90% RH) such decrease cannot be noticed. On the other side fuel cell F (92% RH) stopped working at 10,000 voltage cycles with higher value of active Pt surface area.

4.5.4 H2- Diffusion Measurements

Hydrogen diffusion measurements were performed at the end of the life time of the fuel cells with the nitrogen supply at the cathode side and hydrogen supply at the anode side of the cells.

One cycle of this measurement was drawn with 100 samples (per cycle) between 0.07V and 0.5V for a slew rate of 500 µV/sec. Like CV this measurement was also performed in the open circuit mode. Gas flow was set for a current of 10A.

4.5.4.1 Fuel Cell F1-80% RH

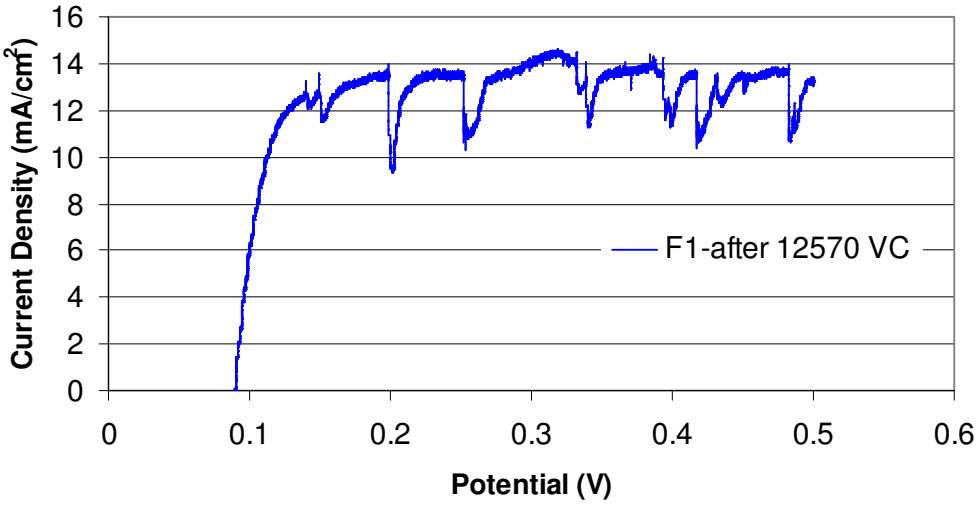

Figure 4.32: Hydrogen diffusion measurement of fuel cell F_1 after 12,570 voltage cycles

4.5.4.2 Fuel Cell F2-90% RH

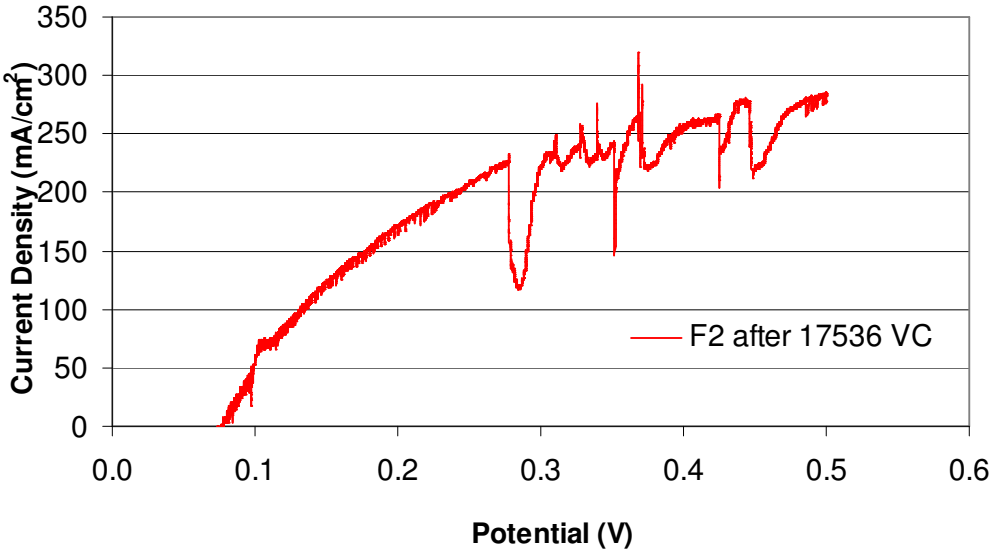

Figure 4.33: Hydrogen diffusion measurement of fuel cell F_2 after 17,536 voltage cycles

4.6 Ex-situ Characterisation of MEA by SEM and EDS

4.6.1 Scanning Electron Microscopy (SEM)

Before and after accelerated voltage cycling tests the cross-section of MEA and the cathode surface of all cells were examined through scanning electron microscopy. For this purpose backscattered electrons were utilised by AsB-detector (Angle Selective BSE-Det.) to get the SEM images at very short working distance of the order of a few millimetres (1-10mm WD).

Figure 4.34 and Figure: 4.35 show explicitly the detail of SEM images of fuel cells F, F_1 and F_2 after 10,000, 12,570 and 17,536 voltage cycles respectively. For comparison the cross-section and the cathode surface SEM images of fresh F-type MEA are also shown.

From these SEM images the thickness of the electrodes of fuel cell F_1 and F_2 at the end of their lifetime was determined as follows:

- Thickness of the cathode of the fuel cell F_1 after 12,570 voltage cycles= 4.757 µm
- Thickness of the anode of the fuel cell F_1 after 12570 voltage cycles= 7.661 µm
- Thickness of the cathode of the fuel cell F_2 after 17,536 voltage cycles=4.556 µm
- Thickness of the anode of the fuel cell F_2 after 17,536 voltage cycles=4.265 µm

A significant difference in the appearance of cathode surfaces of fuel cells F_1 and F_2 after 12,570 VC and 17,536 VC respectively in comparison of the cathode surface of fresh F-type MEA can be detected from Figure: 4.35. More cracks can be observed in the platinum surface of the MEA (F_2) which was subjected to the accelerated voltage cycling test for longer duration.

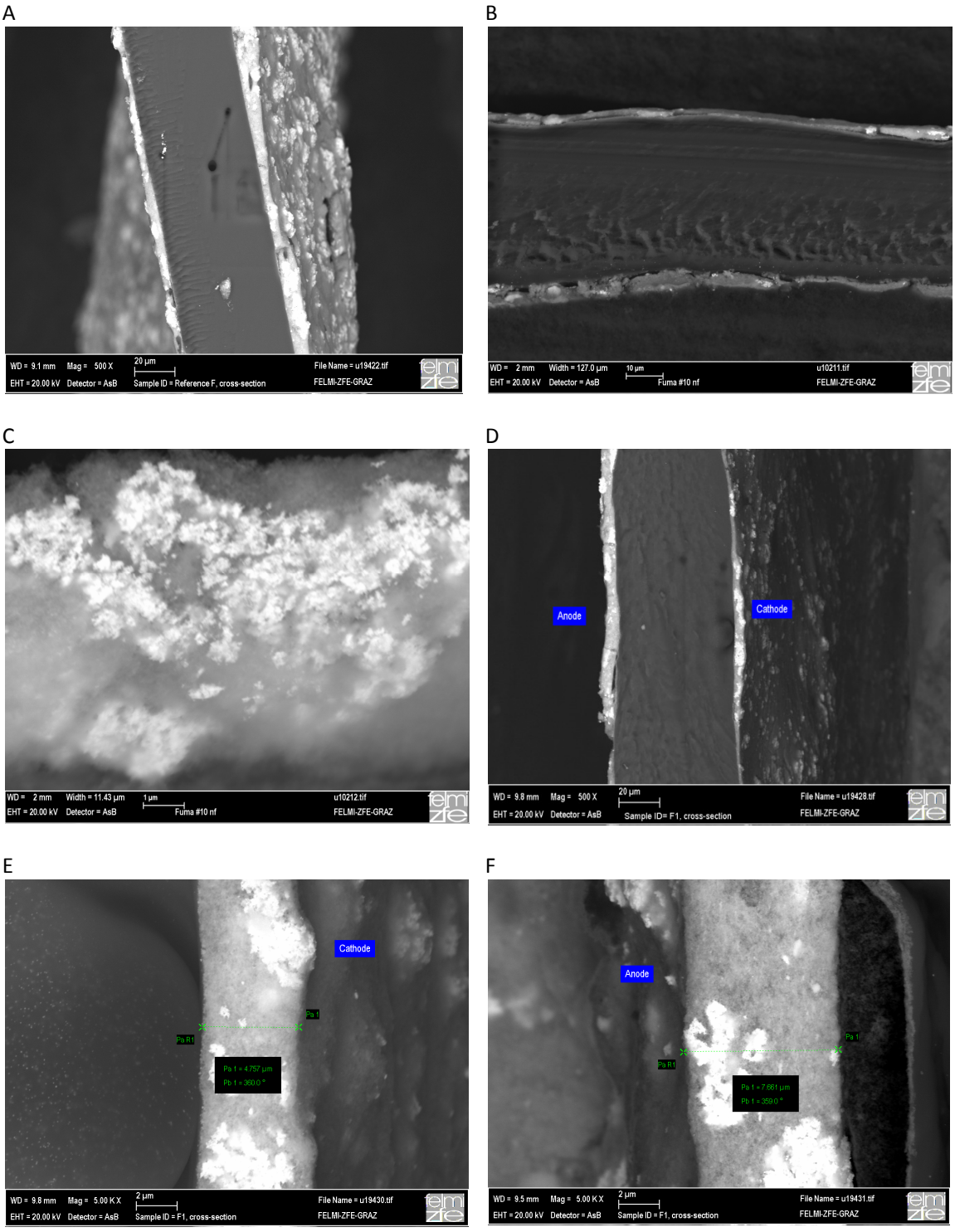

Figure 4.34: SEM images of the fuel cell F and F_1 by using back scattered electron detector, (A) Cross-section Fresh fuel cell F (20 µm), (B) Cross-section fuel cell F after 10,000 VC (10 µm), (C) Agglomeration of Pt particles at the cathode side of fuel cell F (1 µm), (D) Cross-section F_1 after 12,570 VC (20 µm), (E) Cathode of fuel cell F_1 after 12,570 VC (2µm), (F) Anode of fuel cell F_1 after 12,570 VC (2 µm),

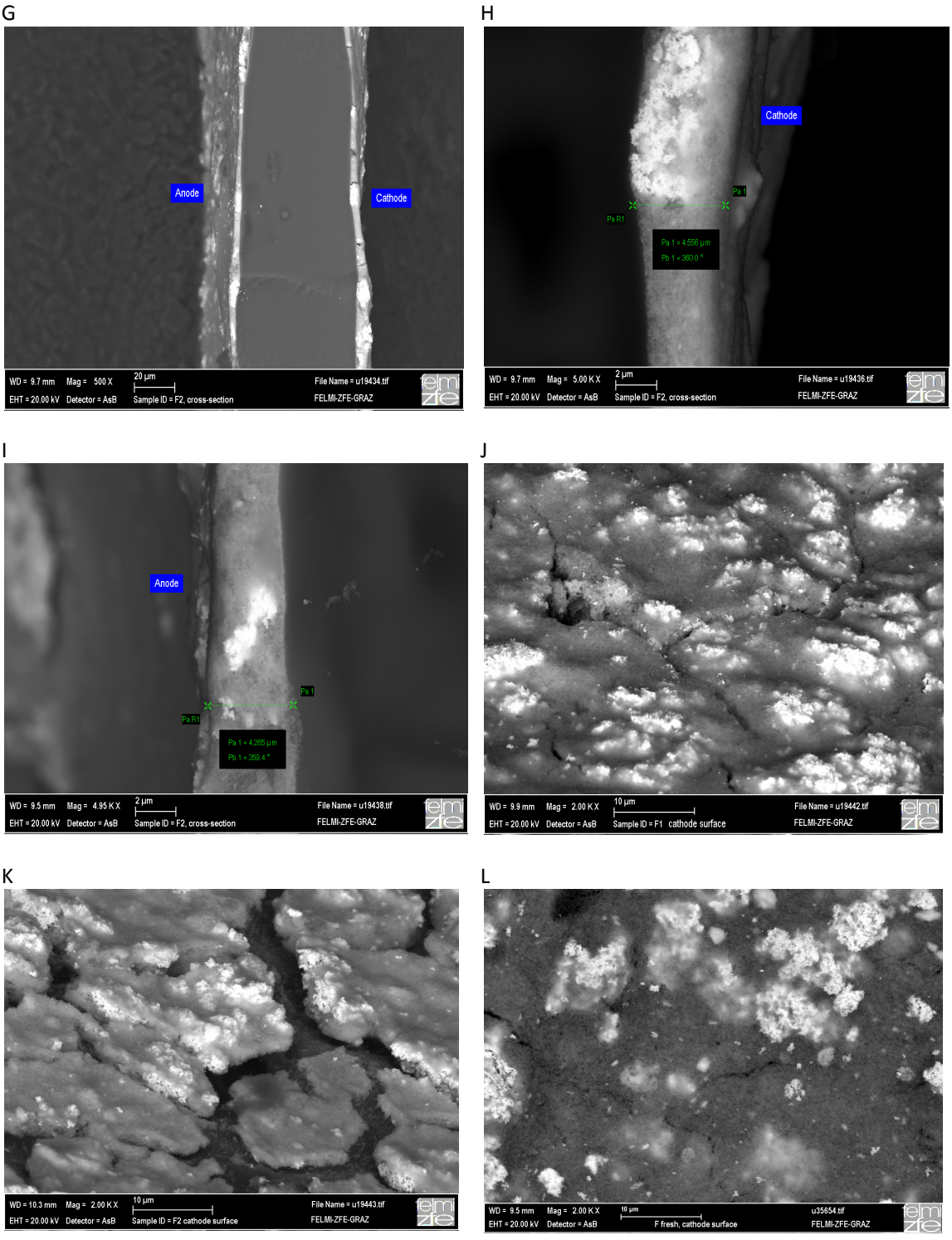

Figure: 4.35: (G) Cross-section of fuel cell F_2 after 17536 VC (20 µm), (H) Cathode of the fuel cell F_2 after 17,536 VC (2 µm), (I) Anode of the fuel cell F_2 after 17,536 VC (2 µm), (J) Cathode surface of the fuel cell F1 after 12,570 VC (10µm), (K) Cathode surface of the fuel cell F_2 after 17,536 VC (10µm), (L) Cathode surface of fresh MEA (10µm),

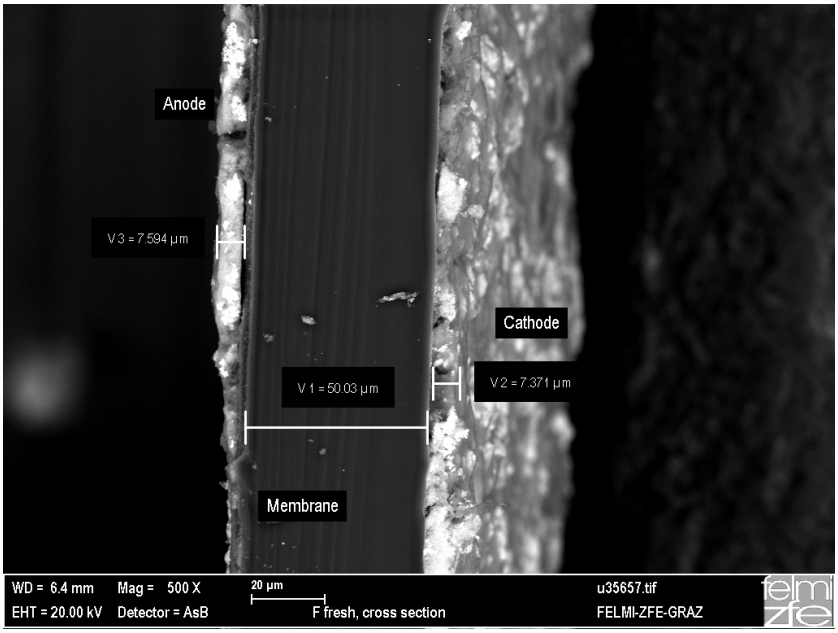

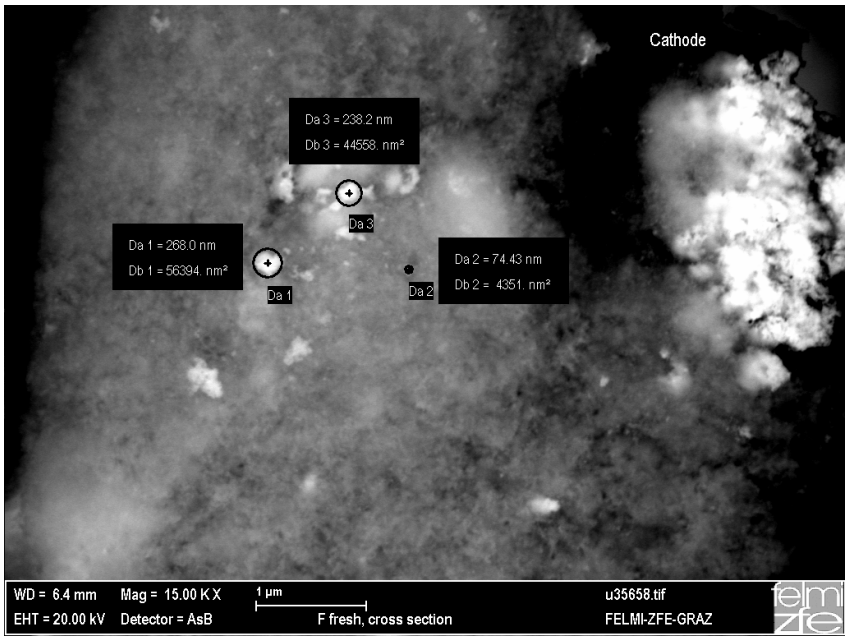

Figure 4.36: Cross-section of fresh f-type MEA (A), Cross-section of cathode of fresh F-type MEA (B)

4.7 Summary

Fuel cells F (92% RH), F_1 (80% RH) and F_2 (90% RH) worked for 10,000, 12570 and 17536 voltage cycles respectively. Among three fuel cells F, F_1 and F_2, the lifetime of the fuel cell F_2 operated at 90% relative humidity is proved as longest. This cell worked for larger number of voltage cycles i.e., 17536 and at this time the limiting current density value with oxygen supply at cathode side of F_2 is greater than that of F and F_1 at the end of their lifetime i.e., 10000 and 12570 voltage cycles respectively. All the three cells showed better performance in terms of limiting current density value through polarization curves when oxygen was fed to the cathode side of each cell. The limiting current density values for all three cells are less with air supply at the cathode side of every cell. The limiting current density values did not reach 2A/cm^2 when the cells were examined with air at cathode

whereas with oxygen at cathode these values exceeded 3A/cm^2. The values obtained from polarization curves are summarized in Table 4.14 and Table 4.15.

Fuel cell F_1 tested at 80% RH exhibited highest cathode resistance (0.069 ohm) at the end of its lifetime i.e. 12,570 voltage cycles whereas F_2 operated at 90 % RH showed slightly low cathode resistance (0.063 ohm) after even larger number of voltage cycles i.e. 17,536. For clarity the detail of cathode resistance of fuel cell F, F1 and F2 are given in the Table 4.16.

From the cyclic voltammograms the active platinum surface area of all these cells were calculated. For fuel cell F_2 examined at high value of relative humidity (90% RH), a gradual reduction in the active platinum surface area was observed in comparison of the loss in active platinum surface area of the fuel cell F_1 operated at low value of relative humidity (80% RH).

From the Table 4.17 it is prominent that the total decrease in active Pt surface area is 52.6%, 72.6% and 63.4% for the cathode of the fuel cells F (92% RH), F_1 (80% RH) and F_2 (90% RH) respectively at the end of their life span. So among these cells the reduction in active Pt surface area is maximum for the fuel cell operated at lowest value of relative humidity i.e. 80% RH.

Table 4.14: Detail from Polarization Curves of all F-type Fuel cells operated with oxygen supply at the cathode side

Fuel Cell	Gas	Voltage Cycles	OCV(V)	Max. Current density (A/cm^2)
F-92% RH	O_2	0	0.989	3.20
		1000	1.01	3.25
		3000	0.999	2.96
		5000	0.972	2.13
		7500	0.961	1.72
		10000	0.923	1.47
F_1-80% RH	O_2	0	0.979	2.11
		1000	0.93	2.19
		3000	0.944	2.38
		5000	0.928	2.39
		7500	0.914	2.33
		10000	0.914	2.35
		12570	0.875	1.75
F_2-90% RH	O_2	0	0.989	2.08
		1000	0.938	2.22
		3000	0.941	1.98
		5000	0.933	1.75
		7500	0.941	2.03
		10000	0.942	2.14
		15000	0.92	1.91
		17536	0.835	1.81

Table 4.15: Detail from Polarization Curves of all F-type Fuel cells operated with air supply at the cathode side

Fuel Cell	Gas	Voltage Cycles	OCV(V)	Max. Current density (A/cm^2)
F-92% RH	Air	0	0.969	1.74
		1000	0.98	1.97
		3000	0.983	1.99
		5000	0.955	1.54
		7500	0.928	1.51
		10000	0.915	1.47
F_1-80% RH	Air	0	0.957	0.89
		1000	0.921	1.25
		3000	0.921	1.22
		5000	0.921	1.28
		7500	0.907	1.26
		10000	0.899	1.19
		12570	0.863	0.88
F_2-90% RH	Air	0	0.957	1.17
		1000	0.909	1.18
		3000	0.924	1.10
		5000	0.921	1.08
		7500	0.925	1.10
		10000	0.937	1.38
		15000	0.919	1.19
		17536	0.882	1.21

Table 4.16: Detail of the resistances of fuel cells F, F_1 and F_2 from Niquist Plots

Fuel Cell	Gas	Voltage Cycles Completed	Membrane Resistance (a) (Ω)	Total Resistance (b) (Ω)	Cathode Resistance (b-a) (Ω)
F-92% RH	O_2	0	0.018	0.043	0.025
		1000	0.018	0.045	0.027
		3000	0.020	0.049	0.030
		7500	0.019	0.073	0.054
		10000	0.021	0.080	0.058
F_1-80% RH	O_2	0	0.021	0.046	0.025
		1000	0.022	0.062	0.040
		3000	0.021	0.064	0.043
		5000	0.022	0.065	0.043
		7500	0.021	0.074	0.053
		10000	0.022	0.079	0.057
		12570	0.027	0.095	0.069
F_2-90% RH	O_2	0	0.033	0.064	0.032
		1000	0.026	0.056	0.030
		3000	0.030	0.065	0.036
		5000	0.029	0.067	0.039
		10000	0.027	0.067	0.041
		15000	0.029	0.083	0.054
		17536	0.032	0.094	0.063

Table 4.17: Detail of Active Pt Surface Area of the fuel cells F, F_1 and F_2

Fuel Cell	Voltage Cycles	Mean Active Pt Surface Area (m^2/g)
F (92% RH)	0	35.2
	1000	27.2
	3000	21.5
	5000	21.0
	7500	16.8
	10000	16.7
F_1 (80% RH)	0	32.8
	1000	25.5
	3000	14.0
	5000	12.8
	7500	12.0
	10000	10.8
	12570	9.0
F_2 (90% RH)	0	23.2
	3000	20.5
	5000	17.6
	7500	14.1
	10000	13.3
	15000	12.2
	17536	8.5

5 Characterization of the MEA G

5.1 Specification of MEA G.

Platinum loading on Cathode 0.4 mg/cm^2

Platinum loading on Anode 0.4 mg/cm^2

Membrane thickness------18 micrometer (between the electrodes)

5.2 Constant System Parameters

Hydrogen stoichiometry : 1.5

Oxygen stoichiometry.: 2.0

Air stoichiometry : 2.2

Cell Temperature : 70°C

Cell Components:

Active Area: 5 cm²

GDS: SGL Carbon Group GDL 25BC

Sealing: WACKER, 2-components Silikon

Carbon Plates: SGL Carbon Group PPG 86

Measurement:

Teststand: Fuel Cell teststand for single cell

Potentiostat: Zahner IM6ex und PP 240

5.3 Experimental Procedure

Same as described in chapter 4.

5.4 Test Sequence for Characterization Curves

All steps were similar as given in chapter 4 except the EIS measurements with air feed on the cathode of the cells. Another important point is that hydrogen diffusion measurements were also recorded after CV at the end of life time for the fuel cells G, G_1, G_2, G_3, G_4, and G_5. For fuel cells G_6 and G_8 hydrogen diffusion measurements were collected through out the experiment after accomplishment of specific number of voltage cycles till the time at which the fuel cell stopped working.

5.5 Electrochemical Analysis

5.5.1 Polarization Curve

5.5.1.1 Polarisation Curve with Oxygen Supply at Cathode

5.5.1.1.1 Fuel Cell G-81% RH

The fuel cell G was operated at 81% relative humiditiy with 70°C cell temperature. Figure 5.1 illustrates the comparison of all Polarization Curves with oxygen supply at cathode of the fuel cell G. The figure shows the decrease in the current density with the increase in the number of the voltage cycles till 3000 voltage cycles. The current density versus voltage curve after 5000 voltage cycles indicates an activation loss as the curve intersects the voltage axis at 0.821 volts instead of at 0.971 volts (OCV value before cycling). This shows a prominent effect of catalyst loss after 5000 voltage cycles.

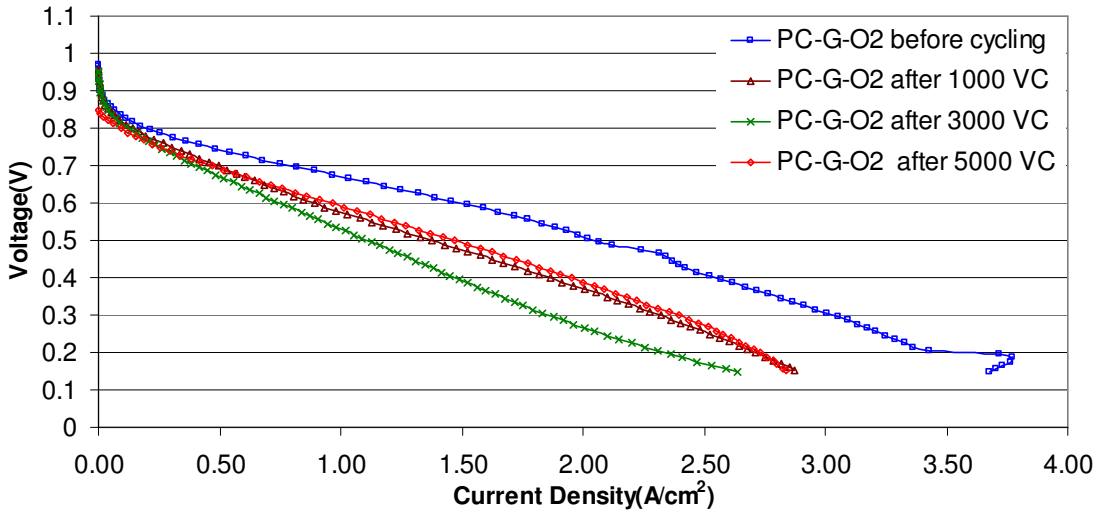

Figure 5.1: Comparison of all Polarization Curve with Oxygen supply at cathode of the fuel cell G (81% RH), Stoichiometry (H_2=1.5, O_2=2.0, Air=2.2), Cell Temperature <80°C, Area of fuel cell=5cm^2, Relative Humidity=90%, Pressure=Ambient (1.013 bar)

Table 5.1: Maximum current densities of fuel cell G with oxygen feed at the cathode.

Voltage Cycles	OCV (V)	Max. Current Density (A/cm^2)
0	0.971	3.68
1000	0.958	2.87
3000	0.951	2.64
5000	0.831	2.84

5.5.1.1.2 Fuel Cell G_1-90% RH

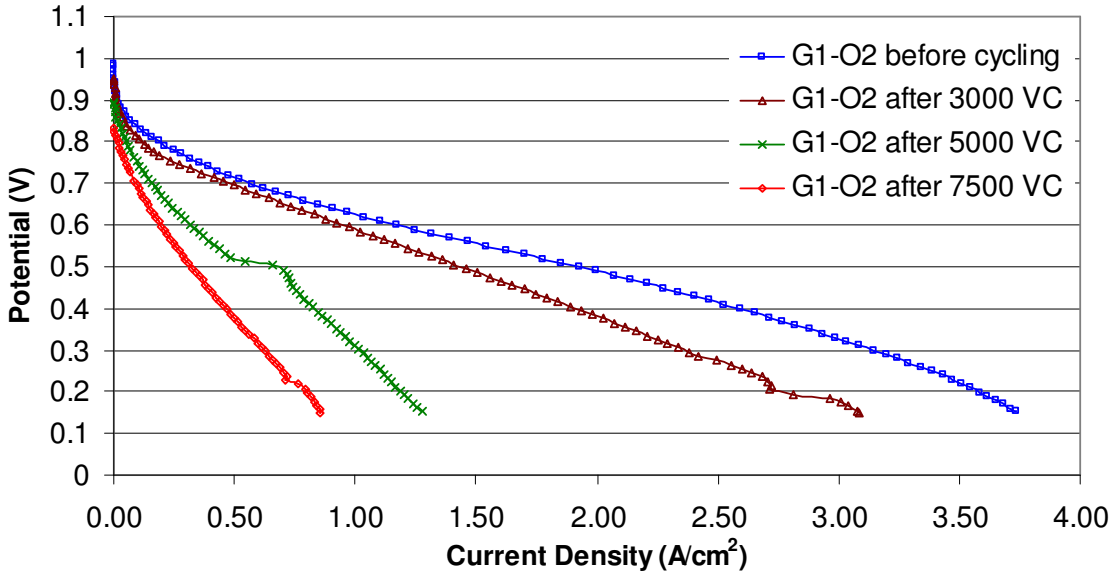

Figure 5.2: Comparison of all Polarization Curve with Oxygen supply at cathode of the fuel cell G_1 (90% RH), Stoichiometry (H_2=1.5, O_2=2.0, Air=2.2), Cell Temperature <80°C, Area of fuel cell=5cm^2, Relative Humidity=90%, Pressure=Ambient (1.013 bar)

The fuel cell G_1 was operated at 90% relative humidity. Figure 5.2 shows all polarization curves with oxygen feed at the cathode side of the fuel cell. The current density is maximum with the fresh MEA but a continuous decrease in the maximum current density can be observed with the increase of number of voltage cycles. A prominent decrease in the open circuit voltage (OCV) after 7500 voltage cycles is obvious from the Figure 5.2. This shows the effect of catalyst loss during potential cycling test. The current density versus voltage curves after 5,000 and 7,500 voltage cycles also present the effect of mass transport limitation due to poor water balance.

Table 5.2: Maximum current densities of fuel cell G_1 with oxygen feed at the cathode.

Voltage Cycles	OCV (V)	Max. Current Density A/cm^2
0	0.981	3.73
3000	0.953	3.08
5000	0.896	1.28
7500	0.831	0.85

5.5.1.1.3 Fuel Cell G_2-69% RH≈70% RH

Figure 5.3 presents all the polarization curves when oxygen was supplied at the cathode of the fuel cell G_2, tested at 70% RH. This cell worked till 3,000 VC. The current density is maximum as 2.96A/cm^2 before voltage cycling test but later on it reduces with the enhancement in the number of voltage cycles. The current density versus voltage curve after 3,000 VC intersects the potential axis at lesser value (0.861V) showing catalytic loss at this time. All three curves have maximum current densities at 0.15 V.

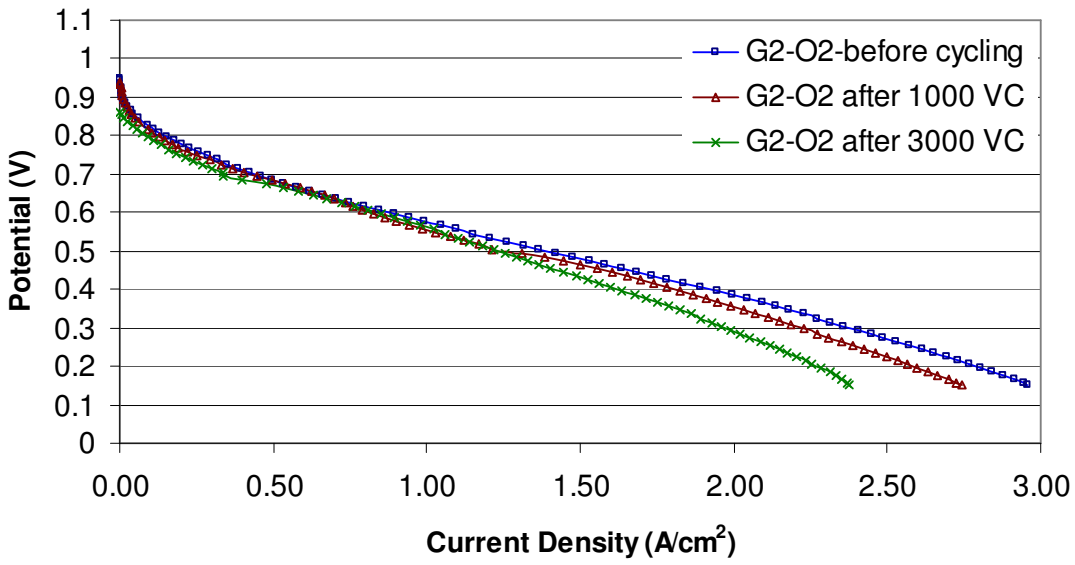

Figure 5.3: Comparison of all Polarization Curve with Oxygen supply at cathode of the fuel cell G_2 (70% RH), Stoichiometry (H_2=1.5, O_2=2.0, Air=2.2), Cell Temperature <80°C, Area of fuel cell=5cm^2, Relative Humidity=70%, Pressure=Ambient (1.013 bar)

Table 5.3: Maximum current densities of fuel cell G_2 with oxygen feed at the cathode.

Voltage Cycles	OCV (V)	Max. Current Density (A/cm^2)
0	0.95	2.96
1000	0.94	2.74
3000	0.86	2.38

5.5.1.1.4 Fuel Cell G_3-90% RH

Details of all polarization curves with oxygen feed at the cathode of the fuel cell G_3 operated at 90% RH, are shown in Figure 5.4. The current density with the fresh MEA is maximum but there is gradual decrease in it with the increase in number of voltage cycles. The current density / voltage characteristics of MEA till 1500 VC show almost the same behaviour, large linear ohmic region without diffusion losses, only with small decrease in the value of maximum current density at 0.15 V but afterward the drastic decrease in the current density after 2000, 3000, 5000 and 7350 voltage cycles can be observed as well as these curves show more diffusion losses due to mass transport limitations.

Table 5.4: Maximum current densities of fuel cell G_3 with oxygen feed at the cathode.

Voltage Cycles	OCV (V)	Max Current Density (A/cm^2)
0	0.977	4.56
400	0.968	4.18
1000	0.99	4.06
1500	0.977	4.04
2000	0.984	2.68
3000	0.989	2.47
5000	0.952	1.89
7350	0.93	1.46

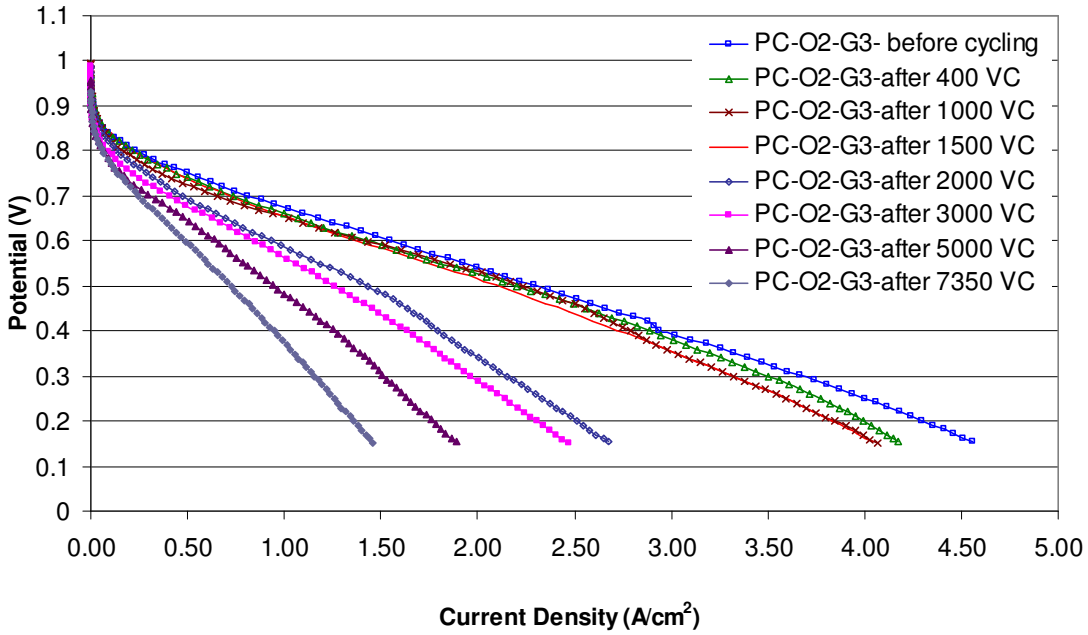

Figure 5.4: Comparison of all Polarization Curve with Oxygen supply at cathode of the fuel cell G_3 (90% RH), Stoichiometry (H_2=1.5, O_2=2.0, Air=2.2), Cell Temperature =70°C, Area of fuel cell=5cm^2, Relative Humidity=90%, Pressure=Ambient (1.013 bar)

5.5.1.1.5 Fuel Cell G_4-90% RH

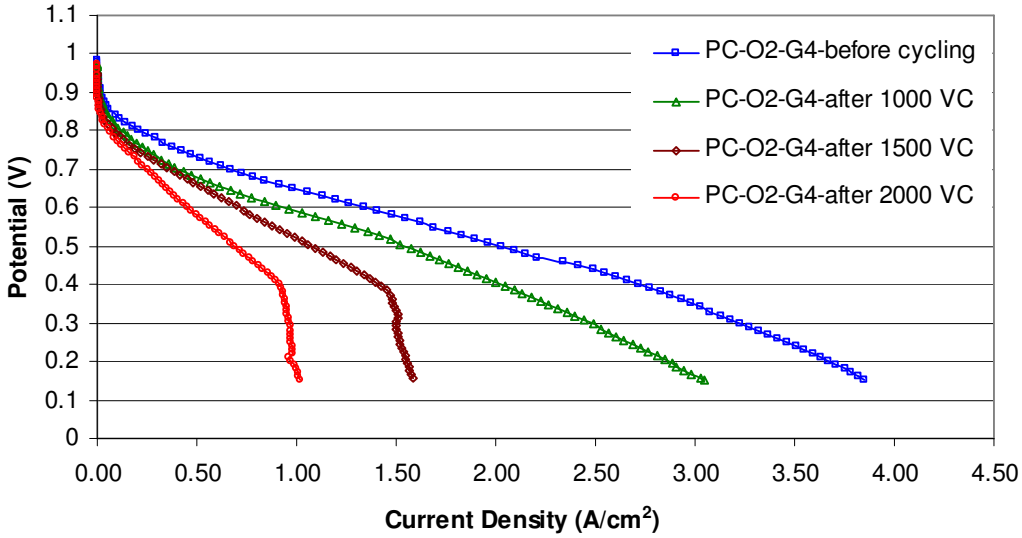

Figure 5.5: Comparison of all polarization curves with oxygen supply at the cathode of the fuel cell G_4 (90%RH), Stoichiometry (H_2=1.5, O_2=2.0, Air=2.2), Humidifier Temperature=68°C, Cell Temperature =70°C, Area of Fuel Cell=5cm^2, Relative Humidity=90%, Pressure= ambient (1.013 bar).

Table 5.5: Maximum current densities of fuel cell G_4 with oxygen feed at the cathode.

Voltage Cycles	OCV(V)	Max Current Density (A/cm^2)
0	0.982	3.85
1000	0.968	3.05
1500	0.952	1.59
2000	0.971	1.02

Fuel Cell G_4 was investigated at 90% RH with 70°C cell temperature. Figure 5.5 shows the current density verses potential curves for fuel cell G_4 when oxygen was fed to the cathode side. The maximum current density has the highest value (3.85A/cm^2) at 0.15 V with the fresh MEA but a small decrease in its value can be observed from the Figure 5.5 after 1,000 voltage cycles. During recording polarization curve after 1,500 VC, the mass flow controller of the test rig did not work well and this mass transportation limitation effects are visible from the figure for the current density versus voltage curve after 1,500 VC. After wards the problem of the mass flow controller was rectified but it already severely affected and deteriorated the MEA of G_4. Due to this reason the current density /voltage curve after 2,000 voltage cycles also shows the similar behaviour of the prominent effect of mass transport limitation with drastically less value of maximum current density.

5.5.1.1.6 Fuel Cell G_5-90% RH

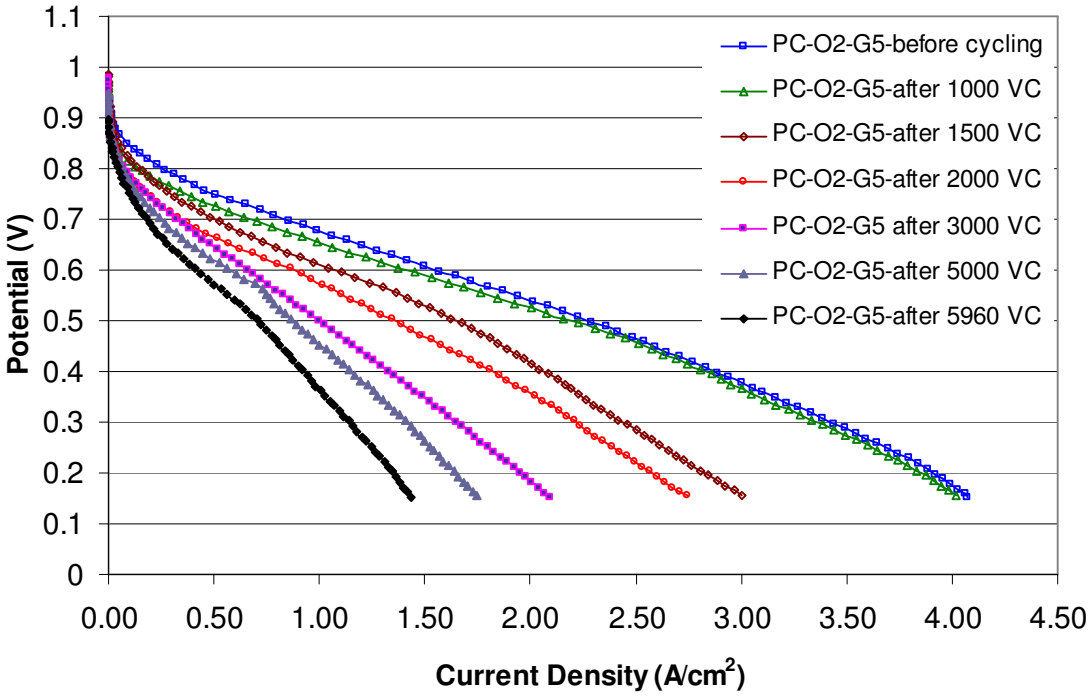

Figure 5.6: Comparison of all polarization curves with oxygen supply at the cathode of the fuel cell G_5 (90%RH), Stoichiometry (H_2=1.5, O_2=2.0, Air=2.2), Humidifier Temperature=68°C, Cell Temperature <80°C, Area of Fuel Cell=5cm^2, Relative Humidity=90%, Pressure= ambient (1.013 bar).

Table 5.6: Maximum current densities of fuel cell G_5 with oxygen feed at the cathode.

Voltage Cycles	OCV (V)	Max. Current Density (A/cm^2)
0	0.981	4.08
1000	0.973	4.02
1500	0.987	3.00
2000	0.984	2.74
3000	0.979	2.09
5000	0.948	1.75
5960	0.897	1.44

Fuel Cell G_5 was tested at 90 % RH. This cell worked till 5,960 voltage cycles. Figure 5.6 represents all the current density versus potential curves for the fuel cell G_5. The value of maximum current density is highest before potential cycling test and then a gradual decrease in it can be observed from the Figure 5.6. The current density /voltage curves for the fresh MEA and after 1,000 voltage cycles show long linear ohmic region without diffusion losses but afterwards the curves show more diffusion losses than the ohmic losses due to poorer water balance and limited gas supply.

5.5.1.1.7 Fuel Cell G_6-60% RH

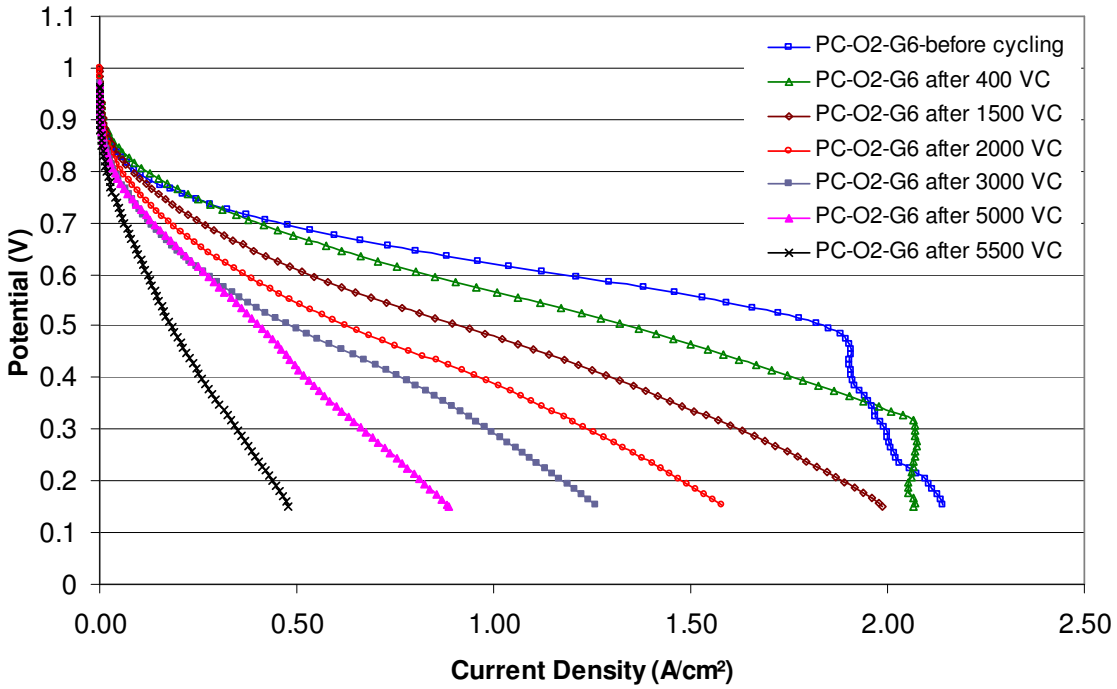

Figure 5.7: Comparison of all polarization curves with oxygen supply at the cathode of the fuel cell G_6 (60%RH), Stoichiometry (H_2=1.5, O_2=2.0, Air=2.2), Humidifier Temperature=59°C, Cell Temperature =70°C, Area of Fuel Cell=5cm^2, Relative Humidity=60%, Pressure= ambient (1.013 bar).

Table 5.7: Maximum current densities of fuel cell G_6 with oxygen feed at the cathode.

Voltage Cycles	OCV (V)	Max. Current Density (A/cm^2)
0	0.96	2.14
400	0.98	2.07
1500	1.00	1.99
2000	0.99	1.58
3000	0.97	1.26
5000	0.97	0.89
5500	0.96	0.48

The fuel cell G6 was operated at 60% relative humidity with 70°C cell temperature. This fuel cell worked till 5,500 voltage cycles. Figure 5.7 illustrates the detail of all polarization curves for the fuel cell G_6 with oxygen feed at the cathode side of the cell. The current density is maximum for the fresh MEA but the current density / voltage curve before potential cycling test shows more diffusion losses due to temporarily limited gas supply. This effect of mass transport limitation is also prominent for the current density/ voltage curve after 400 voltage cycles. Later on a gradual reduction in the value

of maximum current density with the increase in the number of voltage cycles is elaborated from the graphs. The curves after 5000 and 5500 voltage cycles present more diffusion losses due to mass transport limitations than the ohmic losses.

5.5.1.1.8 Fuel Cell G_8-33% RH

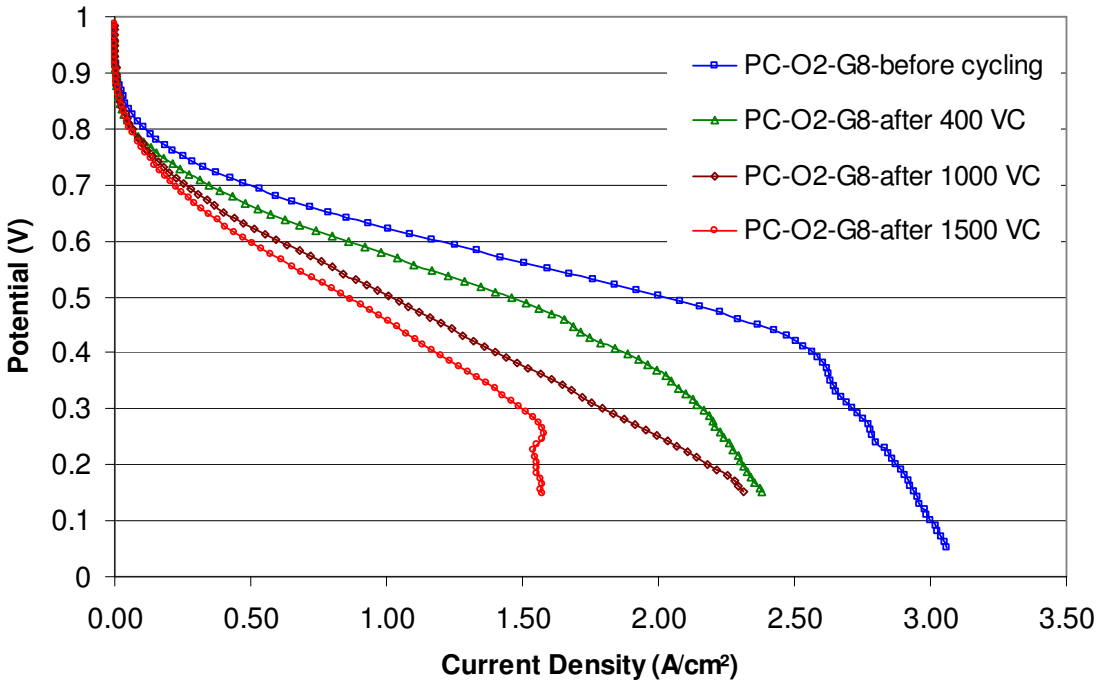

Figure 5.8: Comparison of all polarization curves with oxygen supply at the cathode of the fuel cell G_8 (33%RH), Stoichiometry (H_2=1.5, O_2=2.0, Air=2.2), Humidifier Temperature=47°C, Cell Temperature =70°C, Area of Fuel Cell=5cm^2, Relative Humidity=33%, Pressure= ambient (1.013 bar).

Table 5.8: Maximum current densities of fuel cell G_8 with oxygen feed at the cathode.

Voltage Cycles	OCV (V)	Max. Current Density (A/cm^2)
0	0.966	3.06
400	0.956	2.38
1000	0.983	2.31
1500	0.988	1.57

The fuel cell G_8 was tested at 33% relative humidity with 70°C cell temperature through potential cycling test. This fuel cell worked till 1500 voltage cycles with the set parameters. All the polarization curves obtained with oxygen supply at the cathode side of the cell are presented in the Figure 5.8. The graphs indicate the maximum current density with the fresh MEA. Afterward a regular decrease in the current density value can be observed. The current density verses voltage curve after 1500 voltage cycles shows the mass transport limitation behaviour with less ohmic drop.

5.5.1.2 Polarization Curve with Air Supply at Cathode

Polarization curves were also recorded for the fuel cells G, G_1, G_2, G_3, G_4, G_5, G_6 and G_8 when air was supplied to the cathode of these cells whereas anode of these cells were fed with the hydrogen.

5.5.1.2.1 Fuel Cell G-81% RH

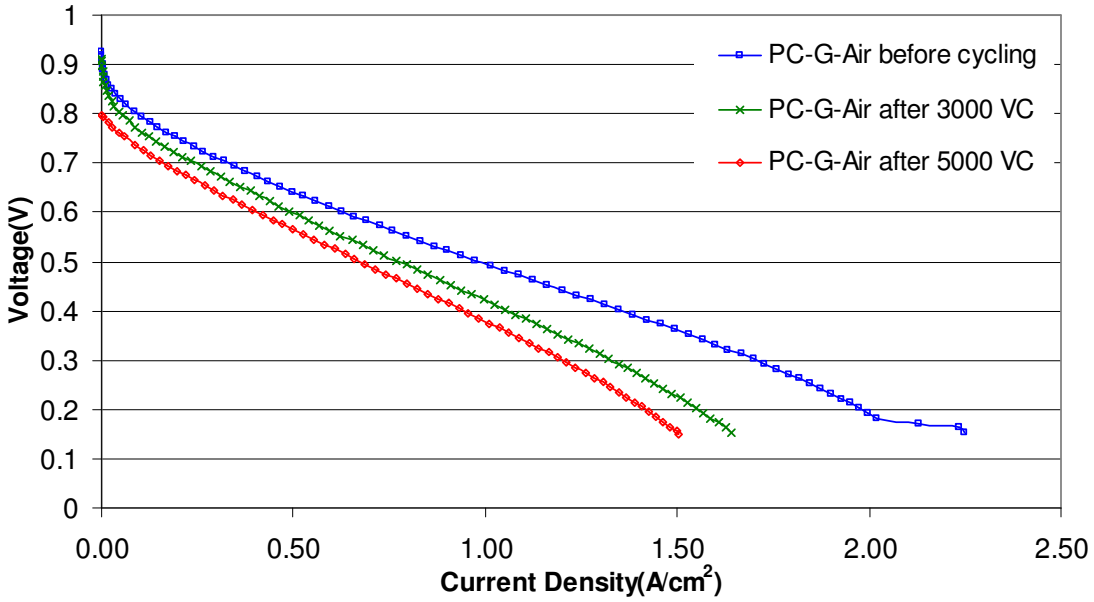

Figure 5.9: Comparison of all polarization curves with air supply at the cathode of the fuel cell G (81%RH), Stoichiometry (H_2=1.5, O_2=2.0, Air=2.2), Cell Temperature <80°C, Area of Fuel Cell=5cm^2, Relative Humidity=81%, Pressure= ambient (1.013 bar).

Table 5.9: Maximum current densities of fuel cell G with air feed at the cathode.

Voltage Cycles	OCV (V)	Maximum Current Density (A/cm^2)
0	0.924	2.25
3000	0.911	1.64
5000	0.798	1.51

The fuel cell G was investigated at 81% relative humidity and worked till 5000 voltage cycles. Figure 5.9 shows all polarization curves with air supply at the cathode of the fuel cell G2. The value of maximum current density is highest (2.25A/cm2) for fresh MEA but with the increase in number of potential cycles the decrease in maximum current density value can be observed from Figure 5.9. The current density versus potential curve after 5,000 voltage cycles touches the potential axis at lower point showing less value of OCV (0.798 V). It means, total catalyst loss has been occurred.

5.5.1.2.2 Fuel Cell G_1-90% RH

The fuel cell G_1 operated at 90% RH. Figure 5.10 illustrates the graphical representation of all the polarization curves. For this cell also the value of maximum current density is greatest before potential cycling test. A decline in the value of maximum current density can be seen with the proceeding of potential cycles. The current density / voltage curve after 5000 voltage cycles shows the mass transport limitation effect. This curve exhibit more diffusion losses than the ohmic drop.

The current density/voltage curve after 7500 voltage cycles also presents the same behaviour with least value of OCV (0.865V) and current density (0.49A).

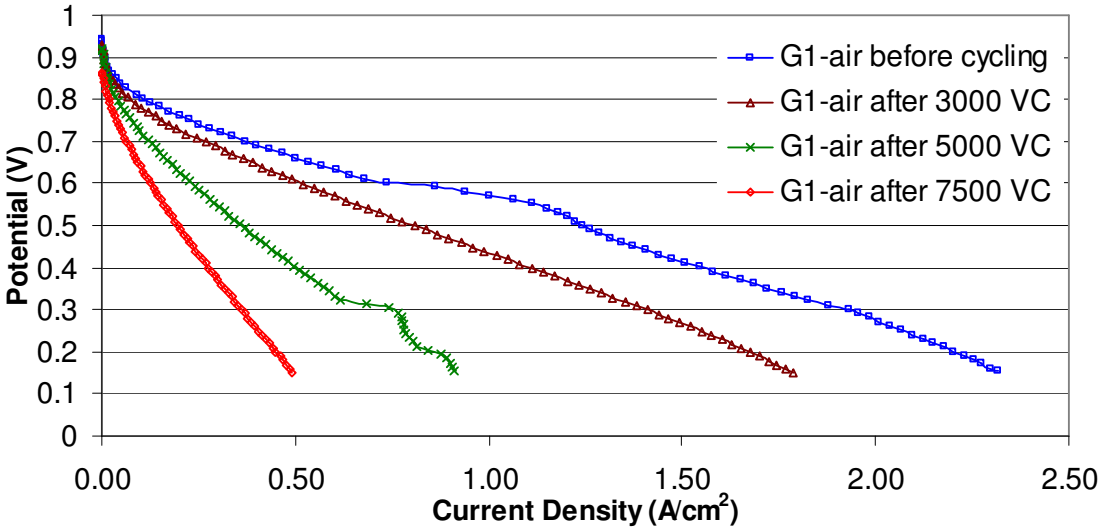

Figure 5.10: Comparison of all porarization curves with air supply at cathode of the fuel cell G_1 (90% RH), Stoichiometry (H_2=1.5, O_2=2.0, Air=2.2), Humidifier Temperature=68°C, Cell Temperature <80°C, Area of Fuel Cell=5cm^2, Relative Humidity=90%, Pressure= ambient (1.013 bar).

Table 5.10: Maximum current densities of fuel cell G_1 with air feed at the cathode.

Voltage Cycles	OCV(V)	Max. Current Density (A/cm^2)
0	0.938	2.32
3000	0.931	1.79
5000	0.92	0.91
7500	0.865	0.49

5.5.1.2.3 Fuel Cell G_2-70% RH

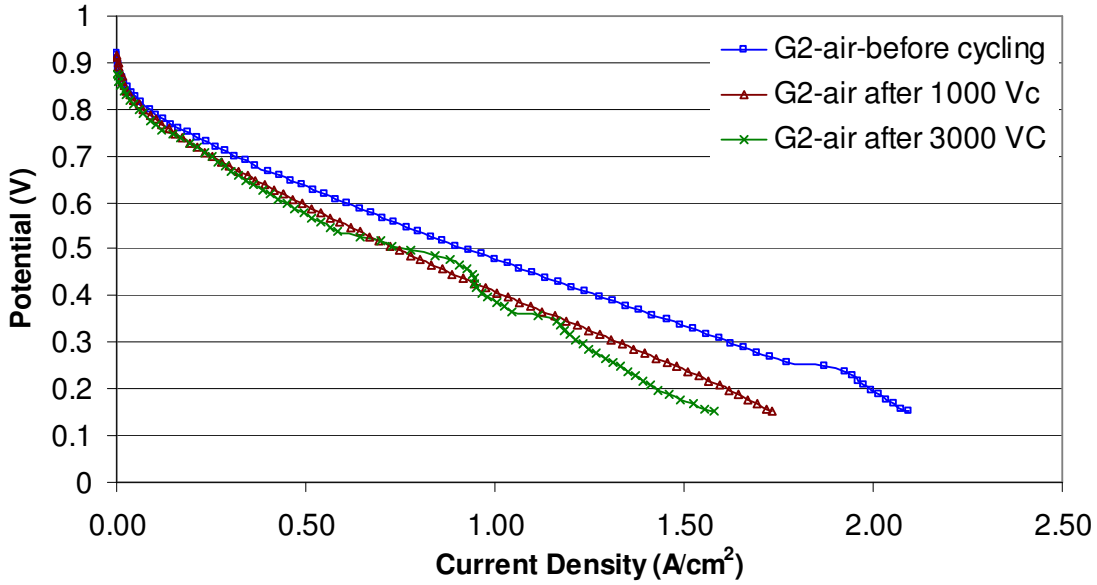

Figure 5.11: Comparison of all porarization curves with air supply at cathode of the fuel cell G_2 (70% RH), Stoichiometry (H_2=1.5, O_2=2.0, Air=2.2), Cell Temperature <80°C, Area of Fuel Cell=5cm^2, Relative Humidity=70%, Pressure= ambient (1.013 bar).

Table 5.11: Maximum current densities of fuel cell G_2 with air feed at the cathode.

Voltage Cycles	OCV (V)	Max.Current Density (A/cm^2)
0	0.921	2.09
1000	0.915	1.73
3000	0.875	1.58

Fuel cell G_2 was tested at 70% relative humidity. Through potential cycling test this cell gave performance till 3,000 voltage cycles having decreasing trend in maximum current density value with the progress in number of potential cycles.

5.5.1.2.4 Fuel Cell G_3-90% RH

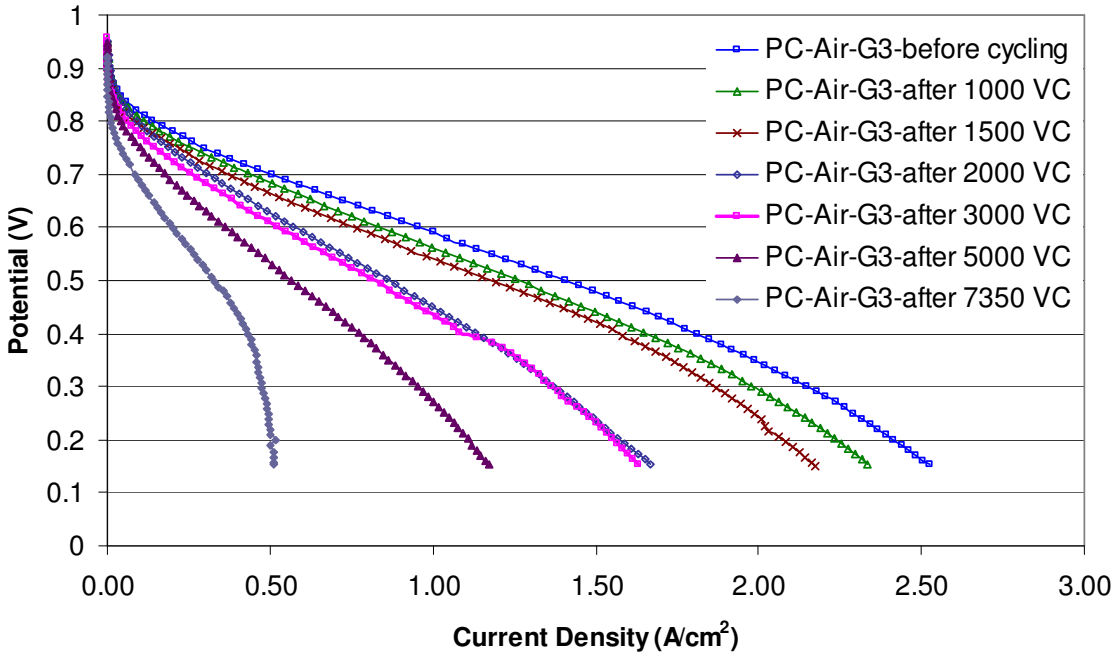

Figure 5.12: Comparison of all porarization curves with air supply at cathode of the fuel cell G_3 (90% RH), Stoichiometry (H_2=1.5, O_2=2.0, Air=2.2), Humidifier Temperature=68°C Cell Temperature =70°C, Area of Fuel Cell=5cm^2, Relative Humidity=90%, Pressure= ambient (1.013 bar).

Table 5.12: Maximum current densities of fuel cell G_3 with air feed at the cathode.

Voltage Cycles	OCV (V)	Max. Current Density (A/cm^2)
0	0.943	2.52
1000	0.953	2.33
1500	0.943	2.18
2000	0.95	1.67
3000	0.957	1.63
5000	0.947	1.17
7350	0.923	0.51

The fuel cell G_3 operated at 90% relative humidity, gave performance till 7,350 voltage cycles. Through out the potential cycling experiment the OCV value remained ever 0.9V. The maximum current density value is greatest for the fresh MEA (2.52A/cm^2) but reduces with the course of the experiment. The current density versus potential curve after 7,350 voltage cycles exhibits more concentration losses due to catalytic loss and poor water balance.

5.5.1.2.5 Fuel Cell G_4-90% RH

Fuel Cell G_4 was also investigated at 90% relative humidity. This cell worked till 2,000 voltage cycles. The current density/ voltage curves before potential cycling test and after 1,000 voltage cycles show long region of linear ohmic drop without diffusion losses whereas the current density/potential curves after 1,500 and 2,000 voltage cycles, show less ohmic resistances and having more concentration losses. Fuel cell G_4 did not exhibit good performance due to the fuel starvation during collecting characterisation curves after 1,500 VC.

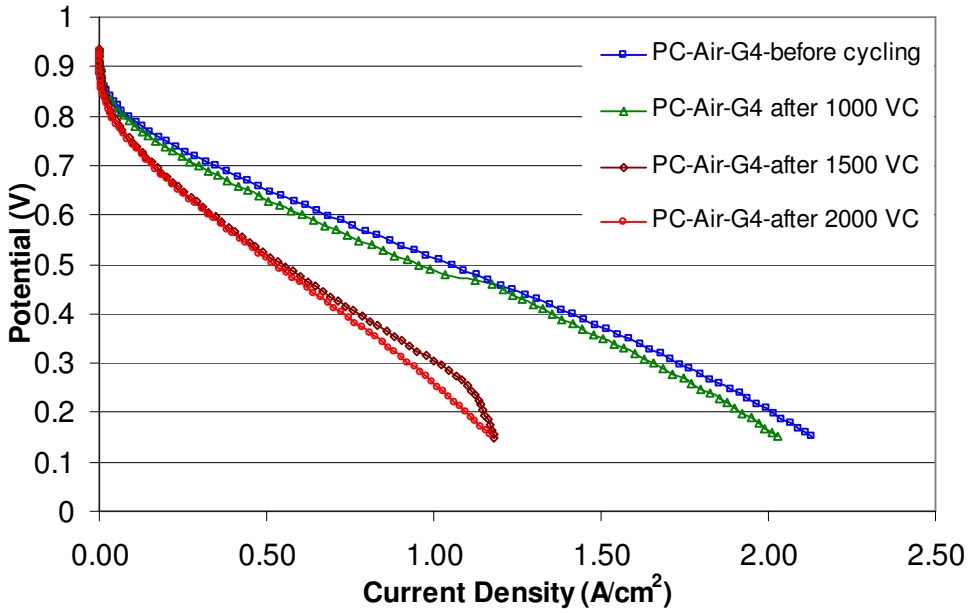

Figure 5.13: Comparison of all porarization curves with air supply at cathode of the fuel cell G_4 (90% RH), Stoichiometry (H_2=1.5, O_2=2.0, Air=2.2), Humidifier Temperature=68°C Cell Temperature =70°C, Area of Fuel Cell=5cm^2, Relative Humidity=90%, Pressure= ambient (1.013 bar).

Table 5.13: Maximum current densities of fuel cell G_4 with air feed at the cathode.

Voltage Cycles	OCV (V)	Max. Current Density (A/cm^2)
0	0.925	2.13
1000	0.936	2.03
1500	0.936	1.18
2000	0.93	1.17

5.5.1.2.6 Fuel Cell G_5-90% RH

Fuel Cell G_5 was tested at 90% relative humidity. This cell worked till 5,960 voltage cycles. The value of maximum current density with the fresh MEA is less than its value after 1,000 voltage cycles. This shoes the complete and proper humidification and activation of the MEA at this stage. Then a continuous decrease in the maximum value of current density can be seen from Figure 5.14.

The current density versus potential curves till 2,000 voltage cycles show more linear ohmic losses but after ward the curves exhibit more concentration losses. The current density /voltage curve after 5,960 voltage cycles does not show any ohmic drop, only mass transport losses exist with poor water management. It means that total catalyst have been lost at this stage as the curve ends with the least value of maximum current density (0.21A/cm^2) at 0.15V.

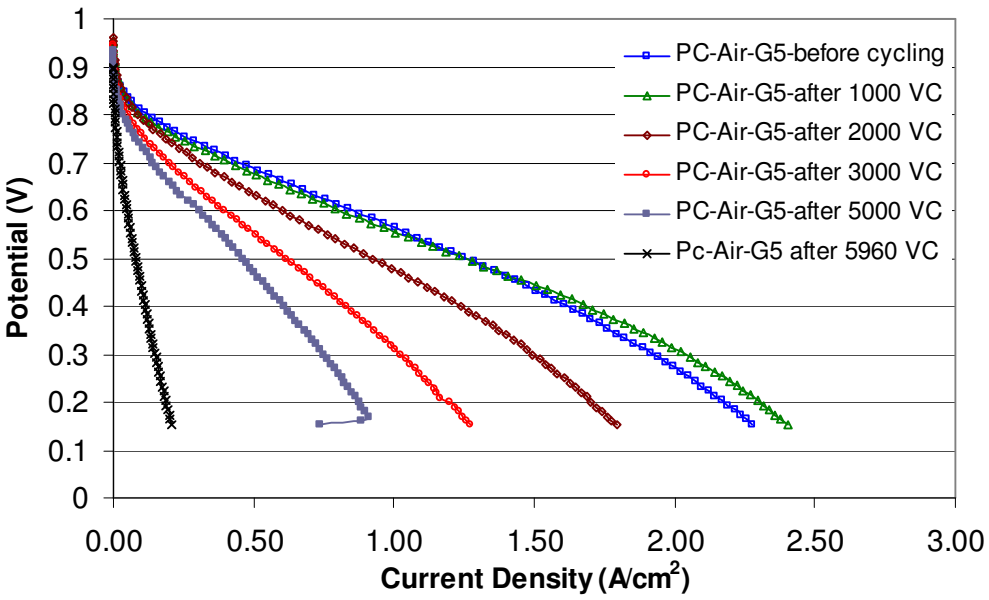

Figure 5.14: Comparison of all porarization curves with air supply at cathode of the fuel cell G_5 (90% RH), Stoichiometry (H_2=1.5, O_2=2.0, Air=2.2), Humidifier Temperature=68°C Cell Temperature =70°C, Area of Fuel Cell=5cm^2, Relative Humidity=90%, Pressure= ambient (1.013 bar).

Table 5.14: Maximum current densities of fuel cell G_5 with air feed at the cathode.

Voltage Cycles	OCV (V)	Max. Current Density (A/cm^2)
0	0.932	2.28
1000	0.954	2.40
2000	0.959	1.79
3000	0.944	1.27
5000	0.935	0.74
5960	0.899	0.21

5.5.1.2.7 Fuel Cell G_6-60% RH

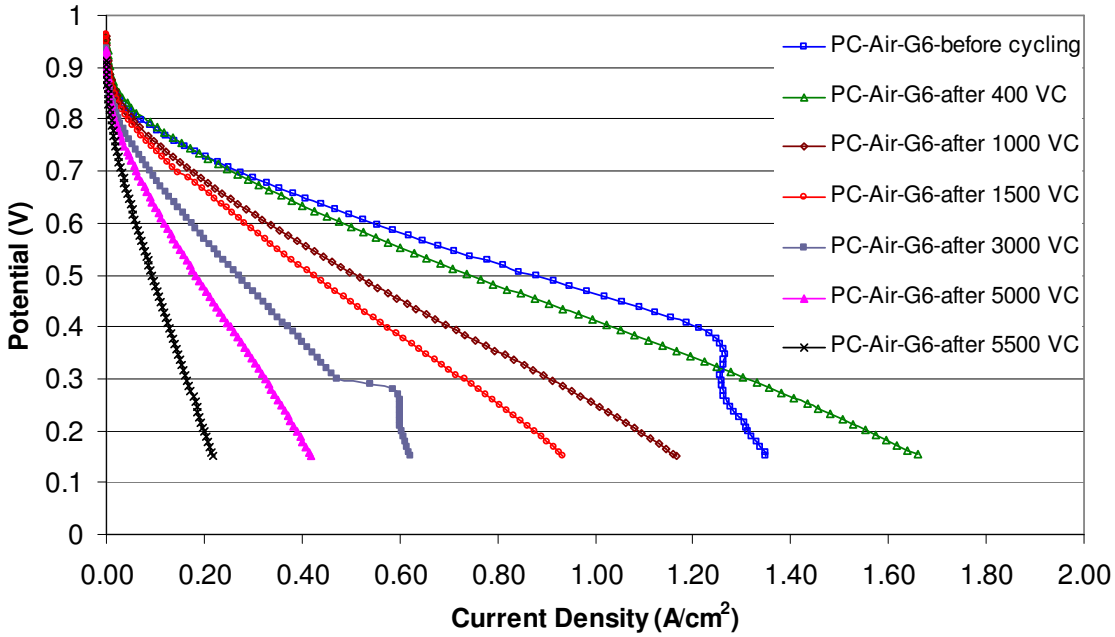

Figure 5.15: Comparison of all porarization curves with air supply at cathode of the fuel cell G_6 (60% RH), Stoichiometry (H_2=1.5, O_2=2.0, Air=2.2), Humidifier Temperature=59°C Cell Temperature =70°C, Area of Fuel Cell=5cm^2, Relative Humidity=60%, Pressure= ambient (1.013 bar).

Table 5.15: Maximum current densities of fuel cell G_6 with air feed at the cathode.

Voltage Cycles	OCV (V)	Max. Current Density (A/cm^2)
0	0.934	1.35
400	0.958	1.66
1000	0.959	1.17
1500	0.963	0.94
3000	0.935	0.62
5000	0.934	0.42
5500	0.912	0.22

Fuel cell G6, operated at 60% relative humidity, worked till 5,500 voltage cycles. This cell gave maximum performance after 400 voltage cycles instead of before potential cycling test. It means the MEA became fully activated at this time but the maximum current density value is not really high (1.66A/cm^2) due to low value of relative humidity (60% RH). Later on there is a gradual reduction in the maximum current density value with the course of the experiment. Also with the increase in the number of potential cycles, the current density verses potential curves show less ohmic drop but more mass transport limitation effect.

5.5.1.2.8 Fuel Cell G_8-33% RH

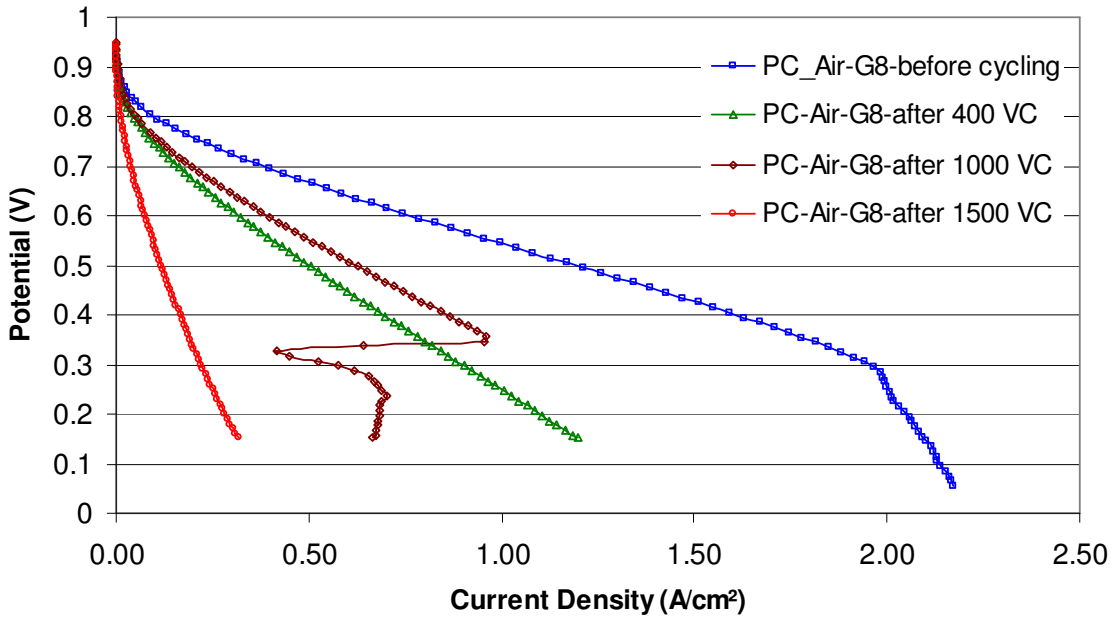

Figure 5.16: Comparison of all Polarization curves with air supply at the cathode of the fuel cell G_8 (33% RH), Stoichiometry (H_2=1.5, O_2=2.0, Air=2.2), Humidifier Temperature=47°C, Cell Temperature=70°C, Area of Fuel cell=5cm^2, Relative Humidity=33%, Pressure=ambient (1.013 bar)

Table 5.16: Maximum current densities of fuel cell G_8 with air feed at the cathode.

Voltage Cycles	OCV (V)	Max. Current Density (A/cm^2)
0	0.933	2.17
400	0.943	1.20
1000	0.95	0.67
1500	0.945	0.32

The fuel cell G_8 was operated at 33% relative humidity and with all other similar parameters this cell worked for just 1,500 voltage cycles. The current density versus potential curve after 1,500 voltage cycles shows the least value of current density.

5.5.2 Electrochemical Impedance Spectroscopy(EIS)

The frequency dependent resistance of the fuel cells operated at different values of relative humidity was investigated by electrochemical impedance spectroscopy. Electrochemical Impedance Spectra were recorded by supplying first oxygen and then air to the cathode side of all these fuel cells. With the help of Nyquist plots, the membrane and the electrode (cathode) resistance can be evaluated because of the frequency dependence.

The impedance spectra were measured in a frequency range between 50 mHZ and 10KHZ with an amplitude of 10mV.All the EIS measurements were made in "Galvanostatic mode'' with (-3A) Current. Gas flow on computer was set with the help of stoichiometric values for the current of 5A.

Lower Limit 50mHZ

Start 10KHZ

Upper	10KHZ
Amplitude	10mV

5.5.2.1 Fuel Cell G 81% RH

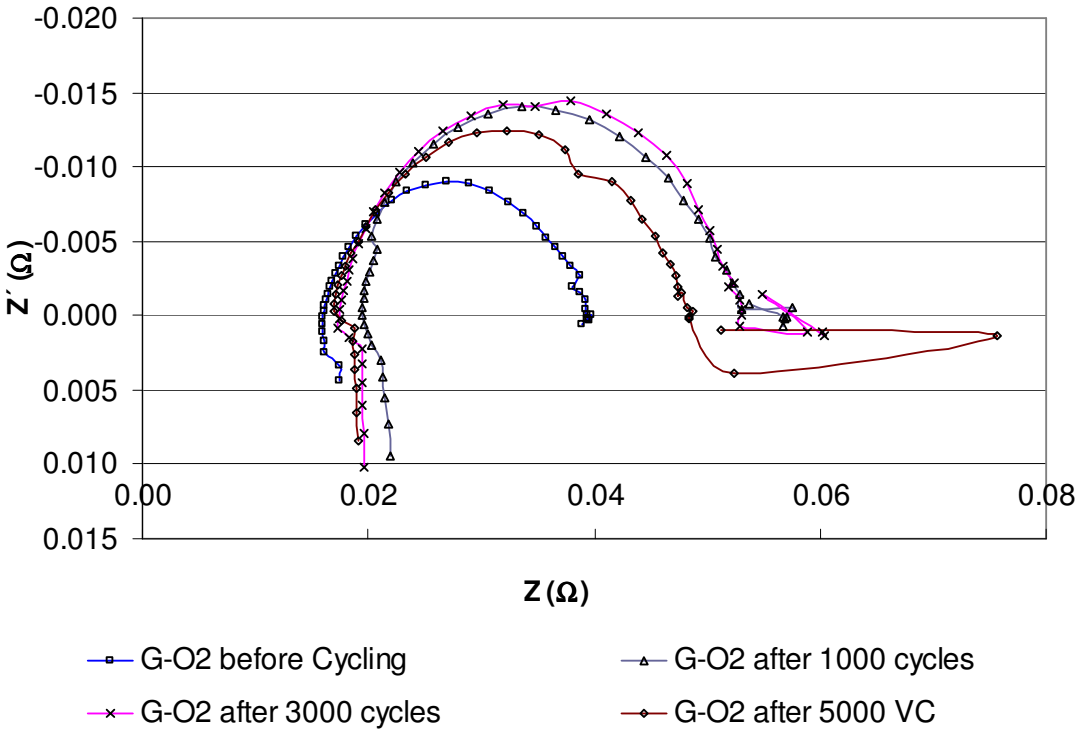

Figure 5.17: Comparison of all Nyquist Plots for the fuel cell G

Table 5.17: Resistances of the fuel cell G

Voltage Cycles Completed	Membrane Resistance (a) (Ω)	Total Resistance (b) (Ω)	Cathode Resistance (b-a) (Ω)
0	0.016	0.039	0.023
1000	0.019	0.051	0.031
3000	0.018	0.053	0.035
5000	0.017	0.048	0.031

Figure 5.17 illustrates all the Nyquist plots with the oxygen supply at the cathode side of the fuel cell G tested at 81% RH by life time potential cycling investigation. During the whole test no prominent increase in the membrane resistance can be exhibited from

Table 5.17 but on the other hand the cathode resistance increases till 3,000 voltage cycles and afterward a decrease in cathode resistance can be seen after 5,000 voltage cycles. Figure 5.18 shows the graphical representation of the change in cathode resistance with the increase in the number of voltage cycles.

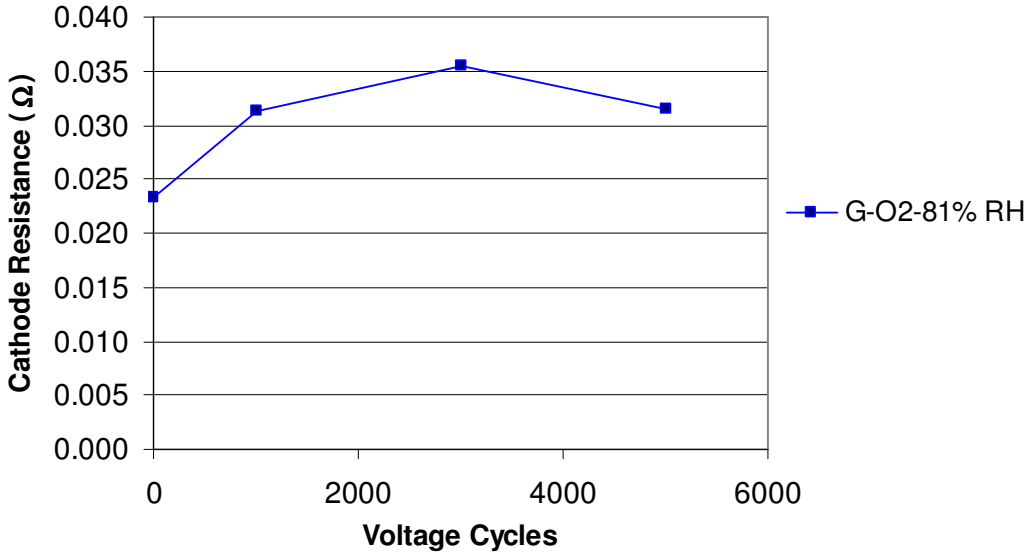

Figure 5.18: Change in Cathode resistance with the increase of number of voltage cycles

5.5.2.2 Fuel Cell G1-90% RH

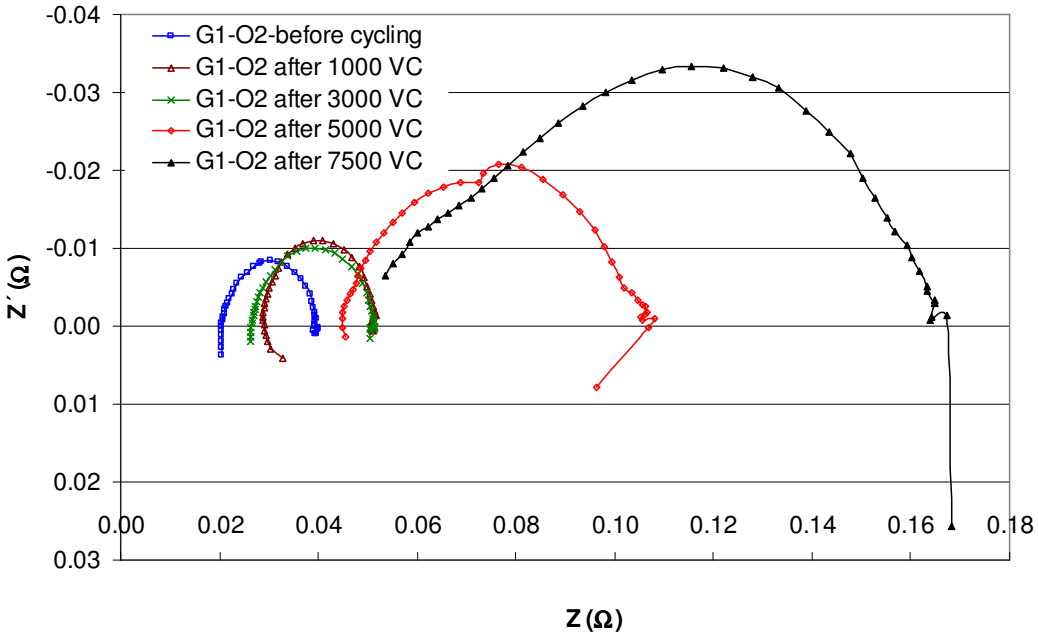

Figure 5.19: Comparison of all Nyquist plots for the fuel cell G_1

Fuel Cell G_1 was tested at 90% relative humidity.

Table 5.18 shows the detail of increase in membrane resistance and cathode resistance during the whole set of experiment. It is obvious from the

Table 5.18 that at the end of potential cycling test the membrane resistance became almost double of its initial value whereas the increase in cathode resistance is more than five times than that of its initial value. Figure 5.20 exhibits this exponential increase in the cathode resistance.

Table 5.18: Resistances of the fuel cell G_1

Voltage Cycles Completed	Membrane Resistance (a) (Ω)	Total Resistance (b) (Ω)	Cathode Resistance (b-a) (Ω)
0	0.021	0.039	0.019
1000	0.029	0.051	0.022
3000	0.026	0.051	0.024
5000	0.045	0.107	0.062
7500	0.054	0.164	0.111

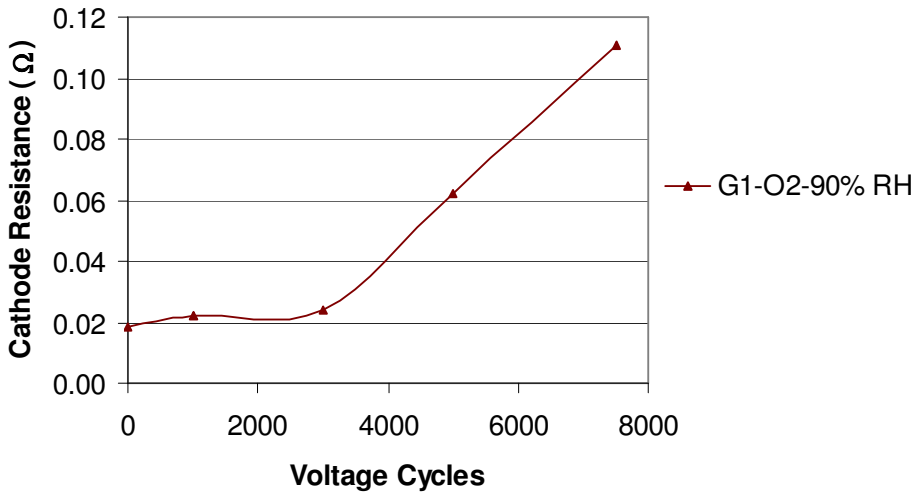

Figure 5.20: Increase in cathode resistance for the fuel cell G_1 as a function of number of voltage cycles.

5.5.2.3 Fuel Cell G2-70% RH

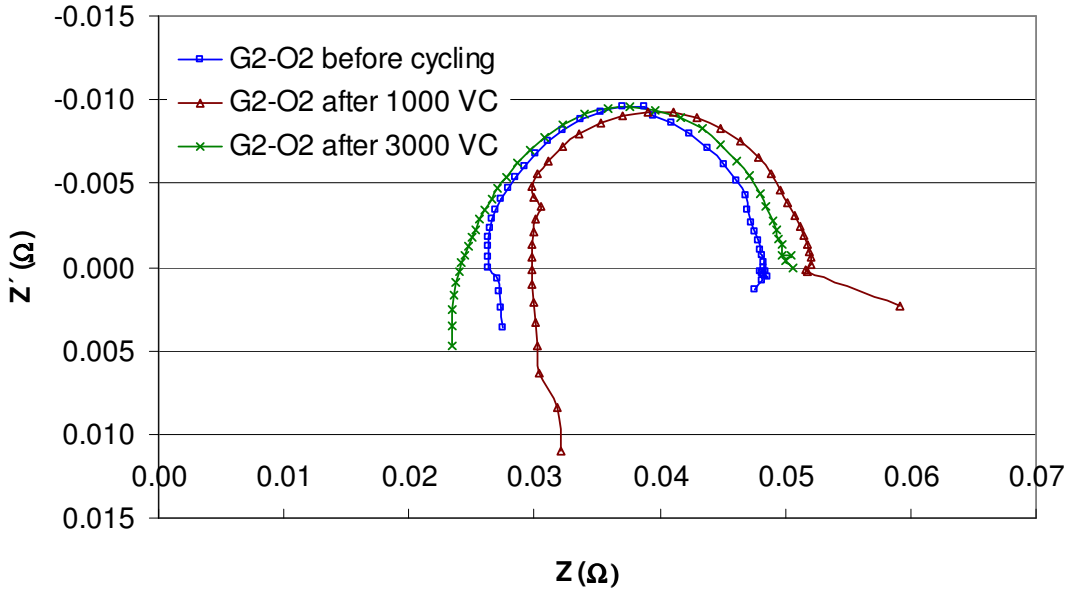

Figure 5.21: Comparison of all Nyquist Plots for the fuel cell G_2

Fuel cell G_2 was investigated at 70% RH. Table 5.19 shows decrease in the membrane resistance and a small increase in the cathode resistance with the progress in potential cycles. Figure 5.22 shows this enhancement in the cathode resistance graphically.

Table 5.19: Resistances of fuel Cell G_2

Voltage Cycles Completed	Membrane Resistance (a)(Ω)	Total resistance (b) (Ω)	Cathode Resistance (b-a) (Ω)
0	0.026	0.048	0.022
1000	0.030	0.052	0.022
3000	0.024	0.051	0.026

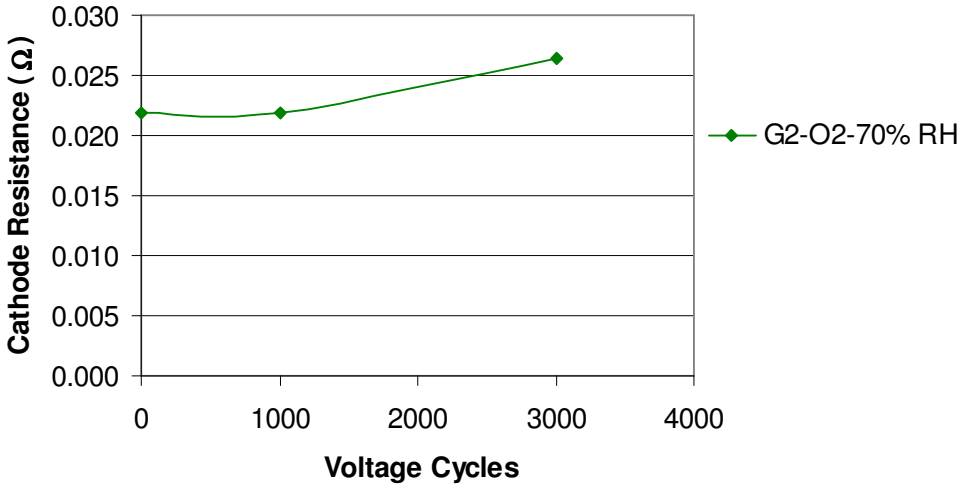

Figure 5.22: Increase in cathode resistance for the fuel cell G_2 as a function of number of voltage cycles.

5.5.2.4 Fuel Cell G_3-90% RH

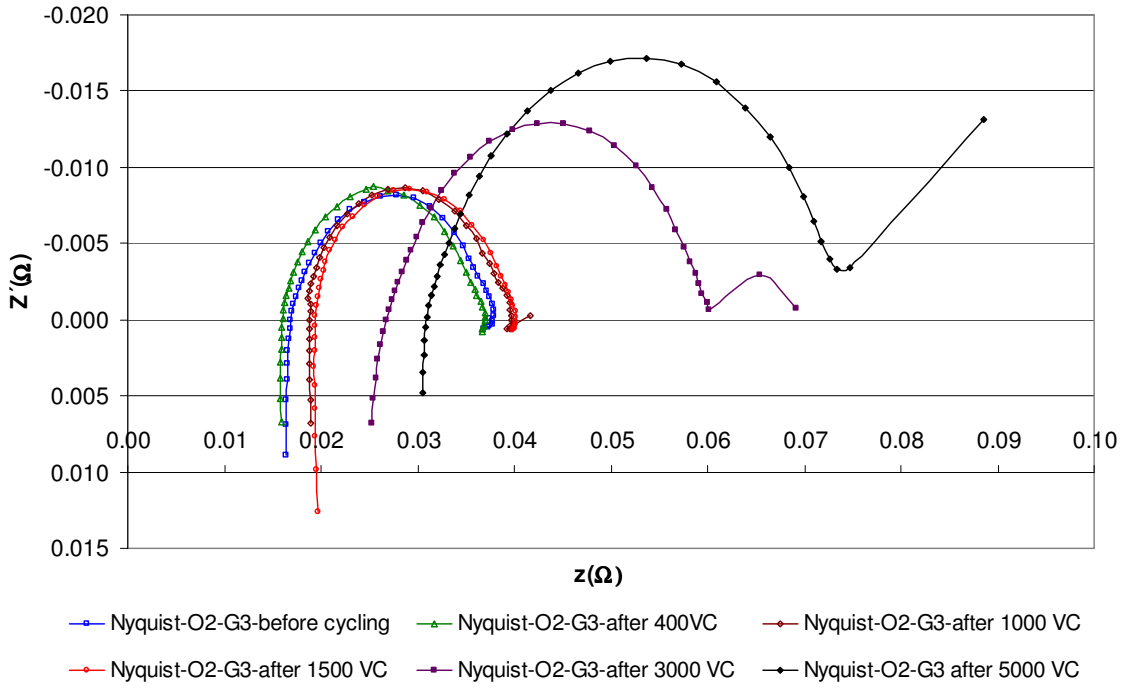

Figure 5.23: Comparison of all Nyquist Plots for the fuel cell G_3

Figure 5.23 shows all Niquist Plots when oxygen was fed to the cathode of the fuel cell G_3 operated at 90% RH. In Table 5.20 two times increase to their initial values occurs in the membrane resistance as well as the cathode resistance after 5,000 voltage cycles.

Table 5.20: Resistances of Fuel Cell G_3

Voltage Cycles completed	Membrane Resistance (a) (Ω)	Total Resistance (b) (Ω)	Cathode Resistance (b-a) (Ω)
0	0.017	0.037	0.0205
400	0.016	0.037	0.0208
1000	0.019	0.040	0.0208
1500	0.019	0.040	0.0208
3000	0.027	0.060	0.0333
5000	0.031	0.073	0.0423

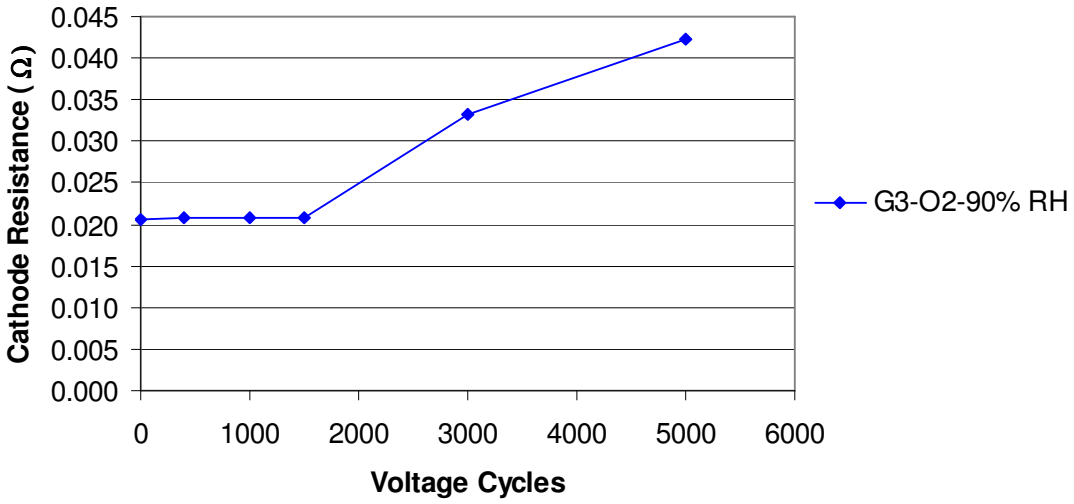

Figure 5.24: Increase in Cathode Resistance of the fuel cell G_3 (Oxygen feed on cathode)

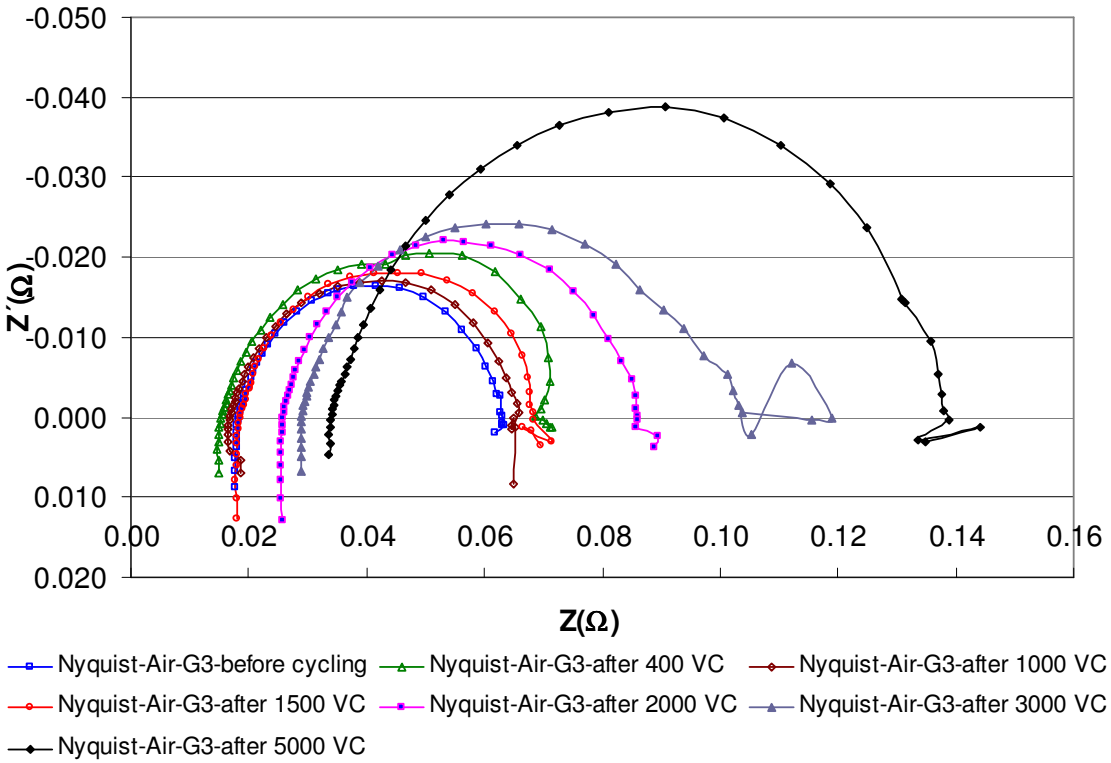

Figure 5.25: Comparison of all Nyquist Plots for the fuel cell G_3 (air supply at cathode side)

Table 5.21: Resistances of the fuel cell G_3 (air supply at cathode side)

Voltage Cycles completed	Membrane Resistance (a) (Ω)	Total Resistance (b) (Ω)	Cathode Resistance (b-a) (Ω)
0	0.018	0.063	0.045
1000	0.017	0.065	0.048
1500	0.019	0.068	0.050
2000	0.026	0.086	0.060
3000	0.029	0.105	0.076
5000	0.034	0.139	0.105

Figure 5.25 shows all Niquist plots for the fuel cell G_3, when air was supplied to the cathode side of the fuel cell. Here again the membrane resistance and the cathode resistance became almost double after 5,000 voltage cycles than their values before potential cycling experiment (

Table 5.21). Figure 5.26 illustrates the graphical representation of increase in cathode resistance with air supply at cathode side of the fuel cell G3.

Figure 5.27 elaborates the comparison in the increase in the cathode resistance with oxygen and air supply at the cathode side of the fuel cell G_3. The figure shows the increase in cathode resistance is higher, almost double, with air supply than that with the oxygen supply at the cathode side. It means that with the potential cycling test structural changes in the carbon support of the cathode occurred in such a way that it has been compressed by forming non porous structure. Due to this non porous structure the diffusion of air was difficult and the ultimate result appeared as higher resistance of the cathode.

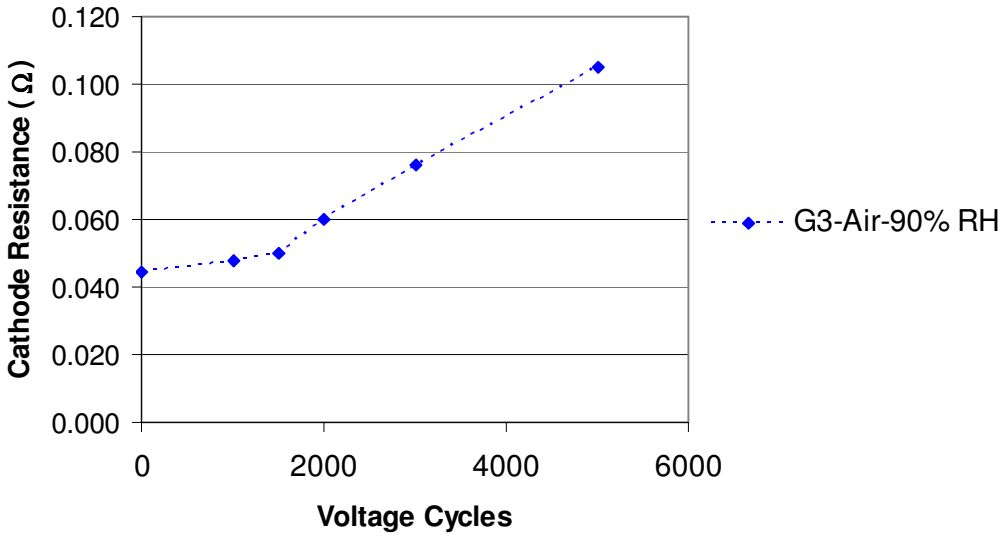

Figure 5.26: Increase in Cathode Resistance of the fuel cell G_3 (Air supply on cathode side)

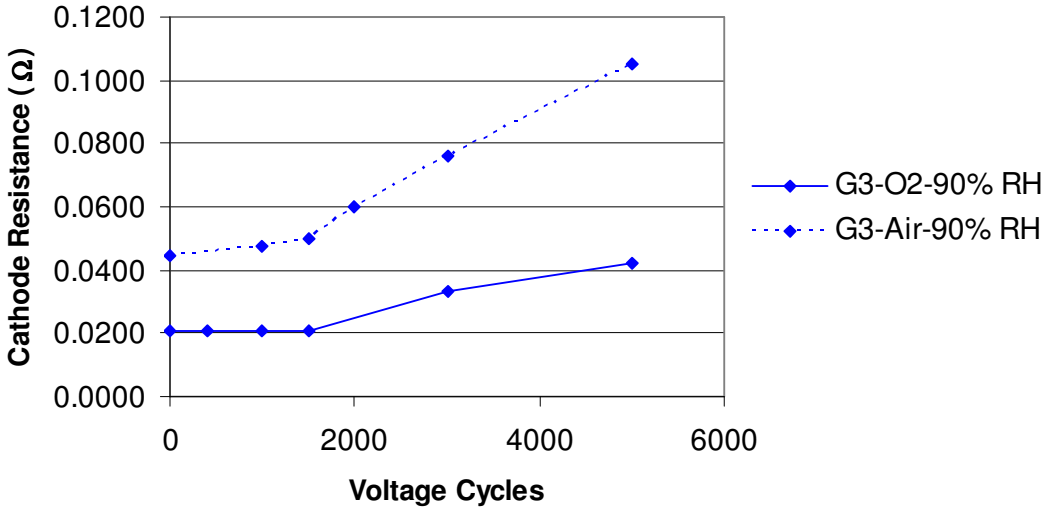

Figure 5.27: Cathode resistance verses voltage cycles for the fuel cell G_3

5.5.2.5 Fuel Cell G_4-90% RH

Fuel cell G_4 was tested at 90% RH. All Nyquist plots with oxygen supply at cathode of fuel cell G_4 are visible from Figure 5.28. After 1,500 VC, during recording the impedance spectrum, the mass flow controller of the test rig became out of order and the gases starvation affected the performance of the fuel cell. Therefore the 92% increase in the cathode resistance after 1,500 VC, as compare to its initial value, can be observed from the

Table 5.22. A prominent increase in the membrane resistance can also be exhibited from

Table 5.22. Figure 5.29 graphically represents this tremendous increase in the cathode resistance.

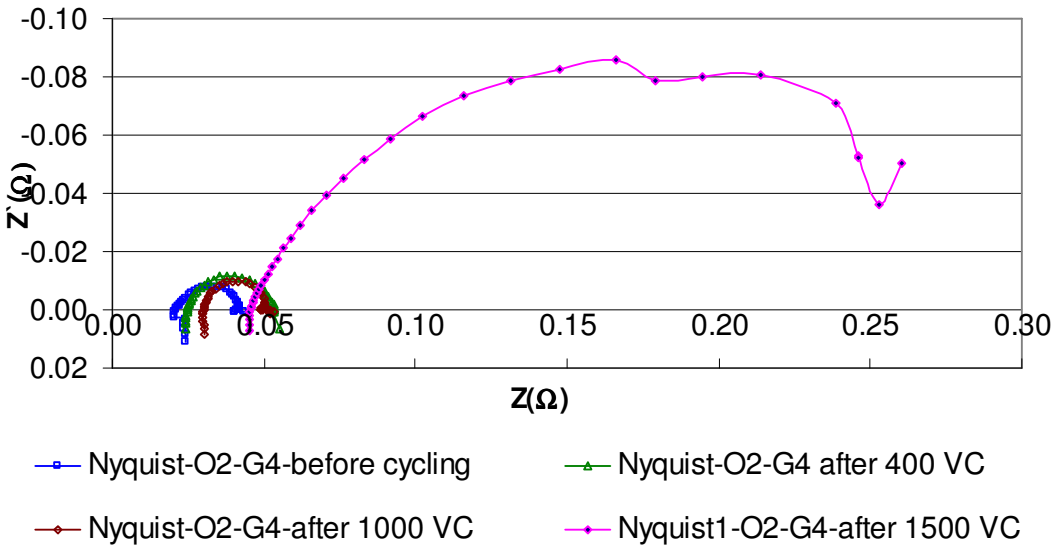

Figure 5.28: Comparison of all Nyquist Plots for the fuel cell G_4 with O_2 supply at cathode

Table 5.22: Resistances of the fuel cell G_4

Voltage Cycles Completed	Membrane Resistance (a) (Ω)	Total Resistance (b) (Ω)	Cathode Resistance (b-a) (Ω)
0	0.021	0.042	0.021
400	0.025	0.053	0.028
1000	0.030	0.052	0.021
1500	0.046	0.300	0.254

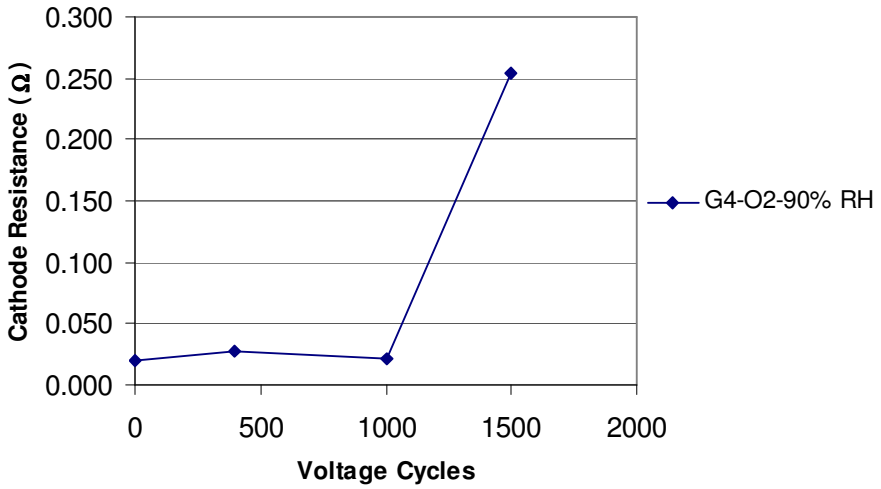

Figure 5.29: Increase in Cathode Resistance of the fuel cell G_4 (Oxygen feed on cathode)

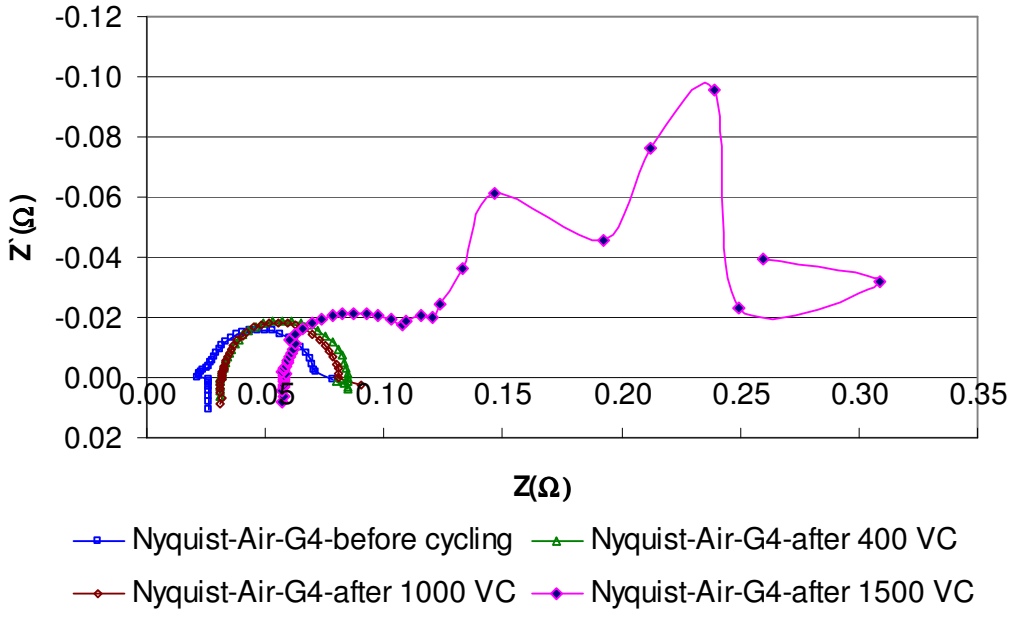

Figure 5.30: Comparison of all Nyquist Plots for the fuel cell G_4 with air supply at cathode

Table 5.23: Resistances of the fuel cell G_4 (air supply at cathode side)

Voltage Cycles	Membrane Resistance (a) (Ω)	Total Resistance (b) (Ω)	Cathode Resistance (b-a) (Ω)
0	0.022	0.078	0.056
400	0.031	0.085	0.054
1000	0.031	0.081	0.050
1500	0.058	0.120	0.062

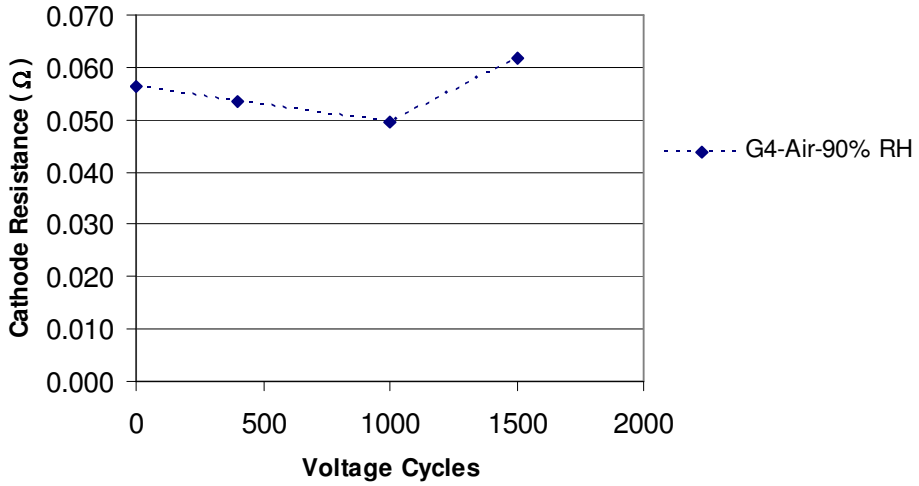

Figure 5.31: Increase in Cathode Resistance of the fuel cell G_4 (Air supply on cathode)

All the Nyquist plots with air supply at the cathode of fuel cell G_4 can be seen from Figure 5.30 and Table 5.23 shows the resistances of this fuel cell during the operation. Since the cell already became damaged, so the impedance spectrum after 1,500 VC also shows the mass transportation limitation effect. Figure 5.31 shows the graphical representation of the increase in cathode resistance of fuel cell G_4, when cathode was fed by air.

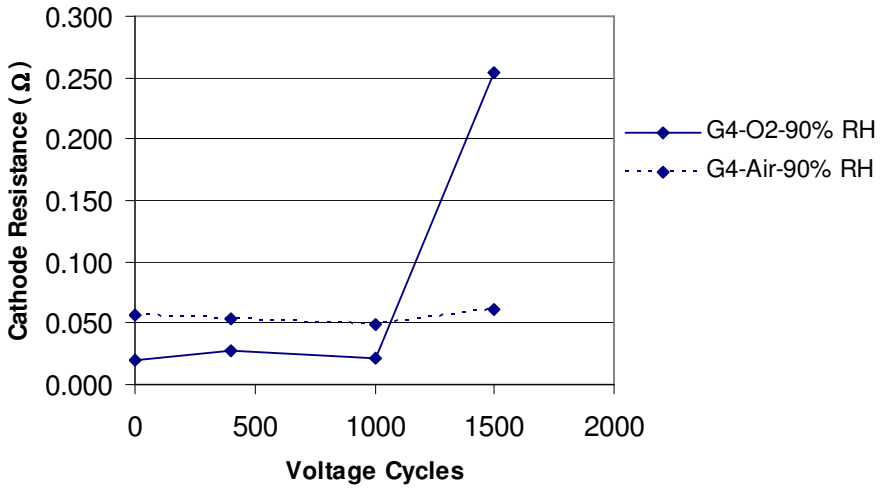

Figure 5.32: Cathode resistance verses voltage cycles for the fuel cell G_4

Figure 5.32 illustrates the comparison of the change in cathode resistance with oxygen and air feed.

5.5.2.6 Fuel Cell G_5-90% RH

Fuel Cell G_5 was operated at 90% RH. Electrochemical impedance spectra for this fuel cell were also collected with oxygen feed as well as with air feed on cathode of the cell G_5. Figure 5.33 shows Nyquist plots when oxygen was supplied to the cathode side of the fuel cell. During the whole test the increase in the membrane resistance as well as the cathode resistance is almost double after 5000 voltage cycles than their original values as elaborated from the Table 5.24. Graphically Figure 5.34 shows the increase in cathode resistance.

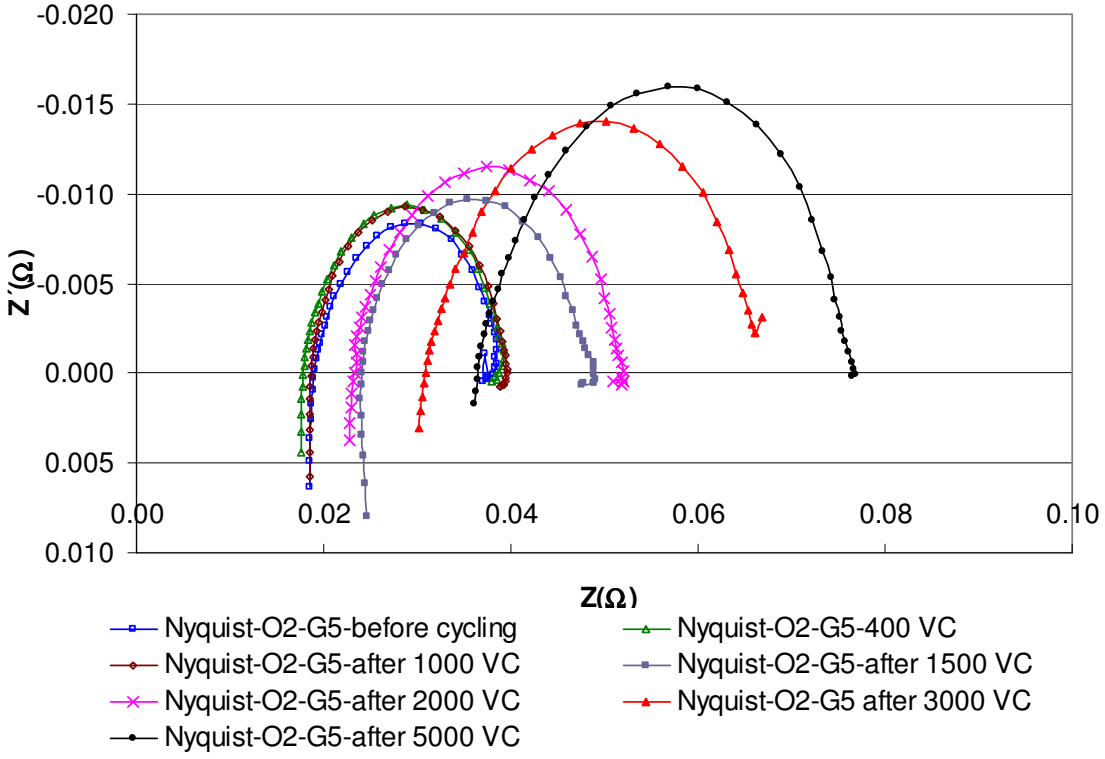

Figure 5.33: Comparison of all Nyquist Plots for the fuel cell G_5 with O_2 supply at cathode side

Table 5.24: Resistances of the fuel cell G_5

Voltage Cycles Completed	Membrane Resistance (a) (Ω)	Total Resistance (b) (Ω)	Cathode Resistance (b-a) (Ω)
0	0.019	0.038	0.0191
400	0.018	0.038	0.0206
1000	0.019	0.040	0.0209
1500	0.024	0.049	0.0248
2000	0.023	0.052	0.0285
3000	0.031	0.066	0.0352
5000	0.036	0.077	0.0405

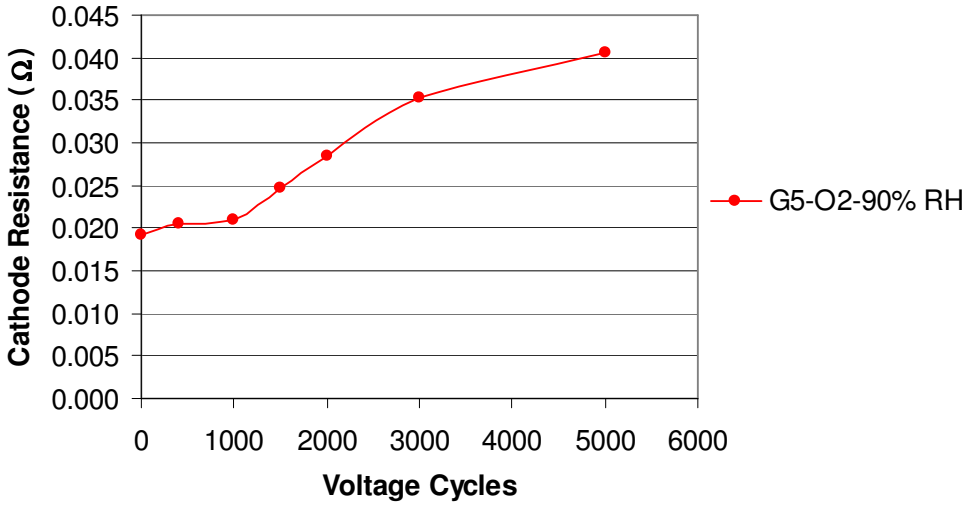

Figure 5.34: Increase in Cathode Resistance of the fuel cell G_5

Figure 5.35 exhibits all Nyquist plots when air was supplied to the cathode side of the fuel cell G_5. With the increase in the number of potential cycles, a continuous increase in the membrane resistance and cathode resistance can be seen from the Table 5.25. Membrane resistance became double whereas the cathode resistance became four times more than the original value after 5000 voltage cycles. Figure 5.36 shows the graphical representation of the enhancement in the cathode resistance with air supply as the experiment proceeds.

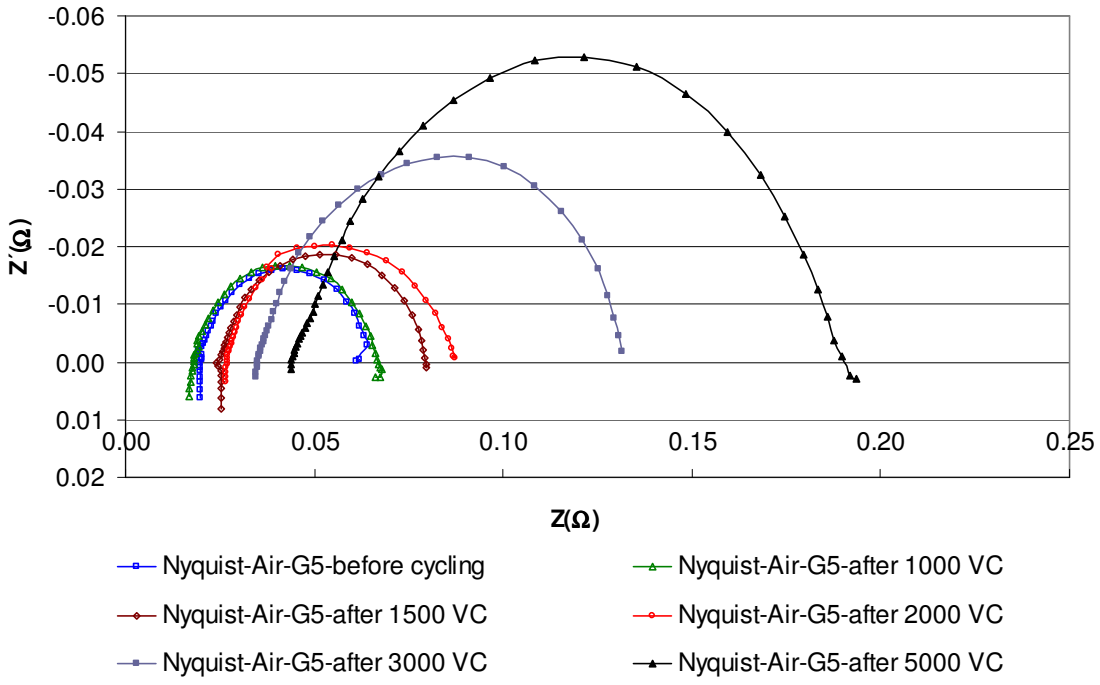

Figure 5.35: Comparison of all Nyquist Plots for the fuel cell G_5 with Air supply at cathode side.

Table 5.25: Resistances of the fuel cell G_5 (air supply at cathode side)

Voltage Cycles Completed	Membrane Resistance (a)(Ω)	Total Resistance (b) (Ω)	Cathode Resistance (b-a) (Ω)
0	0.0201	0.0613	0.0412
1000	0.0182	0.0669	0.0487
1500	0.0240	0.0796	0.0556
2000	0.0269	0.0870	0.0601
3000	0.0350	0.1320	0.0970
5000	0.0443	0.1920	0.1477

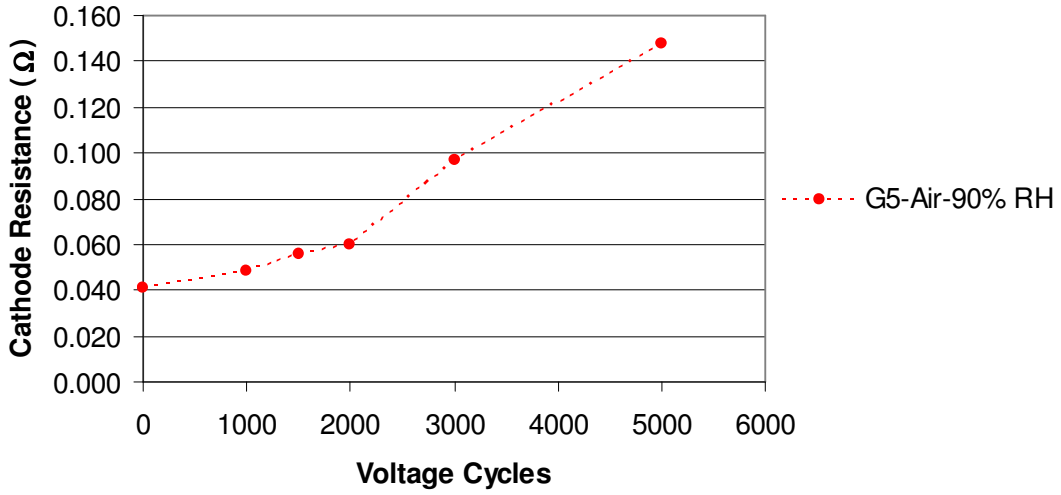

Figure 5.36: Increase in Cathode Resistance of fuel cell G5 (Air supply at cathode side)

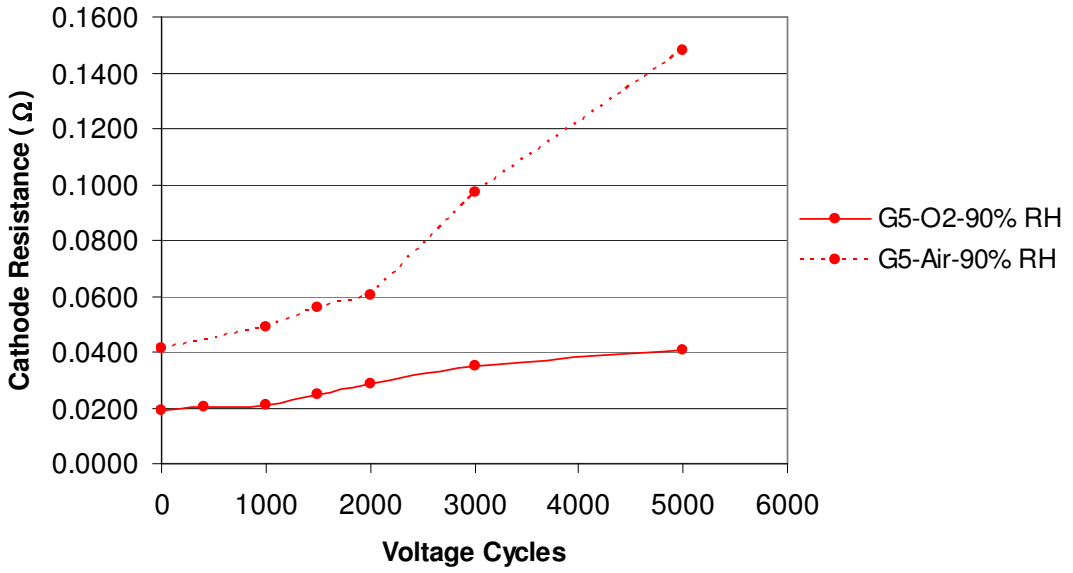

Figure 5.37: Cathode Resistance calculated from Nyquist plots with O2 and Air supply at cathode side of the fuel cell G_5

Figure 5.37 elaborates the comparison in the increase in the cathode resistance with oxygen and air supply at the cathode side of the fuel cell G_5. The figure shows that before potential cycling test the increase in cathode resistance is higher, almost double, with air supply than that with the oxygen supply and with the course of the experiment this difference has been increased. After 5,000 voltage cycles the cathode resistance with air supply is almost four times greater than its value with oxygen supply. It means that with the potential cycling test structural changes in the carbon support of the cathode occurred in such a way that it has been compressed by forming non porous structure. Due to this non porous structure the diffusion of air was difficult and the ultimate result appeared as higher resistance of the cathode.

5.5.2.7 Fuel Cell G_6-60% RH

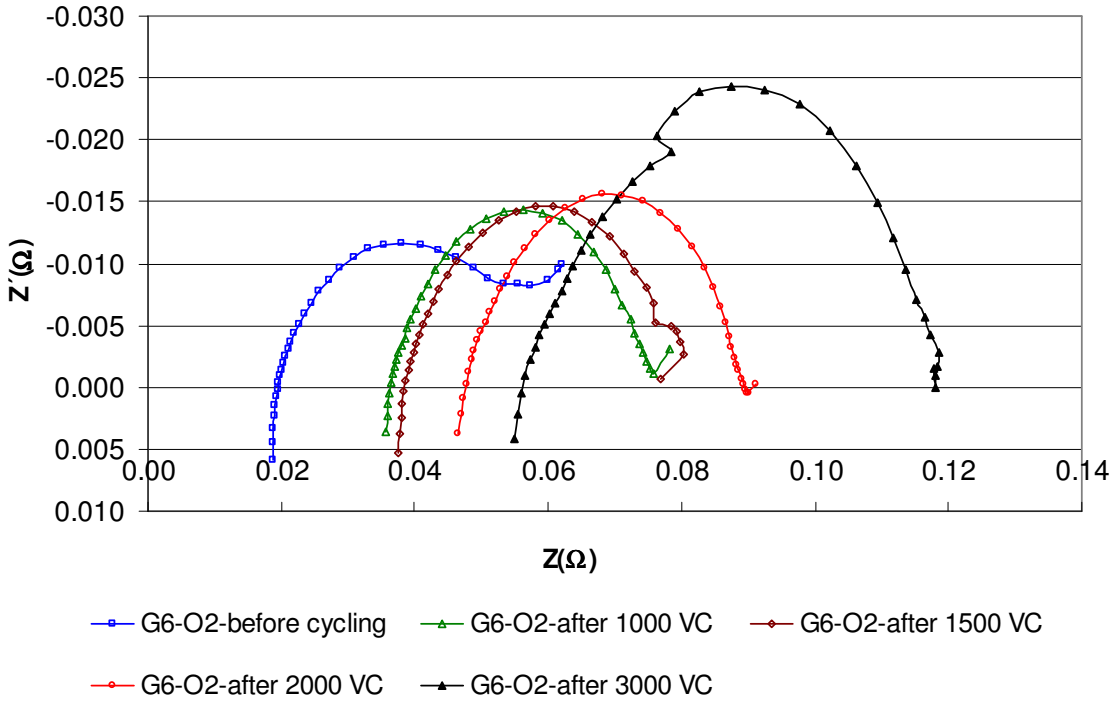

Figure 5.38: Comparison of all Nyquist Plots for the fuel cell G_6 with O_2 supply at cathode side

Table 5.26: Resistances of the fuel cell G_6

Voltage Cycles Completed	Membrane Resistance (a) (Ω)	Total Resistance (b)(Ω)	Cathode Resistance (b-a) (Ω)
0	0.019	0.053	0.034
1000	0.036	0.076	0.039
1500	0.038	0.077	0.039
2000	0.048	0.090	0.042
3000	0.056	0.118	0.062

Figure 5.38 exhibits all Nyquist plots with oxygen feed at the cathode side of the fuel cell G_6. In this case the membrane resistance became three times higher and cathode resistance became double after 3,000 voltage cycles than their values before potential cycling test (Table 5.26). Increase in cathode resistance with aoxygen supply can be shown in the Figure 5.39.

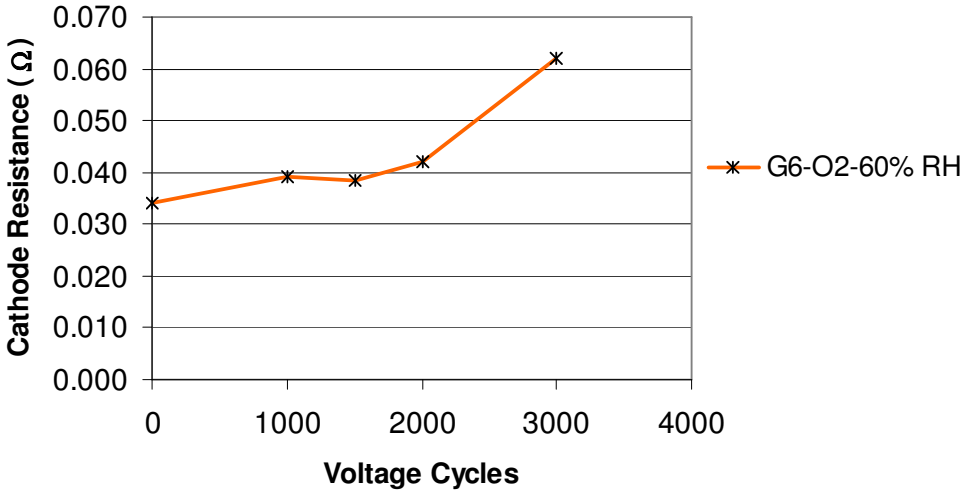

Figure 5.39: Increase in Cathode Resistance of the fuel cell G_6 (O_2 supply at cathode side)

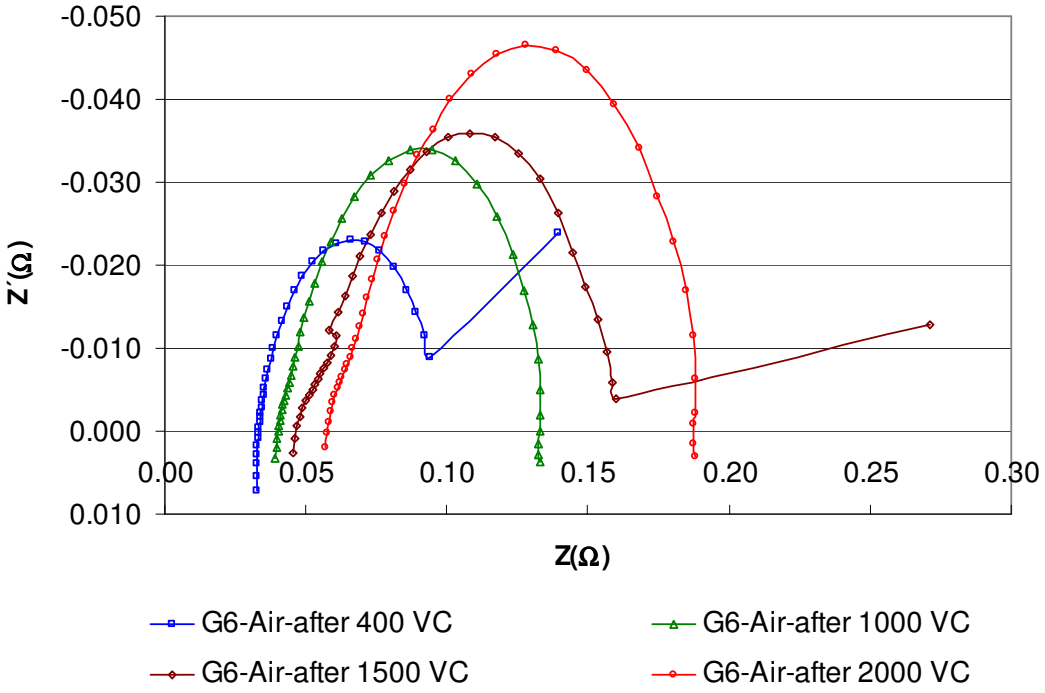

Figure 5.40: Comparison of all Nyquist Plots for the fuel cell G_6 with Air supply at cathode side.

Table 5.27: Resistances of the fuel cell G_6 (air supply at cathode side)

Voltage Cycles Completed	Membrane Resistance (a) (Ω)	Total Resistance (b) (Ω)	Cathode Resistance (b-a) (Ω)
400	0.033	0.094	0.061
1000	0.040	0.133	0.093
1500	0.047	0.160	0.113
2000	0.057	0.188	0.131

Figure 5.40 shows the all Nyquist plots when air was fed to the cathode side of the fuel cell G_6 and elaborates the detail of resistances as the potential cycling test was proceeded. After 2,000 voltage cycles the cathode resistance became more than two times greater than its value before experiment. Figure 5.41 exhibits the graphical representation of the increase in the cathode resistance with air supply.

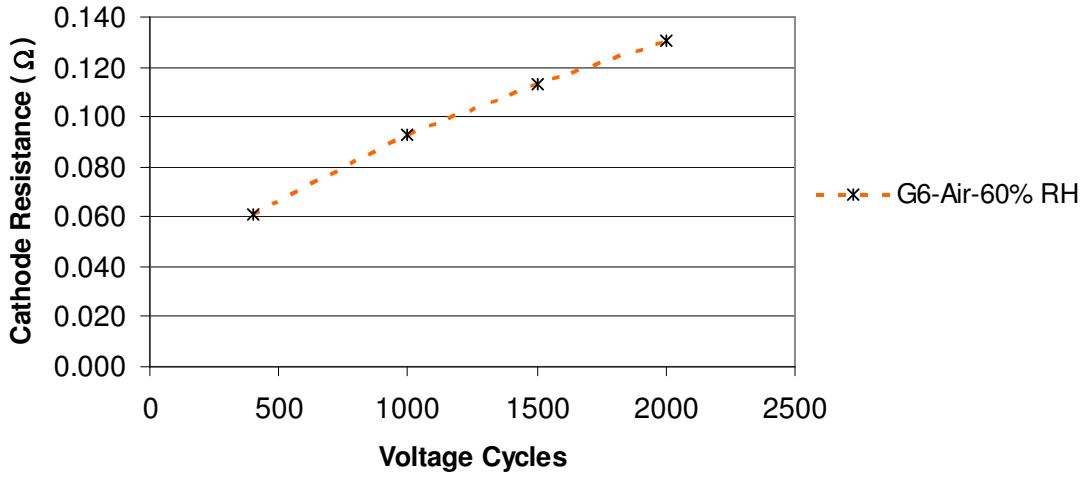

Figure 5.41: Increase in Cathode Resistance of the fuel cell G_6 (air supply at cathode side)

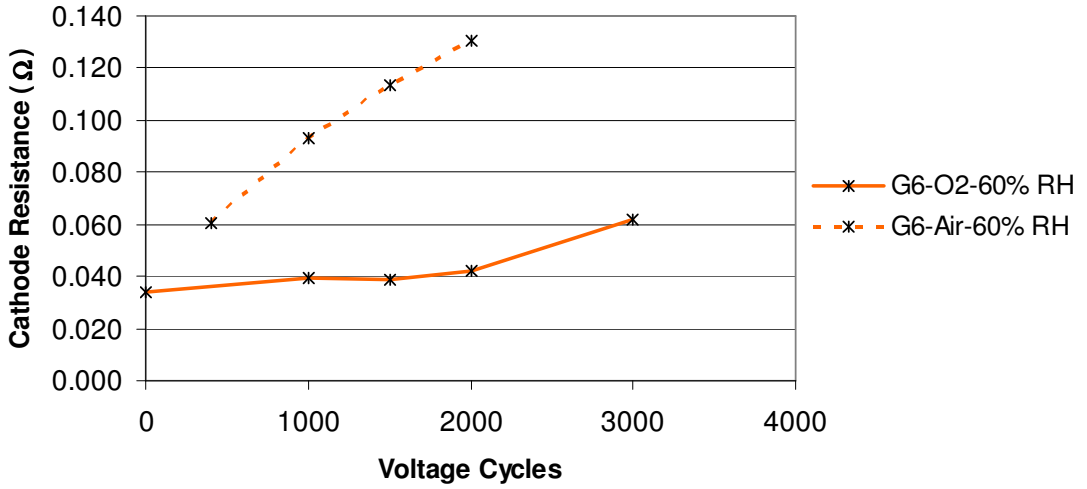

Figure 5.42: Cathode Resistance calculated from Nyquist plots with O2 and air supply at cathode of the fuel cell G_6

Figure 5.42 elaborates the comparison in the increase in the cathode resistance with both oxygen and air supply at the cathode side of the fuel cell G_6. Here again the value of cathode resistance is greater with air supply than that with oxygen supply. In the start of the experiment this difference is less but as the number of potential cycles increased, the difference became wider apart. The reason is diffusion losses due to deformation of the carbon structure, base material of the cathode.

5.5.2.8 Fuel Cell G_8-33% RH

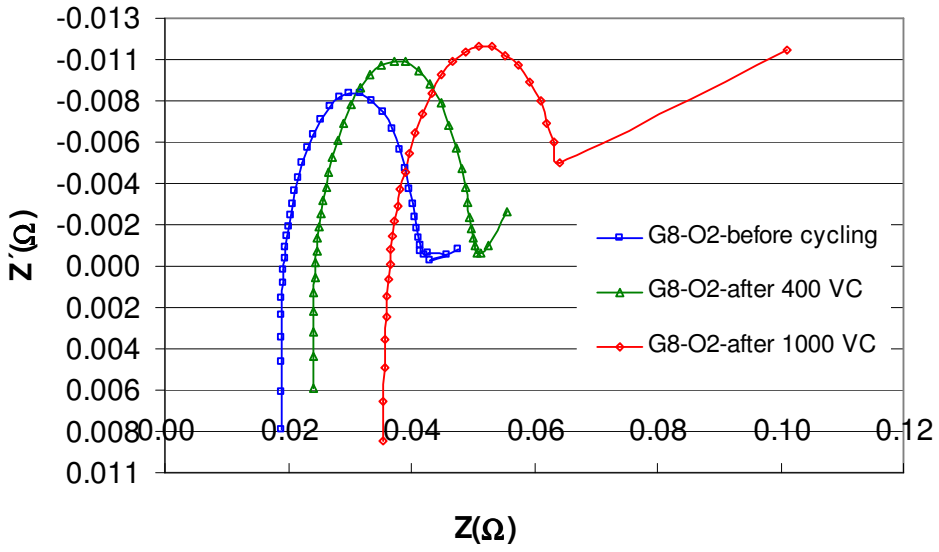

Figure 5.43: Comparison of all Nyquist Plots for the fuel cell G_8 with O_2 supply at cathode side.

Table 5.28: Resistances of the fuel cell G_8

Voltage Cycles Completed	Membrane Resistance (a) (Ω)	Total Resistance (b) (Ω)	Cathode Resistance (b-a) (Ω)
0	0.019	0.042	0.023
400	0.024	0.051	0.027
1000	0.037	0.064	0.028

Fuel cell G_8 was investigated at 33% RH. Figure 5.43 shows all Nyquist plots when oxygen was supplied to the cathode of the fuel cell. During the whole test no prominent increase in the cathode resistance can be exhibited from Table 5.28 but on the other hand the membrane resistance became double at the end of the experiment, just after 1,000 voltage cycles. This means that low value of relative humidity damages more to the membrane. Figure 5.44 shows the graphical representation of the increase in the cathode resistance with the increase in number of voltage cycles.

Figure 5.45 shows the all Nyquist plots when air was fed to the cathode side of the fuel cell G_8 and Table 5.29 elaborates the detail of the resistances of the fuel cell. Here again the increase in membrane resistance is larger than that of cathode resistance with the course of experiment.Figure 5.46 shows the graphical representation of the change in the cathode resistance with the increase in number of voltage cycles.

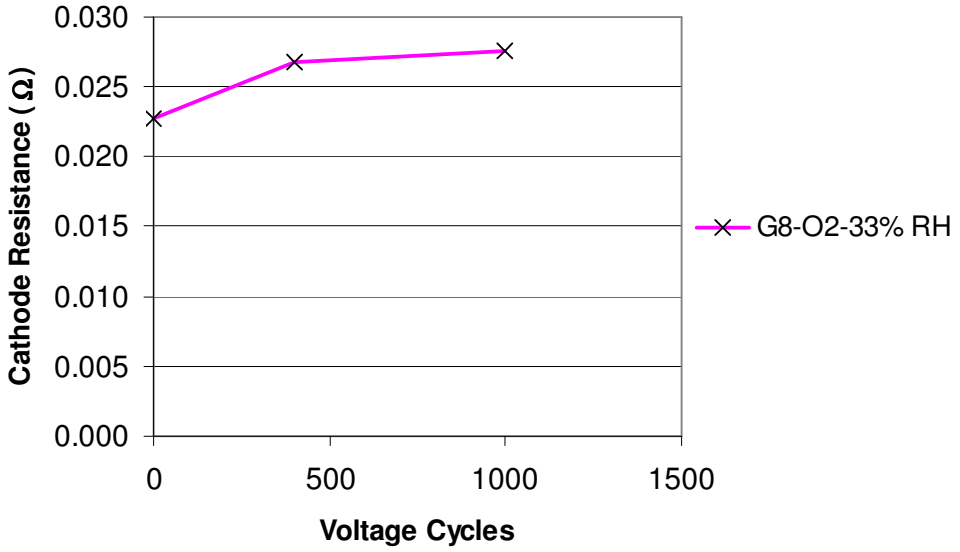

Figure 5.44: Increase in Cathode Resistance of the fuel cell G_8 (O_2 supply at cathode side)

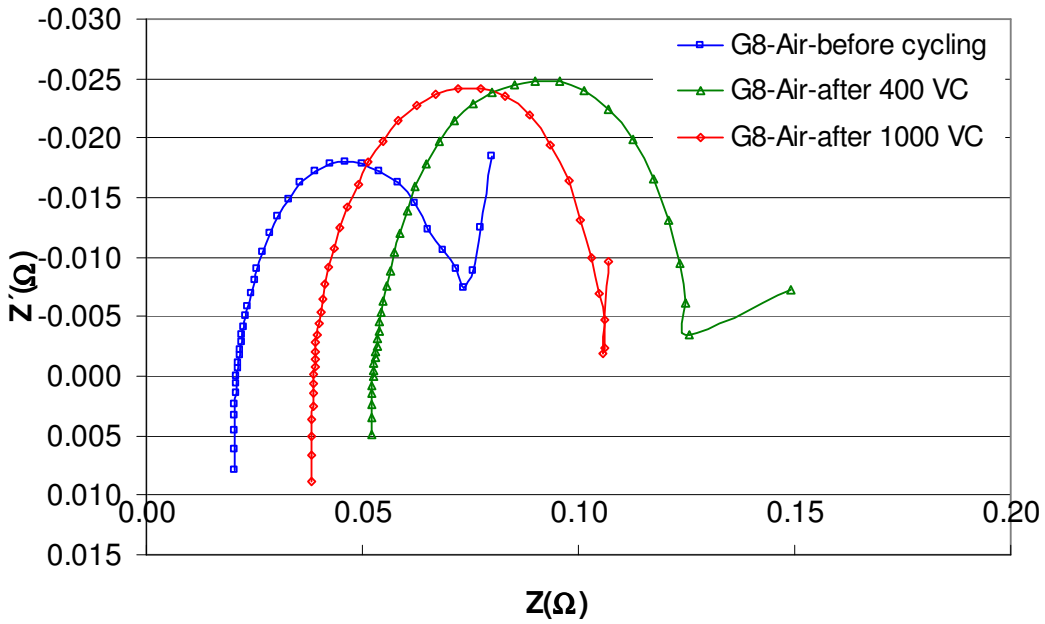

Figure 5.45: Comparison of all Nyquist Plots for the fuel cell G_8 with air supply at cathode side

Table 5.29: Resistances of the fuel cell G_8 (air supply at cathode side)

Voltage Cycles Completed	Membrane Resistance (a) (Ω)	Total Resistance (b) (Ω)	Cathode Resistance (b-a) (Ω)
0	0.021	0.073	0.052
400	0.053	0.126	0.073
1000	0.039	0.106	0.067

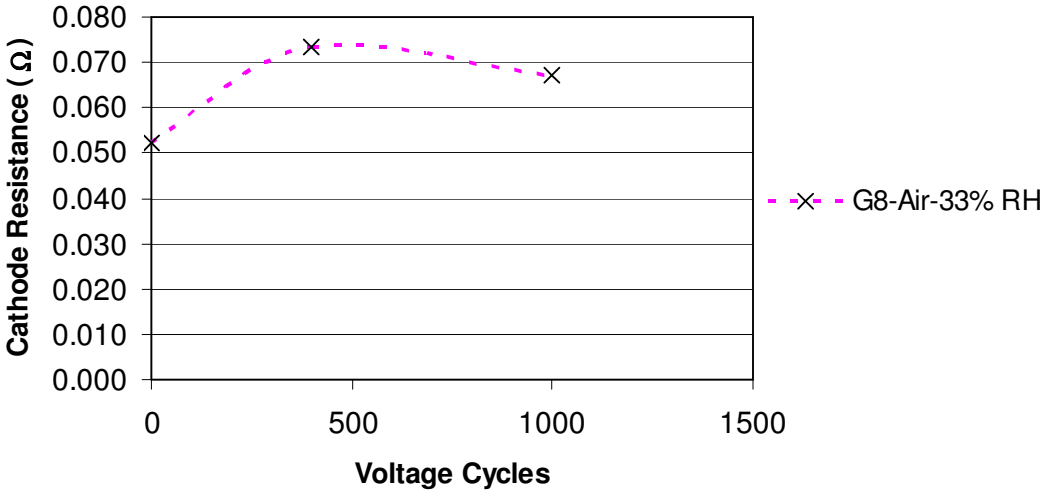

Figure 5.46: Increase in Cathode Resistance of the fuel cell G_8 (Air supply at cathode side)

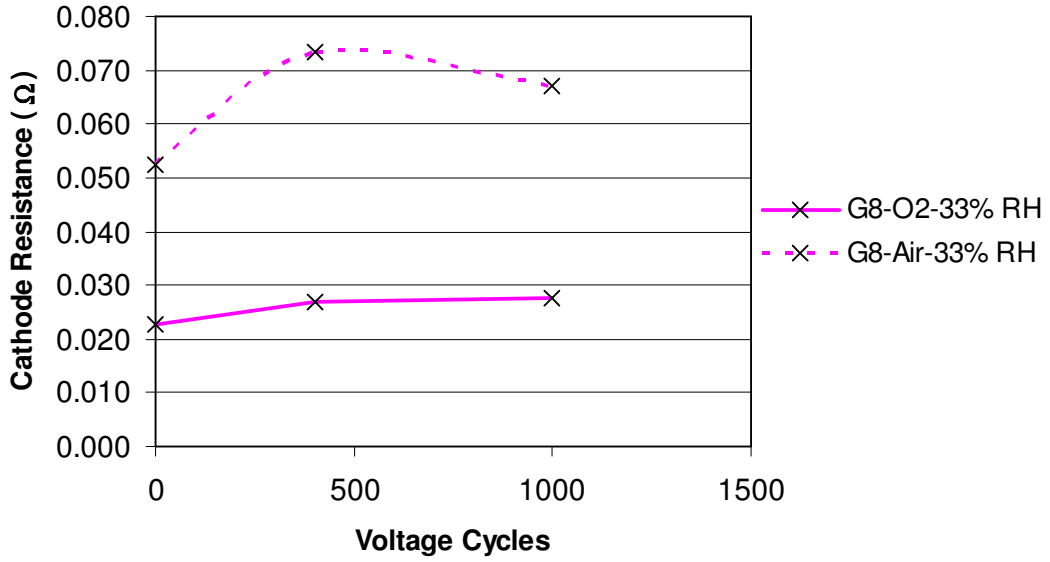

Figure 5.47: Cathode Resistance calculated from Nyquist plots with O2 and Air supply at cathode side of the fuel cell G_8

Figure 5.47 elaborates the comparison of the change in the cathode resistance with both oxygen and air supply at the cathode side of the fuel cell G_8. The figure shows that before potential cycling test the value of cathode resistance is higher, more than two times, with air supply than that with the oxygen supply and with the course of the experiment this difference have been increased. So after 1,000 voltage cycles the cathode resistance with air supply is almost three times greater than its value with oxygen supply. It means that with the potential cycling test, structural changes in the carbon support of the cathode occurred in such a way that it has been compressed by forming non porous structure. Due to this non porous structure the diffusion of air was difficult and the ultimate result appeared as higher resistance of the cathode.

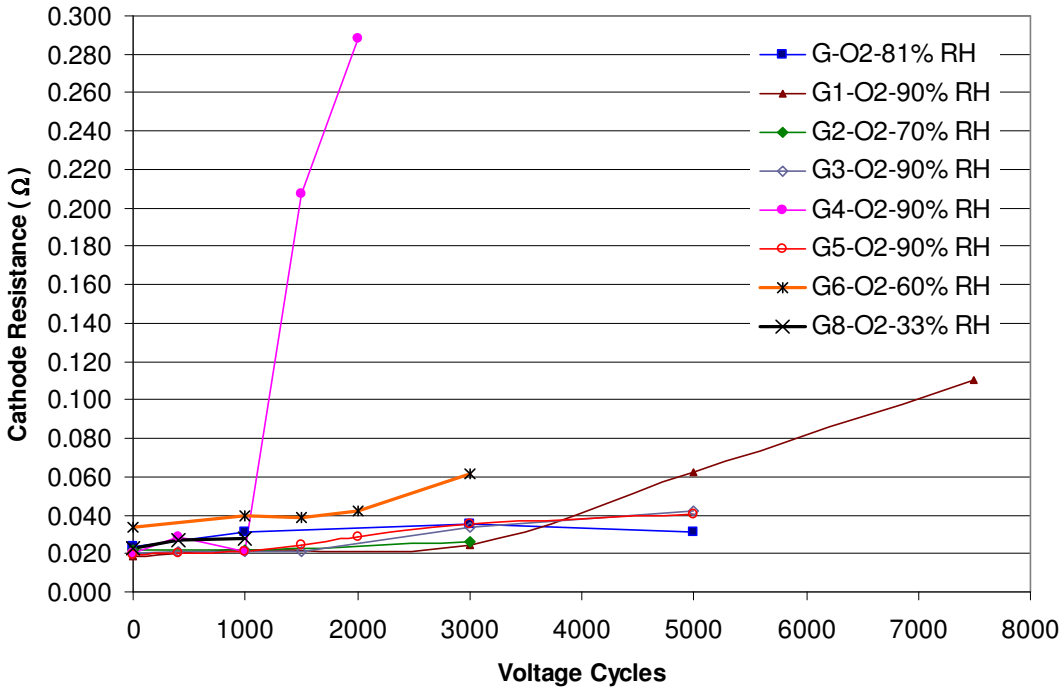

Figure 5.48: Comparison of Cathode resistance for all G type Fuel cells (O_2 supply at cathode)

It is visible from Figure 5.48 that cathode resistance of the fuel cell G_4 is highest as compare to any other fuel cell. This fuel cell suffered fuel starvation problems, which damaged it and resulted in the form of maximum cathode resistance.

5.5.3 Cyclic Voltammetry (CV)

Cyclic voltammetry measurements were performed by supplying nitrogen to the cathode side of each fuel cell to analyse the cathode. Three Cycles of each CV were recorded with 300 samples per cycle between 0.03V and 1.4V for slew rate 50mV/sec and 100mV/sec in the open circuit mode. The anode was used as the counter electrode and the cathode was used as the working electrode. The active platinum surface area was calculated by using the equation **Error! Reference source not found.**.

5.5.3.1 Mean Active Pt Surface Area

The mean active Pt surface areas for the fuel cells with G-type MEA were calculated in the same way as has been explained in chapter 4.The mean active Pt surface areas for three cycles of each measurement with scan rate of 50mV/sec were calculated. Similarly the active Pt surface areas for all three cycles of each measurement with scan rate 100mV/sec were calculated. Afterward the mean value of these two was determined. In this way the active Pt surface area for each measurement after different number of voltage cycles was calculated.

5.5.3.2 Fuel Cell G-81% RH

The value of active Pt surface area for the fuel cell G was determined before potential cycling test and after 1000, 3000 and 5000 voltage cycles as shown in Table 5.30. Figure 5.53 exhibits the decline in the active Platinum surface area with the enhancement of the number of potential cycles.

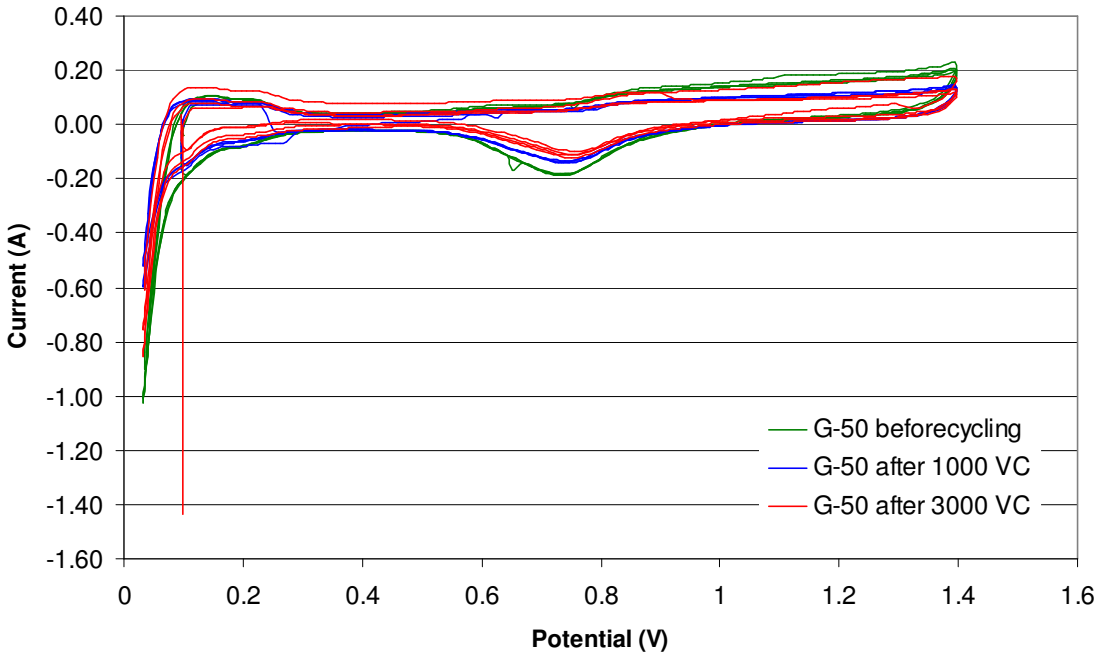

Figure 5.49: Cyclic voltammograms of fuel cell G at 50mV/sec

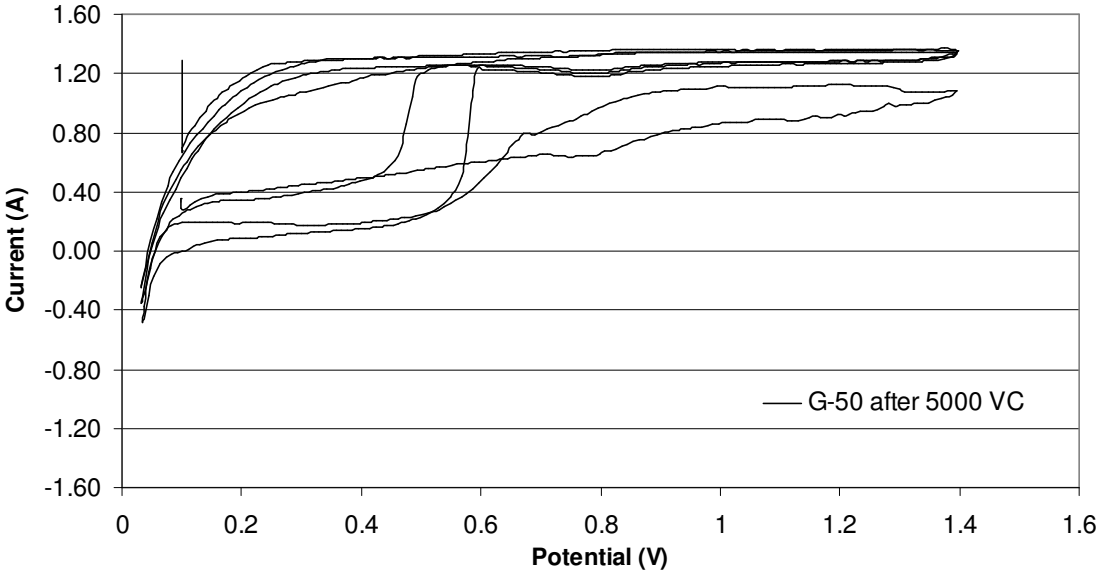

Figure 5.50: Cyclic voltammograms of fuel cell G at 50mV/sec after 5000 voltage cycles

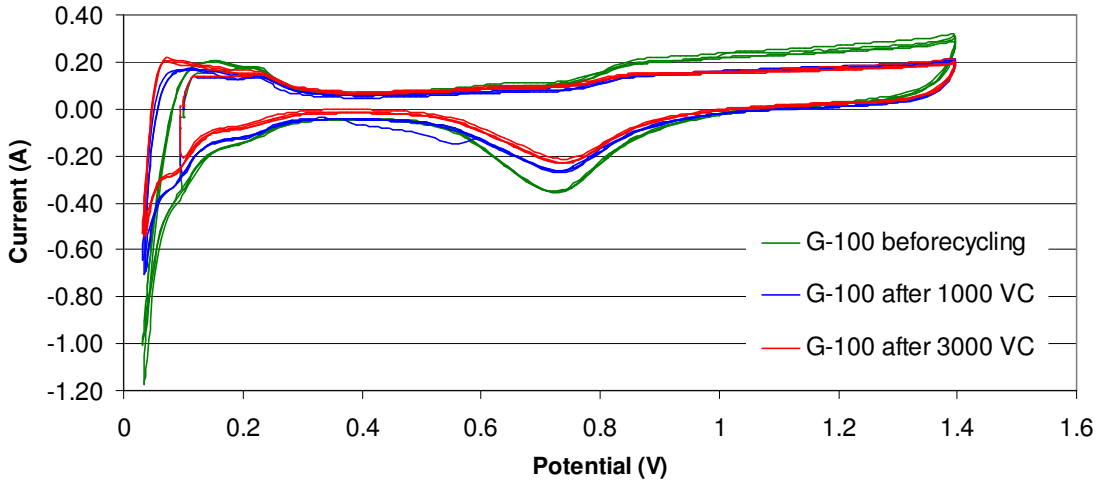

Figure 5.51: Cyclic voltammograms of fuel cell G at 100mV/sec

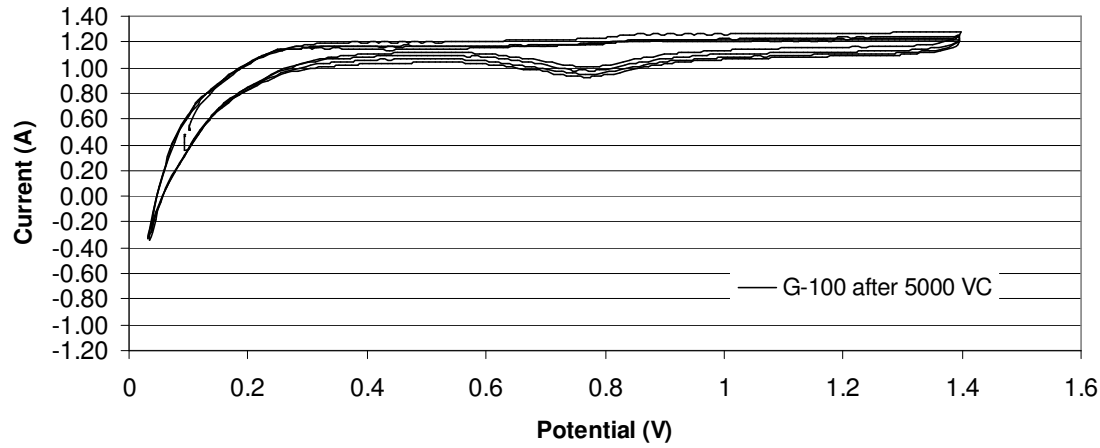

Figure 5.52: Cyclic voltammograms of fuel cell G at 100mV/sec after 5000 voltage cycles.

Table 5.30: Active Pt surface Area for the fuel cell G

Voltage Cycles completed	Mean Active Pt surface Area (m^2/g)
0	50
1000	48
3000	49
5000	7

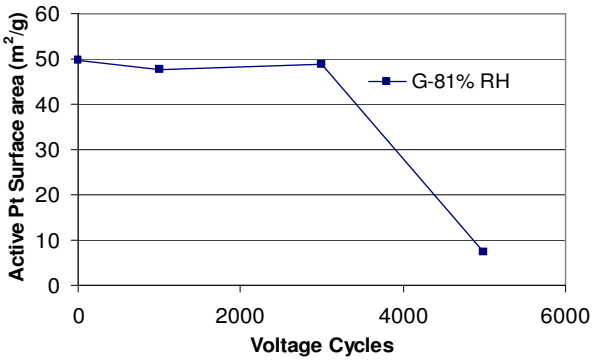

Figure 5.53: Decrease in Active pt Surface Area of fuel cell G

Till 3,000 voltage cycles the active Pt surface area almost remains the same but again when the potential cycling test was carried out for another 2,000 voltage cycles, a prominent reduction in the active Pt surface area on the cathode side of the fuel cell G can be observed from the Figure 5.53

5.5.3.3 Fuel Cell G_1-90% RH

The values of active Pt surface area after different number of voltage cycles for the fuel cell G_1 operated at 90% RH are given in the

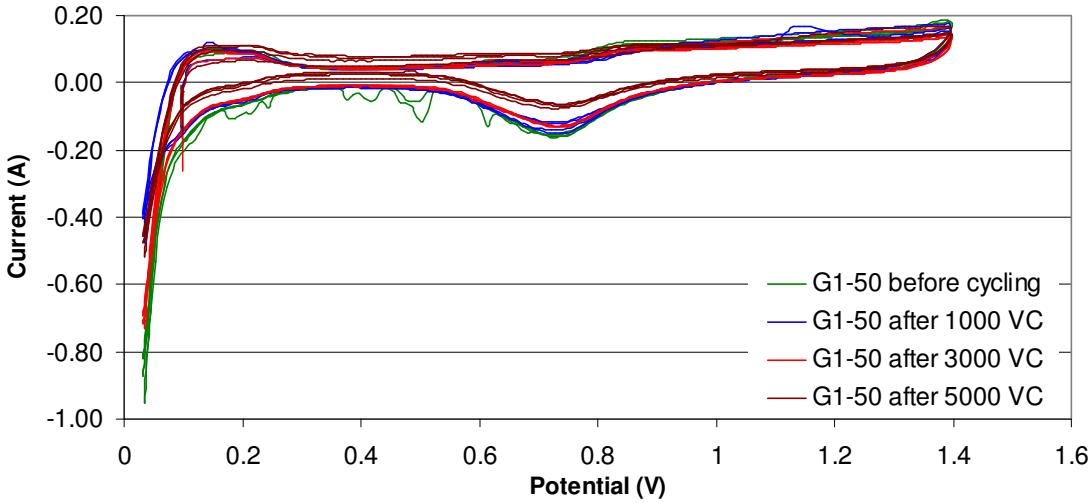

Figure 5.54: voltammograms of fuel cell G_1 at 50mV/sec

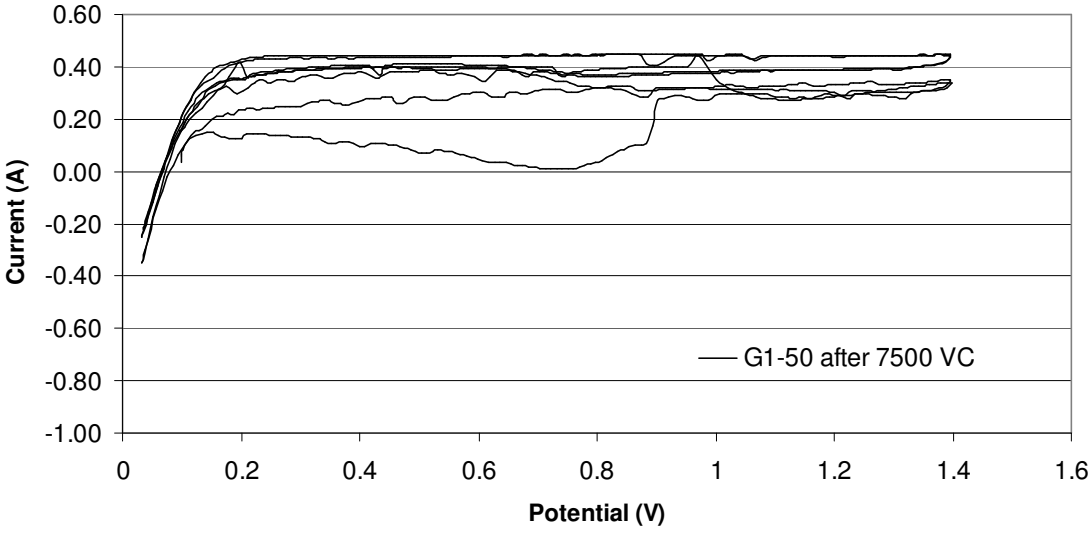

Figure 5.55: voltammograms of fuel cell G_1 at 50mV/sec after 7500 voltage cycles

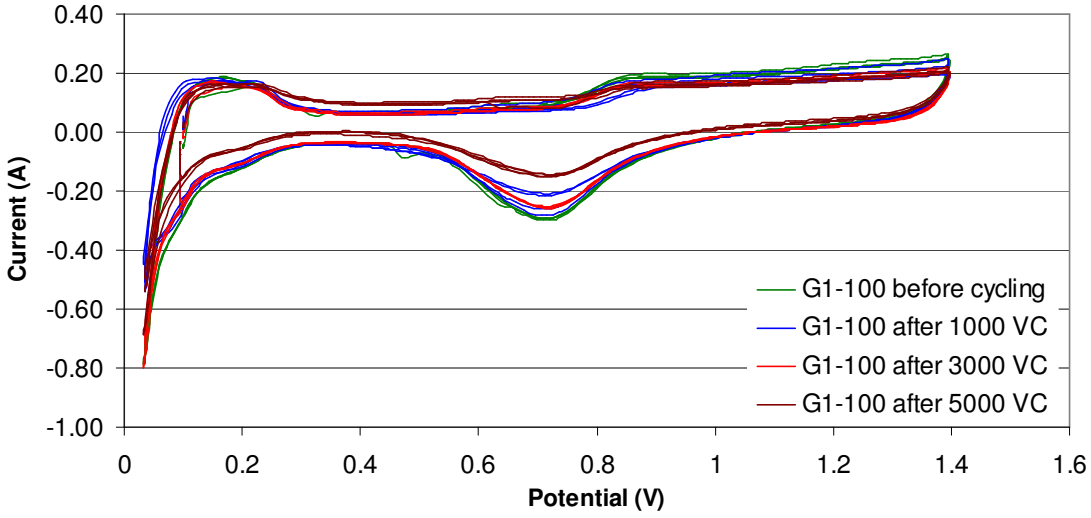

Figure 5.56: voltammograms of fuel cell G_1 at 100mV/sec

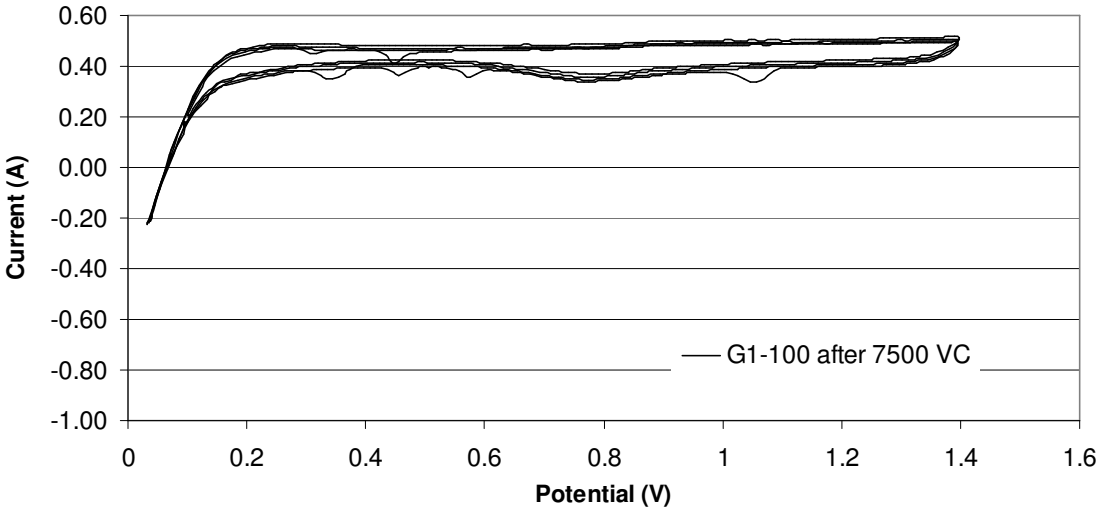

Figure 5.57: voltammograms of fuel cell G_1 at 100mV/sec after 7500 voltage cycles.

Table **5.31**. Before potential cycling experiment its value is a little less but after 1000 voltage cycles it is maximum. Later on with the proceeding of experiment active Pt surface area decreased considerably and as the fuel cell G_1 reached end of its life time after 7,500 voltage cycles. At this stage the active Pt surface area became minimum, just 1.67m^2/g.

Table 5.31: Active Pt Surface Area for the fuel cell G_1

Voltage Cycles completed	Mean Active Surface Area (m^2/g)
0	45.38
1000	47.53
3000	38.93
5000	25.13
7500	1.67

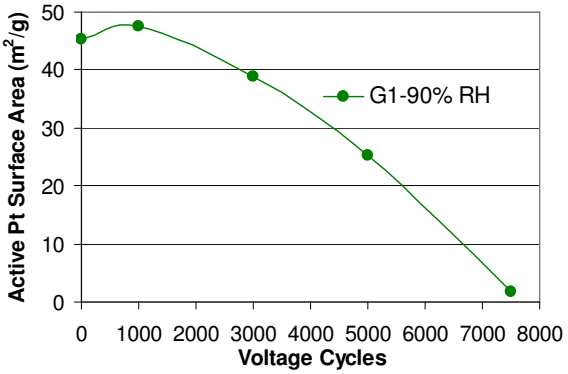

Figure 5.58: Decrease in Active pt Surface Area of fuel cell G_1

5.5.3.4 Fuel Cell G_2-70% RH

Fuel cell G_2 was investigated at 70% relative humidity. This low value of relative humidity cast a pronounced effect on active Pt surface area value. Before potential cycling experiment its value was almost $50m^2/g$ but just after 3000 voltage cycles the active Pt surface area reduced to $0.56m^2/g$. This shows that low value of relative humidity does not provide good environment for better performance of the PEM fuel cell.

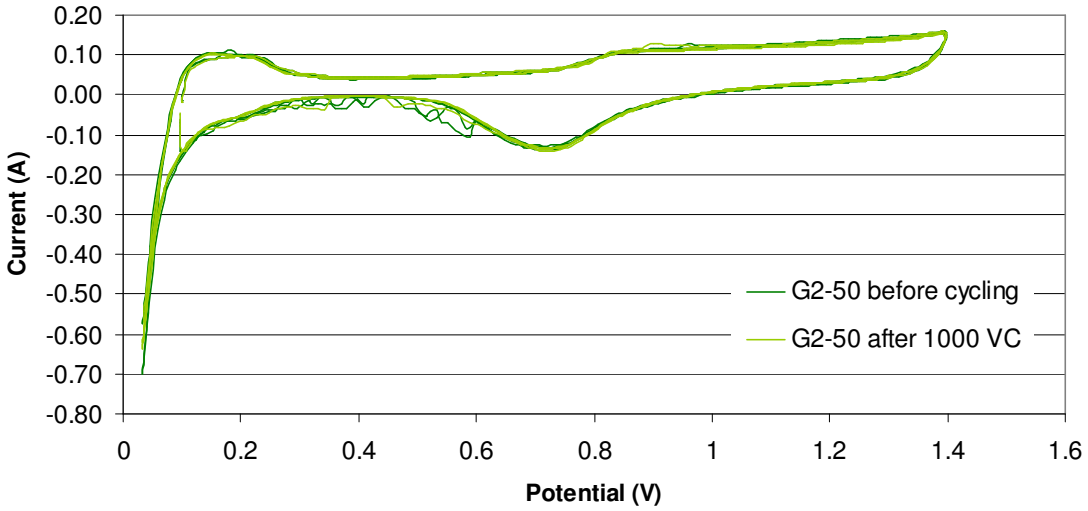

Figure 5.59: voltammograms of fuel cell G_2 at 50mV/sec

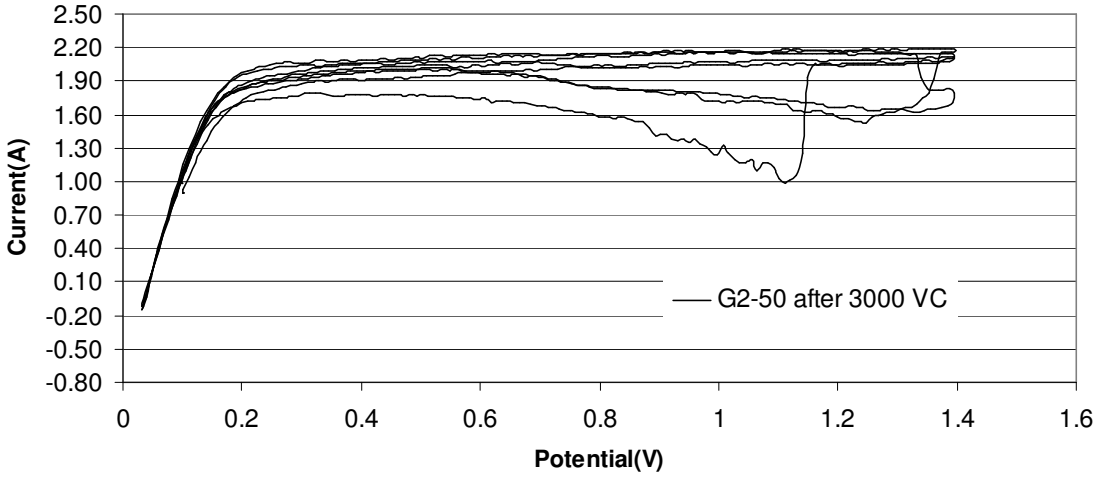

Figure 5.60: voltammograms of fuel cell G_2 at 50mV/sec after 3000 voltage cycles

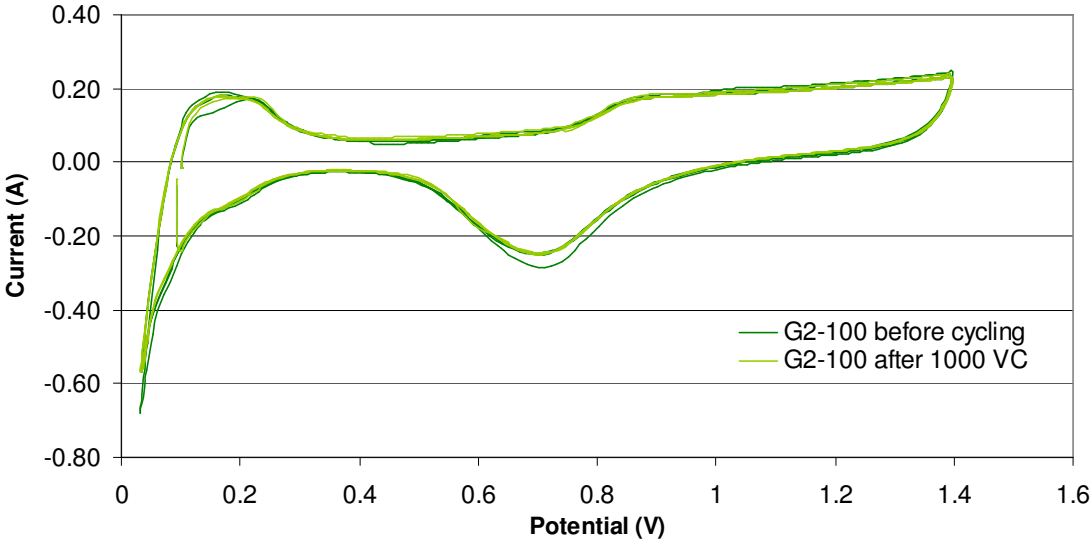

Figure 5.61: voltammograms of fuel cell G_2 at 100mV/sec

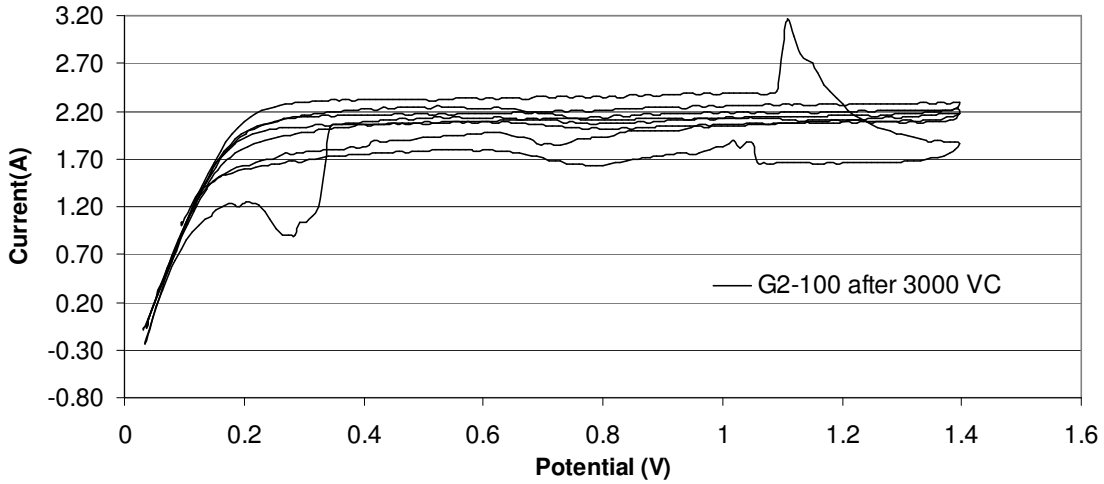

Figure 5.62: voltammograms of fuel cell G_2 at 100mV/sec after 3000 voltage cycles

Table 5.32: Active Pt Surface Area for the fuel cell G_2

Voltage Cycles Completed	Mean Active Pt Surface Area (m^2/g)
0	49.75
1000	44.65
3000	0.56

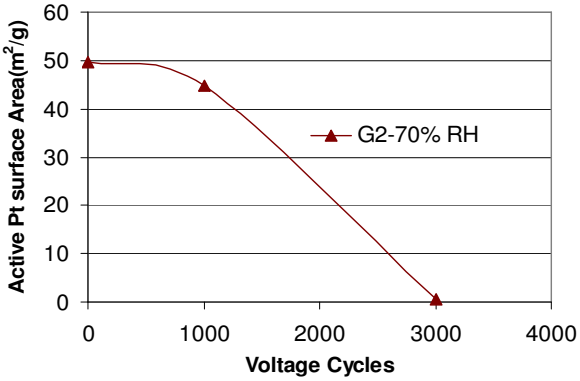

Figure 5.63: Decrease in Active pt Surface Area of fuel cell G_2

5.5.3.5 Fuel Cell G_3-90% RH

Table 5.33 shows the calculated active Pt surface area values after different number of potential cycles. A gradual reduction in the active Pt surface area can be exhibited till 5000 voltage cycles but afterward for another 2350 voltage cycles a gross decline in it is prominent from the Figure 5.68.

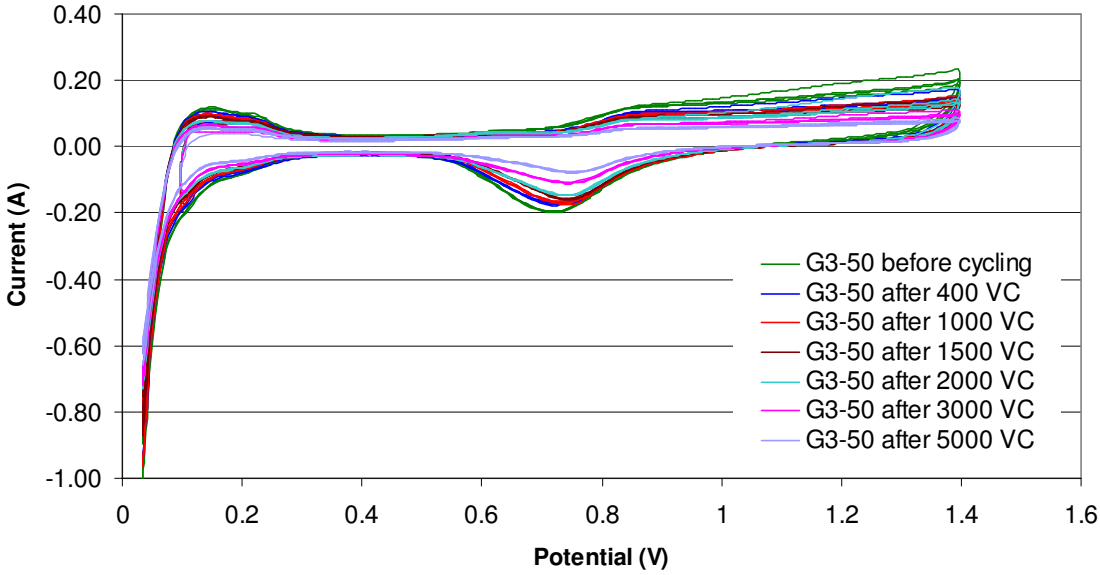

Figure 5.64: voltammograms of fuel cell G_3 at 50mV/sec

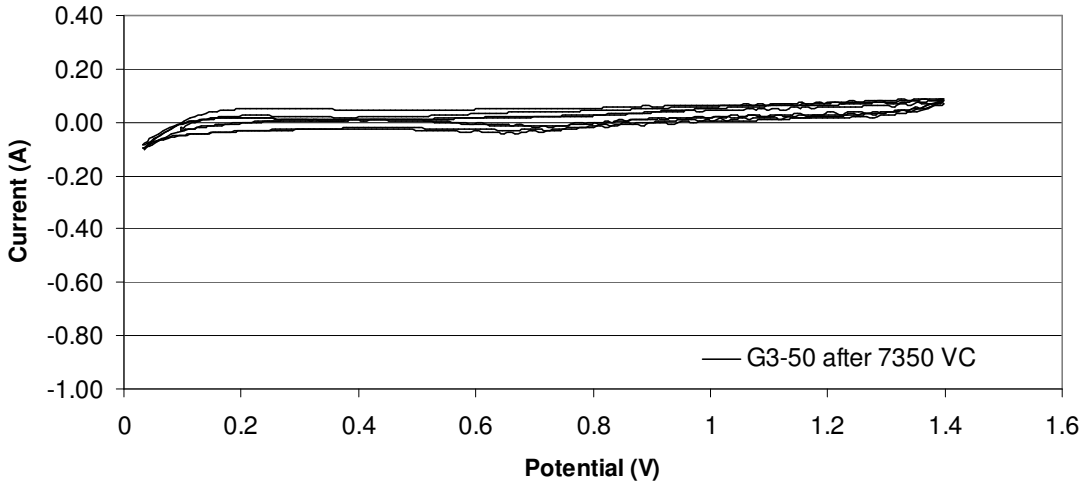

Figure 5.65: voltammograms of fuel cell G_3 at 50mV/sec after 7350 voltage cycles

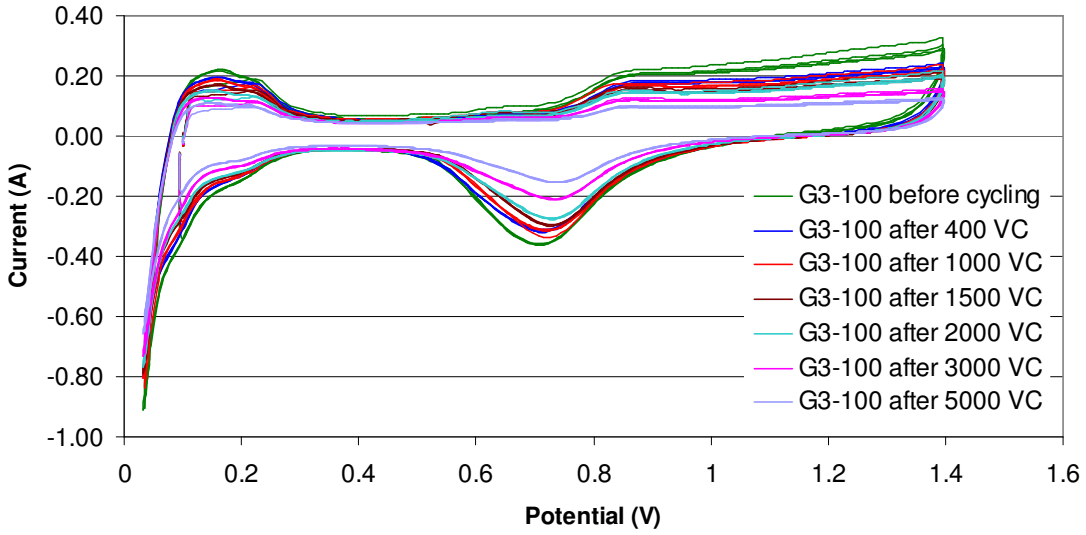

Figure 5.66: voltammograms of fuel cell G_3 at 100mV/sec

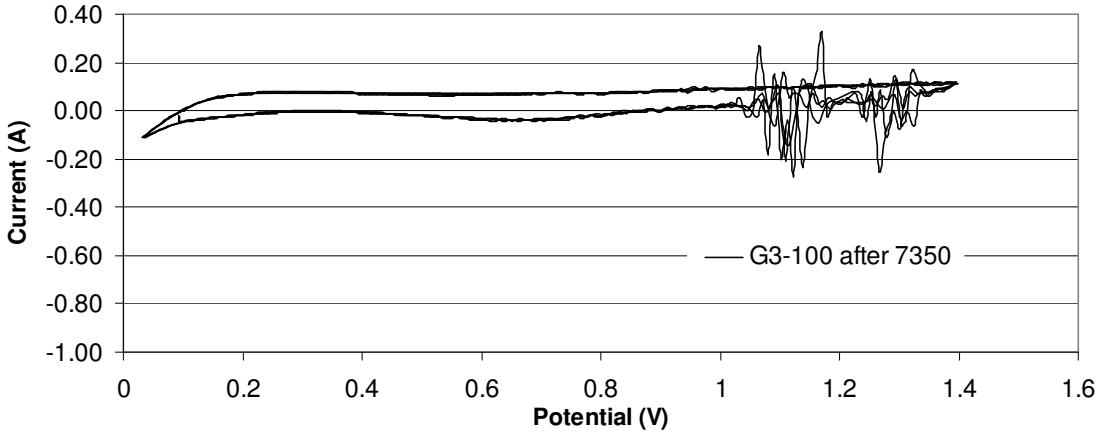

Figure 5.67: voltammograms of fuel cell G_3 at 100mV/sec after 7350 voltage cycles

Table 5.33: Active Pt Surface Area for the fuel cell G_3

Voltage Cycles completed	Active pt surface Area (m^2/g)
0	60
400	57
1000	51
1500	45
2000	38
3000	33
5000	25
7350	4

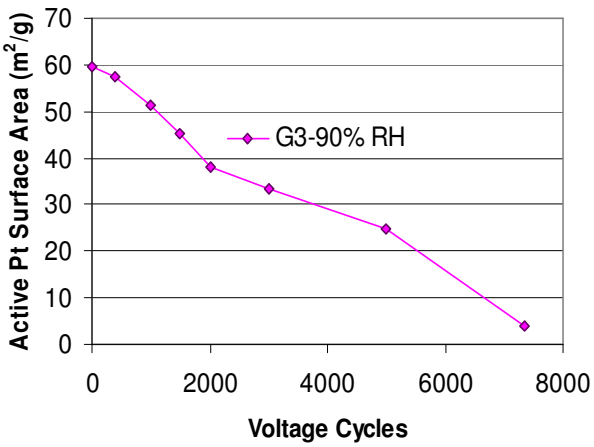

Figure 5.68: Decrease in Active pt Surface Area of fuel cell G_3

5.5.3.6 Fuel Cell G_4-90% RH

Fuel cell G_4 was also operated at 90% relative humidity but this cell arrived at the end of its life time just after 2000 voltage cycles. Before experiment the active Pt surface area at the cathode side is maximum i.e., 63.19 m^2/g among all other fuel cells operated at 90 % RH but after just 400 VC a 28% decrease in its value can be observed from the Table 5.34.

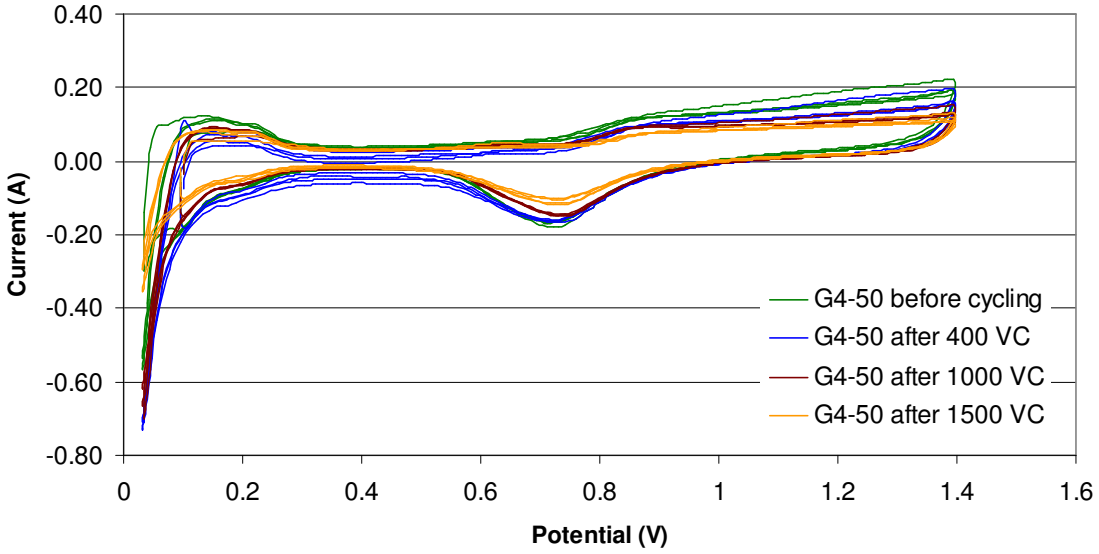

Figure 5.69: voltammograms of fuel cell G_4 at 50mV/sec

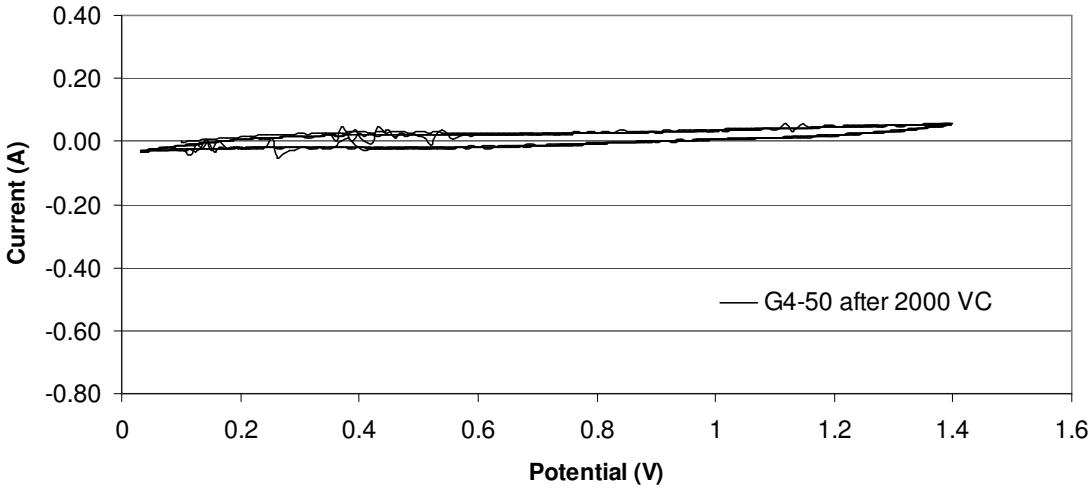

Figure 5.70: voltammograms of fuel cell G_4 at 50mV/sec after 2000 voltage cycles

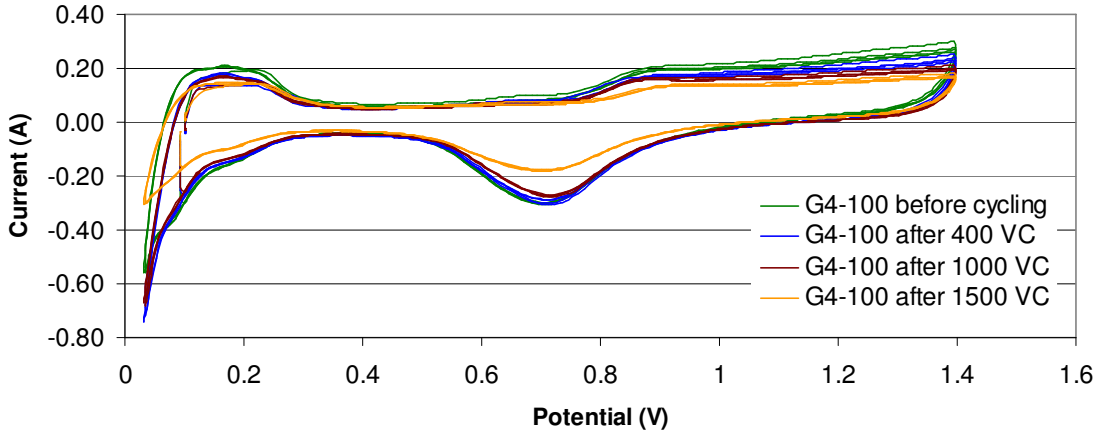

Figure 5.71: voltammograms of fuel cell G_4 at 100mV/sec

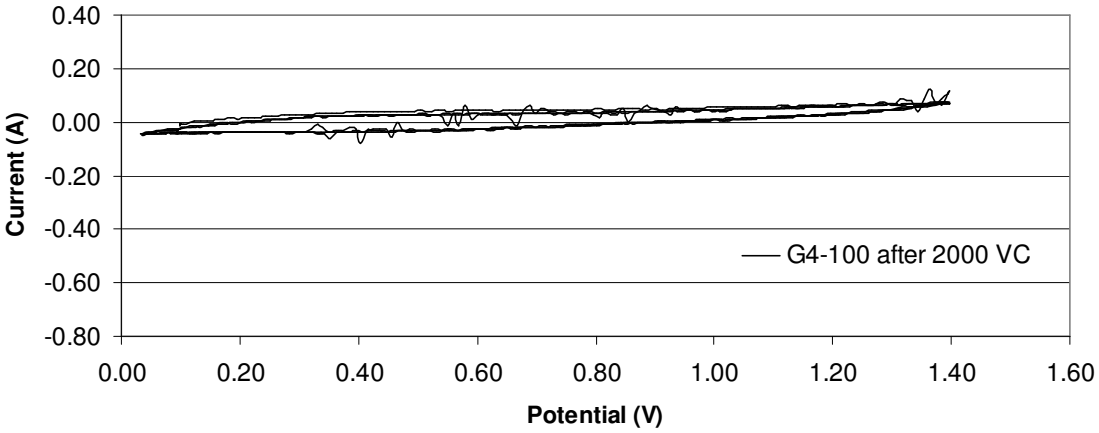

Figure 5.72: voltammograms of fuel cell G_4 at 100mV/sec after 2000 voltage cycles

Table 5.34: Active Pt Surface Area for the fuel cell G_4

Voltage Cycles Completed	Mean Active Pt Surface Area (m^2/g)
0	63.19
400	45.32
1000	44.16
1500	41.05
2000	2.15

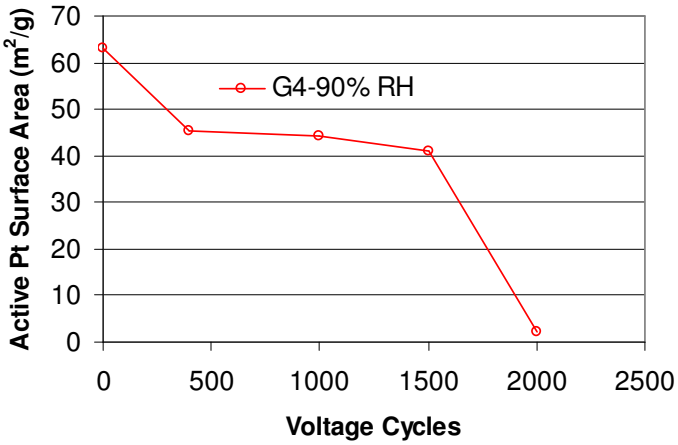

Figure 5.73: Decrease in Active pt Surface Area of fuel cell G_4

Then till 1500 voltage cycles Pt surface area decreases a little bit but afterward for another 500 voltage cycles the life duration of the cell came to end with the Pt active surface area value 2.15m^2/g.

5.5.3.7 Fuel Cell G_5-90% RH

With 90 % RH the fuel cell G_5 worked till 5960 voltage cycles. Till 1000 the active Pt surface area remained almost the same as with the fresh MEA but afterward a gradual decrease in its value can be exhibited from the Figure 5.78

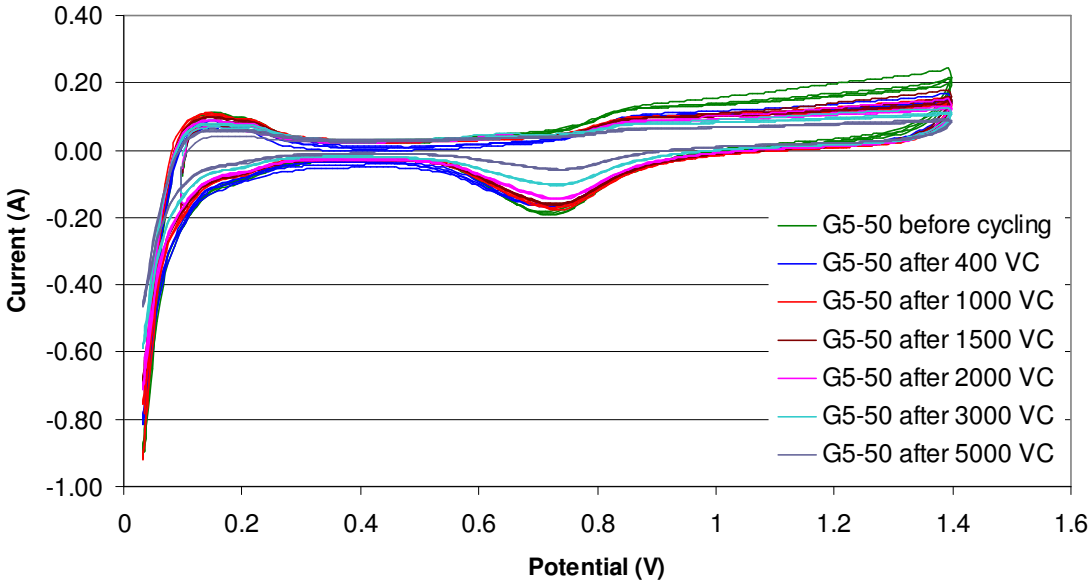

Figure 5.74: voltammograms of fuel cell G_5 at 50mV/sec

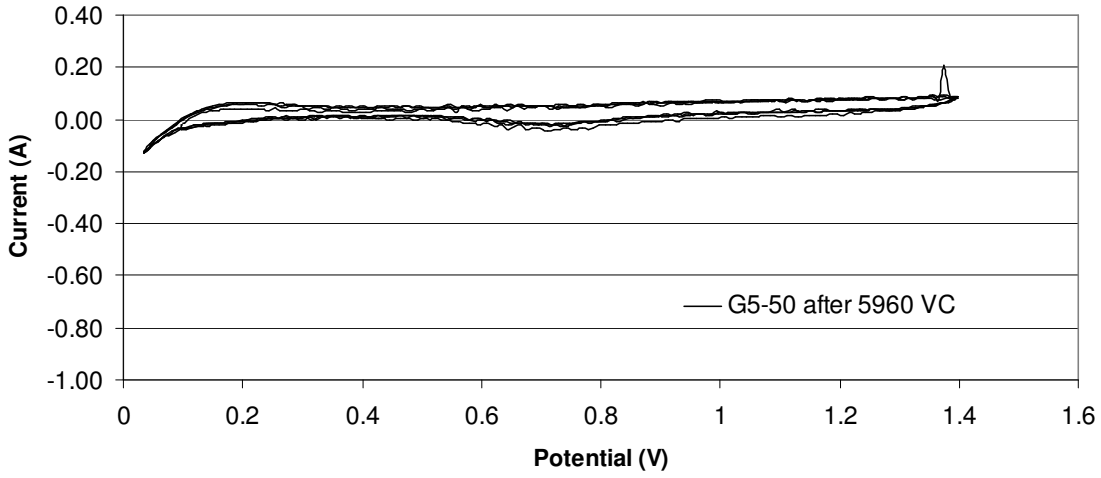

Figure 5.75: voltammograms of fuel cell G_5 at 50mV/sec after 5960 voltage cycles

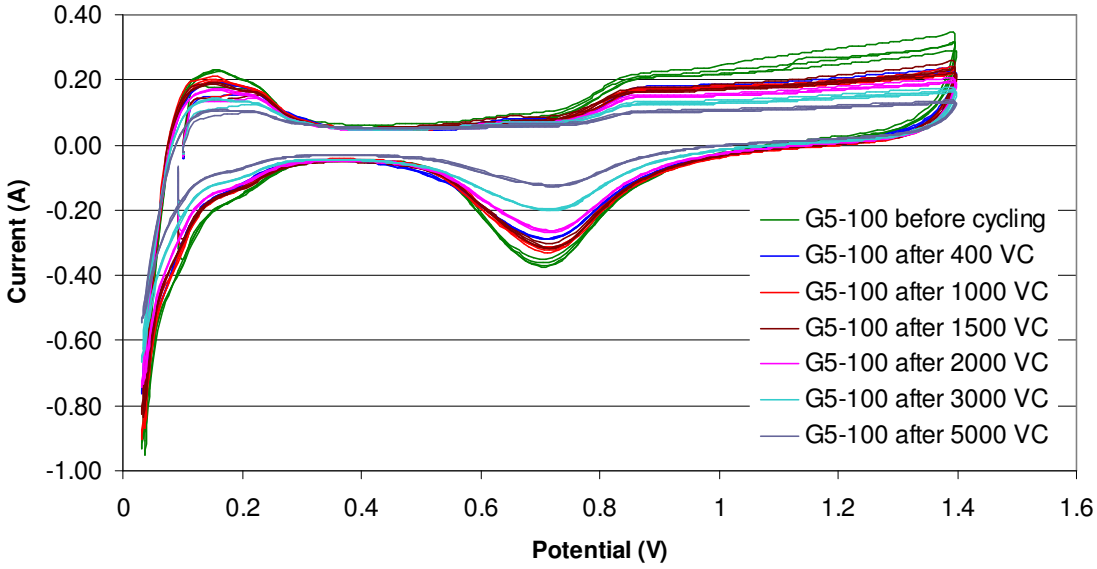

Figure 5.76: voltammograms of fuel cell G_5 at 100mV/sec

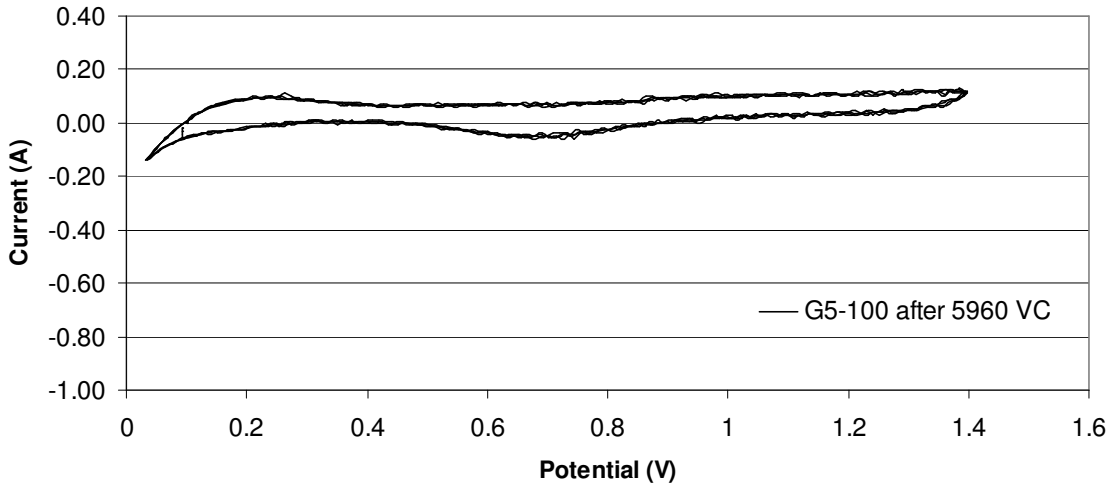

Figure 5.77: voltammograms of fuel cell G_5 at 100mV/sec after 5960 voltage cycles

Table 5.35: Active Pt Surface Area for the fuel cell G_5

Voltage Cycles Completed	Mean Active Pt Surface Area (m^2/g)
0	60.56
1000	59.83
1500	51.87
2000	46.87
3000	36.30
5000	21.48
5960	10.36

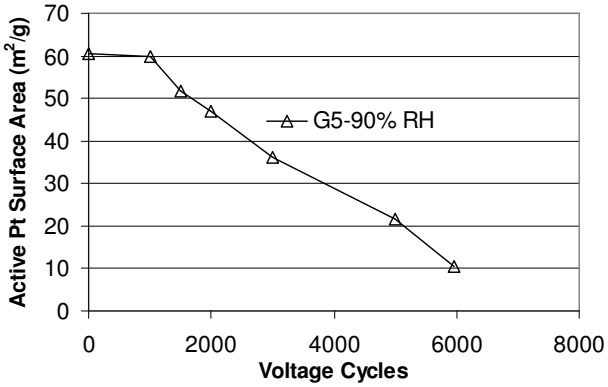

Figure 5.78: Decrease in Active pt Surface Area of fuel cell G_5

5.5.3.8 Fuel Cell G_6-60% RH

Fuel cell G_6 tested at 60% RH, stopped working at 5500 voltage cycles. The active Pt surface area at the cathode side decreased continuously through out the potential cycling test. The reduction in the active Pt surface area is presented graphically from the Figure 5.83.

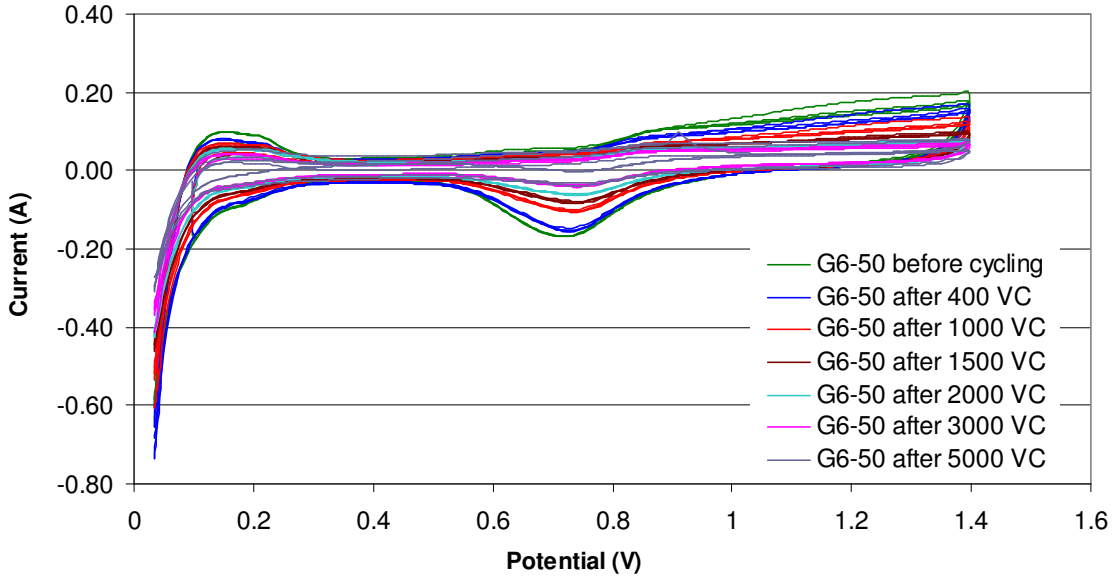

Figure 5.79: voltammograms of fuel cell G_6 at 50mV/sec

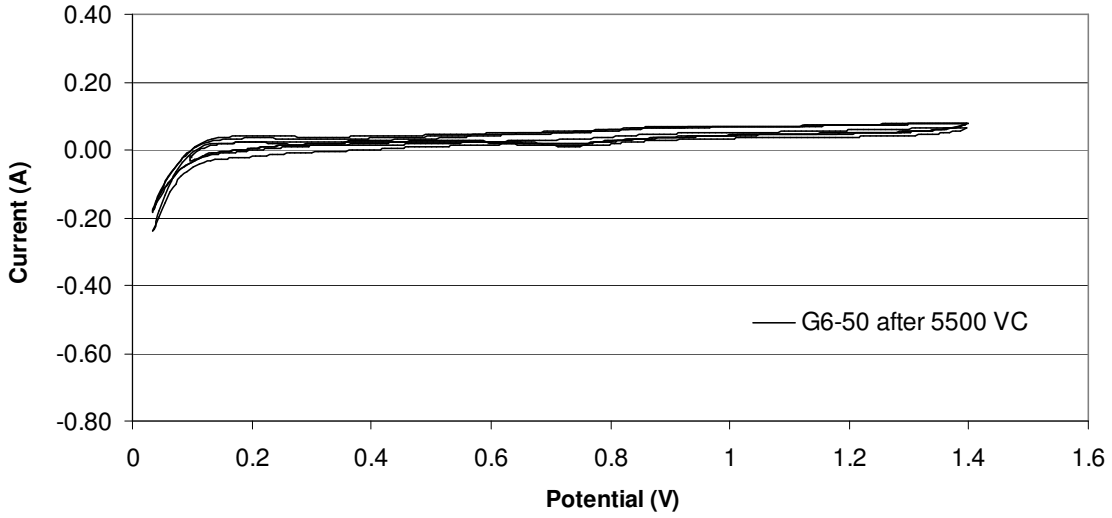

Figure 5.80: voltammograms of fuel cell G_6 at 50mV/sec after 5500 voltage cycles

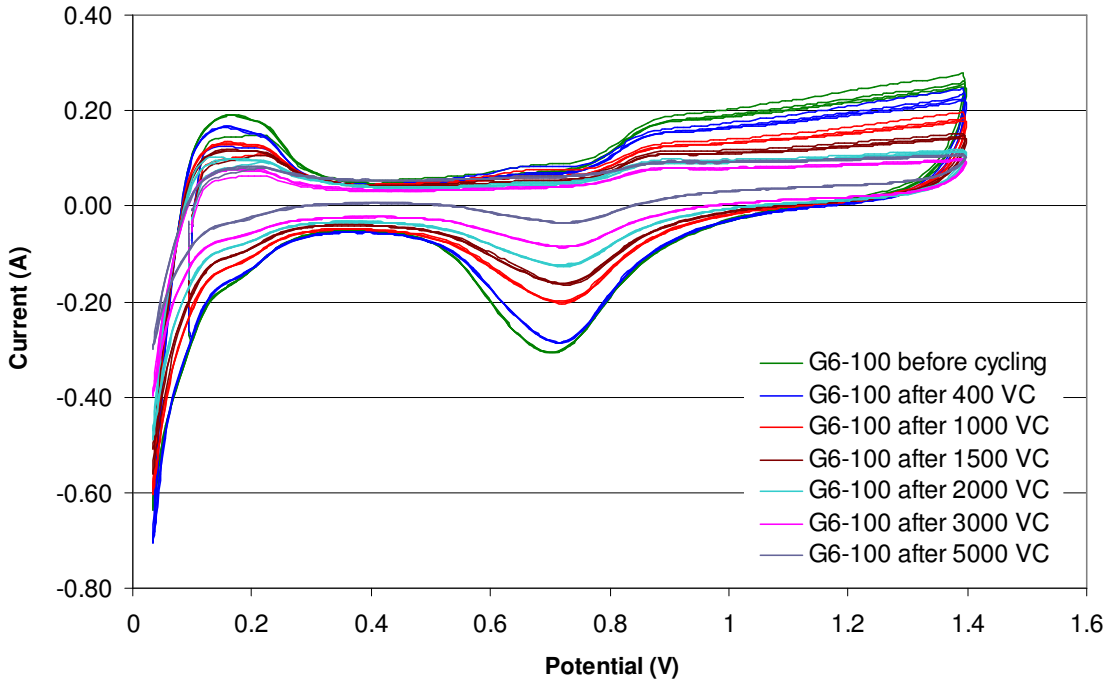

Figure 5.81: voltammograms of fuel cell G_6 at 100mV/sec

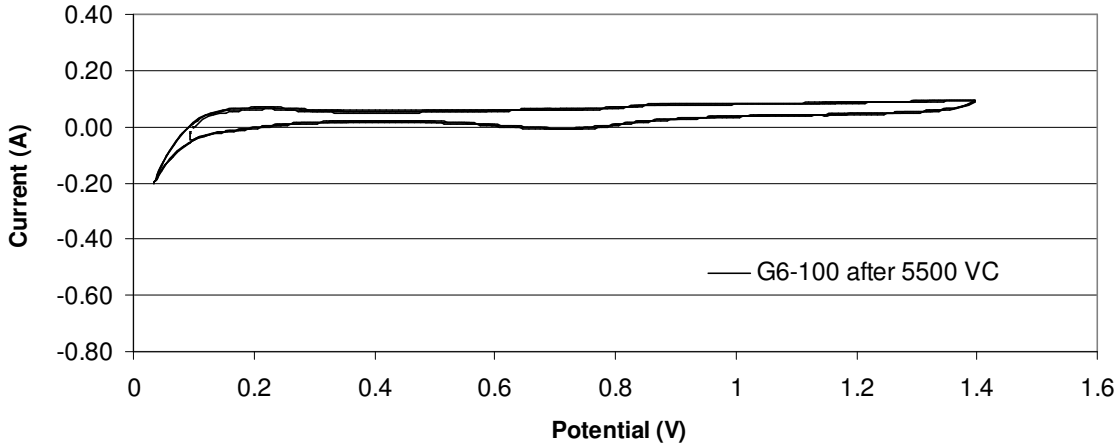

Figure 5.82: voltammograms of fuel cell G_6 at 100mV/sec after 5500 voltage cycles

Table 5.36: Active Pt Surface Area for the fuel cell G_6

Voltage Cycles completed	Mean Active Pt Surface Area (m^2/g)
0	51.70
400	41.62
1000	32.78
1500	29.53
2000	26.15
3000	17.42
5000	10.45
5500	3.37

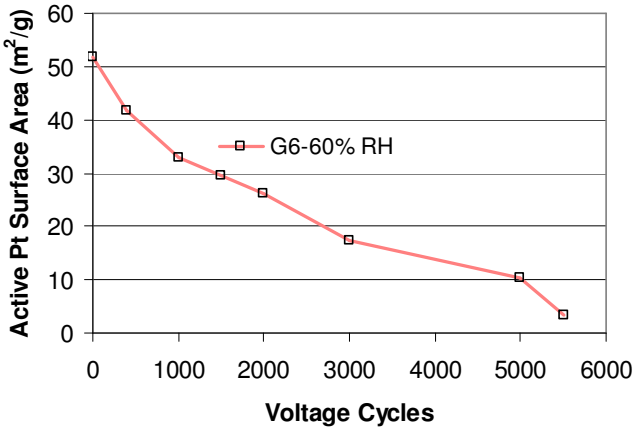

Figure 5.83: Decrease in Active pt Surface Area of fuel cell G_6

5.5.3.9 Fuel Cell G_8-33% RH

The fuel cell G8 operated at 33% RH, gave performance only for 1500 voltage cycles. During this time active Pt surface area reduced so much that at the completion of 1500 voltage cycles its value remained just 50% of its original value with fresh MEA.

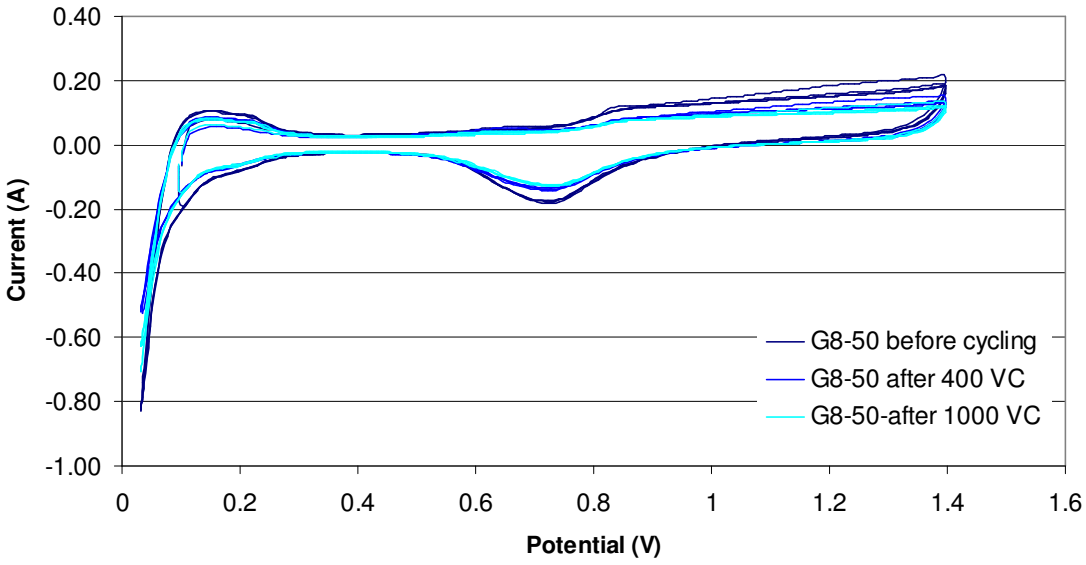

Figure 5.84: voltammograms of fuel cell G_8 at 50mV/sec

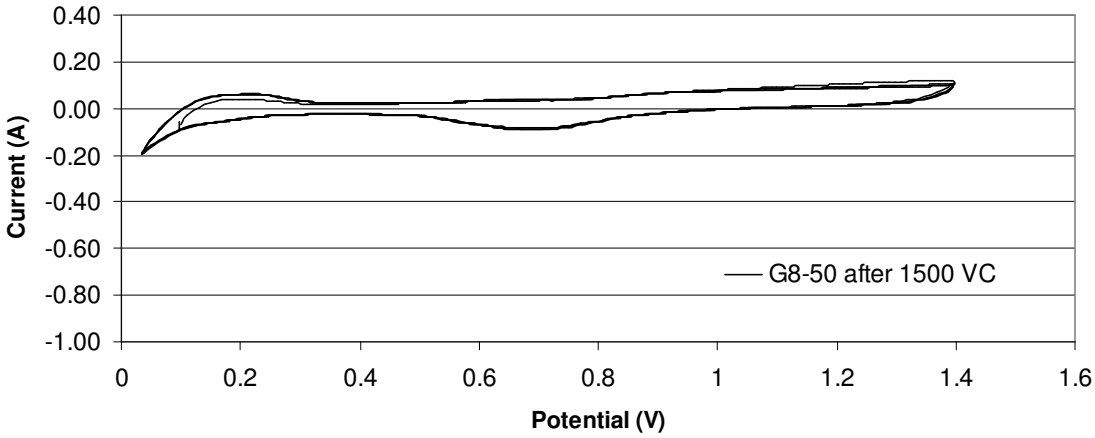

Figure 5.85: voltammograms of fuel cell G_8 at 50mV/sec after 1500 voltage cycles

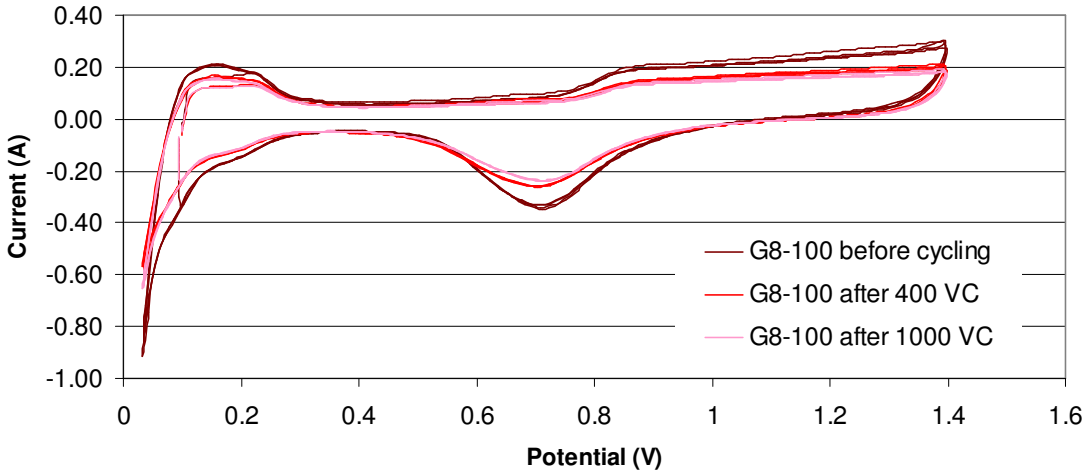

Figure 5.86: voltammograms of fuel cell G_8 at 100mV/sec

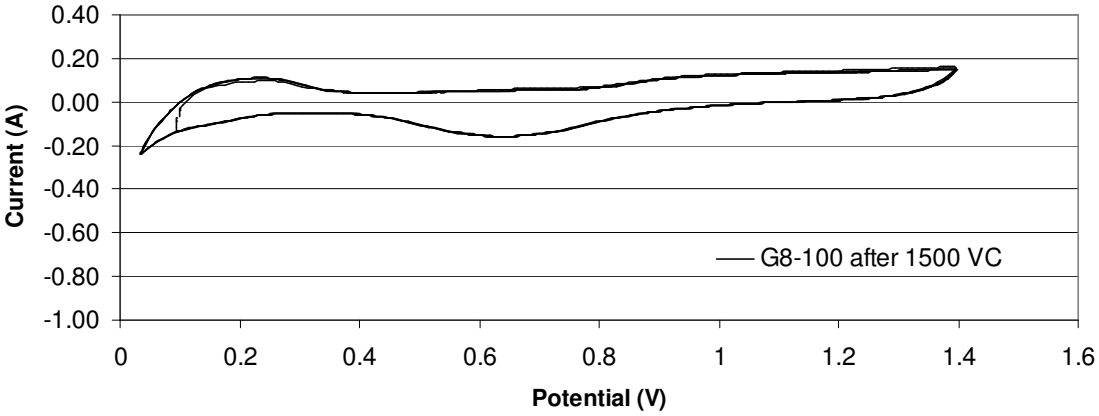

Figure 5.87: voltammograms of fuel cell G_8 at 100mV/sec after 1500 voltage cycles

Table 5.37: Active Pt Surface Area for the fuel cell G_8

Voltage Cycles Completed	Mean Active Pt Surface area (m^2/g)
0	55.13
400	42.20
1000	40.48
1500	27.05

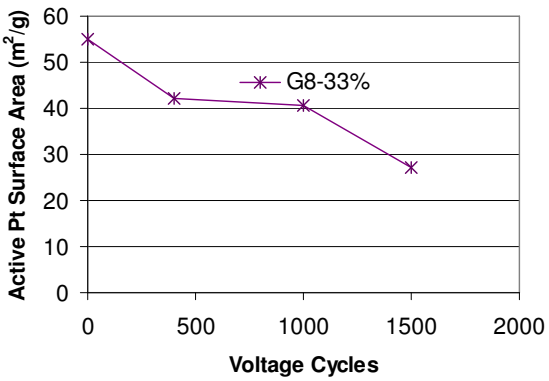

Figure 5.88: Decrease in Active pt Surface Area of fuel cell G_8

Figure 5.89 shows the behavior of all the fuel cells examined at different values of relative humidity. It is clear from the figure that the fuel cells operated at 90 % RH (G_1, G_3& G_5) show longer lifetime with larger values of active Pt surface area at the cathode of the cells.

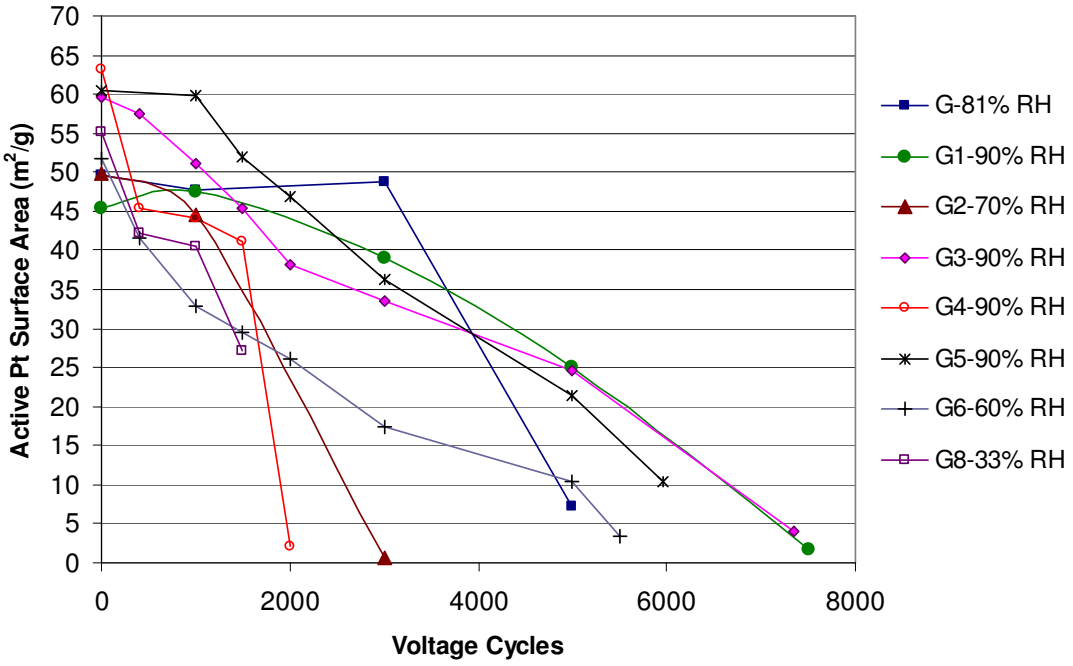

Figure 5.89: Decrease in Active Pt surface area of all the fuel cells

Figure 5.89 exhibits that the fuel cells operated at 70%, 60% and 33% RH show steep slopes regarding reduction in active Pt surface Area (ECSA) whereas the cells operated at 90% RH like G_1, G_3 and G_5 present a gradual decrease in ECSA loss.

5.5.4 Hydrogen Diffusion Measurements

For each fuel cell one cycle of hydrogen diffusion characteristics was recorded with the help of 100 samples per cycle sweeping between 0.07V and 0.5 V for a scan rate of 500µV/sec at the end of the life span of the fuel cells G, G_1, G_2, G_3, G_4 and G_5. These graphs show that the membrane of these cells have been damaged through the course of the accelerated voltage cycling test with the formation of the pin holes in them. Due to the pin hole formation hydrogen can pass through the membrane and reach to the cathode where with the combination of the oxygen a lot of water can be produced which is really hazardous for the cell performance.

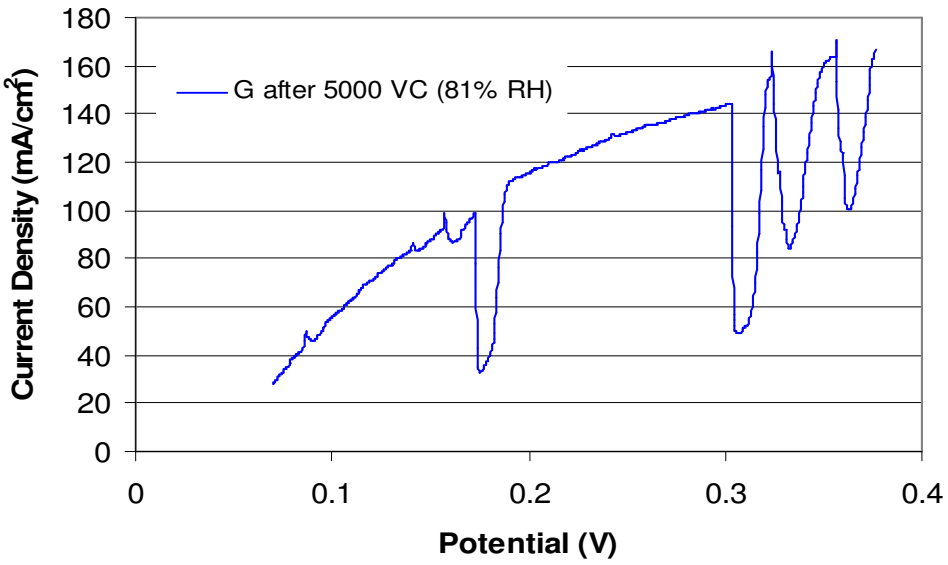

Figure 5.90: Hydrogen diffusion measurement of fuel cell G

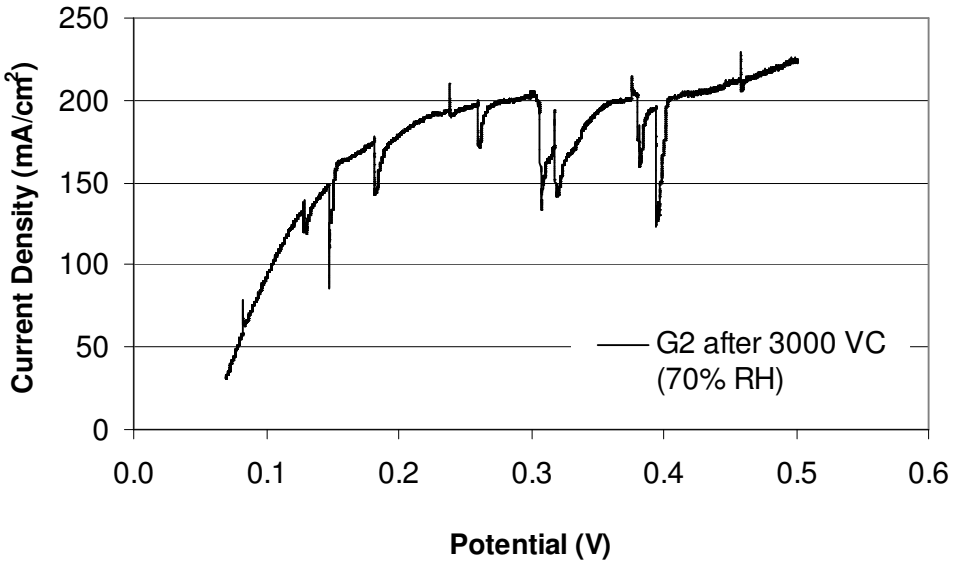

Figure 5.91: Hydrogen diffusion measurement of fuel cell G_2

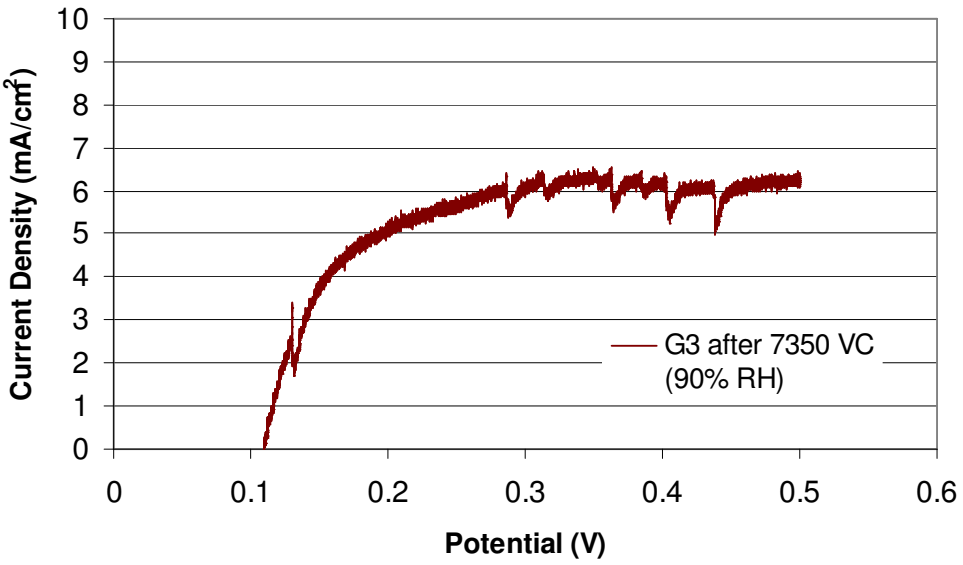

Figure 5.92: Hydrogen diffusion measurement of fuel cell G_3

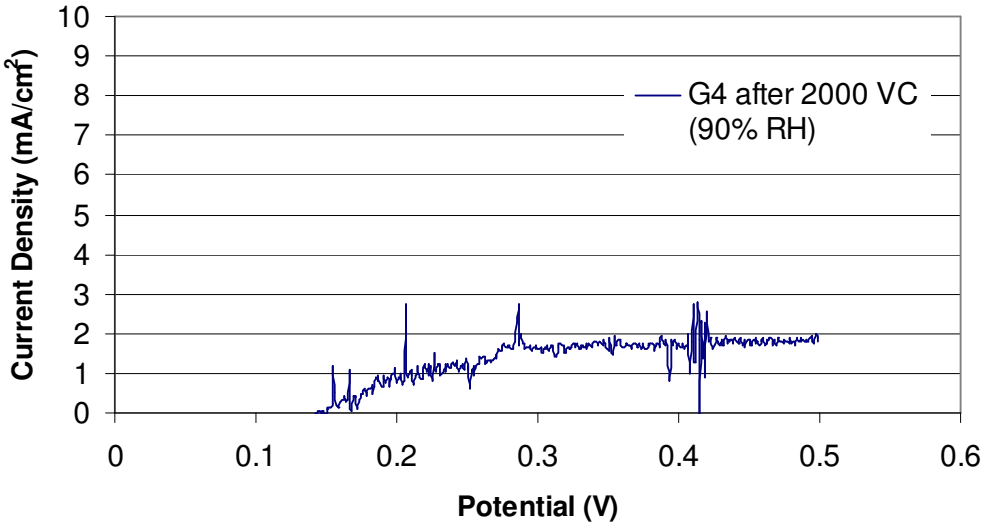

Figure 5.93: Hydrogen diffusion measurement of fuel cell G_4

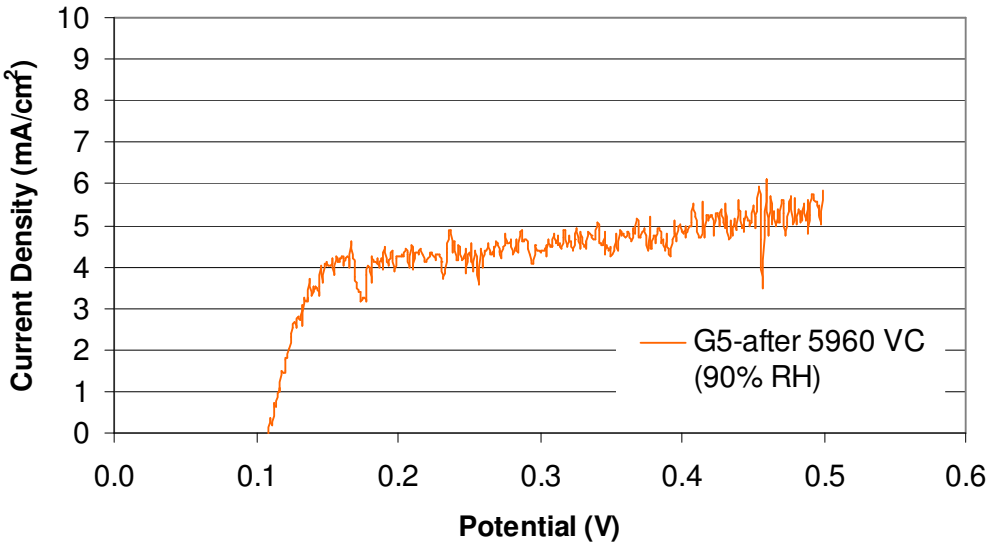

Figure 5.94: Hydrogen diffusion measurement of fuel cell G_5

5.5.4.1 Fuel Cell G_6-60% RH

Fuel cell G_6 was tested at 60% RH. Hydrogen diffusion measurements were recorded before accelerated voltage cycling test and during the experiment after completing 400, 1000, 1500, 2000, 3000, 5000 and 5500 voltage cycles. Figure 5.95 illustrates all these graphs of current density verses potential. Till 2000 voltage cycles the current density remained smooth with the increase of potential. After 3000 voltage cycles a little increase in the current density can be exhibited with the rising potential till 4mA/cm^2 but after finishing 5000 and 5500 voltage cycles a progressive increase in the current density with the ascending potential is prominent from the Figure 5.95. This eminent increase in the current density is a direct measure of pin-hole formation.

5.5.4.2 Fuel Cell G_8-33% RH

Fuel cell G_8 was investigated at 33% RH. This cell gave performance just for 1,500 voltage cycles. Hydrogen diffusion current measurement was performed with fresh MEA, after 400, 1,000 and 1,500 VC but the current density did not exceed even 4mA/cm^2 (Figure 5.96). This shows that pin hole did not create with in the membrane.

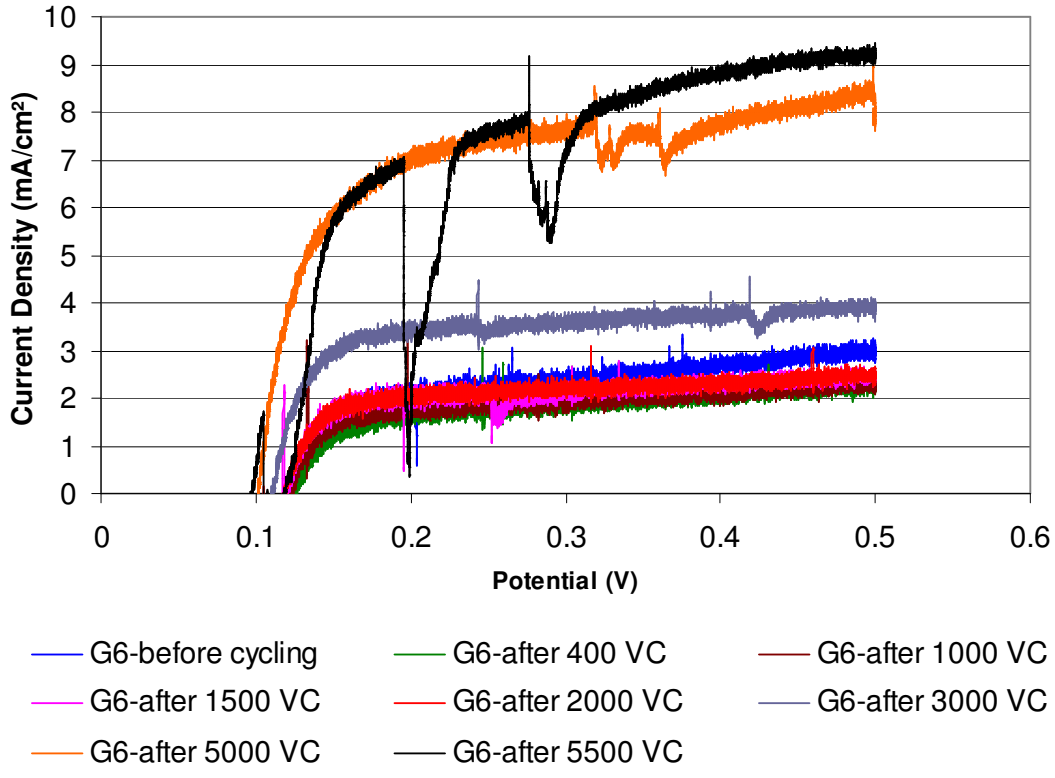

Figure 5.95: Detail of H2 diffusion measurements for the fuel cell G_6

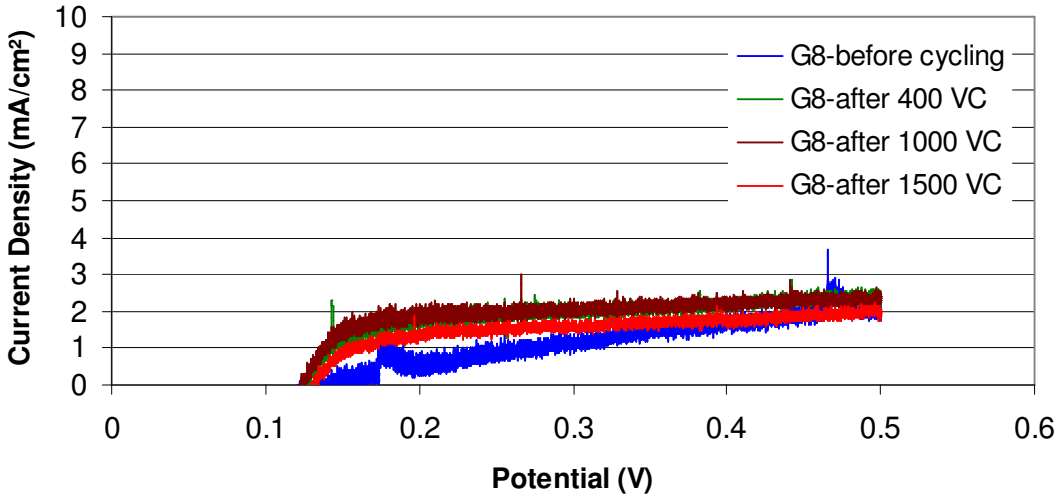

Figure 5.96: Detail of H2 diffusion measurements for the fuel cell G_8

5.6 EX-situ Characterisation of MEA by SEM and EDS

5.6.1 SEM

A (Reference G)

B (G)

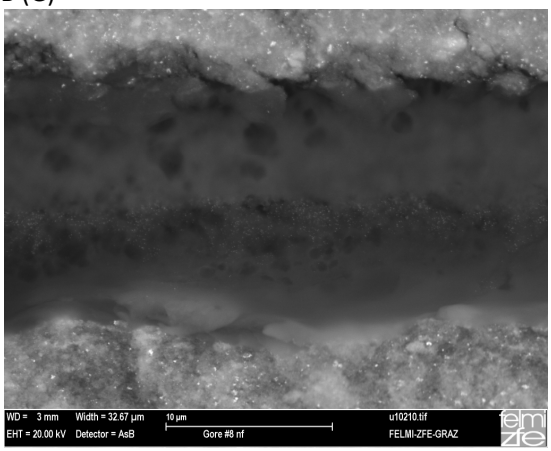

C (G)

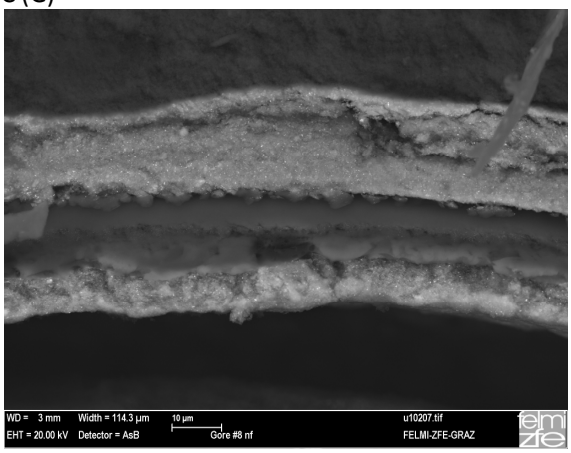

D (G_1)

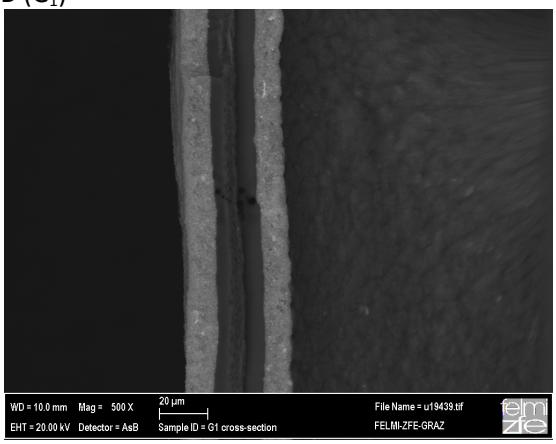

E(G_1)

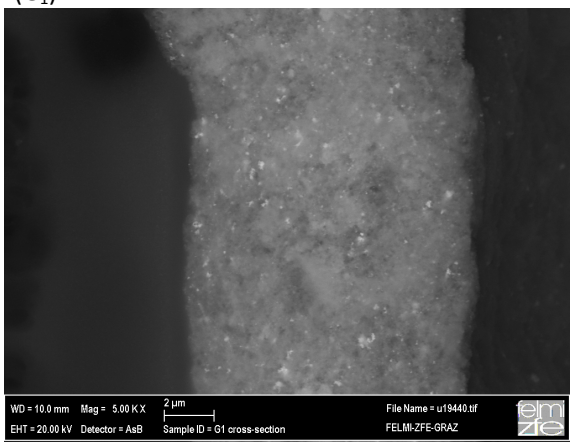

F (G_1)

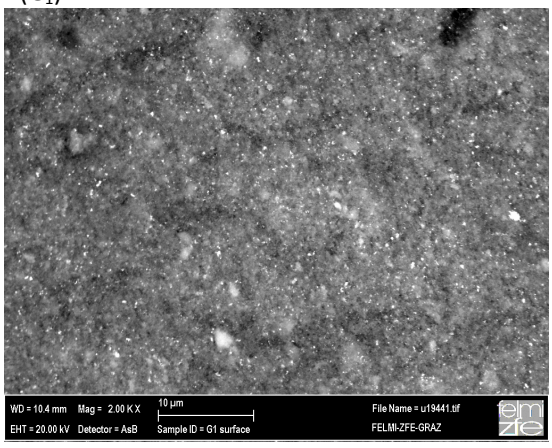

Figure 5.97: (A) Cross-section of Fuel Cell G before test (20µm), (B) Pt particles band inside the membrane of fuel cell G after 5000 VC (10µm), (C) Cross-section of Fuel Cell G after 5000 VC (10µm), (D) Cross-section of fuel cell G_1 after 7500 VC (20µm), (E) Agglomeration of Pt particles on cathode side of fuel cell G_1 (2 µm), (F) Cathode surface of Fuel cell G1 after 5000 VC (10µm)

G (G_2)

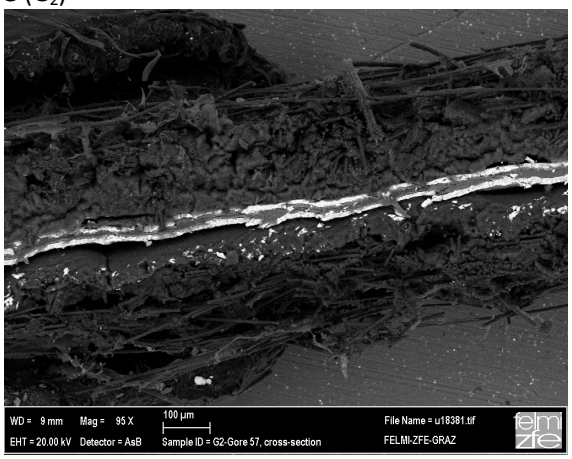

H (G_2)

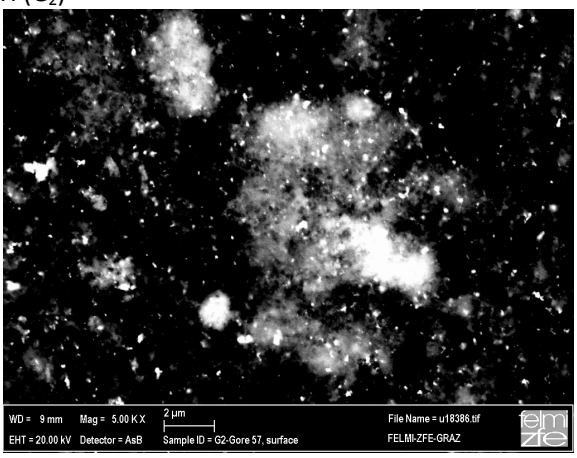

I (G_3)

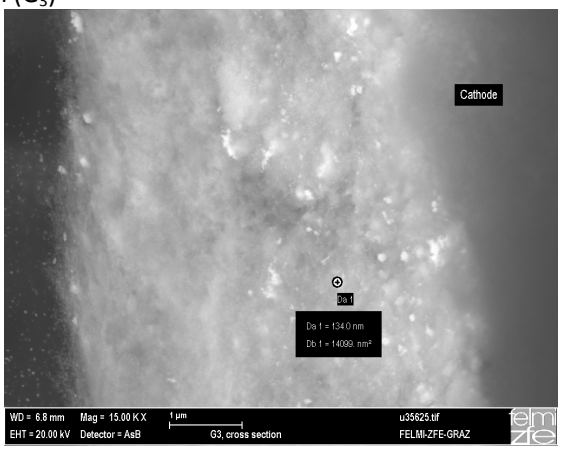

J (G_3)

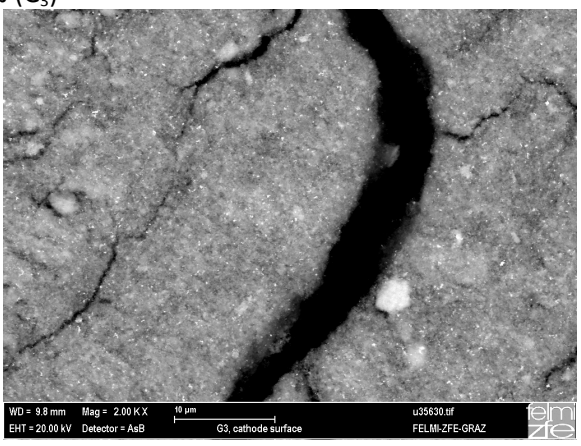

K (G_4)

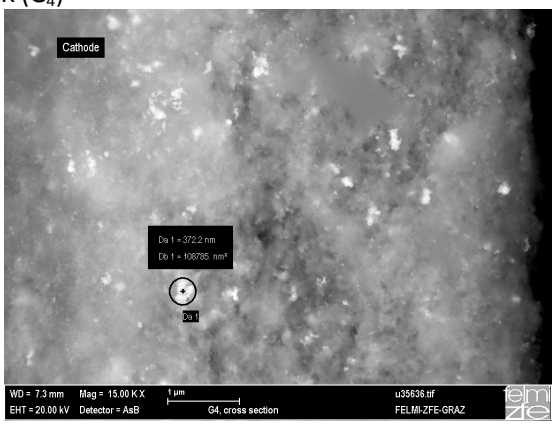

L (G_5)

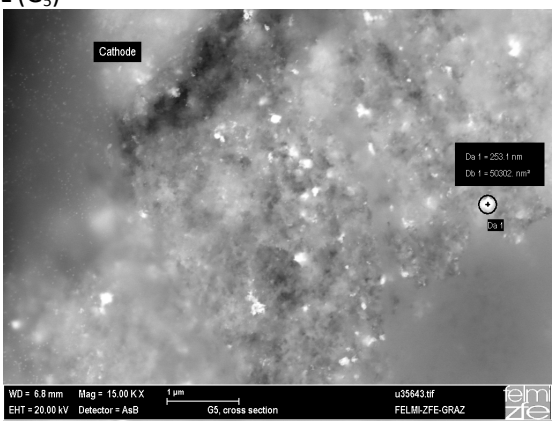

Figure 5.98: (G) Cross-section of fuel cell G_2 after 3000 VC (100 µm), (H) Cathode surface of fuel cell G_2 after 3000 VC (2 µm); (I) Cathode of G_3 (1 µm), (J) Cathode surface of G_3 (10 µm), (K) Cathode cross-section of G_4 after 2000 VC (1 µm), (L) Cathode cross-section of G_5 after 5960 VC (1 µm)

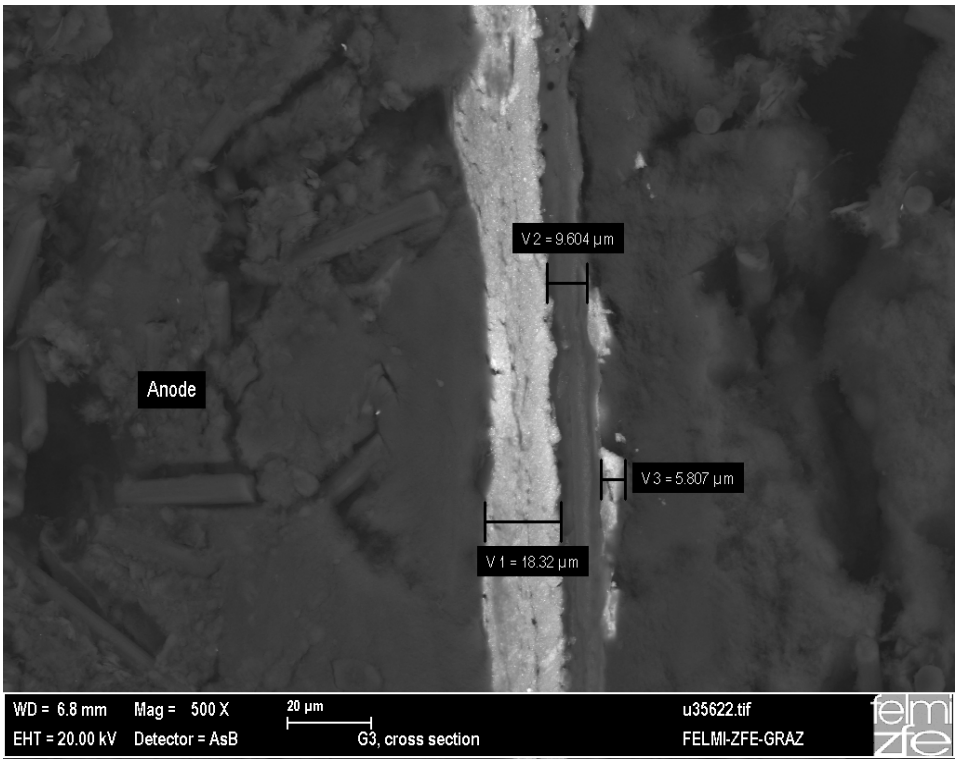

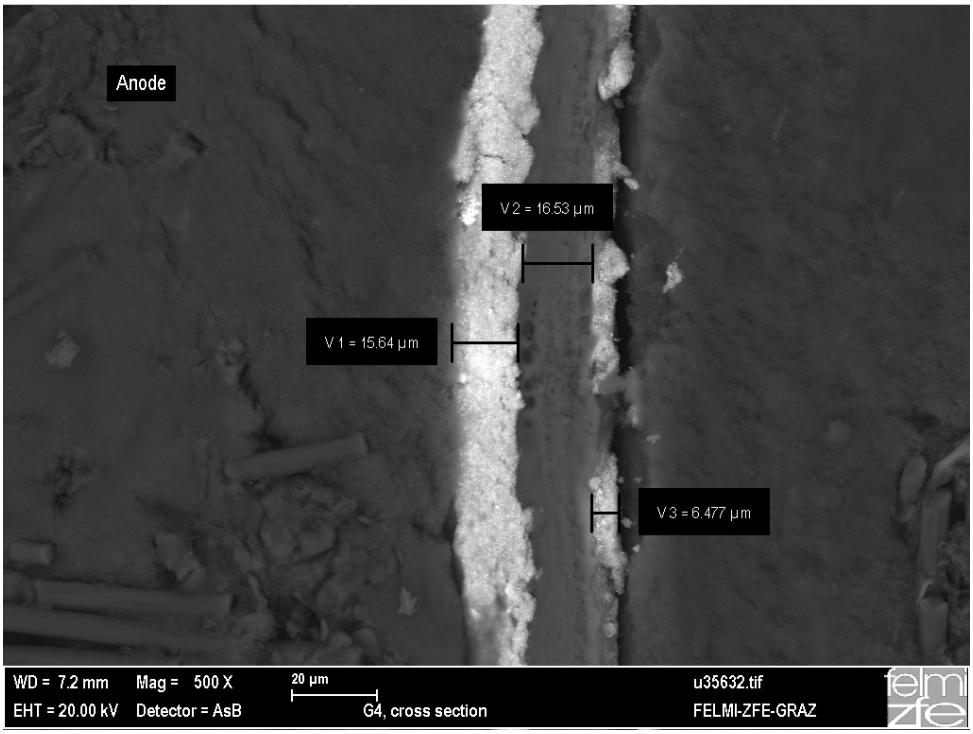

Figure 5.99: Cross-section of G_3 after 7350 VC (20 µm), Cross-section of G4 after 2000 VC (20 µm)

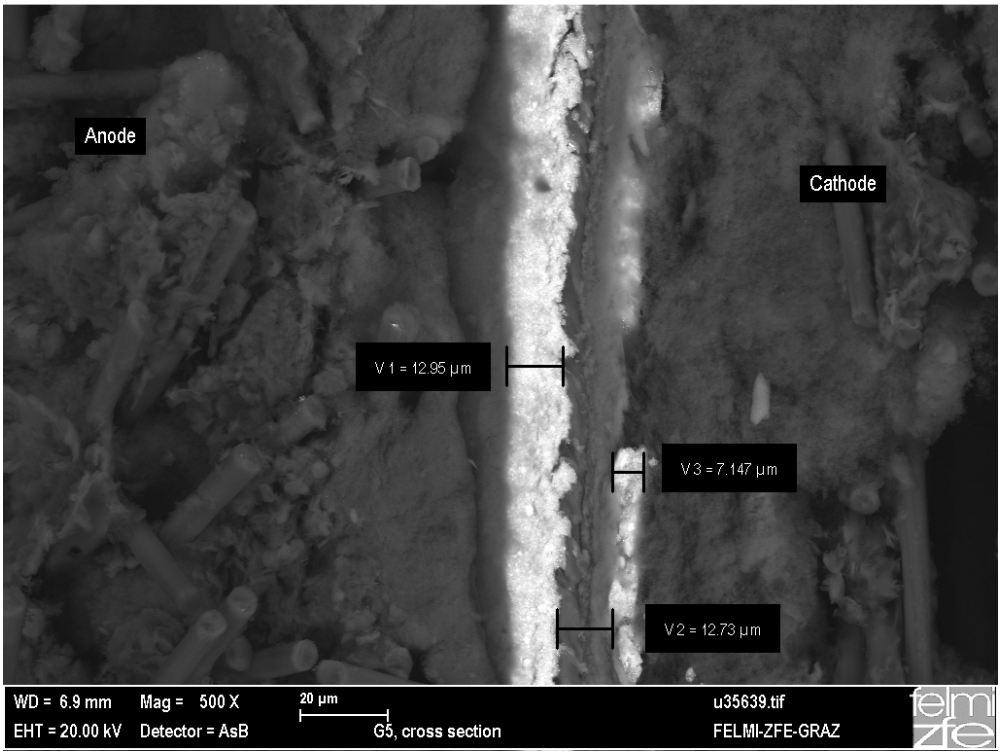

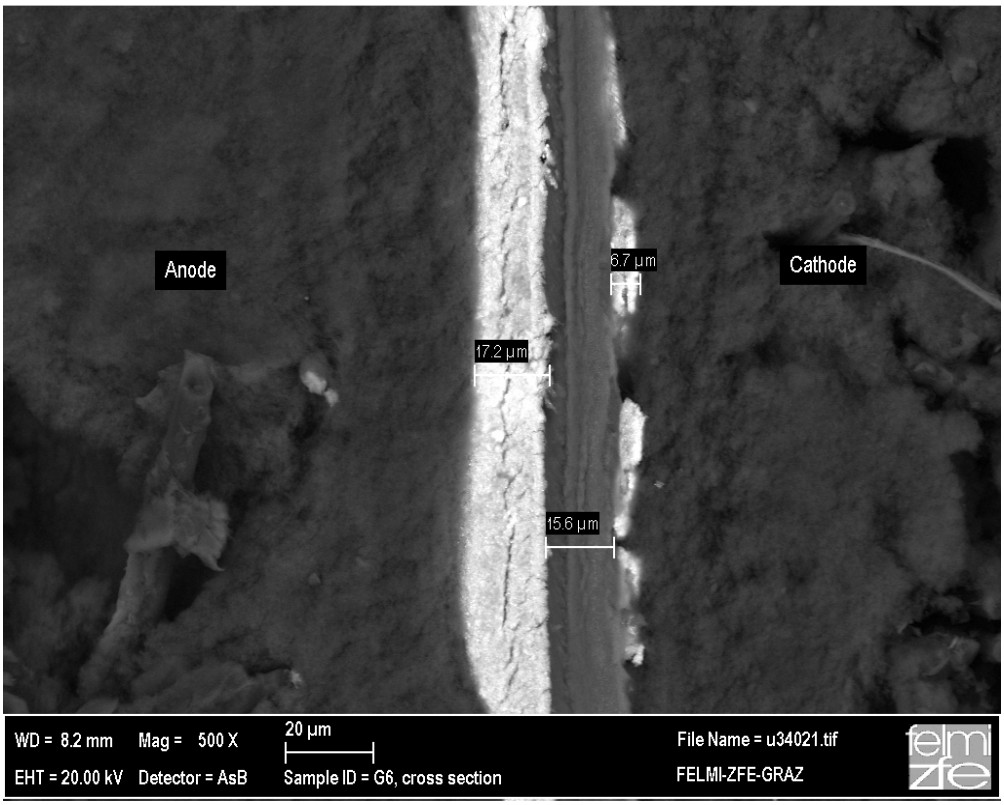

Figure 5.100: Cross-section of fuel cell G_6 after 5500 VC (20 µm)

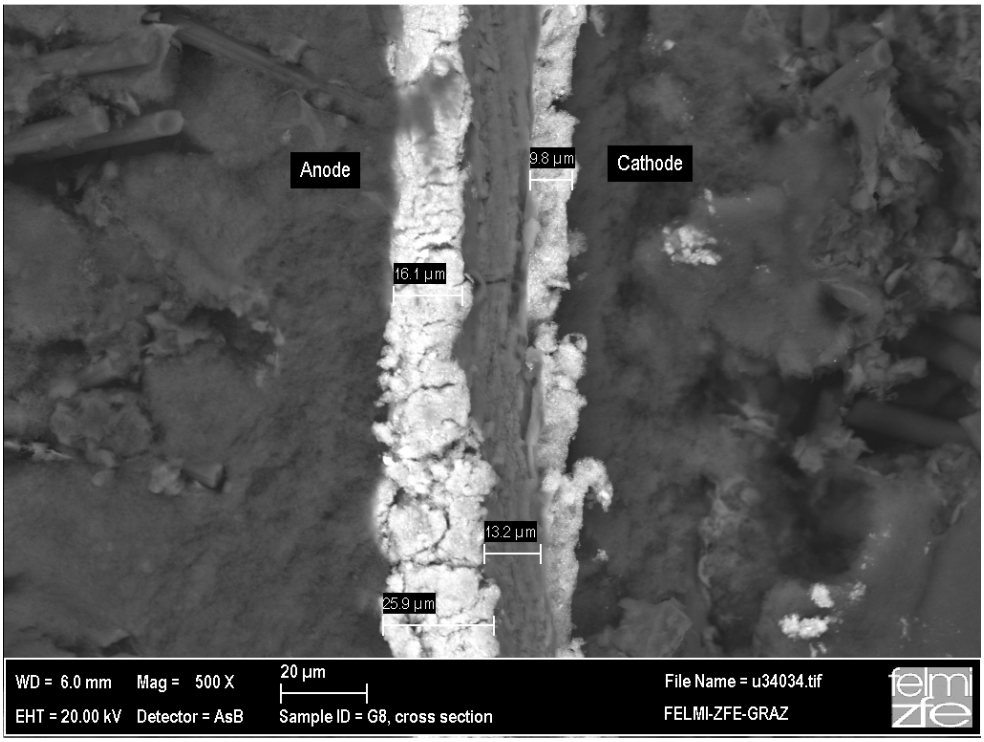

Figure 5.101: Cross-section of fuel cell G_8 after 1500 VC (20 µm)

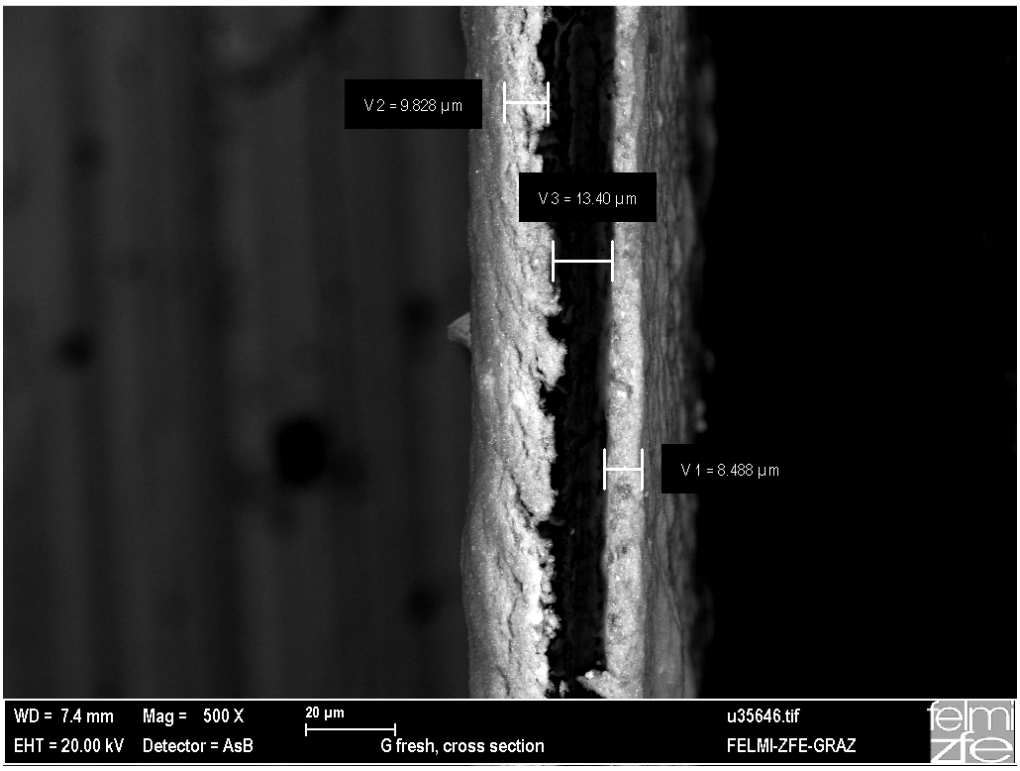

Figure 5.102: Cross-section of fresh G-type MEA (20 µm)

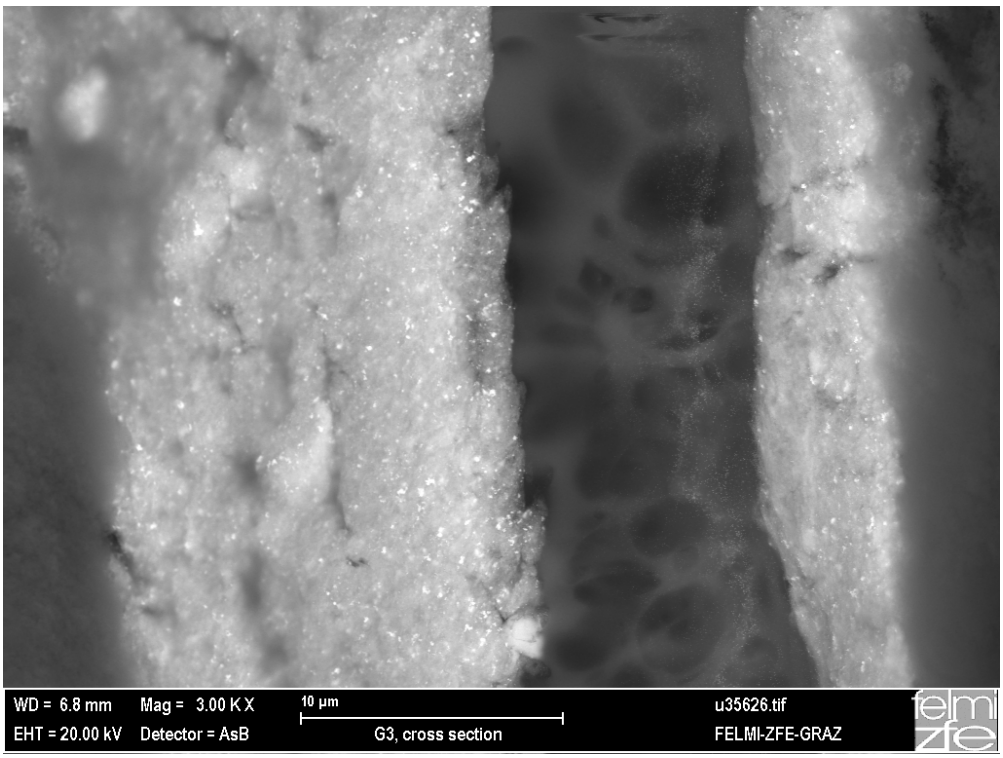

Figure 5.103: Pt particles band in membrane near cathode of fuel cell G_3 after 7350 VC

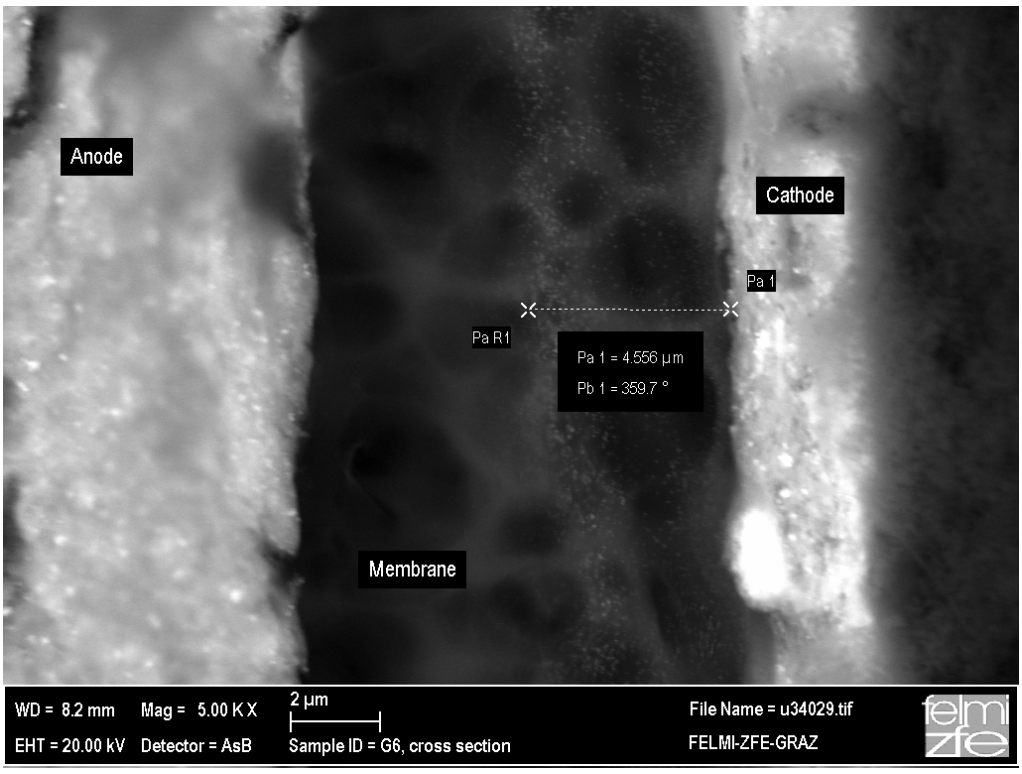

Figure 5.104: Pt particles migration from cathode to inside the membrane of G_6 (2 µm),

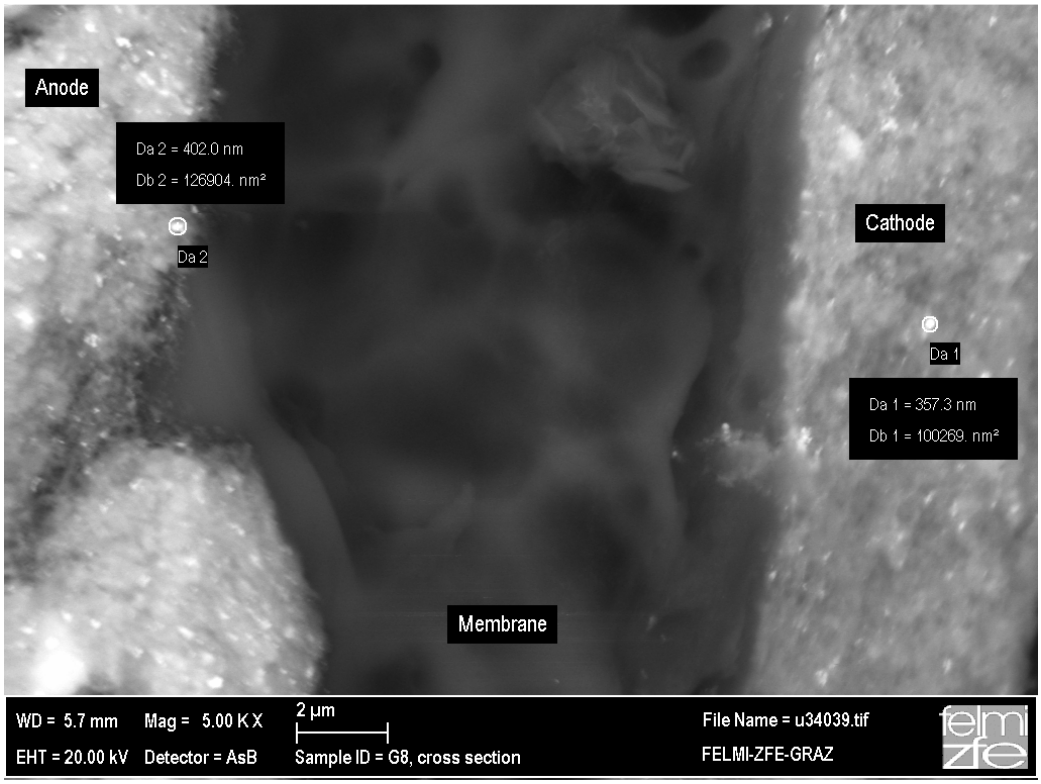

Figure 5.105: Cross-section of fuel cell G_8 after 1500 VC (20 µm)

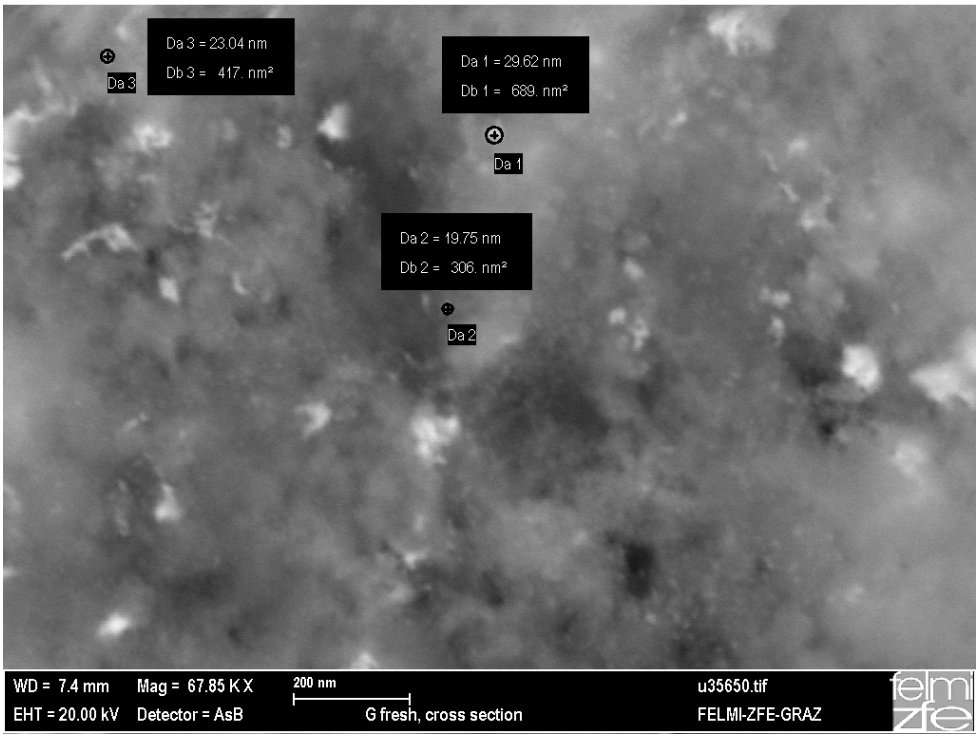

Figure 5.106: SEM image of cathode of fresh G-type MEA

M (G_5)

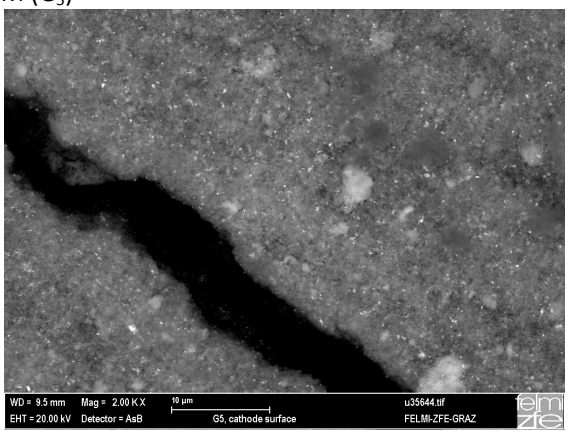

N (Fresh G)

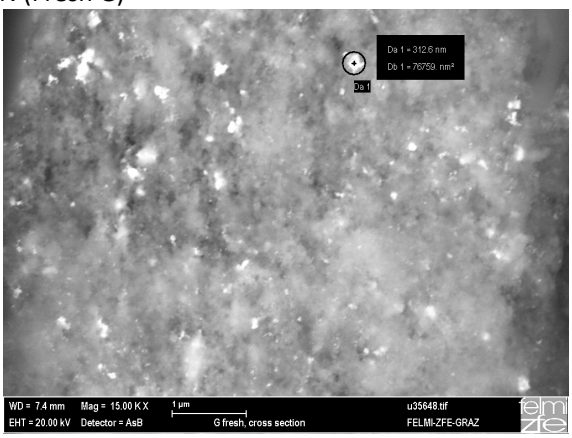

O (Fresh G)

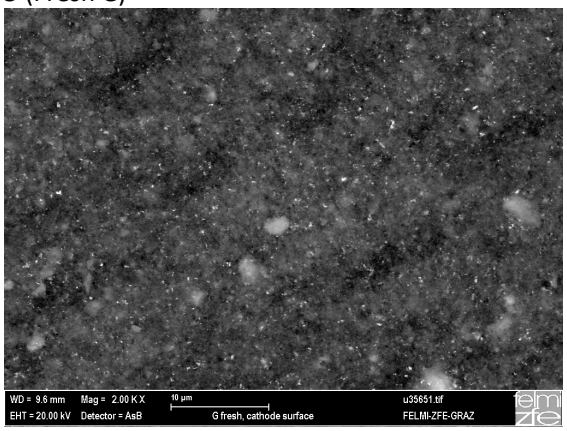

P (G_4)

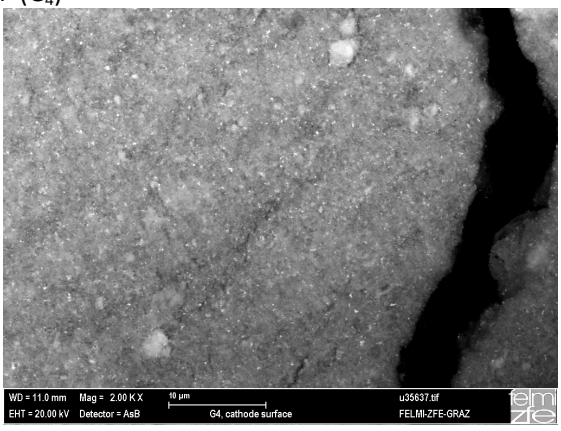

Q (G_6)

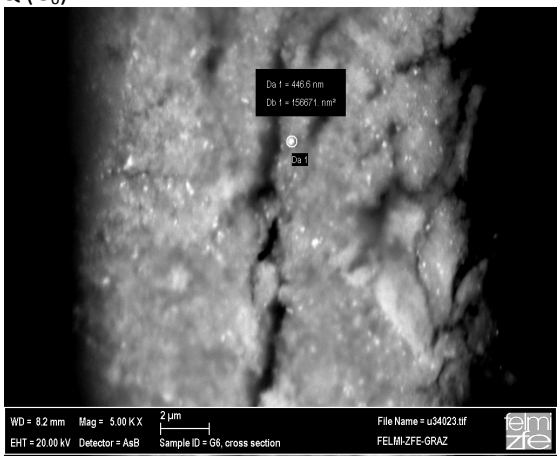

R (G_6)

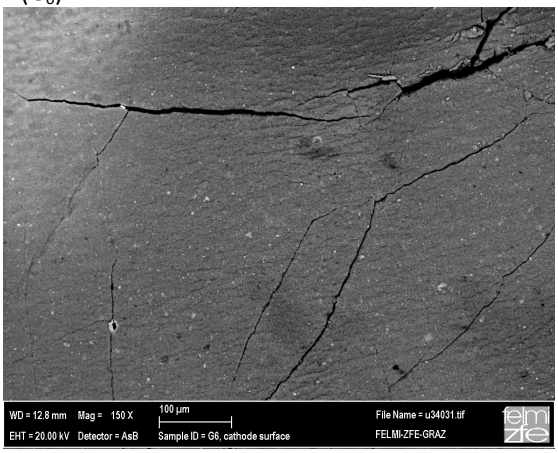

Figure 5.107: (M) Cathode surface of G5 (10 µm), (N) Cathode cross-section of fresh G-type (1 µm), (O) Cathode surface of fresh G-type MEA, (P) Cathode surface of G_4 (10 µm), (Q) Cathode cross-section of fresh G_6 (2 µm), (R) Cathode surface of G6 (100 µm)

S (G_6)

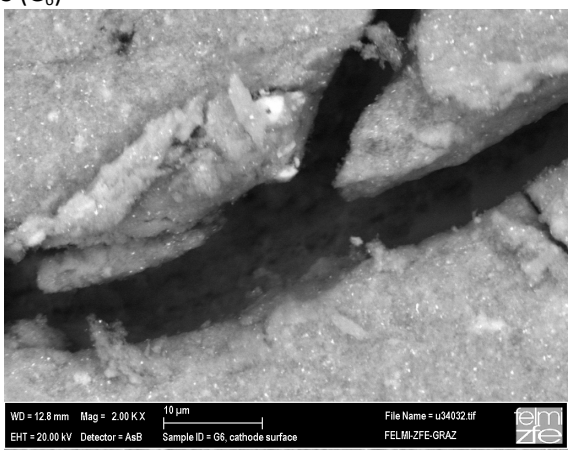

T (G_8)

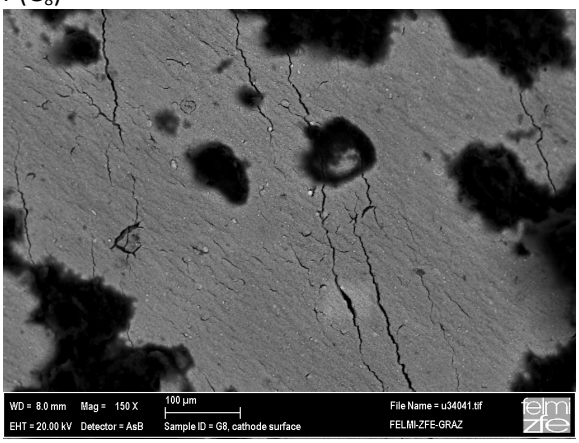

U (G_8)

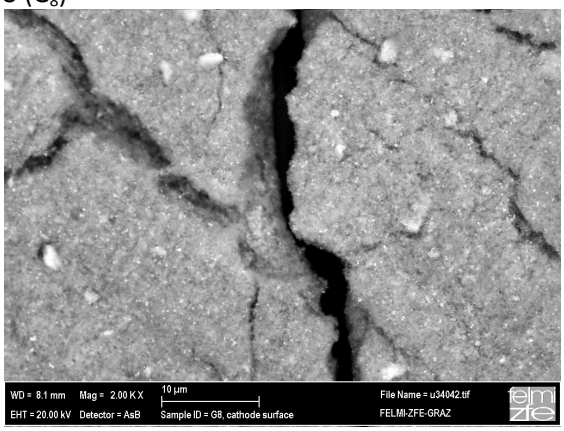

Figure 5.108: (S) Cathode surface of G6 after 5500 VC (10 µm), (T) Cathode surface of G8 after 1500 VC (100 µm), (U) cracks in cathode surface of G8 after 1500 VC (10 µm)

- Cathode Thickness of fuel cell G6 after 5500 VC=6.7 µm
- Anode thickness of fuel cell G6 after 5500 VC=17.2 µm
- Membrane thickness of fuel cell G6 after 5500 VC= 15.6 µm
- Diameter of Pt particle on cathode side of fuel cell G6 after 5500 VC= 466.6nm
- Cathode Thickness of fuel cell G_8 after 1500 VC= 5.8 µm
- Anode Thickness of fuel cell G_8 after 1500 VC= 10.5 µm
- Membrane Thickness of fuel cell G_8 after 1500 VC= 19.4 µm

5.6.1.1 Agglomeration in the Pt particles size

Cathode of the Fuel Cell	Relative Humidity	Total Life (voltage cycles)	Agglomerate size of Pt particles (nm)
G	81%	5000	
G_1	90%	7500	
G_2	70%	3000	
G_3	90%	7350	134.0
G_4	90%	2000	372.2
G_5	90%	5960	253.1
G_6	60%	5500	402.0
G_8	33%	1500	357.3

5.6.2 Energy Dispersive X-Ray Spectroscopy (EDS)

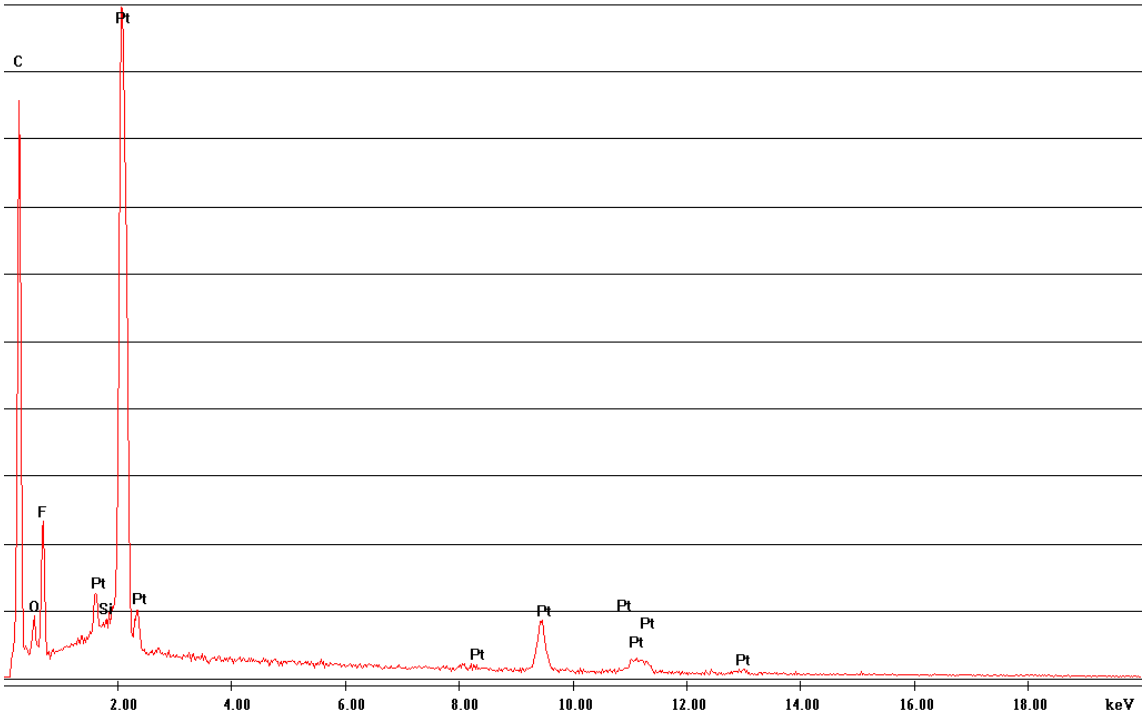

Figure 5.109: EDS of cathode surface of fresh G-type MEA (X-axis: 20KeV, Y-axis: Counts)

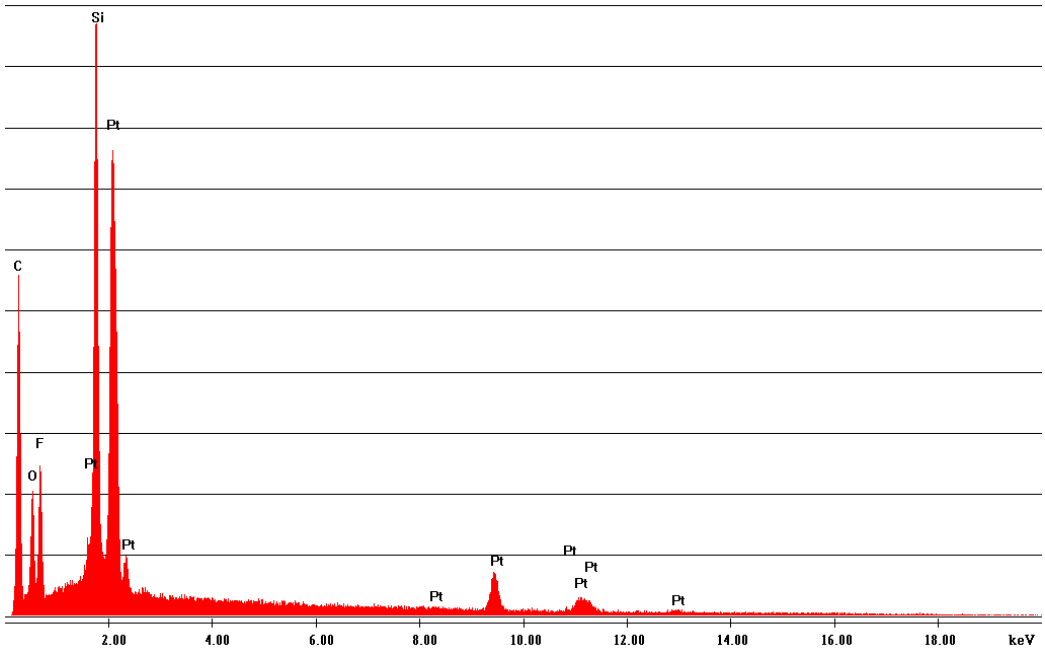

Figure: 5.110: EDS of cathode of G_2 after 3000 VC (X-axis: 20KeV, Y-axis: Counts)

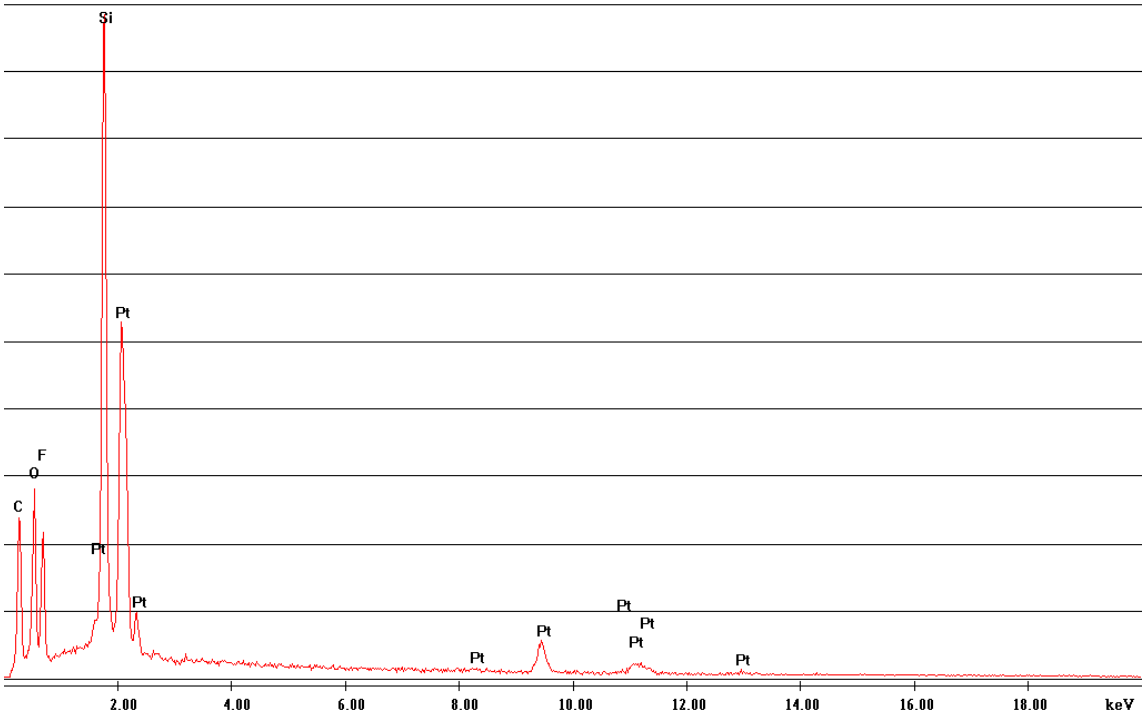

Figure: 5.111: EDS of G_3 after 7350 VC (X-axis: 20KeV, Y-axis: Counts)

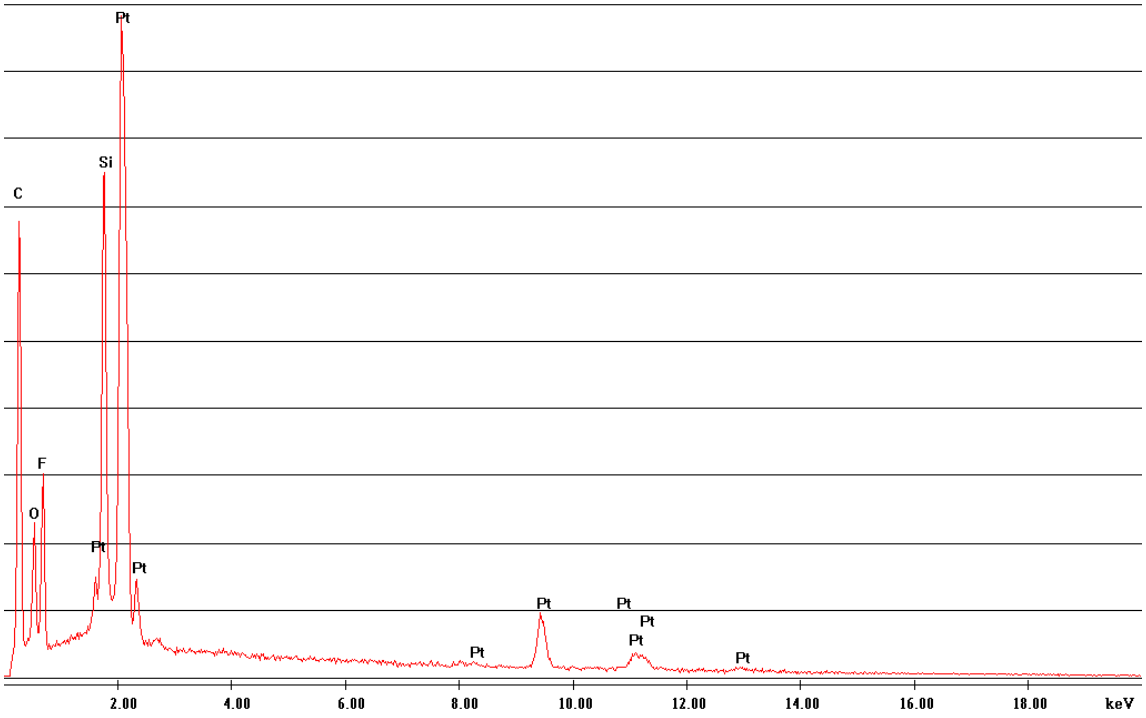

Figure: 5.112: EDS of G_4 after 2000 VC (X-axis: 20KeV, Y-axis: Counts)

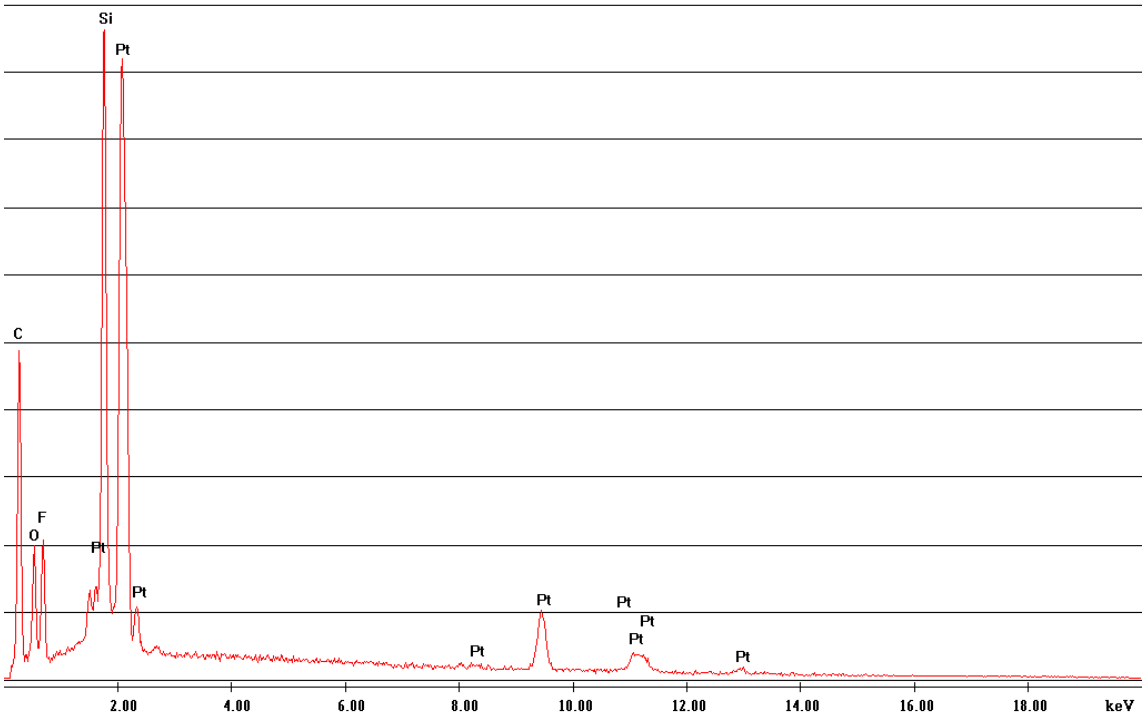

Figure: 5.113: EDS of G_5 after 5960 VC (X-axis: 20KeV, Y-axis: Counts)

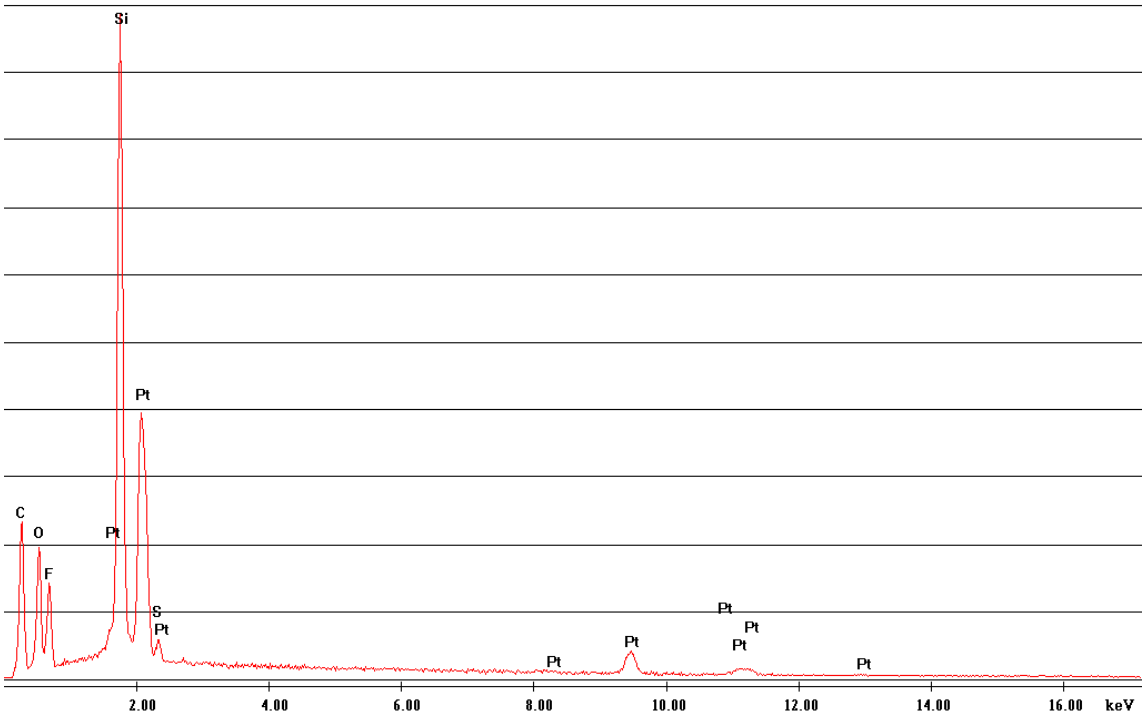

Figure 5.114: EDS of G_6 after 5500 VC (X-axis: 20KeV, Y-axis: Counts)

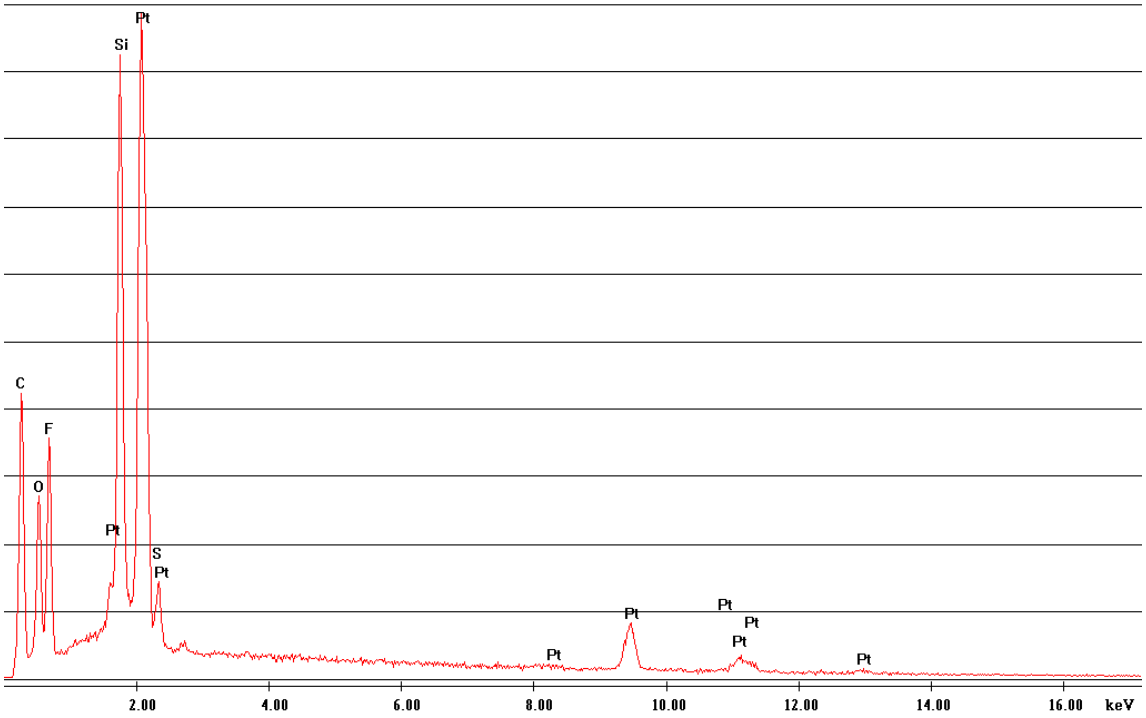

Figure 5.115: EDS of G_8 after 1500 VC (X-axis: 20KeV, Y-axis: Counts)

5.6.3 Summary

Eight fuel cells assembled with same G type of MEA were investigated at different values of relative humidity. The fuel cells G, G_2, G_6 and G_8 were operated at 81%, 70%, 60% and 33% relative humidity respectively whereas the fuel cells G_1, G_3, G_4 and G_5 were tested at 90% RH. On the whole the fuel cells tested at 90% RH show better performance except G_4 than other cells. Among them G_1 and G_3 has maximum lifetime, more than seven thousand voltage cycles i.e., 7500 and 7350 VC respectively and G8 exhibited minimum lifespan just 1500 VC.

5.6.3.1 Limiting Current Density Value

It is evident from the Polarization curves that all the fuel cells exhibited better performance in terms of the value of maximum current density when their cathodes were fed with oxygen rather than with air. With oxygen supply at the cathode side the highest value of limiting current density was evolved as 4.56A/cm^2 (for the fuel cell G_3) whereas with air supply at the cathode side the limiting current density value did not exceed even 3A/cm^2. The maximum value of limiting current density with air feed on cathode side was obtained as 2.52A/cm2 (for the same cell G_3). At the end of the lifetime of fuel cell G_6 operated at 60% RH, the minimum value of limiting current density (0.48A/cm^2) can be observed after 5500 voltage cycles while the cells tested at 90% RH exhibited larger values of limiting current density after completion of 7500 and 7350 VC (almost 2000 voltage cycles more than G_6) at the end of their life span. The values obtained from polarization curves are summarized in Table 5.38 and Table 5.39.

5.6.3.2 Cathode Resistance

For the fuel cells G, G_1 and G_2 Nyquist Plots were drawn only with oxygen supply at the cathode side but for all other cells G_3, G_4, G_5, G_6 and G_8 the Nyquist plots were recorded both with oxygen as well as with air feed on the cathode side of these cells.

Generally the cathode resistance was proved to be higher with air supply than that with oxygen supply at the cathode side of the same fuel cell. These results harmonize with the results obtained from polarization curves as with oxygen supply at the cathode side of the fuel cells higher values of limiting current densities were achieved than that with the air feed at the cathode side of these cells. Among these cells with oxygen feed the cathode of the fuel cell G_4 operated at 90% RH attained the maximum resistance (0.288 ohm) after 2000 voltage cycles whereas the cathodes of the cells G_1, G_3 and G_5 also operated at 90% RH did not gain such a high resistance even after accomplishment of 7500, 5000 and 5000 VC respectively. When air was supplied to the cathodes of the cells then the fuel cell G5 operated at 90% RH exhibited maximum cathode resistance of 0.148 ohm after completing 5000 VC. Table 5.40 and Table 5.41 show that the increase in the cathode resistance depends upon number of voltage cycles as well as value of relative humidity but with less value of relative humidity the cathode resistance was proved to be higher even when the life span of the cell was demonstrated to less number of voltage cycles.

The Electrochemical impedance spectra were recorded in galvanostatic mode with -3A. So when a fuel cell exhibited current less than -3A, EIS can not be measured. This was the case for the fuel cells; G_3 after 7350VC, G_5 after 5690VC, G_6 after 5000 and 5500 VC and G_8 after 1500 VC, with oxygen and air supply at the cathode side. Therefore Nyquist plots at these times were not possible to record.

Table 5.38: Detail from Polarization Curves with Oxygen supply at cathode side of the fuel cells.

Fuel Cells	Gas	Voltage Cycles	OCV (V)	Limiting. Current Density (A/cm^2)
G-81% RH	O_2	0	0.971	3.68
		1000	0.958	2.87
		3000	0.951	2.64
		5000	0.831	2.84
G_1-90% RH	O_2	0	0.981	3.73
		3000	0.953	3.08
		5000	0.896	1.28
		7500	0.831	0.85
G_2-70% RH	O_2	0	0.95	2.96
		1000	0.94	2.74
		3000	0.86	2.38
G_3-90% RH	O_2	0	0.977	4.56
		400	0.968	4.18
		1000	0.99	4.06
		1500	0.977	4.04
		2000	0.984	2.68
		3000	0.989	2.47
		5000	0.952	1.89
		7350	0.93	1.46
G_4-90% RH	O_2	0	0.982	3.85
		1000	0.968	3.05
		1500	0.952	1.59
		2000	0.971	1.02
G_5-90% RH	O_2	0	0.981	4.08
		1000	0.973	4.02
		1500	0.987	3.00
		2000	0.984	2.74
		3000	0.979	2.09
		5000	0.948	1.75
		5960	0.897	1.44
G_6-60% RH	O_2	0	0.96	2.14
		400	0.98	2.07
		1500	1.00	1.99
		2000	0.99	1.58
		3000	0.97	1.26
		5000	0.97	0.89
		5500	0.96	0.48
G_8-33% RH	O_2	0	0.97	3.06
		400	0.96	2.38
		1000	0.98	2.31
		1500	0.99	1.57

Table 5.39: Detail from Polarization Curves with Air supply at cathode side of the fuel cells

Fuel Cells	Gas	Voltage Cycles	OCV (V)	Limiting. Current Density (A/cm^2)
G-81% RH	Air	0	0.924	2.25
		3000	0.911	1.64
		5000	0.798	1.51
G_1-90% RH	Air	0	0.938	2.32
		3000	0.931	1.79
		5000	0.92	0.91
		7500	0.865	0.49
G_2-70% RH	Air	0	0.921	2.09
		1000	0.915	1.73
		3000	0.875	1.58
G_3-90% RH	Air	0	0.943	2.52
		1000	0.953	2.33
		1500	0.943	2.18
		2000	0.95	1.67
		3000	0.957	1.63
		5000	0.947	1.17
		7350	0.923	0.51
G_4-90% RH	Air	0	0.925	2.13
		1000	0.936	2.03
		1500	0.936	1.18
		2000	0.93	1.17
G_5-90% RH	Air	0	0.932	2.28
		1000	0.954	2.40
		2000	0.959	1.79
		3000	0.944	1.27
		5000	0.935	0.74
		5960	0.899	0.21
G_6-60% RH	Air	0	0.934	1.35
		400	0.958	1.66
		1000	0.959	1.17
		1500	0.963	0.94
		3000	0.935	0.62
		5000	0.934	0.42
		5500	0.912	0.22
G_8-33% RH	Air	0	0.933	2.17
		400	0.943	1.20
		1000	0.95	0.67
		1500	0.945	0.32

Table 5.40: Detail of resistances of all G-type fuel cells from Nyquist plots with oxygen supply at the cathode side

Fuel Cell	Gas	Voltage Cycles Completed	Membrane Resistance (a) (Ω)	Total Resistance (b) (Ω)	Cathode Resistance (b-a) (Ω)
G-81% RH	O_2	0	0.016	0.039	0.023
		1000	0.019	0.051	0.031
		3000	0.018	0.053	0.035
		5000	0.017	0.048	0.031
G_1-90% RH	O_2	0	0.021	0.039	0.019
		1000	0.029	0.051	0.022
		3000	0.026	0.051	0.024
		5000	0.045	0.107	0.062
		7500	0.054	0.164	0.111
G_2-70% RH	O_2	0	0.026	0.048	0.022
		1000	0.030	0.052	0.022
		3000	0.024	0.051	0.026
G_3-90% RH	O_2	0	0.017	0.037	0.020
		400	0.016	0.037	0.021
		1000	0.019	0.040	0.021
		1500	0.019	0.040	0.021
		3000	0.027	0.060	0.033
		5000	0.031	0.073	0.042
G_4-90% RH	O_2	0	0.021	0.042	0.021
		400	0.025	0.053	0.028
		1000	0.030	0.052	0.021
		1500	0.046	0.300	0.254
G_5-90% RH	O_2	0	0.019	0.038	0.0191
		400	0.018	0.038	0.021
		1000	0.019	0.040	0.021
		1500	0.024	0.049	0.025
		2000	0.023	0.052	0.029
		3000	0.031	0.066	0.035
		5000	0.036	0.077	0.040
G_6-60% RH	O_2	0	0.019	0.053	0.034
		1000	0.036	0.076	0.039
		1500	0.038	0.077	0.039
		2000	0.048	0.090	0.042
		3000	0.056	0.118	0.062
G_8-33% RH	O_2	0	0.019	0.042	0.023
		400	0.024	0.051	0.027
		1000	0.037	0.064	0.028

Table 5.41: Detail of resistances of all G-type fuel cells from Nyquist plots with air supply at the cathode side

Fuel Cell	Gas	Voltage Cycles Completed	Membrane Resistance (a) (Ω)	Total Resistance (b) (Ω)	Cathode Resistance (b-a) (Ω)
G_3-90% RH	Air	0	0.018	0.063	0.045
		1000	0.017	0.065	0.048
		1500	0.019	0.068	0.050
		2000	0.026	0.086	0.060
		3000	0.029	0.105	0.076
		5000	0.034	0.139	0.105
G_4-90% RH	Air	0	0.022	0.078	0.056
		400	0.031	0.085	0.054
		1000	0.031	0.081	0.050
		1500	0.058	0.120	0.062
G_5-90% RH	Air	0	0.0201	0.0613	0.041
		1000	0.0182	0.0669	0.049
		1500	0.0240	0.0796	0.056
		2000	0.0269	0.0870	0.060
		3000	0.0350	0.1320	0.097
		5000	0.0443	0.1920	0.148
G_6-60% RH	Air	400	0.033	0.094	0.061
		1000	0.040	0.133	0.093
		1500	0.047	0.160	0.113
		2000	0.057	0.188	0.131
G_8-33% RH	Air	0	0.021	0.073	0.052
		400	0.053	0.126	0.073
		1000	0.039	0.106	0.067

5.6.3.3 Active Pt Surface Area

From the cyclic voltammograms the active platinum surface area of all these cells were calculated. The cell examined at minimum value of relative humidity (33% RH) worked for less interval of time whereas the cell tested at highest value of relative humidity (90% RH) survived for long duration. At the end of the lifetime the active Pt surface area was proved to be minimum (0.56 m^2/g) for the cell G_2 operated at 70% RH. For the fuel cells whose lifespan is more than 5000 voltage cycles, the active pt surface area decreased gradually till 5000 VC but afterwards an abrupt reduction in it can be observed from the Table 5.42.

Table 5.42: Detail of active Pt surface area of all fuel cells

Fuel Cell	Voltage Cycles	Active Pt Surface Area (m^2/g)
G-(81% RH)	0	50
	1000	48
	3000	49
	5000	7
G1-(90% RH)	0	45.38
	1000	47.53
	3000	38.93
	5000	25.13
	7500	1.67
G2-(70% RH)	0	49.75
	1000	44.65
	3000	0.56
G3-(90%RH)	0	60
	400	57
	1000	51
	1500	45
	2000	38
	3000	33
	5000	25
	7350	4
G4-(90% RH)	0	63.19
	400	45.32
	1000	44.16
	1500	41.05
	2000	2.15
G5-(90% RH)	0	60.56
	1000	59.83
	1500	51.87
	2000	46.87
	3000	36.30
	5000	21.48
	5960	10.36
G6-(60% RH)	0	51.70
	400	41.62
	1000	32.78
	1500	29.53
	2000	26.15
	3000	17.42
	5000	10.45
	5500	3.37
G8-(33%RH)	0	55.13
	400	42.20
	1000	40.48
	1500	27.05

Table 5.43: % decrease in active Pt surface area at cathode side relative to the value before cycling

Fuel Cells	% loss in active Pt surface Area after 1000 VC	% loss in active Pt surface area after 3000 VC
G(81% RH)	4	2
G1(90% RH)	-4.7	14.2
G2(70% RH)	10.25	98.9
G3(90% RH)	15	45
G4 ((90% RH)	30.12	
G5(90% RH)	1.2	40.1
G6(60% RH)	36.6	66.3
G8(33% RH)	26.6	

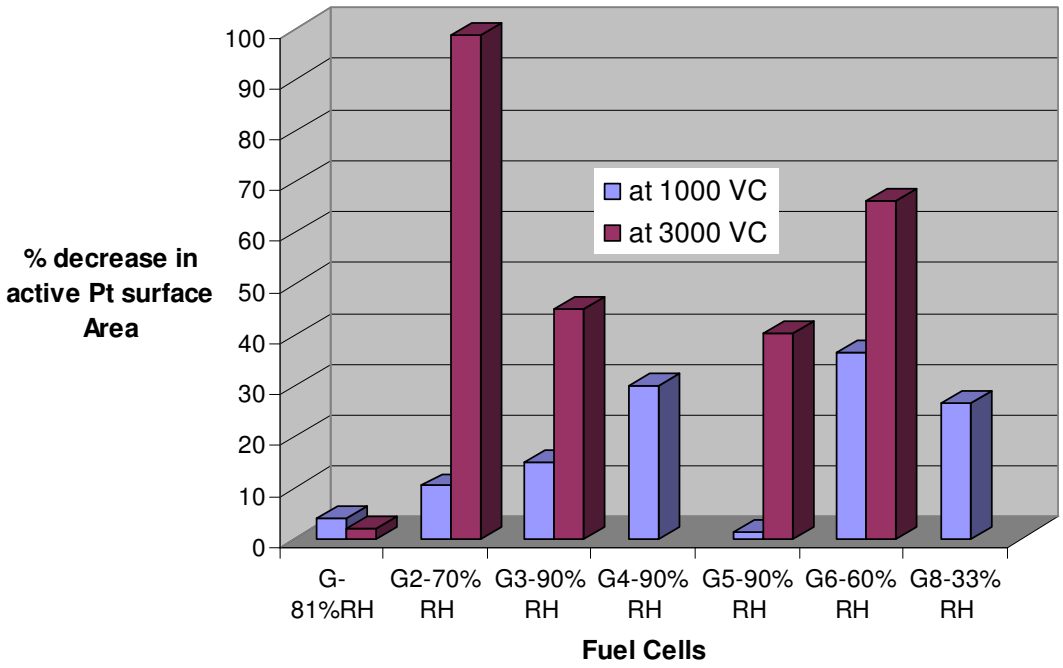

Figure 5.116: % loss in ECSA on cathode side of all G-type fuel cells after 1,000 and 3,000 VC.

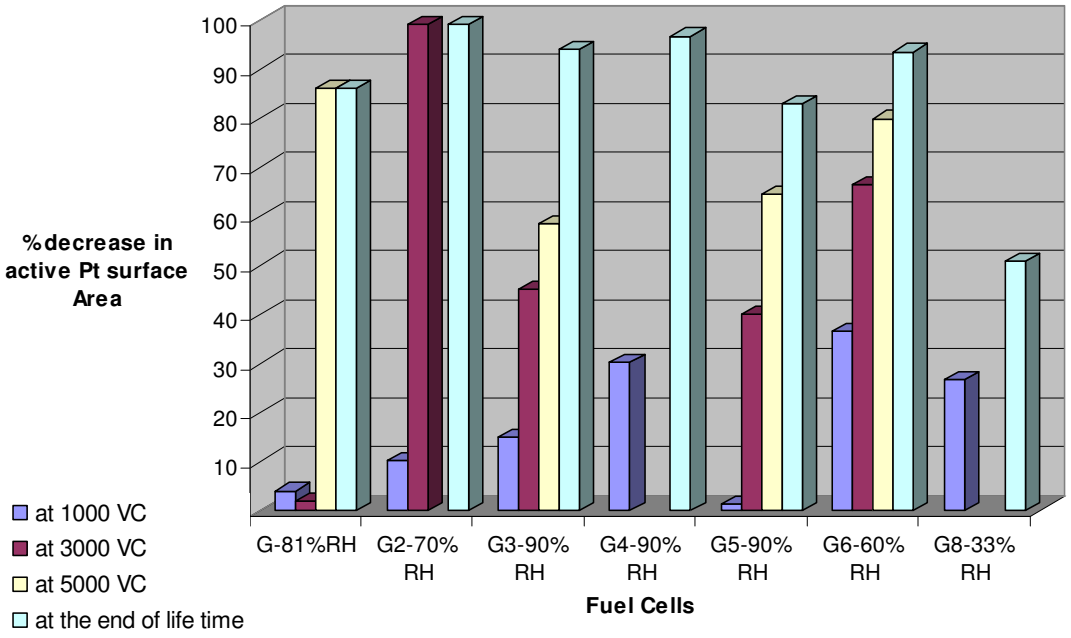

Figure: 5.117: % loss in ECSA on cathode side of all G-type fuel cells with the course of the test series

6 Comparison of the Two MEAs

Eleven fuel cell assemblies were built up to investigate the effect of humidity of reactant gases H2, O2 and air on the performance of the fuel cells with the accelerated voltage cycling tests. These cells were subjected to the relative humidity spanning from 33 to 90 %. Two different types of membrane electrode assemblies were utilized to build up these cells. Three cells were assembled with F type of MEA whereas the remaining eight cells were manufactured with G type of MEA. In F-type MEA the thickness of the membrane (50 micrometers) was higher than in G-type MEA (membrane thickness 18 micrometers). The amount of Pt catalyst loaded on the cathode side of F-type and G-type MEA was 0.6mg/cm^2 and 0.4mg/cm^2 respectively

The fuel cells were characterized by in-situ and ex-situ diagnostic techniques. Through in-situ characterization measurements polarization curves, electrochemical impedance spectra, cyclic voltammogramms and the hydrogen diffusion measurements were recorded and for ex-situ analyses the cathodes of all these cells were examined before starting the accelerated voltage cycling tests and after finishing the test series at the end of lifetime of each cell by scanning electron microscopy (SEM) and energy dispersive spectroscopy (EDS).

The fuel cells with F-type of MEA (F_1, F_2, F)were investigated for three different values of relative humidity (80%, 90% and 92%) respectively whereas the fuel cells with G-type MEA were examined for five different values of relative humidity (33%, 60%, 70%, 81% and 90%). The fuel cells G, G_2, G_6 and G_8 were analyzed at 81%, 70%, 60% and 33% RH respectively and the fuel cells G_1, G_3, G_4 and G_5 were tested at 90% RH The ultimate result of this study is that both types of MEA exhibited the best performance at 90% RH and worst at the lowest value of RH i.e., 80% RH for F-type and 33% RH for G-type of MEA.

6.1 Comparison of Both MEA at 90% RH

At 90% RH the fuel cell F_2 performed till 17536 voltage cycles while fuel cells G_1 and G_3 worked till 7500 and 7350 VC respectively. So the fuel cell F_2 with thicker membrane and higher Pt loading on cathode side gave performance for more than two times larger number of voltage cycles than that of fuel cell G_1 and G_3 having thinner membrane and less Pt loading on the cathode side.

6.2 Maximum value of Limiting Current Density

On the other hand with the oxygen supply at the cathode side the fuel cell with G-type MEA (G_3-90% RH) displayed higher value of limiting current density (4.56 A/cm^2) at 0.15 V as compare to the fuel cell with F-type MEA (F-92% RH) exhibiting maximum value of limiting current density as 3.25 A/cm^2 at the same potential. The difference between these two values is more than 1A/cm^2. Similar is the case when air was fed at the cathode side of the MEAs. The maximum value of limiting current density achieved by G-type MEA (G_3) is 2.52 A/cm^2 and for F-type (F) MEA is 1.99 A/cm^2 at 0.15 V. The difference here is almost 0.53A/cm^2. The F-type MEA F_2 at 90% RH showed limiting current density value as 2.22A/cm^2 and 1.18 A/cm^2 at 0.15 V when treated with oxygen and air respectively. These values are almost half of the values gained by G-type MEA at the same value of relative humidity (90% RH) and potential (0.15 V). It means that greater value of limiting current density can be obtained with thinner MEA having low Pt loading at the cathode side. It can also be distinguished from these results that both types of MEA demonstrated better performance when their cathodes were treated with oxygen rather than with air.

6.3 Cathode Resistance

For the F-type fuel cell maximum value of cathode resistance was emerged as 0.069 Ω after 12570 VC (F_1-80% RH)with oxygen feed at the cathode side while for the G-type fuel cell it is 0.111 Ω (G_1-90% RH) after 7500 VC. The fuel cell G_4 operated at 90% RH exhibited the maximum value of cathode resistance (0.288 Ω) after 2000 VC but the reason for such a high resistance is that after 1500 voltage cycles during recording the characterization curves the mass flow controller of the teststand did not work well and damage the fuel cell G_4 and the fuel cell F_2 operated at 90% RH attained a cathode resistance of 0.063 Ω after 17536 VC. It is evidently clear from these results that G-type MEA exhibited higher cathode resistance than that of F-type MEA after completing just half number of voltage cycles than F-type MEA at the end of their life time. So through electrochemical impedance spectroscopy the performance of F-type MEA was proved to be better than that of G-type of MEA. This was the case when the cathodes of the cells were treated with oxygen.

Electrochemical impedance spectra were also recorded when some G-type cells (G_3, G_4, G_5, G_6 and G_8) were supplied with air also at the cathode side. With air feed the fuel cell G_5, examined at 90% RH, achieved the maximum cathode resistance 0.148 Ω after finishing 5000 VC. The fuel cell G_6 examined at 60% RH, exhibited maximum cathode resistance 0.131 Ω after 2000 VC and the fuel cell G_8 tested at 33% RH have cathode resistance 0.067 Ω at the accomplishment of just 1000 VC. Actually for the fuel cell G_5 G_6 and G_8 after 5960, 3000 and 1500 VC respectively the electrochemical impedance spectra could not be recorded because they exhibited less than 3A current (set parameter).

6.4 Active Pt Surface Area

The active Pt surface area on the cathode side of each fuel cell was figured out with the help of cyclic voltammetry. Their detail is given in Table 4.17 and Table 5.42. For F-type MEA a decline of 52.6%, 72.6% and 63.4% was observed for the fuel cells F (92%RH), F1 (80% RH) and F2 (90% RH) at the end of their life cycle i.e., 10,000, 12570 and 17536 voltage cycles respectively. Actually the fuel cells F_1 between 10,000 to 12570 VC and F_2 between 15000 to 17536 VC were subjected accidently to severely dry operating conditions i.e., 25°C cell temperature instead of 70°C and cathode humidifier temperature 22°C instead of 68°C. These harsh conditions being affected on the overall performance of the fuel cells F_1 and F_2 otherwise they can work for longer duration. The temperature till 80°C has good effect on the performance of the PEM fuel cell due to improved kinetics and conduction processes. So the operation of these cells at low temperatures degraded the fuel cells.

In case of G-type of fuel cells a total reduction of more than 80% in the ECSA on cathode side of all the fuel cells except G_8 can be witnessed from the Table 5.42. The fuel cell G_8 was analyzed at 33% RH and this cell experienced a total decrease of 50.9% in the active Pt surface area (ECSA) on the cathode side at the end of its life time i.e., 1500 voltage cycles. Maximum ECSA loss (98.9%) was occurred in fuel cell G_2 operated at 70% RH (Figure: 5.117).

The electrochemical surface area loss may be attributed to the dissolution of platinum particles due to the crossover of reactant gases, degradation of the carbon support and the increase of ohmic resistance.

6.5 Membrane Degradation

Hydrogen diffusion measurements were recorded at the end of the accelerated voltage cycling test series for all the fuel cells. For the two cells G_6 and G_8, these characteristics were collected through

out the experiment along with the measurements of other characterization curves. At the end of the lifetime of the cells these graphs exhibit the elevated value of current density that is a proof of cracking and pinholes formation in the membranes. Basically cracks and pinholes in the membrane lead the gas crossover across the membrane and due to the chemical reaction taking place between hydrogen and oxygen heat is produced which is enough to melt the polymer, burn the catalyst and form further pinholes in the MEA. Therefore its ultimate effect is cell failure. So the membrane deterioration has a big impact on the cell performance.

6.6 Ex-situ Analyses

When the potential of the fuel cells became less than 0.9V, then they cannot operate through the set parameter of voltage cycles between 0.9V and 0.7V. At this time further accelerated voltage cycling test was stopped and the last time in-situ analyses by recording the characterization curves as well as the first time ex-situ analyses for all the cells were performed with the help of scanning electron microscope and energy dispersive spectroscope. The SEM images represented the deterioration of the cathode of the fuel cells with the agglomeration of the Pt (catalyst) particles, detachment of the Pt particles from the carbon support and migration of Pt particles from the cathode to the membrane. Cracks appeared on the cathode surfaces can also be prominently observed from these images.

The chemical analyses of the cathode surface of the fuel cells with the help of energy dispersive spectra show the high counts of silicon (Si) present on the cathode surfaces of the cells which were not present on the images with fresh MEAs. This silicon may be attributed from the sealing material made up of silicon.

7 Conclusion

The significant (noteworthy) result of this research work is that a decline in the life span of a PEM fuel cell was prominently observed by reducing the relative humidity of the inlet gases. Generally the results can be summarized as follows.

- A continuous decrease in the active Pt surface area can be detected with the increase in number of voltage cycles.
- For the G-type cells whose lifetime was established as more than 5000 VC, a gradual reduction in the active Pt surface area was observed till 5000 VC but afterwards an abrupt decline in the value of active Pt surface area was notified.
- Lifespan of the fuel cells analyzed at 90% RH was proved to be maximum.
- Life time of thicker MEA (50µm membrane thickness) and with higher Pt loading (0.6mg/cm^2) on cathode side is considerably higher than the life time of the thinner MEA (18 µm membrane thickness) with less amount of Pt loading (0.4mg/cm^2) on the cathode side.
- The maximum value of limiting current density was obtained for thinner MEA with less Pt loading.
- Better performance of the MEAs was exhibited with oxygen feed at the cathode side than that of air feed.
- The cathode resistance of the G-type MEA (thinner membrane and low Pt loading) was observed to be higher after completing less than half number of voltage cycles as compare to F-type MEA (thicker membrane and high Pt loading)
- It is also evident from the hydrogen diffusion current measurements for all the fuel cells that accelerated voltage cycling test series (artificial aging test) also affected the membrane of the cells with the formation of cracks and pinholes which are the major reasons of membrane deterioration and finally the fuel cell failure.
- Cross-sectional SEM images exhibit the thinning of the cathode side, the agglomeration of Pt particles and migration of Pt particles from cathode to the membrane with the course of the accelerated voltage cycling test. Prominent cracks can be observed on the cathode surface of the cells.
- Energy dispersive spectra eminently show the high counts of silicon present on the cathode surface of the fuel cells after accelerated voltage cycling test.

8 Appendix

8.1 Table of Abbreviations

AST	Accelerated Stress Test
BSE	Back scattered electrons
CV	Cyclic Voltammetry
CRT	Cathode-Ray Tube
EBIC	Electron Beam Induced Current
ECSA	Electrochemical Active Surface Area
EDXS	Energy Dispersive X-Ray Spectroscopy
EIS	Electrochemical Impedance Spectroscopy
FCV	Fuel Cell Vehicle
GDL	Gas Diffusion Layer
H	Hours
MCA	Multi Channel Analyzer
MEA	Membrane Electrode Assembly
OCV	Open Circuit Voltage
PC	Polarization Curve
PD	Power Density
PEMFC	Polymer Electrolyte Membrane Fuel Cell
RH	Relative Humidity
SC	Specimen Current
SEM	Scanning Electron Microscopy
TEM	Transmission Electron Microscopy
VC	Voltage Cycles

8.2 Table of Figures

8.3 Table of Tables

8.4 Equipments used for Laboratory Analyses

Following equipments were used for characterization of the fuel cells at two different laboratories.

8.4.1 At Laboratory for Fuel Cell Systems

(Steyrergasse 21, 8010 Graz)

Laboratory Balance:	KERN-572, KERN & Sohn GmbH, D-72336 Balingen, Germany Series Nr. W020779
Gasket Preparation:	Elecometer 4340- automatic Film Applicator,
	Elcometer3580,
	Universal Relaisbox. R 10 Elöectronics (mgw Lauda)
Electrochemical Workstation:	Zahner, IM6eX
Power Potentiostat:	Zahner, PP240
Water Heater:	Julabo MC-4
Oil Heater:	Julabo MC-6

8.4.2 At FELMI-ZFE Graz

(Steyrergasse 17, 8010 Graz)

Scanning Electron Microscope:	Zeiss Ultra 55
Energy Dispersive X-Ray Spectrometer:	EDAX phoenix

8.5 References

1 U.S. Energy Information Administration**,** Office of Integrated Analysis and Forecasting, U.S. Department of Energy, Washington, DC, **International Energy out look 2010**, www.eia.gov/oiaf/ieo/index.html.

2 European commission community research, **Hydrogen energy and fuel cells, a vision of our future** downloaded on 11.04.2011. http://ec.europa.eu/research/energy/pdf/hydrogen-report_en.pdf

3 Yun Wang, Ken S. Chen, Jeffrey Mishler, Sung Chan Cho, Xavier Cordobes Adroher, **A review of polymer electrolyte membrane fuel cells: Technology, applications,and needs on fundamental research,** Applied Energy xxx (2010) xxx–xxx.

4 Dr. Dimitrios Papageorgopoulos*,* US DOE Fuel Cell Technologies Program*,* **An Introduction to the 2010 Fuel Cell Pre-Solicitation Workshop,** Lakewood, Colorado March 16, 2010March 2010

5 Craig Gittleman, David Mastenand Scott Jorgensen, James Waldecker, Shinichi Hirano and Mark Mehall**, Automotive Fuel Cell R&D Needs** in DOE Fuel Cell Pre-Solicitation Workshop. Department of Energy, Lakewood, Colorado; 2010

6 Ayfer Veziroglu , Rosario Macario, **Fuel cell vehicles: State of the art with economic and environmental concerns,** international journal of hydrogen energy XXX (2010) 1-19.

7 Munazza Mohsin, Viktor Hacker,**Life time investigation of polymer electrolyte fuel cells under accelerated voltage cycling test,** Fundamentals and Developments of Fuel Cells Conference, 19th-21st January, 2011.

8 Viktor. Hacker, Lecture notes of the course, **Hydrogen Technology and Fuel Cell Systems**, course code 637.013, summer semester 2007, Institute of Chemical engineering and Environmental technology, TUGraz, Austria.

9 **NIST. PEM Fuel Cells. 2006**. <http://www.physics.nist.gov/MajResFac/NIF/pemfuelcells.html >.

10 **DOE-EERE. FCT fuel cells: types of fuel cells; 2009** <https://www1.eere.energy.gov/hydrogenandfuelcells/fuelcells/fc_types.html > [05.28.10]

11 Yun Wanga, Ken S. Chen, Jeffrey Mishler, Sung Chan Cho, Xavier Cordobes Adroher, **A review of polymer electrolyte membrane fuel cells: Technology, applications, and needs on fundamental research**, Applied Energy xxx (2010) xxx–xxx

12 Viktor Hacker, Simon Fraser, Kurt Friedrich, Juergen O. Besenhard, **The Role of Fuel Cells as key Technology in Transition to Clean energy for Transportation**, 19th world energy congress, 5-9 September 2004, Sydney, Australia.

13 Borup R, Meyers J, Pivovar B, Seung Kim Y, Mukundan R, Garland N, et al. **Scientific aspects of polymer electrolyte fuel cell durability and degradation,** Chem Rev 2007;107 (10): 3904-51

14 Rohit Makharia,a Shyam S. Kocha,a Paul T. Yu,a Mary Ann Sweikart,b Wenbin Gu,a Frederick T. Wagner,a Hubert A. Gasteiger a, **DURABLE PEM FUEL CELL ELECTRODE MATERIALS: REQUIREMENTS AND BENCHMARKING METHODOLOGIES,** ECS Transactions, 1 (8) 3-18 (2006)

15 P. J. Ferreira, G. J. la O', Y. Shao-Horn,a, D. Morgan, R. Makharia, S. Kocha, and H. A. Gasteiger, **Instability of Pt/C Electrocatalysts in Proton Exchange Membrane Fuel Cells,** *Journal of The Electrochemical Society,* **152** (11) A2256-A2271 (2005)

16 Rod L. Borup, John R. Davey, Fernando H. Garzon, David L Wood, Michael A. Inbody, **PEM fuel cell electrocatalyst durability measurements,** Journal of Power Sources 163 (2006) 76–81

17 Mark K. Debe∗, Alison K. Schmoeckel, George D. Vernstrom, Radoslav Atanasoski, **High voltage stability of nanostructured thin film catalysts for PEM fuel cells,** Journal of Power Sources 161 (2006) 1002–1011.

18 Ping Yu, Marianne Pemberton, Paul Plasse, **PtCo/C cathode catalyst for improved durability in PEMFCs,** Journal of Power Sources 144 (2005) 11–20

19 Wu Bi, Gary E. Gray, and Thomas F. Fullera, **PEM Fuel Cell Pt/C Dissolution and Deposition in Nafion Electrolyte,** *Electrochemical and Solid-State Letters,* **10** (5) B101-B104 (2007)

20 Rod Borup, John Davey, HuiXu, Axel Ofstad, Fernando Garzon, Bryan Pivovar, **PEM Fuel Cell Durability, 2008 DOE Hydrogen Program Review,** June 9-13, 2008

21 Wu Bi, Qunhui Sun, Yulin Deng, Thomas F. Fuller .**The effect of humidity and oxygen partial pressure on degradation of Pt/C catalyst in PEM fuel cell,** Electrochimica Acta 54 (2009) 1826–1833

22 Dongho Seo, Junghyun Lee, Sangsun Park, Junki Rhee, Sung Won Choi, Yong-Gun Shul, **Investigation of MEA degradation in PEM fuel cell by on/off cyclic operation under different humid conditions,** International Journal of Hydrogen Energy xxx (2010) 1–9

23 Qunhui Guo, Zhigang Qi , **Effect of freeze-thaw cycles on the properties and performance of membrane-electrode assemblies,** Journal of Power Sources 160 (2006) 1269–1274

24 Sang-Yeop Lee, Hyoung-Juhn Kim, EunAe Cho, Kug-Seung Lee, Tae-Hoon Lim, In Chul Hwang, Jong Hyun Jang**, Performance degradation and microstructure changes in freeze thaw cycling for PEMFC MEAs with various initial microstructures,** International Journal of Hydrogen Energy 35(2010) 12888-12896

25 Maji Luo, Chengyong Huang, Wei Liu, Zhiping Luo, Mu Pan**, Degradation behaviors of polymer electrolyte membrane fuel cell under freeze/thaw cycles,** International Journal of Hydrogen Energy 35(2010) 2986-2993

26 Soo-Jin Lim, Gu-Gon Park, Jin-Soo Park, Young-Jun Sohn, Sung-Dae Yim, Tae-Hyun Yang, Bo Ki Hong, Chang-Soo Kim, **Investigation of freeze/thaw durability in polymer electrolyte fuel cells,** International Journal of Hydrogen Energy 35(2010) 13111-13117.

27 Wolfgang Schmittinger, Ardalan Vahidi, **A review of the main parameters influencing the long – term performance and durability of PEM fuel cells**., Journal of Power sources 180 (2008) 1-14

28 Shengsheng Zhang, Xiaozi Yuan, Haijiang Wang, Walter Me´ridaa, Hong Zhu, Jun Shen, Shaohong Wu, Jiujun Zhang, **A review of accelerated stress tests of MEA durability in PEM fuel cells,** International Journal of Hydrogen energy 34(2009) 388-404.

29 Dennis E. Curtin, Robert D. Lousenberg, Timothy J. Henry, Paul C. Tangeman, Monica E. Tisack, **Advanced materials for improved PEMFC performance and life,** Journal of Power Sources 131 (2004) 41–48

30 Mei Cai, Martin S. Ruthkosky, Belabbes Merzougui, Swathy Swathirajan, Michael P. Balogh, Se H. Oh, **Investigation of thermal and electrochemical degradation of fuel cell catalysts,** Journal of Power Sources 160 (2006) 977–986

31 V. A. T. Dam and F. A. de Bruijn, **The Stability of PEMFC Electrodes, Platinum Dissolution vs. Potential and Temperature Investigated by Quartz Crystal Microbalance,** *Journal of The Electrochemical Society,* **154** (5) B494-B499 (2007)

32 Jian Xie, David L. Wood III, Karren L. More, Plamen Atanassov, and Rodney L. Borup, **Microstructural Changes of Membrane Electrode Assemblies during PEFC Durability Testing at High Humidity Conditions,** *Journal of The Electrochemical Society,* **152 (**5) A1011-A1020 (2005).

33 Rod L. Borup, John R. Davey, Fernando H. Garzon, David L Wood, Paul M. Welch and Karren More, **PEM FUEL CELL DURABILITY WITH TRANSPORTATION TRANSIENT OPERATION,** ECS Transactions, 3 (1) 879-886 (2006)

34 Hui Xu, Russell Kunz, and James M. Fenton**, Investigation of Platinum Oxidation in PEM Fuel Cells at Various Relative Humidities,** *Electrochemical and Solid-State Letters,* **10** (1) B1-B5 (2007)

35 Shengsheng Zhang, Xiao-Zi Yuan, Jason Ng Cheng Hin, HaijiangWang, K. Andreas Friedrich, Mathias Schulze, **A review of platinum-based catalyst layer degradation in proton exchange membrane fuel cells,** Journal of Power Sources 194 (2009) 588–600

36 Xiaoping Wang, Romesh Kumar, and Deborah J. Myers, **Effect of Voltage on Platinum Dissolution Relevance to Polymer Electrolyte Fuel Cells,** *Electrochemical and Solid-State Letters,* **9** (5) A225-A227 (2006).

37 Wu Bi, Gary E. Gray, and Thomas F. Fuller**, PEM Fuel Cell Pt/C Dissolution and Deposition in Nafion Electrolyte,** *Electrochemical and Solid-State Letters,* **10** (5) B101-B104 (2007)

38 Wu Bi and Thomas. F. Fuller**, Temperature Effects on PEM Fuel Cells Pt/C Catalyst Degradation,** *Journal of The Electrochemical Society,* **155** (2) B215-B221 (2008)

39 E. Guilminot, A. Corcella, F. Charlot, F. Maillard and M. Chatenet**, Detection of Ptz+ Ions and Pt Nanoparticles Inside the Membrane of a Used PEMFC,** *Journal of The Electrochemical Society,* **154** (1) B96-B105 (2007)

40 Kazuaki Yasuda, Akira Taniguchi, Tomoki Akita, Tsutomu Ioroi, and Zyun Siroma, **Characteristics of a Platinum Black Catalyst Layer with Regard to Platinum Dissolution Phenomena in a Membrane Electrode Assembly,** *Journal of The Electrochemical Society,* **153** (8) A1599-A1603 (2006)

41 Xuan Cheng, Zheng Shi, Nancy Glass, Lu Zhang, Jiujun Zhang, Datong Song, Zhong-Sheng Liu, Haijiang Wang, Jun Shen, **A review of PEM hydrogen fuel cell contamination: Impacts, mechanisms, and mitigation,** Journal of Power Sources 165 (2007) 739–756

42 Fernando H. Garzon, Tommy Rockward, Idoia G. Urdampilleta, Eric L. Brosha and Francisco A. Uribe, **The Impact of Hydrogen Fuel Contaminates on Long-Term PMFC Performance,** ECS, Transactions, 3 (1) 695-703 (2006)

43 R. Mohtadi, W.-k. Lee, J.W. Van Zee, **Assessing durability of cathodes exposed to common air impurities,** Journal of Power Sources 138 (2004) 216–225

44 Wentao Wang, Woo-kum Lee and John W. Van Zee, **A Model for SO2 Impurity in Air Fed to a Proton Exchange Membrane Fuel Cell**, ECS Transactions, 1 (8) 131-137 (2006)

45 Francisco A. Uribe, Shimshon Gottesfeld, and Thomas A. Zawodzinski, Jr, **Effect of Ammonia as Potential Fuel Impurity on Proton Exchange Membrane Fuel Cell Performance,** *Journal of The Electrochemical Society*, **149** (3) A293-A296 (2002)

46 Andrew L. Dicks, **The role of carbon in fuel cells,** Journal of Power Sources 156 (2006) 128–141

47 Kinoshita K. **Carbon, electrochemical and physicochemical properties**. New York: John Wiley & Sons; 1988 in Shengsheng Zhang, Xiaozi Yuan, Haijiang Wang, Walter Me´ridaa, Hong Zhu, Jun Shen, Shaohong Wu, Jiujun Zhang. **A review of accelerated stress tests of MEA durability in PEM fuel cells,** International Journal of Hydrogen energy 34(2009) 388-404.

48 Paul T. Yu, Wenbin Gu, Rohit Makharia, Frederick T. Wagner, Hubert A. Gasteiger, **The Impact of Carbon Stability on PEM Fuel Cell Startup and Shutdown Voltage Degradation**, ECS Transactions, 3 (1) 797-809 (2006)

49 Jeremy P. Meyers and Robert M. Darling, **Model of Carbon Corrosion in PEM Fuel Cells,** *Journal of The Electrochemical Society,* **153** (8) A1432-A1442 (2006)

50 T. F. Fuller and Gary Gray, **Carbon Corrosion Induced by Partial Hydrogen Coverage,** ECS Transactions, 1 (8) 345-353 (2006).

51 T. R. Ralph, S. Hudson, and D. P. Wilkinson, **ELECTROCATALYST STABILITY IN PEMFCs AND THE ROLE OF FUEL STARVATION AND CELL REVERSAL TOLERANT ANODES**, ECS Transactions, 1 (8) 67-84 (2006)

52 Hiroshi Chizawa, Yasuji Ogami, Hiroshi Naka, Atsushi Matsunaga, Nobuo Aoki and Tsutomu Aoki, **Study of Accelerated Test Protocol for PEFC Focusing on Carbon Corrosion,** ECS Transactions, 3 (1) 645-655 (2006)

53 Rohit Makharia, Shyam S. Kocha, Paul T. Yu, Mary Ann Sweikart, Wenbin Gu, Frederick T, Wagner, Hubert A. Gasteiger, **DURABLE PEM FUEL CELL ELECTRODE MATERIALS: REQUIREMENTS AND BENCHMARKING METHODOLOGIES**, ECS Transactions, 1 (8) 3-18 (2006)

54 Hao Tang, Zhigang Qi, Manikandan Ramani, John F. Elter, **PEM fuel cell cathode carbon corrosion due to the formation of air/fuel boundary at the anode,** Journal of Power Sources 158 (2006) 1306–1312

55 Yun Wang**, Analysis of the Key Parameters in the Cold Start of Polymer Electrolyte Fuel Cells,** *Journal of The Electrochemical Society,* **154** (10) B1041-B1048 (2007)

56 Hiroshisa Yoshida and Yuka Miura, **Behavior of water in perfluorinated ionomer membranes containing various monovalent cations,** *Journal* of *Membrane Science, 68* (1992) l-10

57 Yukio Hishinuma, Takemi Chikahisa, Fumio Kagami, Tomohiro Ogawa, **The design and performance of a PEFC at a Temperature Below Freezing**, JSME International Journal Ser B 47(2), 235-41, (2004).

58 L. M. Roen, C. H. Paik, and T. D. Jarvi, **Electrocatalytic Corrosion of Carbon Support in PEMFC Cathodes,** *Electrochemical and Solid-State Letters*, **7** (1) A19-A22 (2004).

59 S. Maass, F. Finsterwalder, G. Frank, R. Hartmann, C. Merten, **Carbon support oxidation in PEM fuel cell cathodes,** Journal of Power Sources 176 (2008) 444–451.

60 Ryan O`Hayre, Suk-won Cha, Whitney, Colella, Fritz B. Prinz, **FUEL CELL FUNDAMENTALS**, second edition, John Wiley & Sons (2009)

61 Vladimir Gurau, Michael J. Bluemle, Emory S. De Castro, Yu-Min Tsou, J. Adin Mann Jr., Thomas A. Zawodzinski Jr., **Characterization of transport properties in gas diffusion layers for proton exchange membrane fuel cells 1. Wettability (internal contact angle to water and surface energy of GDL fibers),** Journal of Power Sources 160 (2006) 1156–1162

62 Soowhan Kim, Byung Ki Ahn, M.M. Mench, **Physical degradation of membrane electrode assemblies undergoing freeze/thaw cycling: Diffusion media effects,** Journal of Power Sources 179 (2008) 140–146

63 Rangachary Mukundan, Yu Seung Kim, Fernando Garzon, and Bryan Pivovar, **FREEZE/THAW EFFECTS IN PEM FUEL CELLS**, ECS Transactions, 1 (8) 403-413 (2006)

64 D. Wood, J. Davey, F. Garzon, P. Atanassov, R. L. Borup, **Fuel cell seminar 2005**. Palm Springs, CA; November 2005

65 J. W. Frisk, M. T. Hicks, R. T. Atanasoski, W. M. Boand, A. K. Schmoeckel, M. J. Kurkowski, **MEA Component Durability,** Fuel Cell Seminar, San Antonio, TX USA, November 2004

66 Charles Lee, Walter M´erida, **Gas diffusion layer durability under steady-state and freezing conditions**, Journal of Power Sources 164 (2007) 141–153

67 D.A. Steven, J.M. Rouleu, R.E. Mar, A. Bonakdarpour, Characterization and PEMFC Testing of Pt1-x Mx (M = Ru, Mo, Co, Ta, Au, Sn) Anode Electrocatalyst composition spreads, Journal of the Electrochemical Society, 154(6), B566-B576, (2007).

68 Gaetano Squadrito , ***PEFC Testing protocol: MEA Preparation****, 3rd International summer school on Advanced Studies of Polymer Electrolyte Fuel Cells, Graz University of Technology, Graz, Austria.*

69 D.A.Jones, **Principles and Prevention of corrosion**, Prentice Hall, Upper Saddle River, NJ (1996), In D.A. Steven, J.M. Rouleu, R.E. Mar, A. Bonakdarpour, **Characterization and PEMFC Testing of Pt1-x** Mx (M = Ru, Mo, Co, Ta, Au, Sn) Anode Electrocatalyst composition spreads, Journal of the Electrochemical Society, 154(6), B566-B576, (2007).

70 T. R. Ralph and M. P. Hogarth, Platinum Met. Rev., 46, 117 (2002).

71 J. H. Wee and K. Y. Lee, J. Power Sources, 157, 128(2006) in D.A. Steven, J.M. Rouleu, R.E. Mar, A. Bonakdarpour, **Characterization and PEMFC Testing of Pt1-x Mx (M = Ru, Mo, Co, Ta, Au, Sn) Anode Electrocatalyst composition spreads**, Journal of the Electrochemical Society, 154(6), B566-B576, (2007).

72 H. A. Gasteiger, N. Markovic, P. N. Ross, and E. J. Cairns, J. Phys. Chem., 98,617(1994) in D.A. Steven, J.M. Rouleu, R.E. Mar, A. Bonakdarpour, Characterization and PEMFC Testing of Pt1-x Mx (M = Ru, Mo, Co, Ta, Au, Sn) Anode Electrocatalyst composition spreads, Journal of the Electrochemical Society, 154(6), B566-B576, (2007).

73 M. Watanabe, M. Uchida, and S. Motoo, J.Electroanal. Chem. Interfacial Electrochem., 229, 395(1987).

74 E. Ticanelli, J. G. Beery, M. T. Paffett, and S. Gottesfeld, J. Electroanal. Chem. Interfacial Electrochem., 258, 61(1989).

75 M. Krausa and W. Vielstich, J. Electroanal. Chem., 379, 307(1994).

76 S. Mukerjee, S. J. Lee, E..,A.Ticianelli,J.McBreen, B. N. Grgur, N. M. Markovic, P. N. Ross, J. R. Giallombardo, and E. S. De Castro, Electrochem. Solid-State Lett

2, 12 (1999).

77] S. Mukerjee and R. C. Urian, Electrochim. Acta, 47, 3219(2002).

78 C. Kwak, T. J. Park, and D. J. Suh, Chem. Eng. Sci., 60, 1211(2005).

79] J. Yan, J. X. Ma, P. Cao, and P. Li, Catal. Lett., 93, 55(2004).

80 T. Page, R. Johnson, J. Hormes, S. Noding, and B. Rambabu, J. Electroanal.Chem., 485, 34 (2000).

81 S. Mukerjee and S. Srinivasan, J. Electroanal. Chem., 357, 201(1993).

82 J. R. C. Salgado, E. Antolini, and E. R. Gonzalez, J. Phys. Chem. B, 108, 17767(2004).

83 E. Antolini, J. R. C. Salgado, M. J. Giz, and E. R. Gonzalez, Int. J. Hydrogen Energy, 30, 1213(2005).

84 E. Antolini, J. R. C. Salgado, and E. R. Gonzalez, Appl. Catal., B, 63, 137(2006).

85 J. Luo, M. M. Maye, N. N. Kariuki, L. Y. Wang, P. Njoki, Y. Lin, M. Schadt, H. R.

Naslund, and C. J. Zhong, Catal. Today, 99, 291(2005).

86 D. Cameron, R. Holliday, and D. Thompson, J. Power Sources, 118, 298(2003).

87 H. A. Gasteiger, N. M. Markovic, and P. N. Ross, J. Phys. Chem., 99, 8945 (1995).

88 F. Colmati, E. Antolini, and E. R. Gonzalez, Electrochim. Acta, 50, 5496 (2005).

89 A. Bonakdarpour, R. Lobel, S. Sheng, T. L. Monchesky, and J. R. Dahn, J. Electrochem.

Soc., 153, A2304(2006).

90 D. C. Papageorgopoulos, M. Keijzer, and F. A. de Bruijn, Electrochim. Acta, 48, 197(2002).

91 N.Travitsky, T.Ripenbein, D.Golodnitsky, Y.Rosenberg, **Pt-, PtNi- and PtCo-supported catalysts for oxygen reduction in PEM fuel cells**, Journal of Power Source, 161 (2006), 782-789.

92 D.A. Landsman, US Patent 4,316,944 (1982).

93 E. Antolini, *Mater. Chem. Phys.* **78** (2003), p. 563).

94 S. Mukerjee, S. Srinivasan, M.P. Soriaga and J. McBreen, *J. Electrochem. Soc.* **142** (1995), p. 1409.

95 V. Stamenkovi´c, T.J. Schmidt, P.N. Ross, N.M. Markovi´c, J. Phys. Chem. B 106 (2002) 11970.

96 T. Toda, H. Igrashi, H. Uchida, M.Watanabe, J. Electrochem. Soc. 146 (10)

(1999) 3750.

97 M. Min, J. Cho, K. Cho, H. Kim, Electrochim. Acta 45 (2000) 4211.

98 E. Antolini, J.R.C. Salgado, E.R. Gonzales, J. Electroanal. Chem. 580 (2005) 145.

99 P. Stonehart, *J. Appl. Electrochem.* **22** (1992), p. 995 in N. Travitsky, T. Ripenbein, D. Golodnitsky, Y. Rosenberg, **Pt-, PtNi- and PtCo- Supported Catalyst for Oxygen reduction in PEM fuel cells**, Journal of Power Source, 161 (2006), 782-789.

100 Vito Di Noto, Enrico Negro, Sandra Lavina, Silvia Gross, **Pd – Co Carbon – nitride electrocatalysts for Polymer electrolyte fuel cells**, Electrochimica Acta, xxx (2007), xxx-xxx.

101 J.L. Fernandez, D.A. Walsh and A.J. Bard, *J. Am. Chem. Soc.* **127** (2005), p. 357.

102 Information retrieved on: http://www.advfn.com/p.php?pid=commodities&cb=1163783522&btn=allcomms&gid=PM in Vito Di Noto, Enrico Negro, Sandra Lavina, Silvia Gross, **Pd – Co Carbon – nitride electrocatalysts for Polymer electrolyte fuel cells**, Electrochimica Acta, xxx (2007), xxx-xxx.

103 M.H. Shao, K. Sasaki and R.R. Adzic, *J. Am. Chem. Soc.* **128** (2006), p. 3526.

104 Abhishek Guha, Weijie Lu, Thomas A.Zawodzinski Jr, David, A.Schiraldi, **Surface – modified Carbons as Platinum Catalyst support for PEM fuel cells**,Carbon, 45 (2007), 1506-1517.

105 K. Kinoshita, **Carbon electrochemical and physicochemical properties**, Wiley (1988) pp. 22–3 in Abhishek Guha, Weijie Lu, Thomas A.Zawodzinski Jr, David, A.Schiraldi, Surface – modified Carbons as Platinum Catalyst support for PEM fuel cells,Carbon, 45 (2007), 1506-1517.

106 P. Serp, M. Corrias and P. Kalck, Carbon nanotubes and nanofibers in catalysis, *Appl Catal A: Gen* **253** (2003), pp. 337–358.

107 M. Maeda, A. Hagiwara, H. Sotouchi, H. Sato,

X. Zhao, S. Morikawa, O. Kato, Electrochemistry 67 (1999) 155. in Yuyan Shao, Geping Yin, Zhenbo Wang, Yunzhi Gao, **Proton exchange membrane fuel cell from low temperature to high temperature,: Material challenges**, Journal of Power Sources, 167(2007), 235-242.

108 V. Lordi, N. Yao and J. Wei, **Method for supporting platinum on single-walled carbon nanotubes for a selective hydrogenation catalyst**, *Chem Mater* **13** (2001), pp. 733–737.

109 R. Yu, L. Chen, Q. Liu, J. Lin, K. Tan and S.C. Ng *et al.*, **platinum deposition on carbon nanotubes via chemical modification**, *Chem Mater* **10** (1998), pp. 718–722.

110 M.J. Toebes, M.K. van der Lee, L.M. Tang, M.H. Huis in 't Veld, J.H. Bitter and A. Jos van Dillen *et al.*, **Preparation of carbon nanofiber supported carbon and ruthenium catalysts: comparison of ion adsorption and homogeneous deposition precipitation**, *J Phys Chem B* **108** (2004), pp. 11611–11619.

111 C. He, S. Desai, G. Brown and S. Bollepalli, *Interface* **14** (2005), p. 41.

112 X. Wang, W.Z. Li, Z.W. Chen, M. Waje and Y.S. Yan, *J. Power Sources* **158** (2006), p. 154.

113 Y.H. Liu, B.L. Yi, Z.G. Shao, D.M. Xing and H.M. Zhang, *Electrochem. Solid State Lett.* **9** (2006), p. A356.

114 P.H. Matter, L. Zhang and U.S. Ozkan, *J. Catal.* **239** (2006), p. 83.

115 P.H. Matter and U.S. Ozkan, *Catal. Lett.* **109** (2006), p. 115.

116 S. Maldonado and K.J. Stevenson, *J. Phys. Chem. B* **109** (2005), p. 4707.

117 C.K. Acharya and C.H. Turner, *J. Phys. Chem. B* **110** (2006), p. 17706

118 D.A. Stevens and J.R. Dahn, *Carbon* **43** (2005), p. 179.

119 T.J. Schmidt, U.A. Paulus, H.A. Gasteiger and R.J. Behm, *J. Electroanal. Chem.* **508** (2001), p. 41.

120 F. Jayat, C. Lembacher, U. Schubert and J.A. Martens, *Appl. Catal. B* **21** (1999), p. 221.

121 R. Burch and D. Ottery, *Appl. Catal. B* **13** (1997), p. 105.

122 J. Després, M. Elsener, M. Koebel, O. Kröcher, B. Schnyder and A. Wokaun, *Appl. Catal. B* **50** (2004), p. 73

123 M.A. Hickner and B.S. Pivovar, Fuel Cells 5 (2005), p. 213. in Yuyan Shao, Geping Yin, Zhenbo Wang, Yunzhi Gao, **Proton exchange membrane fuel cell from low temperature to high temperature,: Material challenges**, Journal of Power Sources, 167(2007), 235-242.

124 S. Litster and G. McLean, *J. Power Sources* **130** (2004), p. 61.

125 H.A. Gasteiger and M.F. Mathias In: M. Murthy, T.F. Fuller and J.W. Van Zee, Editors, **Proceedings of the Third International Symposium on Proton Conducting Membrane Fuel Cells**, 202nd Meeting of ECS Salt Lake City (2002), p. 1. in Yuyan Shao, Geping Yin, Zhenbo Wang, Yunzhi Gao, Proton

exchange membrane fuel cell from low temperature to high temperature,: Material challenges, Journal of Power Sources, 167(2007), 235-242.

126 S. von Kraemer, M. Puchner, P. Jannasch, A. Lundblad and G. Lindbergh, *J. Electrochem. Soc.* **153** (2006), p. A2077.

127 M. Inaba, H. Yamada, J. Tokunaga and A. Tasaka, *Electrochem. Solid State Lett.* **7** (2004), p. A474.

128 S.J. Hamrock and M.A. Yandrasits, *Polym. Rev.* **46** (2006), p. 219.

129 R.I. Kvon, G.N. Il'inich, A.L. Chuvilin and V.A. Likholobov, *J. Mol. Catal. A-Chem.* **158** (2000), p. 413.

130 S.D. Fritts, D. Gervasio, R.L. Zeller and R.F. Savinell, *J. Electrochem. Soc.* **138** (1991), p. 3345.

131 S. Gottesfeld, I.D. Raistrick and S. Srinivasan, *J. Electrochem. Soc.* **134** (1987), p. 1455.

132 L. Zhang, C.S. Ma and S. Mukerjee, *Electrochim. Acta* **48** (2003), p. 1845.

133 E.B. Easton, T.D. Astill and S. Holdcroft, *J. Electrochem. Soc.* **152** (2005), p. A752.

134 P.J. Ferreira, R. Makharia, S. Kocha and H.A. Gasteigerc, *J. Electrochem. Soc.* **152** (2005), p. A2256.

135 Yunfeng Zhai, Huamin Zhang, Danmin Xing, Zhi-Gang Shao, **The Stability of Pt/C catalyst in H_3PO_4 / PBI PEMFC during high temperature life test,** Journal of Power Sources, 164 (2007), 126-133.

136 A. Pozio, M. De Francesco, A. Cemmi, F. Cardellini and L. Giorgi, *J. Power Souces* **105** (2002), p. 13.

137. S.M. Javaid Zaidi, S.U. Rahman, Halim H. Redhwi, **R&D activities of fuel cell Research at KFUPM**, Desalination 209, 319–327(2007).

138 A. Friedl, S.D. Fraser,W.R. Baumgartner, V. Hacker, **Experimental analysis of internal gas flow configurations for a polymer electrolyte membrane fuel cell stack**, Journal of Power Sources 185 (2008) 248–260

139 J. C. Lin, H. R. Kunz, J. M. Fenton, and S. S. Fenton, **The Fuel Cell-An Ideal Chemical Engineering Undergraduate Experiment.** Proceeding of the 2003 American Society for Engineering Education Annual Conference & Exposition, 2003.

140 Barbir, frano, **PEM Fuel Cells: Theory and Practice**, Elsevier Academic Press, Amsterdam, Boston, Heidelberg, London, New York, 1 edition, 2005.

141 Uwe Reimer, **Modeling of Fuel Cells**, 3rd International Summer School on Advenced Studies of Polymer Electrolyte Fuel Cells, TU-Graz, August 26th-September 1st, 2010

142 J. Larminie, A. Dicks, **Fuel Cell Systems Explained, Operational Fuel Cell Voltages**, Chapter 3, J. Wiley and Sons Ltd, 2003.

143 J. Ross Macdonald, William B. Johnson, Fundamentals of Impedance Spectroscopy, Chapter 1, Evgenij Barsoukov, J. Ross Macdonald, Impedance Spectroscopy,Theory, Experiment and Applications, Second Edition, Wiley-Interscience 2005.

144 Ryan O`Hayre, Suk-won Cha, Whitney, Colella, Fritz B. Prinz, **FUEL CELL FUNDAMENTALS, Fuel cell characterization,** Chapter 7, second edition, John Wiley & Sons (2009).

145 Gary A. Mabbott**, An Introduction to Cyclic Voltammetry**, *J. Chem. Educ.*, 1983, *60* (9), p 697

146 W. Vielstich, **Cyclic Voltammetry**, Chapter 14, W. Vielstich, H. Gasteiger, A. Lamm (Hrsg.), **Handbook of Fuel Cells, Fundamentals, Technology and Applications**, Volume 2, J. Wiley and sons Ltd, 2003.

147 H. A. Gasteiger, W. Gu, R. Makharia, M. F. Mathias and B. Sompalli, **Beginning-of-life MEA performance- Efficiency loss contributions** Editors, W. Vielstich, A. lamm, H. A. Gasteiger, **A hand book of fuel cells** volume (3) page 595, john wiley & Sons Ltd. England.

148 C. H. Hamann, A. Hamnett, W. Vielstich, Electrochemistry, Methods for the study of the electrode/ electrolyte interface, Chapter 5, Wiley-VCH, 1998.

149 PURDUE University, Radiological and Environmental Management, Scanning Electron Microscope, http://www.purdue.edu/rem/rs/sem.htm, downloaded on 04.05.2011.

150 Werner Grogger, Lecture notes of the course, **Scanning electron microscopy**, course code 519.003, winter semester 2007, Institute of electron microscopy, TUGraz, Austria.

151 Ralph TR, Hards GA, Keating JE, Campbell SA, Wilkinson DP, David M, et al. **Low cost electrodes for proton exchange membrane fuel cells**. J Electrochem Soc 1997; 144 (11): 3845-57.